Development of carbon-based materials grafted by ionic liquids

Alexandros Ploumistos

Sorbonne Université

Faculté des Sciences et Ingénierie

École doctorale de Chimie Physique et Chimie Analytique de Paris Centre – ED 388

Physicochimie des Électrolytes et Nanosystèmes Interfaciaux - PHENIX (UMR 8234)

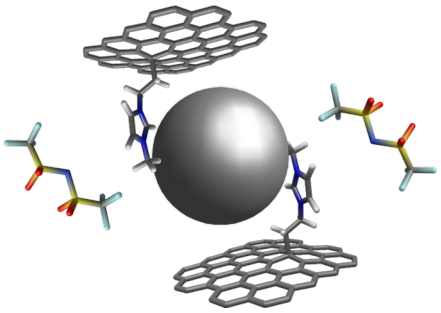

Development of carbon-based materials grafted by ionic liquids

Alexandros Ploumistos

Thèse de doctorat

Dirigée par Laurent GAILLON

Co-encadrée par Cécile RIZZI, Juliette SIRIEIX-PLENET et Anne-Laure ROLLET

Thèse soutenue le 26 avril 2022

Devant un jury composé de :

Mme Petra RUDOLF Hoogleraar, Rijksuniversiteit Groningen	Rapportrice
M. Fabien MIOMANDRE Professeur, École Normale Supérieure Paris-Saclay	Rapporteur
M. Aminou MOHAMADOU Professeur, Université de Reims Champagne-Ardenne	Examinateur
Mme Corinne LAGROST Directrice de Recherche CNRS, Université de Rennes 1	Examinatrice
Mme Virginie LAIR Maîtresse de conférences, Chimie ParisTech - Paris Sciences & Lettres	Examinatrice
Mme Cécile RIZZI Maîtresse de conférences, Sorbonne Université	Co-encadrante
M. Laurent GAILLON Maître de conférences, Sorbonne Université	Directeur de thèse

Table of Contents

Acknowledgments

First of all, I would like to thank Mrs. Corinne Lagrost for presiding over my thesis committee. With a great sense of gratitude I thank Mrs. Petra Rudolf and Mr. Fabien Miomandre for the honor of accepting to review my work and for taking the time to do so. Equally, I wish to thank Mr. Aminou Mohamadou and Mrs. Virginie Lair for agreeing to serve as members of my thesis committee. All of their questions and comments provided for an interesting and vivid conversation.

Pierre Levitz and Laurent Michot, the former and current directors of PHENIX, have welcomed me to the laboratory and were always on hand for scientific discussions or whatever else might arise and they have my gratitude. Laurent Michot, under the tenure of whom I have spent most of my time in the group, was actively involved in my thesis, spending countless hours poring over my SAXS data and also supporting me when it was needed the most and for that, I thank him doubly.

From the bottom of my heart, I wish to thank a quartet of some of the most wonderful, kindest people I have had the pleasure of meeting and getting to know, my supervisors, Laurent Gaillon, Cécile Rizzi, Juliette-Sirieix-Plénet and Anne-Laure Rollet. I am thankful for the chance they took on me and for always standing by me, despite my grasp and occasional misuse of the french language. All of them taught me many things over these years and I consider having worked with them both a pleasure and a privilege. Their different ideas and points of view helped shape and are reflected in this work.

Anything electrochemistry-related is Laurent's privileged domain, yet he approaches every issue and replies to every question in the most unassuming manner. His calm and assured demeanor provided safe anchorage during the most tumultuous times. I deeply regret subjecting him to so many meetings about organic synthesis and NMR spectra and giving him so few batteries in return. His insights and his help with my teaching duties were invaluable and immensely appreciated, as were his concise comments on this manuscript.

Cécile was the *de facto* and almost *de jure* director of this thesis, hadn't it been for the pandemic and the upheaval it caused with everyone's plans. While I am sure there is nothing unknown to her from the arcana of organic chemistry and ionic liquids, she will always refer to the literature, a habit I have come to appreciate and done my best to practice as well. She has been both a great teacher and a great human being to be around. Her inquisitive, keen and Socratic examination of every aspect of this work drove me to better understand everything and constantly learn new things. The diligence she has shown in proofreading this work was above and beyond any expectation.

A colleague recently remarked on the maternal qualities of Juliette, with regard to her patience and the interest she takes in our well-being and personal lives, a view I have come to share as well. Always jovial, it is as if nothing can ruin her mood and she lifts the spirits of everyone around her. Equally formidable as Cécile in the occult matters of organic synthesis, she is capable of assembling the glassware into the most intricate setups within seconds. I took full advantage of her knowledge and experience (and patience) during the long months I wrestled with every reagent and intermediate as I was trying to synthesize my ionic liquid. I also deeply profited from her experience as an educator when I attended her courses on teaching.

Anna-Laure is an expert on anything high energy, high frequency and high field, but this description does not do her justice; she is a multitalented, all-around person with many, diverse interests and a real joy to discuss with, regardless of subject. Perpetually in motion, she appears to be in constant violation of the first and second laws of thermodynamics. I have been lucky enough to receive some enlightening fragments of her compendious knowledge of NMR spectroscopies, X-ray scattering and diffraction and I have been equally lucky to have tasted her exquisite lemon tart. Her targeted and timely help with the writing of this manuscript was truly precious.

Quite early in this work, when some first difficulties arose with the preparation of aerogels, serendipity brought me to Francisco Fernandes from the LCMCP lab. Besides being really good at freezing things, Francisco is a kindhearted, ingenious researcher, full of great

ideas. He gave me full access to his lab and equipment and took the time to teach me all that I needed to know in order to advance my studies. He was my sounding board on multiple occasions and he would always point me to the devil hiding in the details that had escaped me. For all he has done, I am forever grateful.

Florie Lopis, the gifted glassmaker of Sorbonne University and José Gomes, our machinist, they both spent many hours fashioning small and large bits and pieces that I needed for my experimental setups. I could never thank them enough.

I have had many scientific discussions with almost every permanent member of PHENIX and they were all forthcoming in sharing their knowledge, providing insights and coming up with solutions. These great people make the lab what it is: a vibrant, cordial environment, producing quality science.

Amandine, Ana, Aude, Brigitte, Delphine, Frédéric, Gérard, Jeanette, José and Sandrine are the titans bearing the weight of the lab on their shoulders. Nothing would be possible without them, including this work. They all have my thanks.

I have had two generations of office mates; I am lucky to have met each and every one of them, and I have many fond memories with them inside and outside the lab. Such a great person and a friend is Mesut, with whom over these years we shared many awkward stares over our screens, many interesting discussions and plenty of good food. My newer colleagues, Antonio and Alice, have been very fun, supportive and they made the long, stressful days towards the end much more bearable. I thank them all.

I also wish to express my gratitude to all my other colleagues with whom we have shared so many moments during these years, we have helped each other and at times vented our frustrations on each other, but always in good spirit: Claire, Stella, Lydia, Briséïs, Camille, JB, Jeanne, Roxanne, Loïc, Sirine, Alessandra, Laura, Dominika, Ali, Sivagen, Kyle, Jesse, Emilia, Enzo, Cynara, Djamila, Ivette, Imane and I am sure I am forgetting more than one name – apologies for that.

I would be remiss if I did not thank Dramane and Luna, the intern students who worked

alongside me and contributed to the advancement of this study.

I would very much like to thank all the friends and teachers who helped steer me back towards chemistry and who have been accompanying me these years. I am particularly grateful to all the people who stood by me through all the ups and downs leading to the conclusion of this work. Finally, I would like to thank my family for their support.

List of abbreviations used in this work

1-MIm 1-methylimidazole

AAS atomic absorption spectroscopy

ATR attenuated total reflectance (or reflection)

BET Brunauer-Emmet-Teller (theory)

BSE backscattered electrons

CEI cathode-electrolyte interphase (or interface)

CMOS complementary metal-oxide-semiconductor

CV cyclic voltammetry

CVD chemical vapor deposition

DEC diethyl carbonate

DSC differential scanning calorimetry

DMSO dimethyl sulfoxide

DMF *N*,*N*-dimethylformamide

EC ethylene carbonate

EDX energy-dispersive X-ray spectroscopy

EIS electrochemical impedance spectroscopy

EMI^+ 1-ethyl-3-methylimidazolium

FSI^- bis(fluorosulfonyl)imide

GO graphene oxide

HOPG highly-oriented pyrolytic graphite

ICDD International Centre for Diffraction Data

IL(s) ionic liquid(s)

IUPAC International Union of Pure and Applied Chemistry

LCO lithium cobalt(III) oxide

LFP lithium iron phosphate

LMO lithium manganese oxide

MS mass spectrometry

NCA lithium nickel cobalt aluminium oxides

NGO hydrazine-treated graphene oxide

NMC lithium nickel manganese cobalt oxide(s)

NMR nuclear magnetic resonance

NP(s) nanoparticle(s)

PC propylene carbonate

PID (as in PID controller) proportional-integral-derivative

PTFE polytetrafluoroethylene

PXRD polycrystalline (or powder) X-ray diffraction

rGO reduced graphene oxide

SAXS small-angle X-ray scattering

SEI solid-electrolyte interphase (or interface)

SHE standard hydrogen electrode

SEM scanning electron microscopy

TEM transmission electron microscopy

TGA thermogravimetric analysis

$TFSI^-$ $[(CF_3SO_2)_2N]^-$, bis(trifluoromethanesulfonyl)imide

TSIL task-specific ionic liquid

XPS X-ray photoelectron spectroscopy

General introduction

Electrochemical energy storage

Biological systems have devised a rather efficient way of storing energy for their future needs: chemical bonds. When a metabolic process produces more energy than needed at the moment, that energy is stored away in the chemical bonds of molecules. Most plants store that energy in the bonds that make up starch. Animals put it away in triglycerides. Mankind has accessed that energy for its non-biological needs for millennia by setting everything on fire and then working with the released heat. It was only after 1800 and Volta's pile that a new approach to storing and using energy came to be.

A little over two centuries later, electrochemical energy storage has come a long way. Batteries can be found nowadays in anything from toys to pacemakers, to computers and cars. The energy stored in Volta's tabletop contraption can now be stored in a space no larger than a matchbox. Yet electrochemical energy storage and battery technology in particular still have a long way to go. A car battery of the lead-acid type can hold the equivalent of the energy contained in a sandwich[1] and arguably, it is much less portable.

Today more than ever, battery technology is being called upon to fill a number of roles and satisfy many different needs. The ongoing renewable energy transition is being driven in large by wind and solar power, with installed wind capacity increasing globally by 57 % and solar capacity by 37 % in the last decade alone[2,3]. These sources are by nature intermittent and solar power in particular reaches its peak production when demand is at its lowest. That energy should be stored and used when it is actually needed. Even if climate change was not happening, fossil fuels are a finite resource and as such, they will eventually run out.

Besides grid energy production, fossil fuels are mostly consumed for transportation. The switch to electrical motors comes with different energy storage requirements for cars, airplanes, ships and trains and not all of them can be fitted with enough solar panels to

power them. Furthermore, the urgent need to address climate change relies in part on the adoption of alternative, non-polluting technologies. Instead of asking people to change their habits, a technology that functions in the same manner as the already established one is more likely to be adopted. A car battery that does not take longer to charge than it takes to fill up a gas tank is such an example[4]. The rate of adoption is also inextricably tied to the cost. Current generation electric cars are too expensive for most people and a major part of that cost is their batteries.

From all of the above examples it is fairly evident that battery technologies are required to adapt to specific needs dictated by the applications as much as the intended users. The amount of energy stored, the required volume, the weight, the operating limits, safety, the cost and the estimated lifespan are all among the parameters that have to be taken into consideration when designing batteries and when employing them in particular applications (Figure 1). While there is no single battery technology that is perfect for every use case[5], the family of storage technologies built around the chemistry of lithium seems to be the most versatile, as it has been employed in anything from portable devices to grid systems[6].

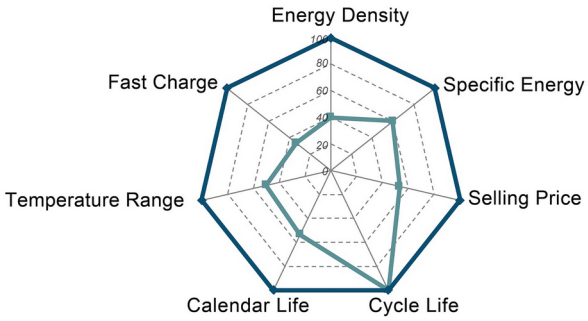

Figure 1: One common set of battery characteristics. Reprinted from [5].

Since their commercialization by Sony in 1991, Li-ion batteries have steadily displaced most other rechargeable battery technologies due to their innate characteristics and through their constant improvement, as there is still a lot of potential left unexploited in lithium chemistry[7]. In fact, during the period of 1990-2015, gains in the amount of energy they can store per unit of mass have been on the order of five percent per year and their price continues to fall (Figure 2). These improvements of every aspect of Li-ion batteries have

been the result of continuous and painstaking efforts, combining diverse disciplines that include chemistry, electrochemistry, materials science, physics, engineering, manufacturing and computer science. These efforts have produced new materials capable of storing more energy, they have reshaped existing materials in ways that augment the performance characteristics of batteries and they have recombined them in new configurations to increase their safety, their stability and to lower the cost. It is forecast that in the coming years, recent advances in analytical techniques, engineering methods and the development of new materials will double the capacity of Li-ion batteries, propelling them closer to the theoretical limits of lithium[6,7].

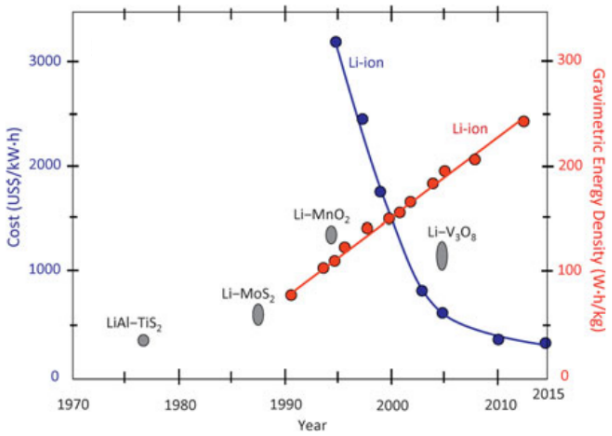

Figure 2: Evolution of the cost (blue, left axis) and the gravimetric energy density (red, right axis) of Li-ion batteries during the period of 1970-2015. The gravimetric energy densities of Li- or LiAl-metal anode batteries against four cathodes, commercialized in the years indicated and withdrawn from the market for reasons of safety or market appeal, are shown in gray. Adapted from [6].

This thesis was conducted within this context, the development of new materials that could endow Li-ion batteries with a higher capacity, lower weight and a faster charging rate. Tin has been considered as a replacement for graphite, which is typically found in Li-ion anodes, as it can store more lithium ions and thus, more energy and at a higher rate[8]. However, as the battery charges and discharges, the volume of tin increases three-fold, with damaging effects on the battery itself.

In order to utilize tin as an anode material, the very first step is reducing its size to the nanoscale. This, combined with enmeshing it in another substrate, could contain the volume changes, while maintaining the structural integrity of the electrode. This supporting

material would have to be flexible so as to adapt to the structural changes of tin. That was probably the weak point in the use of intermetallic alloys of tin such as Sn-Cu[9], Sn-Ni[10], Sn-Sb[11], Sn-Co[12], Sn-Fe[13], Sn-Al[14]. This supporting material would have to be conductive, in order to transfer electrons from tin out of the battery and vice versa. It would also have to possess an affinity for tin, so as to remain in contact with it as it contracts and expands, so that the battery may continue to function.

The present work was an effort to accomplish all of the above. An ionic liquid (IL), that had been previously found to be exhibiting favorable interactions with tin nanoparticles would grant the support material the aspect of affinity. A graphene-based matrix was chosen as the flexible, conductive scaffold onto which the ionic liquid would be affixed. Tin would be nanostructured and combined with the support material. Finally, composite materials would have to be studied and evaluated as active anode materials for lithium ion batteries. This work is divided into three chapters in the present document.

The first chapter presents the basic aspects, the functioning and the materials found in current generation lithium-ion batteries. It is followed by an introduction to ionic liquids, their key properties and some of their applications, with specific mention of applications pertaining to electrochemical energy storage. Tin and its oxides are also discussed, from the point of view of their use in Li-ion batteries. There is also a brief presentation of graphite and how its derivatives, graphene and graphene oxide (GO) could play a role in the next generations of batteries, especially combined with tin. The reasoning behind the design of the ternary composite material is presented at the end of the chapter.

The second chapter is focused on the synthesis and characterization of the three components of the composite material. Some of their relevant chemical aspects are also discussed. First comes the synthesis of graphene oxide and an investigation of how it could best play the role of the base of the matrix. The second section of the chapter is devoted to the preparation and characterization of tin nanoparticles. Finally, the third part of the chapter, presents the work that went into functionalizing the $EMI^{+}TFSI^{-}$ ionic liquid with an amino group, so that it could be grafted onto the matrix.

The third chapter details some of the experiments with binary systems, constituted of various graphene morphologies and $EMI^{+}TFSI^{-}$ and the grafting of the functionalized IL to GO, before thermal treatment. Investigations were carried out in order to prove the grafting of the IL. A comparative study of the behavior of the various graphene scaffolds towards lithium ions charge and discharge, allowed to select one among them for the preparation of the ternary composite. Next are described the combination of the three materials into a ternary composite and its characterization in terms of morphology and structure. Some preliminary battery tests of the targeted ternary material are presented at the end of the chapter.

The last part of the manuscript recapitulates and draws some general conclusions and discusses some of the perspectives that were opened in the course of this study.

References

(1) Munroe, R. Zippo Phone https://what-if.xkcd.com/128/.

(2) IRENA. *Renewable Power Generation Costs in 2020*; International Renewable Energy Agency: Abu Dhabi, 2021.

(3) Grubb, M.; Drummond, P.; Mercure, J.-F.; Hepburn, C.; Barbrook-Johnson, P.; Ferraz, J. C.; Clark, A.; Anadon, L. D.; Farmer, D.; Hinder, B.; Ives, M.; Jones, A.; Jun, G.; Kelkar, U.; Lam, A.; Mathur, R.; Pasqualino, R.; Penasco, C.; Pollitt, H.; Ramos, L.; Roventini, A.; Salas, P.; Sharpe, S.; Songli, Z.; Vercoulen, P.; Waghray, K.; Xiliang, Z. The New Economics of Innovation and Transition: Evaluating Opportunities and Risks. 72.

(4) Tomaszewska, A.; Chu, Z.; Feng, X.; O'Kane, S.; Liu, X.; Chen, J.; Ji, C.; Endler, E.; Li, R.; Liu, L.; Li, Y.; Zheng, S.; Vetterlein, S.; Gao, M.; Du, J.; Parkes, M.; Ouyang, M.; Marinescu, M.; Offer, G.; Wu, B. Lithium-Ion Battery Fast Charging: A Review. *eTransportation* **2019**, *1*, 100011. https://doi.org/10.1016/j.etran.2019.100011.

(5) Sagoff, J. The continuing quest to find a better battery https://www.anl.gov/article/the-continuing-quest-to-find-a-better-battery.

(6) Crabtree, G.; Kócs, E.; Trahey, L. The Energy-Storage Frontier: Lithium-Ion Batteries and Beyond. *MRS Bull.* **2015**, *40* (12), 1067–1078. https://doi.org/10.1557/mrs.2015.259.

(7) Winter, M.; Barnett, B.; Xu, K. Before Li Ion Batteries. *Chemical Reviews* **2018**, *118* (23), 11433–11456. https://doi.org/10.1021/acs.chemrev.8b00422.

(8) Obrovac, M. N.; Chevrier, V. L. Alloy Negative Electrodes for Li-Ion Batteries. *Chem. Rev.* **2014**, *114* (23), 11444–11502. https://doi.org/10.1021/cr500207g.

(9) Pu, W.; He, X.; Ren, J.; Wan, C.; Jiang, C. Electrodeposition of Sn–Cu Alloy Anodes for Lithium Batteries. *Electrochimica Acta* **2005**, *50* (20), 4140–4145. https://doi.org/10.1016/j.electacta.2005.01.041.

(10) Hassoun, J.; Panero, S.; Simon, P.; Taberna, P. L.; Scrosati, B. High-Rate, Long-Life Ni–Sn Nanostructured Electrodes for Lithium-Ion Batteries. *Adv. Mater.* **2007**, *19* (12), 1632–1635. https://doi.org/10.1002/adma.200602035.

(11) Wachtler, M.; Winter, M.; Besenhard, J. O. Anodic Materials for Rechargeable Li-Batteries. *Journal of Power Sources* **2002**, *105* (2), 151–160. https://doi.org/10.1016/S0378-7753(01)00934-X.

(12) Ferrara, G.; Arbizzani, C.; Damen, L.; Guidotti, M.; Lazzari, M.; Vergottini, F. G.; Inguanta, R.; Piazza, S.; Sunseri, C.; Mastragostino, M. High-Performing Sn–Co Nanowire Electrodes as Anodes for Lithium-Ion Batteries. *Journal of Power Sources* **2012**, *211*, 103–107. https://doi.org/10.1016/j.jpowsour.2012.03.066.

(13) Yoon, S.; Lee, J.-M.; Kim, H.; Im, D.; Doo, S.-G.; Sohn, H.-J. An Sn–Fe/Carbon Nanocomposite as an Alternative Anode Material for Rechargeable Lithium Batteries. *Electrochimica Acta* **2009**, *54* (10), 2699–2705. https://doi.org/10.1016/j.electacta.2008.11.060.

(14) Hu, R.; Shi, Q.; Wang, H.; Zeng, M.; Zhu, M. Influences of Composition on the Electrochemical Performance in Immiscible Sn−Al Thin Films as Anodes for Lithium Ion Batteries. *J. Phys. Chem. C* **2009**, *113* (43), 18953–18961. https://doi.org/10.1021/jp9076257.

Chapter 1:
Introduction – state of the art

1. On lithium-ion batteries

Though most people rarely think about them, (at least not until they have run out), lithium-ion – or "Li-ion" or "LIB" for short – batteries have played a central role in shaping our daily lives and habits in the last three decades. The ubiquity of portable devices, such as cell phones, laptops, fitness trackers, electric toothbrushes, wearable medical monitors, power tools and so on, is largely due to the advent of Li-ion batteries. Humanity's overdue energy shift from fossil fuels is also in part propelled by the same technology: electric unicycles, skateboards, bicycles, motorcycles, cars, vans, buses and trucks owe their existence to – or at the very least have benefited from – recent advances in Li-ion technology. Even battery-powered trains may soon become a reality. At even larger scales, Li-ion batteries complement renewable energy sources, offsetting their intermittence at residential, rural or even city-wide levels, taking over when the sun doesn't shine or when the wind doesn't blow and then they recharge when energy production exceeds demand[1–4].

"Lithium-ion battery" is an umbrella term that encompasses a broad range of secondary cell (or plainly, rechargeable battery) technologies, all of which share the same basic principle of operation: lithium metal is oxidized at the anode and its ions migrate towards the cathode, while at the same time, the electrons move in the same direction, but in the external circuit, performing useful work along the way. When the batteries are being charged, the process is reversed and electrons and ions make the journey back in the opposite direction. By convention, the terms anode and cathode refer to the polarity of the terminals during discharge. Both processes, charging and discharging, and the basic components of a lithium-ion electrochemical cell are represented schematically in Figure 1.1. For anyone not familiar with battery technologies, the term "lithium-ion" might be a little misleading; after all, it's hard to imagine a redox system comprising lithium, where its ionic form is not present. This term actually refers to systems where Li is hosted in another material, in contrast to batteries with purely metallic lithium anodes. Except for very small

batteries, in which case the terms “battery” and “cell” refer to the exact same thing, most Li-ion batteries consist of several electrochemical cells, the smallest units capable of electrochemical energy conversion and storage. For applications with higher energy demands, such as vehicles or home energy storage systems, several batteries are combined and arranged in packs. Most batteries more complex than a single cell also contain an integrated circuit (BMS, battery management system), which can perform different functions such as monitoring the health of the battery and taking the battery offline in case of failure.

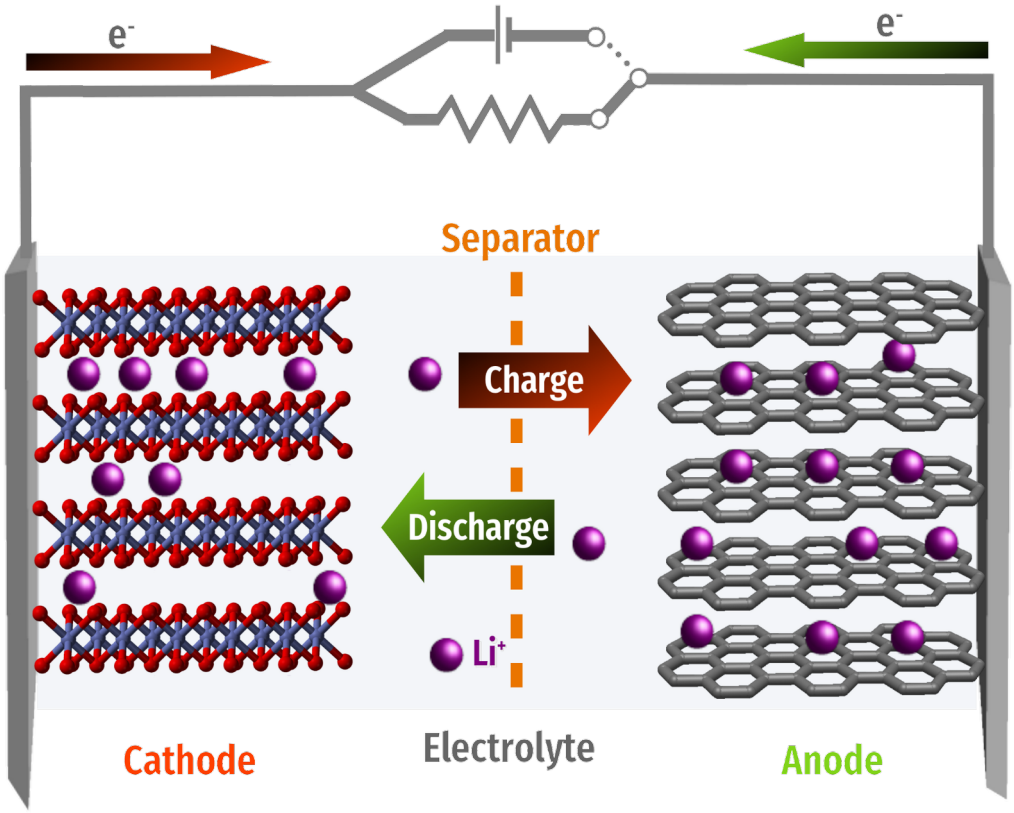

Figure 1.1: Operating principle of Li-ion batteries.

The ever-increasing global demand for more and better performing batteries has led to fierce competition among businesses in the sector. As a result, the exact makeup of the latest generations of lithium-ion batteries is almost always a closely guarded trade secret. Despite that, it is still possible to describe the composition of modern commercialized lithium-ion batteries in somewhat broad terms. The active material of the anode is always made of some form of graphitic carbon, between the sheets of which the lithium ions are hosted when the

battery is charged. Cathodes typically consist of lithium-containing mixed metal oxides or salts; the lithium ions are stabilized in the structure through interactions with the oxygen atoms or anions in the material as the batteries discharge and then migrate towards the anode during charging. These crystalline materials can be layered, as in the case of lithium cobalt oxide, $LiCoO_2$, (the cathode material depicted in Fig. 1.1) with the lithium ions occupying the space between adjacent layers. They can also be continuous crystals, usually adopting olivine (*e.g.* $LiFePO_4$) or spinel (*e.g.* $LiMn_2O_4$) structures, where the lithium ions are spread evenly throughout the crystal. Commercial Li-ion electrolytes comprise lithium salts dissolved in organic, aprotic solvents. The anion in these salts is usually voluminous (*e.g.* PF_6^-, BF_4^-, $CF_3SO_3^-$) and hence weakly interacting with the cation, so that it doesn't impede the movement of lithium ions into the electrode materials. The organic solvents are most often mixtures of organic carbonate esters (such as ethylene carbonate and diethyl carbonate) and/or various ethers (*e.g.* dimethoxyethane, dioxolane and tetrahydrofuran). There is also a subclass of Li-ion batteries, in which conductive polymers – usually semisolid or gel-like – are substituted for the liquid solvent. These batteries are named "lithium polymer" or more properly "lithium-ion polymer" batteries, often abbreviated as "LiPo", "Li-poly", "LIP", *etc.*. Not having to contain a liquid component allows for a greater leeway in the design of the cells and alleviates the need for a rigid, sturdy shell, resulting in a decrease in their weight. Given these traits, LiPo batteries are generally preferred when the application calls for very specific battery shapes and low weight; the manufacture of cell phone batteries is a case in point.

Before going any further, a few key concepts need to be introduced, as they constitute the metrics based on which battery materials and technologies are evaluated. The first criterion in assessing the active material of a battery is its "specific capacity" or "gravimetric capacity". This refers to the capacity per unit of mass and for batteries, this is usually expressed in milliampere hours per gram, mAh/g. Another concept is the "specific power" of a battery, expressed in watts per gram, W/g. Equally important is the "volumetric capacity", the capacity per unit of volume. Its dimensions are usually milliampere hours per cubic

centimeter, mAh/cm^3. The rate of charge or discharge of a battery, usually referred to as the C-rate, is defined as the current drawn from the battery divided by the theoretical current under which the battery would deliver its nominal rated capacity in one hour. As an example, a battery with a nominal capacity of 400 mAh, discharged at a current of 400 mA, which corresponds to a C-rate of 1C, will be emptied within one hour. Conversely, the same battery charged at a C-rate of C/4, so at a current of 100 mA, will take four hours to recharge. C-rates depend on charge and mass transport phenomena, electronic and ionic conductivity and electron-transfer kinetics. It is calculated on the basis of the capacity of a given battery. Besides the specific capacity of an active material, the practical or useful capacity of the resulting cell is an equally important metric[5]. This takes into account the actual capacity of the finalized battery employing that material, in a specific design and with the "dead weight" and limitations made necessary by the specific material and its chemistry (*e.g.* choice of materials, structuring, operating conditions, *etc.*). For instance, $LiCoO_2$ has a theoretical capacity of 274 mAh/g. However, for structural and safety reasons, batteries employing pristine $LiCoO_2$ in their cathodes cannot exceed a useful capacity of 165 mAh/g[6,7]. Other important factors that need to be taken into account when assessing a battery can also be mentioned, such as its discharge voltage, its lifetime, its safety, its cost, its operating temperature range and its environmental friendliness.

Since their commercialization in 1991[8], Li-ion batteries have seen numerous improvements, with each generation paving the way to new potential applications. In turn, some of these new applications have brought to light the shortcomings of the state of the technology and driven new advances. For instance, it did not make sense to use lithium-ion batteries to power electric vehicles until their energy density had sufficiently increased, *i.e.* a higher charge in a lighter battery. Once the technology had matured enough and the first Li-ion powered cars reached consumers, it became obvious that charging times needed to be shortened and the safety of the batteries to be improved, if they were to see wider adoption.

Such challenges have usually been addressed by a variety of different means. Modifying

the chemistry of the battery, in essence the choice of materials and electrolyte, can have an impact on almost all of the battery's properties, from its capacity to its safety. The geometry and the structure of the components also play an important role at different levels: both the nanostructure and the macrostructure are intricately connected to how fast the battery can charge and discharge, to its mechanical stability and to its heat dissipation ability.

First and foremost though, it was the chemical modifications that brought Li-ion batteries out of the laboratory and led them to steadily displace other types of rechargeable batteries, eventually making them the predominant electrochemical energy storage technology used in anything from microelectronics to electric vehicles. At the same time, the specific needs of such applications fueled the research that enabled them. These modifications endowed them with high energy and power densities (up to 705 Wh/L and 10000 W/L respectively[9]), rather fast charging times, a relatively elevated electrochemical potential (up to 4V for certain types of batteries[10]), and a convenient operating temperature window (5-45°C). Meanwhile, the selection of materials and synthetic methods (along with the economies of scale) have contributed to their steadily decreasing cost[11,12].

Compared to the rate at which other technologies, *e.g.* microelectronics have matured, the pace of the evolution of electrochemical energy storage and that of lithium-ion batteries in particular, seems rather slow. This is by no means due to a lack of interest or effort. The three main components of a LIB presented above, the anode, the cathode and the electrolyte, and – to a lesser extent – the separator (and in reality, anything else that might be in contact with the system, *e.g.* casings, current collectors, *etc.*) have to be improved, but moreover they should be or remain compatible with each other. This is to ensure the usefulness, the safety and the longevity of the battery – the latter both on the shelf and while in operation. Essentially, being compatible means that each of them should not react spontaneously with the others and that all of them should be stable within the operating conditions and vitally, these conditions should not exceed the electrochemical window of the electrolyte and the solvent, *i.e.* the potentials exhibited by the system should not result in

their oxidation or reduction. Whenever a breakthrough comes along in one of the components, it cannot just replace the old one in the system; all of the other constituents need to be adjusted to work with the modified chemistry. In the case of lithium, it is the same innate characteristic – its low reduction potential, one of the lowest among metals – that makes it attractive for use in batteries, that also renders the task of finding compatible materials herculean.

Lithium has a reduction potential of -3.04 V[13] (*vs.* standard hydrogen electrode). What this means practically, is that the half reaction $Li^+ + e^- \rightharpoonup Li^0$ will preferentially take place in the opposite direction than the one it is written in, so lithium metal has a tremendous propensity to lose its electron and get oxidized. This makes Li an excellent reducing agent, but also extremely difficult to work with. For instance, it will readily react with the nitrogen and the moisture in the atmosphere, producing Li_3N, LiOH (and $LiOH \cdot H_2O$) and a subsequent reaction between the hydroxide and carbon dioxide yields Li_2CO_3[14]. Incidentally, this excessive reactivity is also the reason why lithium was first identified in 1817, but was isolated in its metallic form four years later[15]. The low reduction potential and the other elemental properties of lithium directly translate to Li-ion batteries' key advantages. That same potential is responsible for the batteries' high voltage. The low atomic mass makes the batteries light. The small size of the lithium ion, 0.59 Å[13], as well as it being monovalent facilitate its diffusion and make it relatively easy to shed its solvation sphere; for a battery, this means faster charging and discharging.

It is often stated that the history of lithium-ion batteries begins with the one made by Stanley Whittingham at Exxon Mobil in the 1970s[16]. While technically true and certainly a major breakthrough, as this was the first battery employing lithium ions instead of lithium metal, many decades of fundamental research and practical inventions preceded and led to that moment. It is hard to pinpoint the genesis of lithium-based electrochemical storage. Alessandro Volta had demonstrated his battery in 1799 and the first quarter of the 19th century was marked by the isolation of a number of metallic elements, among them lithium.

This lead to a frenzy to produce batteries with an ever higher electromotive force, by trying different elemental combinations, in setups similar to that of Volta. Keeping in mind lithium's reactivity, it is easy to guess why it took almost a century for someone to document its use in a battery. In 1919, Thomas Edison, who had been trying to come up with a suitable energy source for his electric vehicles, filed a patent for a nickel-iron battery containing lithium hydroxide in its electrolyte formulation[17]. According to another source[18], he had probably also filed a patent for a lithium battery in 1907.

Over the years, many detailed retrospectives of Li-ion batteries have been published. Among them, two stand out: a well-researched recent one by Winter et al.[15] and that of Brandt[19], though the latter fails to account for the last two and a half decades, since it was written a little after the first lithium-ion batteries had been commercialized. That missing time span is covered by a highly cited review by Etacheri et al.[20]. What follows is not another chronicle of the evolution of Li-ion batteries, but rather a concise highlighting of some of the events that brought the technology to its current state, with regard to the electrolytes, the electrode materials and the passivation layers.

1.1. Electrolyte

Following Winter's narrative, the groundwork for identifying suitable electrolytes for lithium-based batteries and understanding the corresponding solvation mechanisms was laid in the 1950s and 1960s. The first noteworthy milestone in that quest was published by William S. Harris in 1958[21]. Harris was investigating the suitability of various nonaqueous aprotic solvents (all of them cyclic esters) for the electrodeposition of metals whose reduction potentials were too high – in absolute value – for water. Though his work was focused on the isolation of the metals from their halide salts, its importance for battery chemistry is immediately apparent. When charging a Li-ion battery, lithium ions are reduced at the anode, much like during electrodeposition. Since water is split (through electrolysis) at

a potential difference of approximately 1.23 V at 25°C[22], it was critical to have available a solvent that could tolerate the high potential differences exhibited by a system where lithium is oxidized and reduced. Among the solvents Harris experimented with were ethylene carbonate (EC) and propylene carbonate (PC) (Fig. 1.2). These two – especially ethylene carbonate – along with a host of other members of the carbonate esters family, make up the bulk of the solvents of choice in modern Li-ion batteries. Harris's observations on the interactions of the solvents with lithium halides and his hypothesis that the anions would be less preferentially solvated than the cations, would prove crucial for the studies that followed. Even before Li-ion batteries, the organic carbonates were fundamental in the creation of primary (*i.e.* single-use) lithium metal batteries, allowing for the first time to harness lithium's high specific capacity (3.86 Ah/g[23]).

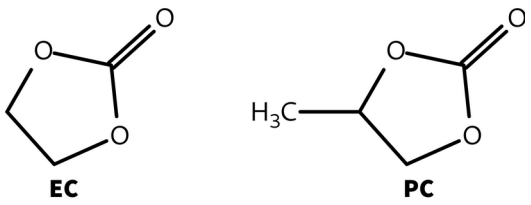

Figure 1.2: Ethylene carbonate (left) and propylene carbonate (right)

1.2. Lithium storage in the anode and the cathode

Lithium ions can be reversibly hosted in the structure of the cathode and the anode, without undergoing any chemical reaction, as illustrated in Figure 1.1 by lithium cobalt oxide and graphite, which are both examples of insertion and intercalation materials, respectively. Such materials, which expand on the chemistry of host-guest systems[24], had been described since the late 1960s[25]. Not long after that, they begun to be investigated as potential electrode materials for novel types of batteries, in contrast to the conversion-reaction electrodes employed so far and typically in primary cells.

Conversion electrodes release their stored energy through a reaction (irreversible in the

case of primary batteries), which entails the transformation of one or both electrodes into a different chemical compound in the process. For example, nickel-cadmium batteries exhibit such behavior in both their electrodes. During discharge, the cadmium anode is converted to cadmium hydroxide and the nickel(III) oxide hydroxide cathode in turn becomes nickel hydroxide, giving the following net reaction:

$$2\ NiO(OH) + Cd + 2\ H_2O \rightarrow 2\ Ni(OH)_2 + Cd(OH)_2$$

In the case of Li-ion batteries, transition metal oxides are examples of conversion anodes, where the metal oxide, M_xO_y, transforms into a solid mixture of $M_xO_y/M^0/Li_2O$, when the battery is charged and reverts back to the oxide as it discharges[26].

In a host-guest system, the guest is retained in the structure of the host through non-covalent interactions; as such, under specific circumstances, the guest can be released. Batteries operating in that manner, with a suitable guest ion being inserted and removed from a host electrode were known under many names over the years, such as “ion transfer cells”, “shuttle-cock batteries”, “rocking chair batteries” and others.

There is an obvious advantage in switching from a conversion system to a host-guest one. As a conversion material transitions from one form to another, it is impossible to precisely control the reformation of a solid phase. While precautions may be taken in order to limit or eliminate elements that could induce unwanted nucleation elsewhere in the battery, it is nearly impossible to control the direction of growth, or the sites at which it will take place in the active material. This can produce an inhomogeneous structure, which in turn may induce mechanical failure or short circuits in the battery. This is one of the main problems of Li metal anodes. When the Li^+ ions return from the cathode, nucleation on the surface of the metal is uneven. As crystallization happens with a preferential growth pattern, small wire-like structures, known as “dendrites” begin to form on the anode. After several cycles, the dendrites become big enough to pierce the separator and short-circuit the battery.

In the case of intercalation materials (*i.e.* olivine, layered and spinel-type[27]), the anode

and the cathode of a battery may experience different volume changes during cycling and they usually do. However, they do so in a consistent, predictable manner. Knowing beforehand the amount of expansion and contraction permits the pairing of compatible materials and the calculation of any extra mechanical tolerance the system may have to be endowed with, *e.g.* in the form of a spring. For some materials, this volume expansion is so significant, that their lifespan is inevitably reduced due to mechanical stress, that technical solutions need to be applied.

Such is the case of alloying host materials, *e.g.* Sn or Si. Their behavior lies somewhere between these of conversion materials and intercalation hosts. Alloys are not considered compounds and they do not undergo a chemical reaction when they form. However, there exist alloys with well-defined (stoichiometric) structures, often called intermetallic alloys, which can be formed electrochemically as they incorporate lithium into their mass.

For a long time, researchers were convinced that a Li metal anode would soon appear for use in a rechargeable battery. As a result, much more effort went into the preparation of an intercalation cathode and the anode was neglected, at least at first. Among the first cathode intercalation materials tested were chalcogenides and metal oxides (*e.g.* TiS_2, WO_3, NbS_2, CrO_x, MoO_3, and V_2O_5)[15]. While these successfully demonstrated the lithium intercalation concept, the cells suffered from low voltage and energy density. The first major breakthrough came from Gooodenough's group in 1980[28], in the form of lithium cobalt oxide, $LiCoO_2$ (or LCO for short). After examining a series of layered transition metal oxides of the type $LiMO_2$ (M = V, Cr, Co, Ni and Fe) LCO was found to be the best-performing, reaching a potential of 4.7 V *vs.* Li/Li^+ and being capable of releasing up to 93.3 % of the intercalated lithium[28]. LCO is still being used today, mostly to power consumer electronics. LCO reignited interest in cathode intercalation materials and the renewed focus on them in the following years led to the other, now common, intercalation cathode structures.

Lithium nickel manganese cobalt oxides (NMC), $LiNi_xMn_yCo_zO_2$, with x + y + z = 1, belong to the same family of lamellar oxides as LCO. Their combination of characteristics in terms

of energy density, safety and manufacturing costs have led to NMC being the dominant cathode chemistry used in car batteries. Also part of the group of lamellar oxides, lithium nickel cobalt aluminium oxides (NCA), $LiNi_xCo_yAl_zO_2$, with x + y + z = 1, are seeing increased usage in recent years, despite their higher material costs and potential safety issues[29,30]. This is in part due to their higher energy density and fast charging capabilities, but also due to their extended lifespan, which translates to a lower cost over the lifetime of the battery. A lot of research efforts into lamellar mixed oxide chemistry have focused on the properties derived from the relative ratio of each metal in the mixture[31–33]. Through variations in the stoichiometry of the metals, it has been possible to lower the cost, increase the capacity and improve the safety of such Li-ion batteries.

Lithium manganese oxide (LMO), $LiMn_2O_4$, is the main representative of the spinel family. The three-dimensional structure permits the faster intercalation and deintercalation of lithium ions and consequently can sustain higher battery charge and discharge rates than two-dimensional layered structures[34]. Manganese is a relatively earth-abundant element, which contributes to the low cost of batteries of this type.

Lithium iron phosphate (LFP), $LiFePO_4$, is another commonplace Li-ion cathode material[35]. Unlike the previously mentioned chemistries, LFP constituents are much more abundant and as a result, less costly. That, combined with LFP batteries' extended lifespans (67% longer than NMC cells[36]) and safety characteristics has granted them considerable market acceptance, despite their lower energy density. Also, the olivine structure of the material allows the fast diffusion of lithium ions, so LFP batteries can attain high charge-discharge rates.

On the anode side of the battery, the transition to intercalation materials was not as fast. Besides the optimism about Li metal anodes sometime "soon" becoming available, another obstacle that delayed the advent of the graphite intercalation anode used today, by almost twenty years, was the choice of solvent. Reasoning that ethylene carbonate and propylene carbonate were essentially "the same", since they only differ by a methyl group, PC was the

preferred solvent in most studies, as its melting point, - 49.2°C, is lower than that of EC (36.4°C)[21]. Dey and Sullivan discovered in 1970 that propylene carbonate cointercalates with Li^+ and decomposes on the graphite anode, exfoliating it in the process[37]. Thinking that ethylene carbonate would produce the same result, no one bothered to check the combination of EC and graphite until 1991.

Early commercial Li-ion battery anodes made use of carbonaceous materials with a rather disordered structure, such as petroleum coke, under the impression that structural disorder was important in order to avoid exfoliation from PC-based electrolytes[15]. However around the mid-eighties, Japanese researchers, started producing successful designs, with hard carbon anodes, resembling the structure of graphite, which cast doubt on the assumption that structural disorder was requisite. At the same time period, a number of patent claims for batteries with PC-free and EC-based electrolytes and graphite or graphite-like materials also appeared from Japan. One of them from Sanyo in 1991 detailed the intercalation of Li^+ in natural and synthetic graphite, positively demonstrating the electrochemical synthesis of LiC_6, the structure of fully lithiated graphite[15].

1.3. Solid-electrolyte interphase

The electrochemical synthesis of LiC_6 had been in fact first documented a year earlier, by the group of Dahn[38] and interestingly provided clues to the final component of modern Li-ion battery chemistry, the solid-electrolyte interphase, or SEI. While their electrolyte formulation contained some PC, which affected the first-cycle coulombic efficiency, in their Li/graphite cells* they measured a capacity close to the theoretical value for graphite (372 mAh/g) at a potential of 0.10 V *vs.* Li/Li^+. More importantly, they recognized that irreversible electrolyte decomposition takes place during the first discharge, which creates a film on the

* While graphite is typically an anode material in Li-ion batteries, in a cell with metallic Li it will function as the cathode.

surface of the graphite cathode. The quantity of decomposed electrolyte was proportional to the surface of graphite. They also found that intercalation and deintercalation proceed fully and reversibly once that initial film is formed. They were unable to identify the nature of the passivation layer, but they suggested it was Li_2CO_3-based. Through these insights, researchers started to recognize the importance of the passivation layer (SEI) in the functioning of the battery and realized that a similar phenomenon must also take place on the cathodes of Li-ion batteries, leading to the formation of what is now called cathode-electrolyte interphase (CEI). This work paved the way for modern electrolyte formulations, that take into account the nature of the electrodes and include additives consumed during the first cycle of the battery, in order to form stable passivation layers, that prevent further unwanted reactions, without hindering lithium ion intercalation.

1.4. An endless quest

As hopefully this introduction has demonstrated, the evolution of Li-ion technology has been gradual and the product of the efforts of thousand of researchers, over a long time span. To the casual user a battery may seem as a simple, inconsequential object. Yet it is remarkably intricate and like every complex system, it requires not only an extensive study of the individual parts, but also how all of them are tied together in a concerted manner.

It is clear that the current state of the art does not yet fully exploit the potential of the materials. Every single element of a battery can be made better, by chemistry and by engineering. Understanding the phenomena at play has not been easy, nor fast and more often than not, every question answered raises even more questions. Very few of the possible avenues that could be explored for the refinement of the basic components have been presented here. There remains a myriad of other aspects that could be crucial in the next iterations of the technology. Anything from creating nanopatterns on an active material to controlling the temperature at which the battery is charged might be key in giving Li-ion

batteries a little extra energy, some more charge-discharge cycles, a faster charging rate, more mechanical strength, or in making them safer or easier to recycle. At the same time and while the technology is still being improved, environmental, humanitarian and political motives are also driving its evolution in different directions and even paving the way for its replacement.

2. Ionic liquids

2.1. Definition and structure

Ionic liquids (ILs) are a class of ionic compounds with the defining characteristic of being liquid at temperatures below 100°C[39]. Yet another, more recent definition states that they are "water-free organic salts showing a melting point at temperatures below their decomposition"[40]. They belong to the same family as classic molten salts (usually mixtures like NaCl-KCl, LiCl-KCl, LiF-BeF_2, *etc.*)[41], but with their low melting points differentiating them from the rest of the family. Because of this key property, they are often referred to in the literature as "room temperature ionic liquids" (RTILs), "room/low/ambient temperature molten salts", "liquid organic salts", *etc.*[42].

Ionic liquids are salts, usually consisting of an organic cation and an inorganic or organic anion. Unlike molten salts, the voluminous, dissymmetric nature of the cation prevents the close packing of the ions, restricting the interactions of the ion pair and preventing the adoption of stable spatial conformations. The most obvious result of this hindrance, is the low melting of ILs. However, the interactions between the ionic species endow ionic liquids with a characteristic property, negligible vapor pressure[42].

Some of the most common cations or cationic structures of ionic liquids are based on quaternary ammonium salts, such as tetraalkylammonium and heterocyclic aromatics, *e.g.* imidazolium and pyridinium, or not, such as pyrrolidinium, but there also exist ionic liquids with cations based on sulfonium, phosphonium and others (Figure 1.3). In the case of the anions there also exists a wide selection. Among the most frequently encountered inorganic anions are halides, nitrate, tetrafluoroborate and hexafluorophosphate. As for organic anions, dicyanamide (DCA), bis(fluorosulfonyl)imide (FSI) and bis(trifluoromethylsulfonyl)-imide (TFSI) are often present[42,43]. A few of the possible choices for anions are shown in

Figure 1.4.

Without taking into account combinations of more than two ionic species or the variations offered by functionalization, it is estimated that over a million ionic liquids are possible[44]. Of course, different combinations of ionic pairs will have different properties, as will be the case for variations of length or the form of the substituents of the main ions.

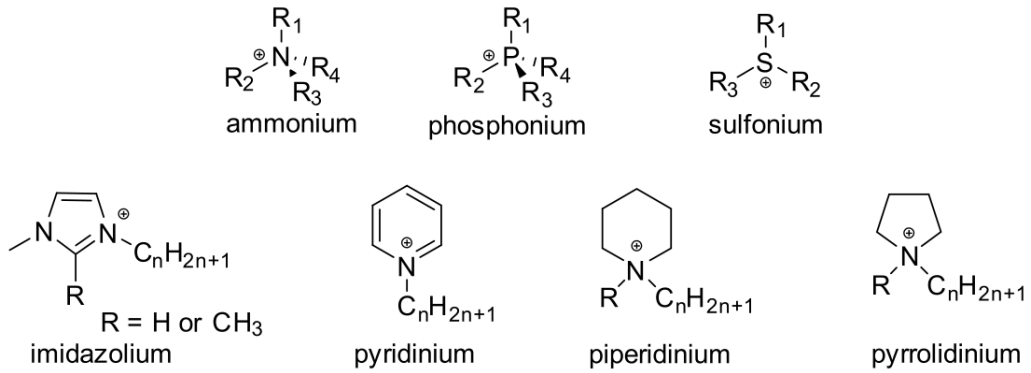

Figure 1.3: Cations which are widely used for ionic liquids.

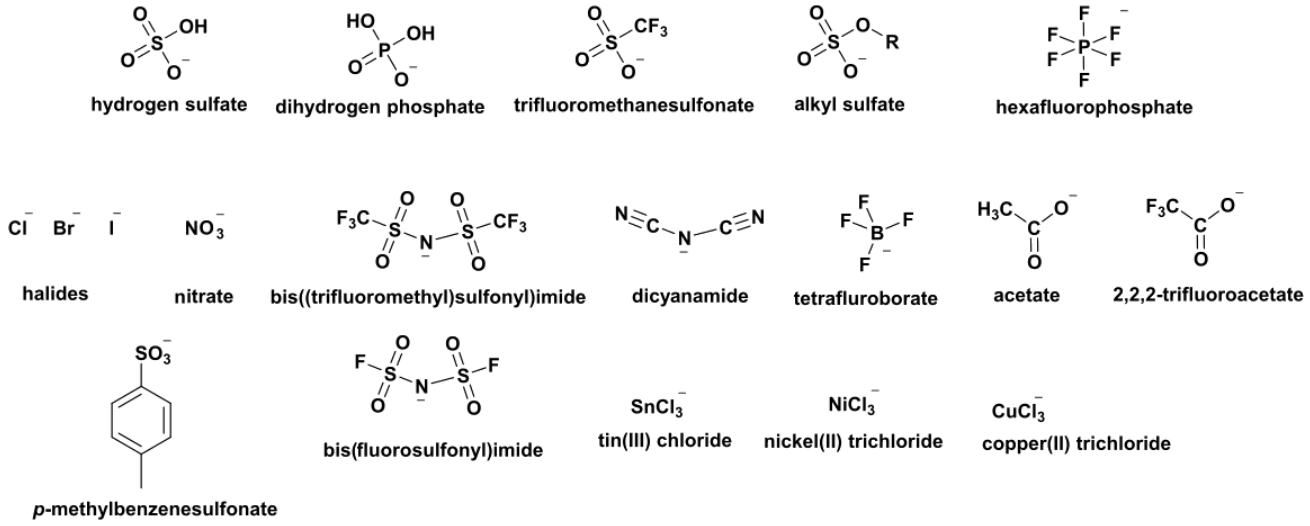

Figure 1.4: Anions which are widely used for ionic liquids. Adapted from [42].

While the IUPAC nomenclature is more than sufficient to describe the complex organic ions found in ionic liquids, for practical reasons, a simpler, but non-standardized shorthand notation with several variations is often employed with the most common ILs. As an example, the ionic liquid 1-ethyl-3-methylimidazolium bis(trifluoromethylsulfonyl)imide, which has been used in this study (Fig. 1.5), can be found in the literature written as any of

the following – among others: [EMIm][TFSI], [EMI][NTf_2], EMITFSI, EMI^+TFSI^-. This document follows that last convention, with the cation written as EMI^+ and the anion as $TFSI^-$.

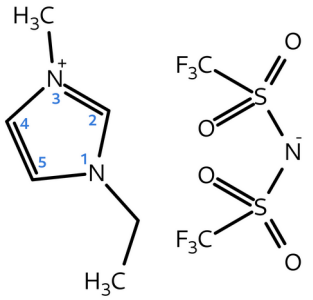

Figure 1.5: The EMI^+TFSI^- ionic liquid.

2.2. Task-specific ionic liquids

With ionic liquids being, well, liquid at a wide range of temperatures, the most obvious and most common use for them is as solvents. Initially they were proposed as alternatives to organic solvents due to their negligible vapor pressure and consequently the lower risk posed to users. Their synthesis however, can require the use of organic solvents anyway and in recent years more data has become available about the toxicity of several families of ionic liquids[45]. Moreover, their purification and isolation can be challenging. In any case, most of the organic ionic species lend themselves well to chemical modification or functionalization. By employing any reaction or series of reactions from the vast arsenal of general organic chemistry, it is possible to add any number of different functional groups, such as amines, carboxylic acids, alcohols, thiols, ethers, esters, unsaturated bonds, *etc.*[46–48], or form stereogenic centers, making the ions chiral[49]. Through functionalization, new properties are imparted upon the ionic liquids, or their preexisting ones can be tailored to a specific application.

The purposeful modification of ionic liquids in order to make them suitable for a given function led to the term “task-specific ionic liquids” (TSILs), coined by James H. Davis[50]. As

explained by C. Chiappe and C.S. Pomelli, TSILs are organic salts with covalently bound functional groups on the cation and/or the anion, whose role is not limited to that of a solvent, but they serve a specific function. A more recent definition encompasses any salt exhibiting the properties associated with ionic liquids – melting point below 100°C, being liquid in a wide temperature range and negligible vapor pressure – that has been functionalized explicitly with the purpose to accomplish a given task, without necessarily being the reaction medium[51]. A task-specific ionic liquid with an added amine group could be used for instance for the capture of CO_2[47], or the addition of thioether, thiourea and urea functionalities would permit the complexation with metals for metal extraction or catalysis[52]. In the same field of metal extraction, the introduction of hydrophobic groups to the cation, coupled with a strongly coordinating anion has produced stable biphasic systems with high extraction efficiency (up to 100%)[53].

Moreover, ionic liquids could be designed to be simultaneously the reaction media, the catalysts that enable a reaction[43,54] and even the reaction vessels as they have been described as nanoreactors themselves[55,56]. Another increasingly common approach concerns the grafting of ionic liquids onto supports, either to alter the properties of the surface of the substrate (*e.g.* wettability, selectivity, tribological properties, electrochemical response, *etc.*), or to prevent the leaching of the ILs in heterogeneous processes, thus improving their recoverability and reusability[57]. Grafting could be done directly on the unmodified surface of the support, or if the surface lacks suitable anchoring points, those are introduced in an intermediate step. Among the functional groups that have been introduced to ILs for their immobilization are azides and thiols[58], amines[59], trimethoxysilane[60], phosphonic acid[61], alkenes[62] and functional units that can take part in polymerization reactions[63]. Still, endowing an ionic liquid with task-specific properties is not always straightforward, as the traits that make ionic liquids stand out, may also pose additional problems in terms of the synthetic protocols that might have to be adopted and especially their purification, which if incomplete, can be deleterious to the desired application[42].

2.3. Properties

The properties of ionic liquids can vary dramatically if impurities, co-solvents or humidity are present. Since their synthesis can require multiple steps, traces of reagents from previous steps (especially halides, water and organic solvents) sometimes find their way into the final product, causing an array of issues[64]. This is the main reason why different values for a given property of a specific IL are often encountered in the literature[50,65].

2.3.1. Melting point

The size of the ions, their charge and its distribution are all factors influencing the melting point of ionic liquids. Unlike "classic" molten salts, where the strong interactions between the small, inorganic ions lead to high melting points, the bulky organic ions with delocalized charges contribute to the depression of the melting point of ionic liquids. The effect of charge delocalization is clearly seen when comparing ionic liquids with aromatic cations (*e.g.* imidazolium, pyridinium) to those where that added delocalization is not present (*e.g.* ammonium, phosphonium, pyrrolidinium), with the former exhibiting lower melting temperatures than the latter.

It has been reported that imidazolium-based ionic liquids often exhibit supercooling[66], which prohibits the determination of their melting point, as the ions remain in a glassy state even at very low temperatures. It was postulated that the interactions between the ionic species did not allow them to reorganize past the vitreous state[65].

Studies on the effect of the length of the side chain of several alkylmethylimidazolium-based ILs have found that surprisingly, the melting point steadily decreases as the length increases, reaching a minimum for 6 to 8-membered alkyl substituents. Beyond that length, the melting point progressively becomes higher and upon melting, lamellar ionic liquid

crystalline phases form[50].

2.3.2. Density

The density of most ionic liquids is higher than that of water. It is typically between 1.2 and 1.6 g/cm^3 at 25°C and for some ionic pairs that include the heavy $[Al_2Br_7]^-$ anion, values of 2.2 g/cm^3 have been reported[50]. Some ionic liquids containing dicyanamide, have a density close to 1 g/cm^3 or less[67]. The length of the alkyl chain of ILs with imidazolium, ammonium and sulfonium cations also has an effect on their density, which decreases as the chains become longer[65].

2.3.3. Viscosity

Ionic liquids are more viscous than aqueous systems and "classic" molten salts. This is due to Van der Waals interactions and hydrogen bonding[68]. The viscosity is usually between 30 and 50 cP at 25°C, but for certain ionic liquids values higher by an order of magnitude have been observed[50]. As one might expect, their viscosity decreases with the temperature, though the opposite has been reported for some imidazolium-based ILs with hexafluorophosphate[65,69]. Since mainly the side chains exhibit Van der Waals interactions, viscosity increases with their length[68,70]. Lastly, viscosity also depends on the nature of the anion, on its symmetry and on how localized its charge is[50,65].

2.3.4. Thermal stability

Ionic liquids possess remarkable thermal stability, especially considering their organic

nature. For many, their thermal decomposition does not take place below 200°C, while some are stable at even higher temperatures[65,71]. Thermal stability is the product of several factors, but the most important one is the nature of the anion[65,72]. In series of ionic liquids with the same cation, lower decomposition temperatures were recorded for halides than anions such as BF_4^-, PF_6^-, and $TFSI^-$[65]. It was also observed that the presence of water was detrimental to thermal stability and that the hydrophilicity of the ILs was largely dependent on the anion and its capacity for intermolecular interactions[65], a conclusion shared by other studies as well[72]. On the contrary, the nature of the cation seems to play a smaller role in thermal stability. In a series of experiments with piperidinium-based ionic liquids, as the chain length of the alkyl substituents increased, the thermal decomposition temperature decreased (albeit slightly). This was explained by "the higher stability of the progressively longer alkyl carbocations and/or free radicals originating from the breakdown of the C–N bond of the cation ring"[73].

2.3.5. Chemical stability

Ionic liquids are considered to be inert in general, but their chemical stability is largely dependent on the hygroscopic character imparted by the anion of the ionic liquid. As such, ionic liquids comprised of the $TFSI^-$, PF_6^- and BF_4^- anions exhibit an increased stability with regard to atmospheric humidity as compared to alkylsulfate anion towards hydrolysis[74]. However, the presence of water tends to catalyze the decomposition of perfluorinated anions such as PF_6^- and BF_4^- to hydrofluoric acid, which then contributes to the overall decomposition of the ionic liquid[75]. The $TFSI^-$ anion can express a heightened hydrophobic character when paired with a number of cations[76] and yields stable ionic liquids.

The protons of the imidazolium ring and mainly that at position 2, have an important effect on the reactivity of ionic liquids that comprise it[77]. In basic conditions or in the presence of certain metals, deprotonation of the ring takes place, leading to the formation of

carbenes[78]. Consequently, imidazolium-based ionic liquids are more stable when the proton at position 2 of the imidazolium ring has been substituted[79], *e.g.* by a methyl group.

2.3.6. Conductivity

Contrary to what might be expected based on the charged nature of ionic liquids, their conductivity is rather low and varies for different ion pairs. For many common ionic liquids, it lies in the range of 0.2 to 20 mS/cm at room temperature. Like with most substances, at higher temperatures the conductivity increases linearly, but close to the glass transition temperature, T_g, there is significant negative deviation from linear behavior. As conductivity depends on both the charge and the mobility of charge carriers, it follows that in ionic liquids with stronger interactions between the ions, the conductivity will be lowered, because of phenomena like ion pairing and ion aggregation. Also, the large size of some of the ions negatively affects their mobility. The conductivity follows a trend inverse to that of their viscosity, so any factor that leads to an increase of the viscosity (*e.g.* more Van der Waals interactions due to longer alkyl chains), will cause a decrease in conductivity. While a correlation between cation type and conductivity has been drawn, with conductivity decreasing in the order imidazolium > sulfonium > ammonium > pyridinium, a similar general conclusion about anion type or size has not been possible yet. It has been found that the addition of co-solvents to ionic liquids, greatly increases their conductivity, as co-solvent molecules solvate the ions and minimize ion pairing and ion aggregation.[50]

2.3.7. Electrochemical stability

The range of voltages over which a solvent is inert, is a measure of its electrochemical stability. In the case of ionic liquids, this potential “window” is defined by the potentials at

which generally the cation is reduced and the anion is oxidized. For many common ionic liquids, this range can exceed 4 V and reported values are typically between 2 and 6 V[50]. These windows are much wider than those of most common solvents, *e.g.* that of water is just 1.23 V at 25°C[22]. This tremendous advantage of ionic liquids over conventional solvents makes them very attractive for a host of electrochemical applications, some of which will be discussed later on. However, it should be noted that the choice of electrode materials and the presence of contaminants such as humidity or leftovers from the synthesis of the IL, even at minuscule amounts, all can lead to the formation of electroactive species that pose a challenge when determining the potential window of ILs. They can also severely impact their stability in the course of such applications by degrading ILs[50] and reducing the electrochemical window.

2.3.8. Interactions and supramolecular structure

A very interesting property of many ionic liquids is their structural organization. The coexistence of different types of functional groups and parts of the structure capable of manifesting different kinds of interactions results in the self-assembly of supramolecular structures and according to molecular dynamics simulations, depending on the nature of the ionic species, it is possible to exhibit microphase separation between polar and nonpolar nanodomains[55].

Using an imidazolium-based cation as an example, as illustrated in Figure 1.6, it can participate in several types of interactions. First, its charge is located, but delocalized, on the aromatic ring. This part of the ion is capable of the strongest electrostatic interactions with negatively charged ions, but also with polar groups or dipoles, as is the case with water. Secondly, because of the π system, the ring of the imidazolium ion can take part in π-π interactions, as well as cation-π interactions. Third, the hydrogen atoms of the ring can form hydrogen bonds. Being part of an aromatic system that stabilizes a positive charge, they have

a more pronounced acidic character and specifically the hydrogen atom at position 2 of the ring. Lastly, the alkyl substituents of the nitrogens make up the hydrophobic segments of the ion. Through Van der Waals interactions with their neighbors, they form apolar domains, the extent of which will be affected by the chain length and shape[54].

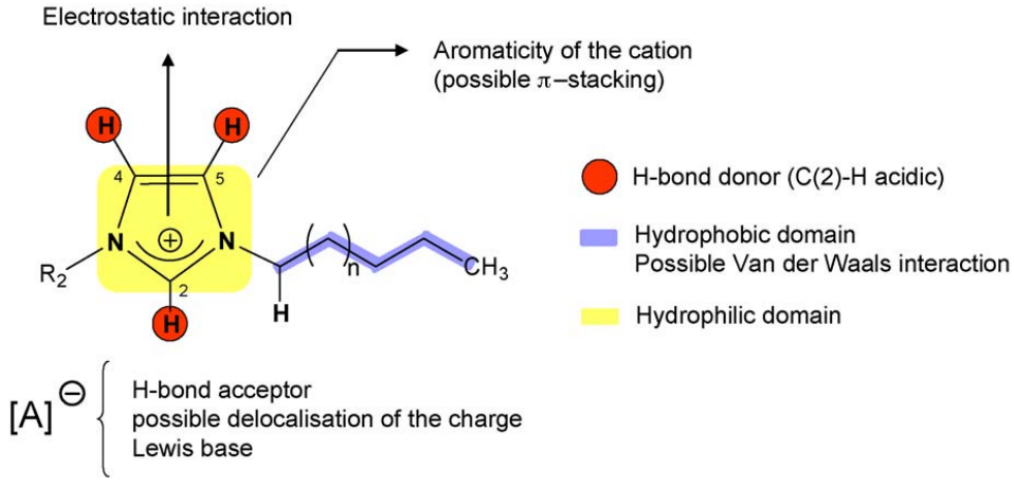

Figure 1.6: Representation of the different types of interactions present in imidazolium-based ILs. Reprinted from [54]

The sum of all of these interactions and the choice of the anion can be a less or more well-ordered superstructure, which even at the liquid state can be crystalline-like[80]. Imidazolium ILs have been reported to adopt a conformation where stacked cations form channels, in which small anions reside[81]. The size and affinity of these different nanodomains for different chemical species (charged – uncharged, polar – non-polar, *etc.*) can be tailored to accommodate the confinement of specific solutes or reactants and the exclusion of others[56,82,83].

By selecting specific ionic pairs and/or by modifying their chemical makeup, the higher order organization of ionic liquids can be adjusted to be compatible with systems of interest[84]. This offers an added tool to synthetic chemists for taking advantage of confinement effects, with all the benefits these may confer on designing processes based on green chemistry principles, even though ionic liquids themselves have been wrongly labeled as “green” solvents. Waste prevention, atom economy, less hazardous synthesis, energy

efficiency, catalysis and safety can be achieved by using ionic liquids as nanoreactors[85].

2.4. Applications

Because of the variety of properties afforded by the choice of ions that can be paired and the further tuning of these properties through functionalization, ionic liquids have been called “designer solvents”[43,86]. While their usefulness as solvents with adjustable affinities for different solutes is indisputable, this wealth of properties can also be used for many other purposes.

The viscosity of ionic liquids along with the different possible interaction types, have led to their consideration as lubricants[87,88]. Good adhesion or wetting capability is possible with surfaces of very diverse compositions. Their tunable hydrophilicity can also make them successful corrosion inhibitors[87,89]. However, thermal and chemical stability, in particular in the presence of impurities can be an issue[49].

Early in the history of ionic liquids, the catalytic properties of impurities dissolved in them, had led to the mistaken attribution of catalytic properties to the ILs[49]. However, further research into their properties and of course, their functionalization, has made ILs competent catalysts themselves and excellent supports or solvents for other catalysts, suitable for a wide range of homogeneous and heterogeneous catalytic processes. The applications of ILs are currently one of the most vividly researched topics in the domain[43,46,90,91].

The variable affinity of ionic liquids for different solvents and solutes is an asset for the formation and utilization of biphasic systems. Such systems are put to use in a range of very different fields, such as synthesis of organic and inorganic products[44,49,91], the liquid-liquid separation and extraction of precious or toxic metals[92], or the entrapment of particular analytes in analytical applications[93].

2.4.1. Ionic liquids as components of electrochemical energy storage devices

The ionic nature of ILs, but mostly their high electrochemical stability in comparison to common solvents has made them very attractive for almost any electrochemical application. Their most obvious use, that relies on both of these aspects, is as electrolytes. Their performance has been investigated in Li-ion, Na-ion, lithium-air and lithium-sulfur batteries, among others[39,94]. As for the "conventional" role of the battery electrolyte, several benefits have been reported for the ILs as the solvent or as a co-solvent. They have been found to increase the temperature operating range of batteries, their lifespan, charge and discharge rates and their safety, with regard to flammability[95–101]. In Li-ion batteries, ionic liquids have also been examined and proposed as binders for active materials and as components of gel electrolytes[102].

Ionic liquids appear to be particularly promising in dual-ion batteries, a type of cell, where both anions and cations are intercalated in the opposite electrodes[103–105]. There, they can be used as both the electrolyte and the intercalated species. Supercapacitors are a very similar application, with the differences being that instead of intercalation, it is surface adsorption that takes place and that the energy is stored as the electric field that results from the separation of charges[106]. It is perhaps the electrochemical energy storage application of ionic liquids that has seen wide market adoption[39,86].

2.4.2. Ionic liquids in the preparation of electrochemical energy storage device components

Besides their proposed uses as battery components, there are other aspects of the life cycle of Li-ion batteries that could benefit from the adoption of ionic liquids. They can be employed at different stages, such as the extraction of lithium from solutions[107], which could be useful for the exploitation of lithium brine and for recycling. ILs have also been studied

and used to manufacture high-purity, structured active electrode materials[108,109]. The electrochemical stability of most ionic liquids makes them excellent media for electrodeposition. In that process, their tunable hydrophilicity is an added asset, as they can solubilize a wide range of precursors and also they can exert control on the growth rate and crystallinity of the deposited material, affecting its morphology. In that regard, the electrodeposition of active electrode materials in ionic liquids is a very promising avenue. A high deposition current efficiency can be achieved in ILs and unlike aqueous electrolytes, the deposit does not suffer from oxide formation and H_2 evolution. Furthermore, the active material can be formed directly on the current collector, so it can be used directly in a battery, without the need for binders and other additives[108]. Such is also the case of ceria (CeO_2), a material that can be used as an electrolyte in solid oxide fuel cells. Ceria, which is hydrophobic, was electroplated on stainless steel substrates from solutions of $Ce(NO_3)_3$ in ionic liquids, producing smooth and adherent thin films[110].

Our group has been in the forefront of the synthesis of metal nanoparticles in IL media, with the specific intent to be used in batteries. The syntheses of tin and tin-copper intermetallic nanoparticles have been studied in different ionic liquids and optimized, so as to control their size and produce almost monodisperse populations. By integrating these nanoparticles in various electrode designs, precious insights were gained into factors that affect battery performance and the degradation of the materials during operation. Conclusions drawn from these works and in particular, the interactions of the forming nanoparticles with the ionic liquids, have established the basis for the current study.

There are undoubtedly advantages in bringing the broad family of ILs to the domain of Li-ion batteries. For the time being, this has been hampered by the inherent production costs[111], however more and more chemical manufacturers are starting to produce a widening selection of ionic liquids and the associated economies of scale can drive down those costs.

3. Tin and its oxides as anode materials

Tin and its oxides, SnO and SnO_2 have been proposed and studied extensively as potential anode materials in Li-ion batteries, due to their theoretical capacities being superior to that of graphite (372 mAh/g). The estimated gravimetric capacities for Sn, SnO and SnO_2 are ~993 mAh/g, ~875 mAh/g and ~782 mAh/g respectively[112,113]. Unlike intercalation materials, tin hosts lithium ions reversibly into its volume via electrochemical alloying. This process produces ordered, stoichiometric structures at different potentials (Figure 1.7), according to the reaction:

$$Sn + x\ Li^+ + x\ e^- \rightarrow Li_xSn \qquad (0 \leq x \leq 4.4)$$

The packing of lithium atoms in the most lithium-rich alloy, $Li_{4.4}Sn$, is close to that in pure lithium metal, 75.46 mol/L *vs.* 76.36 mol/L respectively[114]. Based on this value, the volumetric capacity of tin would be 7262 mAh/cm^3, more than ten times the 719 mAh/cm^3, the volumetric capacity of graphite[112]. Crystallographic studies suggested that the realistic form

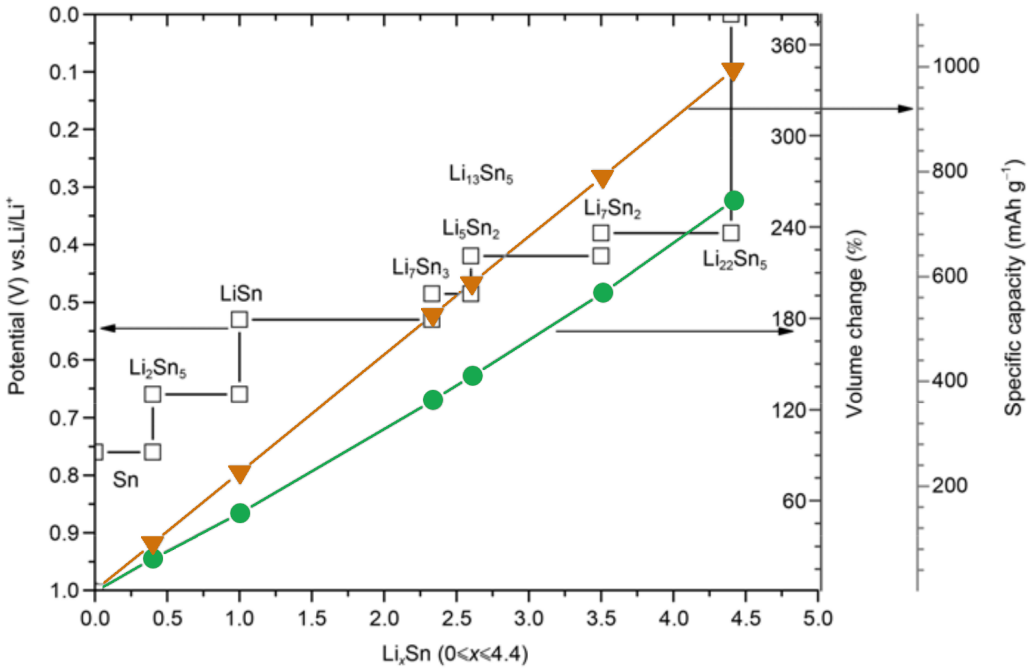

Figure 1.7: The theoretical formation potentials (black), specific capacities (orange), and volume changes (blue) of Li_xSn phases. Adapted from [114].

of this end phase could be $Li_{17}Sn_4$ (thus 4.25 Li atoms per Sn atom)[115,116]. Therefore its maximum gravimetric capacity could actually be 959.5 mAh/g, which is still much higher than most common graphite anodes.

Tin being almost three times more efficient than graphite in terms of weight and more than ten times in terms of volume, the work being done to integrate it in Li-ion battery designs is more than justified. However, as it can be seen in the green curve of Figure 1.7, which quantifies the problem that plagues all alloy-based electrode materials: extreme volume changes occur. A full-metal tin anode would increase three times in volume when going from the discharged to its charged state, which would be catastrophic for the battery and the device that battery would power. It is not just the impracticality of the huge difference between the expanded and contracted forms, but also what that would mean for the connectivity of the electrode with the rest of the cell. Much like with conversion materials, it is not possible to impose a specific growth pattern, direction or location on the (re)forming solid. As a result, in the course of a few cycles, pieces of the active material could crack and become isolated from the internal circuit, no longer contributing to the capacity, while others could grow in directions that would be damaging to the integrity of the battery, causing electrical or mechanical failures.

The nature of tin itself poses another problem. It has two main allotropes; white, soft, metallic β-Sn, which is stable at room temperature, but below 13.2°C, the stable form is gray, brittle, semiconducting α-Sn. The α polymorph is cubic ($Fd\bar{3}m$ space group, Fig. 1.8a), whereas the β form is tetragonal, compressed along one axis ($I4_1/amd$ space group, Fig. 1.8b). The transition from the β to the α structure, known as “tin pest”, because of its destructive effects, entails a volume increase of 26%[117,118]. For tin-based batteries, this transition would limit their lower operating temperature, and would also be an issue with regard to their storage and transportation. Even if the cells were manufactured to tolerate this expansion, the transformation from metallic to semiconducting incurs yet another penalty, the energy cost required for the electrons to flow to and fro the material. Moreover,

because the voluminous structure of α-Sn is more similar to that of the lithiated alloys than β-Sn, after a few cycles of lithiation and delithiation, the dominant form in the anode becomes the α polymorph, which permits the faster diffusion of lithium ions[119,120].

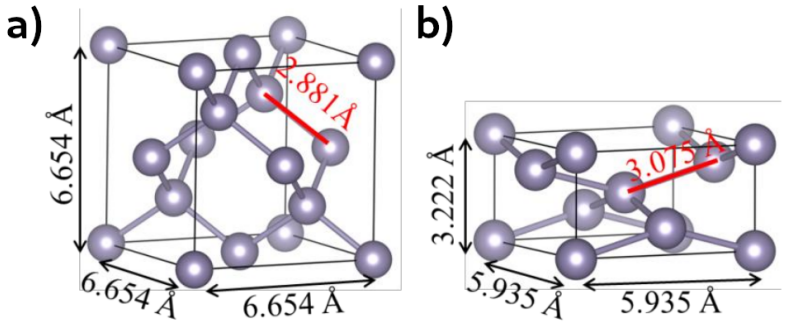

Figure 1.8: Crystalline structure of α-Sn (a) and β-Sn (b). Adapted from [119]

A feasible solution to the above problems appears to be the nanostructuring of a tin anode. By using tin nanoparticles (NPs) instead of bulk tin, several studies have demonstrated improvements in the lifespan and performance characteristics of the cells[112,120,121]. The mechanical stability stems from the accommodation of the expansion of individual nanoparticles in the intergrain space. The increased surface area, compared to bulk tin, facilitates the diffusion of lithium ions in the structure on one hand and the transfer of electrons from the active material to the electrode contact, on the other hand. These phenomena account for the observed increase in capacity and higher attainable C-rates. Furthermore, structuring the anode as nanoparticles permits the full exploitation of the active material[122] and the difference in surface energy at the nanoscale[123] can also benefit the operation of the battery, by lowering the energy barrier of lithiation[124]. Another reported advantage of working at the nanoscale is that within a certain size range, the β → α transition is significantly hindered[125,126].

There exist several approaches to the synthesis of Sn nanoparticles. The most common one is the so-called "polyol process"[127], i.*e.* the reduction of metal precursors in a polyol solvent. Another common method is the "amine-borane route"[128], where the reduction is achieved through the use of amine-borane adducts. A third approach is sputtering[129], a form

of physical vapor deposition technique, in which ion bombardment of a target material can cause its atoms to be ejected and then to be deposited on a substrate. The preparation of Sn NPs by ultrasonication of molten tin in paraffin oil has also been reported[130]. The bottom-up synthesis of tin nanoparticles for use in Li-ion anodes has previously been researched by our group[84,109] using ionic liquids as solvents. The resulting anodes demonstrated prolonged lifespans, even though the electrode formulation did not permit a significant capacity increase.

For the prevention of structural and electrical degradation of the electrodes, in addition to nanostructuring, some general options, such as the use of specific coatings and binders with a good level of adhesion to the nanoparticles are also available[112]. For alloy-based electrodes there are two more possibilities: alloying the active material with another metal that is either active (*e.g.* Ag, Sb) or inactive (*e.g.* Ti, V, Cr, Co) towards lithium. In the first case, the stabilization seems to come from the coexistence of different phases that are formed during lithiation. In the case of bimetallic alloys with inactive metals, the inactive matrix appears to buffer volume expansion and/or the formation of the fully lithiated phase, leading to better cycling stability[112].

In the case of the tin oxides, the alloying process is preceded by two conversion reactions with the lithium ions in the electrolyte, that produce Li_2O irreversibly while simultaneously generating metallic Sn *in situ*[131]:

$$SnO_2 + 2\ Li^+ + 2\ e^- \rightarrow SnO + Li_2O$$

$$SnO + 2\ Li^+ + 2\ e^- \rightarrow Sn + Li_2O$$

These reactions consume lithium ions from the electrolyte, hence induce differences in capacity of the oxides compared to metallic tin. However, the lithium oxide phase that forms, can have a stabilizing effect on the anode material, buffering the volume expansion induced by Sn-Li alloying[114] and while the phase is electronically insulating, it does not prevent the diffusion of ions. This bodes well for the future of Sn-nanoparticle-based anodes,

because it appears that the formation of this passivating layer is unavoidable, since Sn NPs have a propensity for oxidation, once they come in contact with air[109,132]. Even if care is taken to avoid oxidation, reactions between the electrolyte, tin and lithium will lead to Li_2O production[114,120].

Given all of tin's idiosyncrasies, working with them or around them, rather than trying to prevent them, would seem like a more effective approach in the manufacturing of tin-based anodes. Nanostructuring the anode is a good strategy, but it is not enough and it cannot even guarantee the structural integrity of the particles[133]. The nanoparticles already require the addition of other materials to provide form, such as binders and conductive pathways between them (*e.g.* carbon black) and the electrode contacts. It would make sense to combine them with a suitable, flexible and conductive matrix that could contain them and that could remain in contact with them regardless of them being in the α or β form, devoid of lithium and compact or fully lithiated and expanded. This approach, which has been the point of focus of several research efforts and appears as the most promising, has already yielded a commercial battery. The "Nexelion" cells by Sony, were made with the active material consisting of an intermetallic alloy of Sn and Co – with Co being inactive towards Li – within a carbon matrix[112,131,134].

4. Beyond graphite

Graphite has been the workhorse for Li-ion battery anodes for more than three decades and realistically speaking, it does not seem like it will be displaced by another material sometime soon. During that same time span, a lot of work has focused on alloy anode materials, the most promising replacement candidates so far, but only tin and more recently silicon have managed to find their way into actual, commercial batteries and then only as additives, with graphite still being the major active material. As several studies have suggested, every alternative material or formulation that has been proposed so far could not exceed graphite in every aspect and most crucially, in terms of gravimetric and volumetric capacity simultaneously. While there exist materials that on paper surpass graphite in both these values, the structural modifications made necessary by their intrinsic disadvantages (mainly their volume expansion) end up negating any benefits[112,135].

Even though graphite has a specific capacity much lower than that of metallic lithium or many conversion or alloying alternatives, it is still relatively high and in fact, 2-3 times higher than that of most cathode materials in use. The same is true for its volumetric capacity, which is on par with that of LCO in the cathode. It has a very low lithiation-delithiation potential (on average 0.2 V *vs.* Li/Li^+), which means that graphite-based cells are capable of high voltages, very close to that of pure Li. Its rate capability has proven adequate for most of the applications where it is being used. The first cycle irreversible capacity, or initial coulombic efficiency, *i.e.* the amount of lithium from the electrolyte consumed during SEI formation, is also good by comparison. The volume increase during lithiation is approximately 10.4% and when considering the mass transfer from the cathode, the actual variation in a full cell is even smaller, which results in low mechanical stress during operation, with everything that implies for the structural integrity and safety of a battery. Both the thermal and electrical conductivity of graphite are also quite good. The effect of graphite on capacity fade, *i.e.* how much the capacity is reduced after each cycle, is rather

minimal. Just as importantly, graphite is abundant, inexpensive and also easily synthesized, with a relatively low increase in cost[112,136].

It is painfully clear that finding a material that excels in all of these aspects and manages to outmatch graphite is no easy feat. Yet the need to move away from fossil fuels has turned the spotlight on the limitations of Li-ion technology, some of which are tied to graphite. The first limitation that has been brought up several times already, is the low gravimetric capacity of graphite, which is a full order of magnitude lower than that of pure lithium. Even though the prospect of a lithium anode appears now more distant than a graphite replacement, the chemistry could be exploited further than it is at the moment. Every incremental improvement beyond the current state would translate into considerable practical gains, *e.g.* lighter cars with a longer range, portable devices that require charging less often, *etc.*.

The second shortcoming that is specific to graphite is its rate capability. Current Li-ion batteries can be discharged at a rate of up to 10C, but the charging rate cannot exceed 1C[136]. Charging at or close to the maximum achievable rate has been associated with accelerated aging of the cells and capacity fading and even more importantly, with the risk of Li metal plating on the surface of the electrode, which can lead to short-circuits and the catastrophic failure of the batteries. Despite the widespread use of Li-ion batteries and the tremendous amount of studies that have been conducted over the years, some of the mechanisms behind this problem are still not completely understood. In large part, this is due to the complexity of a battery as a system and the lithiation of the anode is not much less complex in itself. It appears that the issue is the sum of several factors: the size and structure of graphite particles, the mechanics of intercalation, the effects of the choice of solvent on lithium ion desolvation and the eventual composition of the SEI, even the temperature at which the battery is charged. Of these factors, the ones that are inherent to graphite are its structure and how exactly lithiation proceeds and they are both connected. They will be discussed below, as they are important to understanding the problem and what, if any, solutions could

be envisaged.

The structures of pristine α-graphite and the fully lithiated compound, LiC_6, are shown in Figure 1.9. Graphite is made of stacked graphene sheets held together by Van der Waals forces, with an interlayer distance of 3.35 Å. In the most stable form, α-graphite, the sheets adopt an ABAB-type arrangement, resulting in a hexagonal lattice. The insertion of the lithium ions in the structure causes a slight shift in the sheets, which then adopt an AIAIA arrangement (I: intercalated species) and the interlayer distance increases to 3.70 Å.

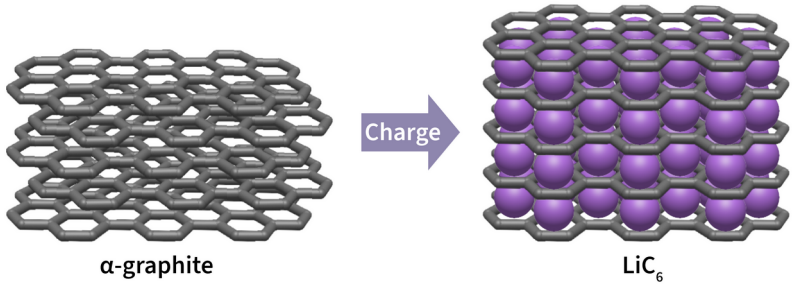

Figure 1.9: Formation of the intercalation compound LiC_6 at the battery anode.

Several studies have demonstrated that the lateral movement of the lithium ions between the sheets is rather fast, with diffusion coefficients in the range of 10^{-7} to 10^{-5} cm^2/s[137]. Based on these numbers, it was estimated that a crystalline domain with a size of 45 nm could be lithiated within 0.2 ms, which is contradicted by the actual rate, that is ~1C. Without any other knowledge about the system, it is apparent that for geometric reasons, the speed of the ions cannot be the same in every direction. Also, arrangements where the graphite crystals are placed with the graphene sheets perpendicular to the path between the anode and the cathode will hinder the diffusion of the ions. Indeed, the ion transport in that direction has been measured to be in the order of 10^{-11} cm^2/s[137].

The actual graphite particles do not possess the neatness of the above schematics and in both natural and synthetic graphite, several types of structural defects are often encountered: crystallites with different orientations than their neighbors, interpenetrated graphene strata and folds. In order to maximize the use of space in the electrodes, graphite

is typically subjected to processing and made into spherical particles. This can increase the structural disorder, especially on the surface of the particles, with folded or broken graphene sheets covering the outside and consequently leaving fewer entryways for the lithium ions. SEM images of natural graphite flakes with dimensions up to 2 mm are shown in Figure 1.10. While much bigger than the particles used in batteries, they demonstrate the listed defects. In the center of Fig. 1.10b some interpenetrated graphene sheets are visible. A fold can be observed in the middle of Fig. 1.10c. Damage from the processing of the flakes in the form of discontinuities, deformations and voids is observed in Fig. 1.10d. Folded sheets are wrapped around the side of the platelet in Fig. 1.10b.

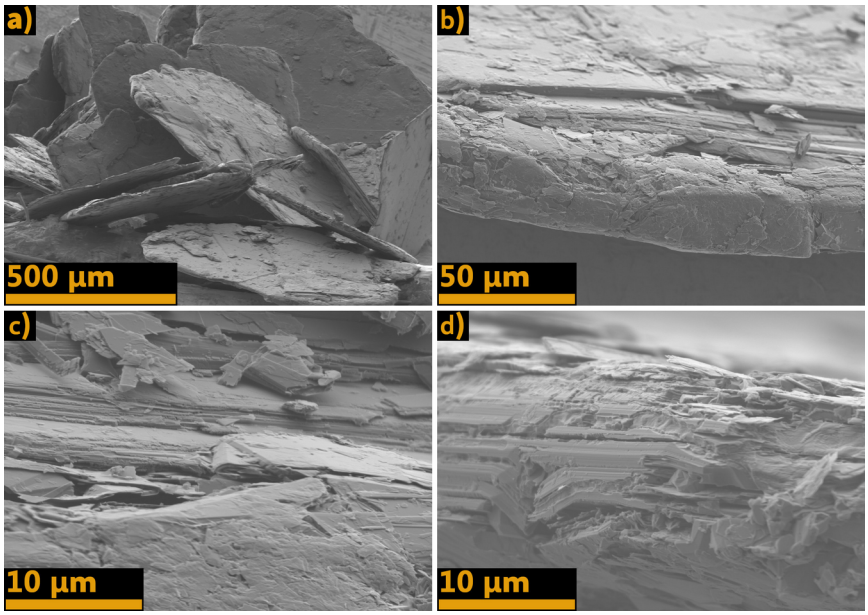

Figure 1.10: SEM images of natural graphite flakes.

4.1. Effects of interlayer spacing

The anisotropic structure of graphite is only part of the problem. The intercalation of lithium ions follows a “staging mechanism”, a concentration-dependent feature, with several discrete steps. Insertion of the ions in the structure does not happen all at once or randomly;

it goes through a number of separate phases, with evolving Li to C ratios, all with different kinetics. These stages can be monitored electrochemically, as they correspond to a series of galvanostatic potential plateaus. A lot of studies over the years have revealed details of this mechanism, but it is not fully understood yet[136]. The first attempt at explaining the behavior was made by Rüdorff and Hofmann in 1938, who at the time studied the intercalation of hydrogensulfate anions (HSO_4^-) in graphite[15]. Summarily, according to their model, the system adopts a periodical structure at each stage, in which graphite layers incorporating the intercalating species alternate with empty layers. As the structure fills up, less and less layers remain empty at each stage. The exact structure at each stage is defined by the energy required to increase the interlayer spacing of adjacent graphene sheets and the repulsion exhibited between layers of intercalating species. A limitation of this model recognized by its authors, was that it required the complete deintercalation of some layers and re-intercalation of the ions in a neighboring layer in order to advance to the next, more concentrated stage. In 1969, Daumas and Herold proposed a revised model, in which they considered the flexibility of the unfilled graphene layers around partially filled domains in the structure. That way, the periodicity of the older model was maintained – albeit locally – and the intercalated species would just need to diffuse between different domains for the structure to move towards the next stage. Both models are presented in Figure 1.11.

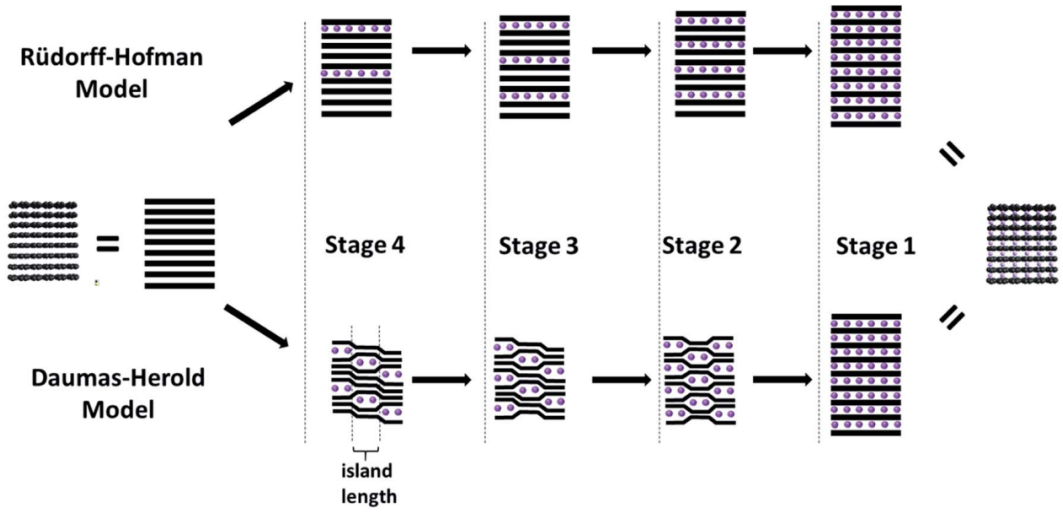

Figure 1.11: Graphite intercalation mechanisms proposed by Rüdorff and Hofman (top) and Daumas and Herold (bottom). Graphite is represented by the black lines and the purple spheres represent the intercalant. Reprinted from [136]

In recent years, after the isolation of graphene brought the humble constituent of graphite to the center of researchers' attention, several studies examined the lithiation mechanisms of single-layer, bilayer and few-layer graphene. Few layer graphene was found to behave like graphite, whereas single-layer graphene, that had been theorized to be capable of hosting lithium ions on both its surfaces, was found to attain a very low coverage of ~5% [138]. Interestingly, in the case of bi-layer graphene, reversible multi-layer deposition of lithium was observed[139].

Furthermore, in structures that resemble that of graphite, but with a larger interlayer distance between adjacent sheets, faster lithiation rates are attained. Vertically grown graphene sheets[140–142] or arrays of carbon nanotubes[143] have broken the barrier of 1C, reaching 6C and paving the way to exceptionally fast-charging batteries. The galvanostatic curves of these systems do not exhibit the same plateaus observed for graphite, which means that the lithiation kinetics are not the same and that they do not follow the same complex staging mechanism. One might argue that the microstructure of these systems is too dissimilar to graphite and that the speed gains stem from the decrease in tortuosity[144]. While indisputably the tortuosity is lowered, increased lithiation rates have also been observed in graphite with bulky intercalated species, that keep the graphene sheets further apart[145–148].

In addition, most of these structures seem capable of hosting more lithium per unit of mass, which would suggest that the Li to C ratio is higher than in LiC_6. Recent studies have suggested that graphene-based structures with voids, or graphite with increased interlayer spacing attain higher gravimetric capacities than pristine graphite, up to 1000 mAh/g or more[135] and by a combination of intercalation and reversible lithium plating, even higher capacities may be possible[149].

Besides the increased internal voids in these materials, there is another aspect they have in common and may play an important role in the fast and increased lithium uptake: their flexibility. The partially lithiated intermediate forms of graphite in the Daumas-Herod staging model, while more complex in reality, have been verified by structural studies[136]. In

order for the model to be rational, the flexibility of the graphene sheets was key. Kühne *et al.*, who observed the superdense ordering of lithium in bi-layer graphene, postulated that the two sheets can spread more easily since they were not constrained as they would be in a graphite crystal and perhaps for that reason they were capable of accepting that amount of Li. They also pointed out that Li-graphite compounds occupy only a small region of the C-Li binary phase diagram[139]. Flexible layered structures made from reduced graphene oxide and lithium have demonstrated capacities close to that of pure metallic Li and rate capabilities up to 10C, with reversible capacity loss[150]. A flexible host material could not only accept more lithium, but it could also help contain volume changes during cycling and prevent the unwanted growth of dendrites, while at the same time maintaining structural integrity and electrical conductivity.

To sum up, despite graphite's numerous advantages, its much lower than expected capacity, the slow lithiation rate and finally problems related to its sourcing, induced a lot of research works devoted to seeking alternatives. Graphene appears as a promising option.

4.2. Graphene and graphene oxide

The unique traits of graphene have made it an ideal candidate for a plethora of applications and particularly in the context of the present study, *i.e.* electrochemical energy storage. Graphene has excellent mechanical properties: a breaking strength of 42 N/m and Young modulus close to 1 TPa[151]. A valence electron of each carbon atom is delocalized in the extended conjugated system formed by the sp^2-hybridized orbitals, endowing graphene with a high intrinsic mobility of 200000 $cm^2/V{\cdot}s$ and a thermal conductivity of approximately 5000 $W/m{\cdot}K$[152]. Graphene can be obtained by exfoliating graphite or it can be synthesized in several different bottom-up methods[153,154]. It can be grown by chemical vapor deposition (CVD) from carbon-containing gases on metal surfaces or other substrates. This is the method currently used in industrial processes for electronics applications, as it can produce

large enough sheets, with relatively few defects. Graphene can be made by annealing SiC crystals under vacuum. It can be synthesized chemically through polymerization reactions of suitable monomers, or via the oxidation of polyaromatic precursors, in cyclodehydrogenation[155]. It can also be formed by the pyrolysis of carbon-based precursors on catalytically active substrates, under vacuum or inert atmosphere. Through CVD or pyrolysis on templates, graphene can be made directly in specific shapes, *e.g.* graphene foam grown on metal foam, which is then etched away[156]. Also, by adding specific precursors in the CVD or pyrolysis chambers, it is possible to dope the lattice of graphene with heteroatoms, *e.g.* nitrogen or boron[157].

A top-down method of production of graphene involves the oxidation of graphene to graphene oxide (GO) and its subsequent reduction. Through treatment with strong oxidizers, oxygen-bearing groups attach to the carbon atoms and defects and vacancies are created in the lattice. The added functional groups and the sp^3 geometry adopted by some of the carbon atoms push the sheets apart and cause their exfoliation. The resulting material is substantially different from graphene and importantly, it is an insulator. However, the polar functional groups of graphene oxide can take part in a number of reactions, permitting its further chemical and structural modification and also allow it to be dispersed in polar solvents, such as water[152,154,158]. The possibilities in the covalent functionalization of graphene oxide are practically unlimited. For instance, by employing reagents with two or more reactive functional groups, such as chlorotetrazines, GO sheets can be cross-linked together, forming superstructures[159].

For applications that require the properties of the material to be close to those of pristine graphene, graphene oxide must be reduced. This results in the loss of oxygen-bearing groups and the restoration of the lattice – usually partially. The reduction can be done thermally, which typically produces a material closer to pristine graphene, or chemically[154]. Among the reducing agents commonly employed for the reduction of GO to reduced graphene oxide, are hydrazine, ascorbic acid, hydroxylamine and metal powders in acidic media[160]. A third

option for the reduction of GO exists in the form of electrochemical reduction. This has been used for example for the simultaneous reduction of GO and the surface modification of electrodes by the deposition of the rich in electrochemically active sites rGO sheets[161]. Reduced graphene oxide (rGO) possesses properties between those of graphene oxide, depending on the selected reduction method and the extent of reduction. Their chemical aspects (synthesis, functionalization, reduction, *etc.*) are discussed in more detail in Chapter 2.

Given graphene's electronic and mechanical properties, combined with its very low weight, it makes perfect sense to adopt it and graphene-based materials in metal-ion batteries either as the active hosts of metal ions or in auxiliary roles. In particular, three-dimensional functional structures based on graphene that have been proposed over the last few years have produced auspicious results[156,162–167], but there is still a lot of work to be done. A review was recently published[168] that examines the roles and performances of such architectures in detail. Here we will summarize some highlights in the domain and in the following section we will focus on the combination of graphene and tin, which is at the core of this study. Graphene as an active material can accommodate metal ions via intercalation (when multiple layers are stacked) and by adsorption on its surface. Li^+, Na^+, K^+, Al^{3+} can be intercalated between graphene sheets. Aluminium ions, which have trouble penetrating in depth in graphite, when paired with a graphene-based structure with 3D channels exhibited good capacity at relatively high C-rates, 120 mAh/g at 400 mA/g and superb cycling performance, with 91.7% capacity retention after 250000 cycles[169]. These batteries also had a wide temperature operating range, -40 to 120°C. As for the surface adsorption of Li^+, Na^+, K^+, the presence of defects, heteroatoms and the spatial arrangement of the graphene layers can significantly increase the capacity of the batteries. A sulfur-doped, interconnected cellular structure developed by Islam *et al.*[170] when used as an anode in Li-ion and Na-ion batteries demonstrated high specific capacities of 1697 mAh/g at 100 mA/g and 472 mAh/g at 50 mA/g, respectively. In composite anodes and cathodes where 3D-structured graphene serves an accessory function to the main active material, its role is nonetheless important: it supports

the metal-ion host and provides an electron conduit between it and the electrode contact, it prevents the aggregation of the host material, mitigates its volume expansion and facilitates the diffusion of metal ions in the structure. A wide variety of active materials (intercalation, conversion and alloying hosts, *e.g.* TiO_2, SnS_2, SnS, Si, Ge, *etc.*) have been studied in tandem with such structures, again with very good results, especially compared to the performance of the active material by itself[168]. For instance, one of the early nanocomposites of tin nanoparticles anchored on graphene exhibited a reversible capacity of 795 mAh/g at 55 mA/g, with a retention of 64% after 100 cycles[171]. While early results have been encouraging, great challenges still lie ahead. Self-assembled graphene-based structures usually contain a lot of defects and oxygen groups that require removal, accomplished by thermal treatments at high temperatures, which are not compatible with every system and increase the costs. The porosity of many systems is random and that poses homogeneity problems for the electrodes, that accumulate over cycles. A number of techniques employed in the preparation of 3D structured graphene are difficult to scale up. Perhaps more importantly, irrational design and poor control of the porosity of the structures lead to low volumetric energy densities, rendering such materials impractical.

4.3. Graphene-based anodes with tin

The potential advantages of using tin as an anode material were presented earlier in this chapter, along with its main disadvantage, extreme volume expansion and contraction, that makes its integration into Li-ion batteries difficult. A lot of effort has focused on taming the structural changes of tin, by pairing it with other elements or materials. There have been quite a few examples of composite materials comprised of tin or tin oxides (or tin phosphide in a couple of cases) and a graphene-based matrix. The synthetic methods employed are rather varied, but the materials can be generally classed under two broad categories: tin nanoparticles entrapped in graphene-like or graphene-based structures and tin

nanoparticles supported on such structures, with the graphene sheets "decorated" with the NPs. While the results do not indicate a clear advantage in taking the first or the second approach, each strategy appears to have its own merits. In many cases, the reported materials are used as synthesized, meaning that no additives or other components are required to shape the materials or to provide conductive pathways. Besides, the use of a graphene network ensures the conductivity of the whole system[172]. Several examples of each approach will be examined below.

4.3.1. Inclusion

In the first strategy presented here, tin-based nanoparticles are enclosed in a graphene superstructure. The latter can be in the form of a shell, such as hollow spheres, open-ended nanotubes, disordered, crumpled sheets, lamellar forms in which tin is sandwiched, 3D networks and structures where both materials have been grown from suitable precursors, with the tin-based nanoparticles ending up trapped between layers of graphene. As for the preparative methods employed, they vary from one-pot type syntheses to multistep synthetic routes.

A recurring theme is the use of sacrificial templates, usually in the form of polystyrene beads[173,174], which could be further functionalized by amino groups[175], for the purpose of creating hollow spheres that encapsulate the tin-based particles. Graphene oxide nanosheets are wrapped around the spheres, because of electrostatic attraction. After annealing or chemical removal of polystyrene, the sheets retain the spherical shape. Sacrificial polystyrene templates have also been used in combination with Ni foam, to produce a hierarchical structure[176]. Another sacrificial template used to create macroporous composite structures is melamine, which presents the advantage of being soluble in hot water. Melamine was also added with the intent to protect the oxygen groups on the interior of the GO sheets during thermal treatment[177].

Wang and He demonstrated that it is possible to grow graphene-tin heterostructures in a single step[178]. By decomposing tin oleate on Na_2CO_3, Sn/SnO nanoparticles formed simultaneously with graphene sheets. Na_2CO_3 crystals present smooth, flat facets and as such, they can support the growth of both materials. The tin nanoparticles, which were covered by a thin SnO layer, were well dispersed within the mass of the graphene sheets that grew on top and around them.

A different kind of hollow nanoparticle, "dry-plum-like yolk-shell" was produced via spray pyrolysis of microdroplets of tin oxalate and polyvinylpyrrolidone[179]. Within seconds, oxidation, polymerization, and thermal annealing take place, consecutively. The hollow particles contained SnO_x integrated in a carbon matrix.

A layer-by-layer assembly method was employed by Zhan *et al.*[180] to produce SnO_2 nanoparticles covered by graphene sheets on a Ni foam substrate. The foam was dipped successively in suspensions of tin oxide NPs and graphene oxide and the composite was thermally annealed when enough layers had been deposited.

Two more methods have been reported in which the structured composite is enclosed in another carbon layer. Luo *et al.*[181] prepared a GO/SnO_2 hydrogel which was then freeze-dried and the resulting material was coated in glucose, which was subsequently graphitized. Li *et al.*[182] synthesized a 3D graphene support, onto which Sn@SnO_2 particles were anchored and then its surface was covered with polydopamine, which after thermal annealing, gave a nitrogen-doped film.

Finally, a composite employing carbon nanotubes has been reported by Zhang *et al.*[183]. The nanotubes had been subjected to a treatment that perforated their walls and were then impregnated with a solution of tin chloride, which was hydrolyzed to SnO_2 by water vapors in an autoclave. The fast growth of carbon nanotubes by CVD from acetylene around a tin oxide precursor which is simultaneously reduced into tin nanowires has also been reported. This method could be easily adapted to produce similar structures for battery applications[184].

4.3.2. Tin supported on graphene

In the vast majority of composites of both categories, tin or tin oxide is formed *in situ* on the graphene oxide sheets from a solution of Sn^{4+} or Sn^{2+} salts. The oxygen-bearing functional groups of graphene oxide serve as anchoring points for the metal ions and become the nucleation sites for the growth of tin nanoparticles. Depending on the environment, the NPs then are either oxidized – partially or totally – to SnO_2 or $Sn@SnO_x$. In some of the syntheses, the oxidation of tin takes place concurrently with the reduction of graphene oxide[185]. It seems that there is a conscious choice to forgo trying to preserve tin in its metallic form, which renders processing of the materials more difficult. Another explanation for this choice would be that the structural changes exhibited by tin during lithiation are much more dramatic than those of its oxides.

Two slight variations of this approach, reported by Gu *et al.*[186] and Yang *et al.*[187], make use of mixtures of ionic liquids as the medium in which the anchoring of the nanoparticles to the sheets takes place, as a means to control their growth. In the latter work, the synthesis is performed in an autoclave, which results in the partial decomposition of the IL (1-butyl-3-methylimidazolium dicyanamide) and the subsequent nitrogen-doping of the GO sheets.

There are some works that follow a different synthetic route altogether. Zeb *et al.* functionalized sheets of mechanically cleaved highly-oriented pyrolytic graphite (HOPG) with sulfophenyl and aminophenyl groups via diazonium reactions[188]. These grafted groups served as the nucleation sites for Sn nanoparticles and microplatelets deposited from a solution of $SnCl_2$. Borude *et al.*[189] also started with graphite, which was used as an electrode for in-liquid plasma discharge in a solution of $SnCl_2$ in ethanol. With each discharge, simultaneous exfoliation of graphene sheets and deposition of SnO_2 particles took place. Yan *et al.*[190] developed a composite based on the self assembly of a planar complex of Sn with 1,2,4,5-benzenetetracarboxylic acid on rGO sheets. Xie *et al.*[191] prepared an ultrathin film of SnO_2 via atomic layer deposition onto thermally exfoliated rGO. The as-deposited SnO_2 was

amorphous, which contributed to low structural deformation during lithiation and delithiation of the composite anode. Huang *et al.*[192] irradiated GO suspensions with an electron beam, which induced the exfoliation of nanosheets, their amorphization and introduction of defects, while partially eliminating oxygen-containing functional groups. The final composite was formed after a hydrothermal reaction with the GO nanosheets with $SnCl_4$.

For the most part, graphene-based composites where tin is supported on the surface of the structure exhibit a low morphological complexity. They consist of 2D sheets, more or less wrinkled, with tin/tin oxide nanoparticles dispersed on their surface. There are a few exceptions to this. Pan *et al.*[193] prepared a composite aerogel, which later in the process was crushed, leading to a disordered, mesoporous structure. Ji *et al.*[185] reported the synthesis of nitrogen-doped rGO composite hydrogels, with dense coverage of the sheets with SnO_2 nanoparticles and a disordered 3D structure.

Lastly, it is worth mentioning two more materials, that differ significantly from what has been presented so far. Kim *et al.*[194] subjected a mixture of GO and Sn nanometric (150 nm) powder to treatment with NH_4OH and hydrazine, resulting in the etching of the nanoparticles and their transformation into echinoid (sea urchin-like) nanostructures, supported on wrinkled rGO sheets. Jiang *et al.*[195] created heterostructures of alternately stacked SnO_2 and graphene sheets. This was done by exfoliating SnO_2 particles via sonication and mixing them with a suspension of expanded and exfoliated graphite. The 2D materials reassembled in microparticle-sized stacks.

It should be noted that while most of the materials discussed above present interesting forms at the nano or the microscale, a lot of them – with a few notable exceptions – have no macrostructure. This means that they have to undergo the "traditional" processing of active materials for battery electrodes, *i.e.* to be mixed with binders and other additives, so as to become tangible electrodes. For some reason, the wealth of hierarchical structures at every scale afforded by graphene chemistry and processing[156,162,163,165–168] has not been fully

exploited. It seems highly plausible that moving in that direction could bring interesting results in composites comprised of graphene and tin as an alloying host material.

Among the composite materials presented, there were a couple that made light use of ionic liquids in their preparation, as modulators of the growth of tin nanoparticles[186,187]. In one of these materials, the IL was further used to dope the graphene lattice with nitrogen heteroatoms as it decomposed on its surface. The insights gained by the study of the synthesis of metal nanoparticles in IL media as hinted earlier in this chapter, suggested that perhaps ionic liquids could play a more active role in composites with tin and graphene.

5. Towards a ternary material

In the closing remarks of her thesis[196] on the synthesis of metal nanoparticles in various ionic liquids, N. Soulmi comments on the interactions between the forming tin nanoparticles and the EMI^+TFSI^- ionic liquid, the reaction medium. It was shown that the nanoparticles interacted strongly with the EMI^+ cation, which constituted their first solvation sphere and which also formed heterocyclic carbenes on the surface of the particles. $TFSI^-$, a weakly coordinating anion due to its structure, exhibited very little interaction with the NPs. The EMI^+TFSI^- pair, constituted an ionic liquid with properties that were favorable to the structural control and evolution of the nanoparticles, such as its low viscosity and its hydrophobic character, that shielded the reaction mixture from the detrimental effects of humidity. The synthesized nanoparticles had an average size of 7 nm, with a narrow size distribution.

The ultimate goal of that work was the nanostructuring of tin, so that it could be used in lithium-ion batteries. However, the nanoparticles were incorporated in a typical electrode formulation, where they comprised 30 wt% of the material. Another 45 wt% belonged to a 1:1 mixture of carbon black and graphite, used to prevent the agglomeration of the nanoparticles and to provide conductive pathways between the NPs and the current collector. Carboxymethyl cellulose, a nonconductive cellulose derivative used as binder, accounted for the remaining 25 wt% of the electrode. This formulation that works adequately for most of the materials used in actual batteries, severely hampered the performance of the anode, while it could not prevent the loss of active material due to pulverization and aggregation. The battery exhibited high capacity, but mostly when cycled between 0.05 and 0.8 V, as at higher potential differences the electrolyte kept decomposing on the large surface area of the NPs. The structure of the anode could not adapt to the volume changes and over time, parts of active material became disconnected from the rest of the electrode, reflected in the 25% capacity loss after 40 cycles.

With these findings in mind, it was postulated that the interactions of the tin nanoparticles with $EMI^{+}TFSI^{-}$ could perhaps be put to use to maintain the stability of the anode, by anchoring the nanoparticles in place and preventing the migration of tin atoms during cycling. Obviously, a liquid could not provide by itself anchorage for a solid and even more so an ionic liquid inside a battery, so the IL would have to be immobilized on some support. Both members of the ion pair could be modified to that end. Nevertheless, it was decided to recreate the Sn NPs – IL system of the synthesis as faithfully as possible. For that reason, the grafting would be done by the longer side chain of the imidazolium ring, since it had no direct influence on the nanoparticles, as opposed to the strong interactions with the cation ring and the weak interactions with the anion. For the same reason, when exploring the potential synthetic approaches, the decision was made to keep the length of the ethyl side chain constant, *i.e.* to keep the number of carbon atoms at two.

As for the scaffold onto which the IL would be grafted, from the works cited in the previous section and from past experience with graphene-based materials, it was decided to turn towards graphene. In particular, it's oxidized form, graphene oxide, is perfectly suited to functionalization via a multitude of synthetic methods, in both polar and nonpolar solvents. This property was convenient, as the hydrophilicity of the modified ionic liquid could not be deduced in advance. In addition, graphene oxide being dispersible in a variety of solvents opened the possibility of combining functionalization and shaping, through solution processing. Many different architectures based on graphene have been reported in the literature and a lot of them exhibit sufficient mechanical stability and flexibility, that could allow the high loading of the structure in tin and the mitigation of its volume changes. An important decision in the beginning of this work was to attempt to create a nanostructured material, that would also be self-supporting and shaped at the macroscale. This would mark a departure from the customary electrode designs, where the active material is ground into a fine powder and then it is combined with additives and binders to gain form and conductivity. This choice was made in the hope that the resulting anode would contain zero extraneous components and so, no "dead" weight. Lithium would be hosted

mainly by tin and partially by the graphene support, which would provide form, mechanical strength and electron conductivity. The ionic liquid would mitigate the degradation of the tin nanoparticles during cycling. The forms of the support that were initially selected were membranes and foams. The latter, while they possess a lot of voids, are compressible without breaking[197,198], so the porosity of the composite could be tuned either during the assembly of the batteries or at an earlier step, in order to achieve an acceptable trade-off between volumetric capacity, gravimetric capacity and cycling rate.

Looking in the literature for similar constructs, we could find none. Graphene-based structures are routinely used in combination with ionic liquids in supercapacitors. Task-specific ionic liquids supported on graphene are nothing uncommon. In the only examples where tin, graphene and ionic liquids were combined structurally into a composite material, the ionic liquids were being used as precursors for the doping of the graphene lattice with heteroatoms[199–203] and in another one, the 1-propyl-3-methylimidazolium cation was grafted onto GO after silylation and then combined with a chlorostannate anion, to be used as a catalyst[204].

With the nature of the supporting structure positively decided, several different functional groups that would permit the grafting of the EMI^+ cation were initially examined and eventually, the amino group was selected, as detailed in the second chapter. At that moment, some of the more evident potential problems that might be encountered in the process were identified. In order to take advantage of graphene's conductivity, the composite material would have to be reduced afterwards, but without damaging the graft or the nanoparticles. Another potential pitfall was the documented affinity of the imidazolium cation for graphene through π-π and cation-π interactions[205–207]. This could prove problematic for the grafting, if the cations of the IL got stuck on sp^2 domains, away from possible reaction sites. On a related note, proving that the ionic liquid was indeed grafted and not adsorbed on the surface of the graphene structure would be challenging.

6. References

(1) Thien, T.; Axelsen, H.; Merten, M.; Zurmühlen, S.; Münderlein, J.; Leuthold, D. M.; Sauer, D. D. U. Planning of Grid-Scale Battery Energy Storage Systems: Lessons Learned from a 5 MW Hybrid Battery Storage Project in Germany. **2015**, 10.

(2) Wahlquist, C. South Australia's Tesla Battery on Track to Make Back a Third of Cost in a Year. *The Guardian*. September 27, 2018.

(3) Geuss, M. Nissan's New XStorage Battery Wants to Compete with Tesla's Powerwall in Europe. *Ars Technica*. May 13, 2016.

(4) Popovich, N. D.; Rajagopal, D.; Tasar, E.; Phadke, A. Economic, Environmental and Grid-Resilience Benefits of Converting Diesel Trains to Battery-Electric. *Nat Energy* **2021**. https://doi.org/10.1038/s41560-021-00915-5.

(5) Betz, J.; Bieker, G.; Meister, P.; Placke, T.; Winter, M.; Schmuch, R. Theoretical versus Practical Energy: A Plea for More Transparency in the Energy Calculation of Different Rechargeable Battery Systems. *Adv. Energy Mater.* **2019**, *9* (6), 1803170. https://doi.org/10.1002/aenm.201803170.

(6) Liu, Q.; Su, X.; Lei, D.; Qin, Y.; Wen, J.; Guo, F.; Wu, Y. A.; Rong, Y.; Kou, R.; Xiao, X.; Aguesse, F.; Bareño, J.; Ren, Y.; Lu, W.; Li, Y. Approaching the Capacity Limit of Lithium Cobalt Oxide in Lithium Ion Batteries via Lanthanum and Aluminium Doping. *Nat Energy* **2018**, *3* (11), 936–943. https://doi.org/10.1038/s41560-018-0180-6.

(7) Whittingham, M. S. Lithium Batteries and Cathode Materials. *Chem. Rev.* **2004**, *104* (10), 4271–4302. https://doi.org/10.1021/cr020731c.

(8) Press Release: The Nobel Prize in Chemistry 2019. NobelPrize.Org, 2019.

(9) Ma, S.; Jiang, M.; Tao, P.; Song, C.; Wu, J.; Wang, J.; Deng, T.; Shang, W. Temperature Effect and Thermal Impact in Lithium-Ion Batteries: A Review. *Progress in Natural Science: Materials International* **2018**, *28* (6), 653–666. https://doi.org/10.1016/j.pnsc.2018.11.002.

(10) Goodenough, J. B.; Park, K.-S. The Li-Ion Rechargeable Battery: A Perspective. *Journal of the American Chemical Society* **2013**, *135* (4), 1167–1176. https://doi.org/10.1021/ja3091438.

(11) Lee, T. Battery Prices Have Fallen 88 Percent over the Last Decade. *Ars Technica*. December 18, 2020.

(12) Lee, T. The Story of Cheaper Batteries, from Smartphones to Teslas. *Ars Technica*. September 22, 2020.

(13) Haynes, W. M.; Lide, David R; Bruno, Thomas J. *CRC Handbook of Chemistry and Physics: A Ready-Reference Book of Chemical and Physical Data.*, 97th ed.; CRC Press, 2017.

(14) *Kirk-Othmer Encyclopedia of Chemical Technology*, 1st ed.; John Wiley & Sons, Inc, Ed.; Wiley, 2000. https://doi.org/10.1002/0471238961.

(15) Winter, M.; Barnett, B.; Xu, K. Before Li Ion Batteries. *Chemical Reviews* **2018**, *118* (23), 11433–11456. https://doi.org/10.1021/acs.chemrev.8b00422.

(16) Whittingham, M. S. Electrical Energy Storage and Intercalation Chemistry. *Science* **1976**, *192* (4244), 1126–1127. https://doi.org/10.1126/science.192.4244.1126.

(17) Edison, T. A. Storage Battery. US1379088A, May 24, 1921.

(18) Carmichael, L. E. *Hybrid and Electric Vehicles*; Innovative technologies; ABDO Publishing Company: Minneapolis, MN, 2013.

(19) Brandt, K. Historical Development of Secondary Lithium Batteries. *Solid State Ionics* **1994**, *69* (3–4), 173–183. https://doi.org/10.1016/0167-2738(94)90408-1.

(20) Etacheri, V.; Marom, R.; Elazari, R.; Salitra, G.; Aurbach, D. Challenges in the Development of Advanced Li-Ion Batteries: A Review. *Energy Environ. Sci.* **2011**, *4* (9), 3243. https://doi.org/10.1039/c1ee01598b.

(21) Harris, W. S. Electrochemical Studies in Cyclic Esters, University of California, Berkeley, United States, 1958. https://doi.org/10.2172/4305596.

(22) Kühnel, R.-S.; Reber, D.; Battaglia, C. Perspective—Electrochemical Stability of Water-in-Salt Electrolytes. *J. Electrochem. Soc.* **2020**, *167* (7), 070544. https://doi.org/10.1149/1945-7111/ab7c6f.

(23) Xu, K. Nonaqueous Liquid Electrolytes for Lithium-Based Rechargeable Batteries. *Chem. Rev.* **2004**, *104* (10), 4303–4418. https://doi.org/10.1021/cr030203g.

(24) Cram, D. J.; Cram, J. M. Host-Guest Chemistry: Complexes between Organic Compounds Simulate the Substrate Selectivity of Enzymes. *Science* **1974**, *183* (4127), 803–809. https://doi.org/10.1126/science.183.4127.803.

(25) Hever, K. O. Ion Mobility in Crystals of a Mixed-Alkali Ferrite: $K_xNa_{1-x}Fe_7O_{11}$. *Journal of The Electrochemical Society* **1968**, *115* (8), 826–829.

(26) Taberna, P. L.; Mitra, S.; Poizot, P.; Simon, P.; Tarascon, J.-M. High Rate Capabilities Fe_3O_4-Based Cu Nano-Architectured Electrodes for Lithium-Ion Battery Applications. *Nature Mater* **2006**, *5* (7), 567–573. https://doi.org/10.1038/nmat1672.

(27) Heubner, C.; Lein, T.; Schneider, M.; Michaelis, A. Intercalation Materials for Secondary Batteries Based on Alkali Metal Exchange: Developments and Perspectives. *J. Mater. Chem. A* **2020**, *8* (33), 16854–16883. https://doi.org/10.1039/D0TA03115A.

(28) Mizushima, K.; Jones, P. C.; Wiseman, P. J.; Goodenough, J. B. $LixCoO_2$ ($0<x\leq1$): A New Cathode Material for Batteries of High Energy Density. *Materials Research Bulletin* **1980**, *15* (6), 783–789. https://doi.org/10.1016/0025-5408(80)90012-4.

(29) Purwanto, A.; Yudha, C. S.; Ubaidillah, U.; Widiyandari, H.; Ogi, T.; Haerudin, H. NCA Cathode Material: Synthesis Methods and Performance Enhancement Efforts. *Mater. Res. Express* **2018**, *5* (12), 122001. https://doi.org/10.1088/2053-1591/aae167.

(30) Lim, B.-B.; Yoon, S.-J.; Park, K.-J.; Yoon, C. S.; Kim, S.-J.; Lee, J. J.; Sun, Y.-K. Advanced Concentration Gradient Cathode Material with Two-Slope for High-Energy and Safe Lithium Batteries. *Adv. Funct. Mater.* **2015**, *25* (29), 4673–4680. https://doi.org/10.1002/adfm.201501430.

(31) Ohzuku, T.; Ueda, A.; Nagayama, M.; Iwakoshi, Y.; Komori, H. Comparative Study of $LiCoO_2$, $LiNi_{1/2}Co_{1/2}O_2$ and $LiNiO_2$ for 4 Volt Secondary Lithium Cells. *Electrochimica Acta* **1993**, *38* (9), 1159–1167. https://doi.org/10.1016/0013-4686(93)80046-3.

(32) Yabuuchi, N.; Ohzuku, T. Novel Lithium Insertion Material of $LiCo_{1/3}Ni_{1/3}Mn_{1/3}O_2$ for Advanced Lithium-Ion Batteries. *Journal of Power Sources* **2003**, *119–121*, 171–174. https://doi.org/10.1016/S0378-7753(03)00173-3.

(33) Lu, Z.; MacNeil, D. D.; Dahn, J. R. Layered Cathode Materials $Li[Ni_xLi_{(1/3-2x/3)}Mn_{(2/3-x/3)}]O_2$ for Lithium-Ion Batteries. *Electrochem. Solid-State Lett.* **2001**, *4* (11), A191. https://doi.org/10.1149/1.1407994.

(34) Thackeray, M. M.; Johnson, P. J.; de Picciotto, L. A.; Bruce, P. G.; Goodenough, J. B. Electrochemical Extraction of Lithium from LiMn2O4. *Materials Research Bulletin* **1984**, *19* (2), 179–187. https://doi.org/10.1016/0025-5408(84)90088-6.

(35) Padhi, A. K.; Nanjundaswamy, K. S.; Goodenough, J. B. Phospho-olivines as Positive-Electrode Materials for Rechargeable Lithium Batteries. *J. Electrochem. Soc.* **1997**, *144* (4), 1188–1194. https://doi.org/10.1149/1.1837571.

(36) Mongird, K.; Viswanathan, V.; Alam, J.; Vartanian, C.; Sprenkle, V.; Baxter, R. *2020 Grid Energy Storage Technology Cost and Performance Assessment*; 2020; p 117.

(37) Dey, A. N.; Sullivan, B. P. The Electrochemical Decomposition of Propylene Carbonate on Graphite. *J. Electrochem. Soc.* **1970**, *117* (2), 222. https://doi.org/10.1149/1.2407470.

(38) Fong, R. Q Studies of Lithium Intercalation into Carbons Using Nonaqueous Electrochemical Cells. *J. Electrochem. Soc.* **1990**, *137* (7), 5.

(39) Watanabe, M.; Thomas, M. L.; Zhang, S.; Ueno, K.; Yasuda, T.; Dokko, K. Application of Ionic Liquids to Energy Storage and Conversion Materials and Devices. *Chem. Rev.* **2017**, *117* (10), 7190–7239. https://doi.org/10.1021/acs.chemrev.6b00504.

(40) Mariani, A.; Bonomo, M.; Gao, X.; Centrella, B.; Nucara, A.; Buscaino, R.; Barge, A.; Barbero, N.; Gontrani, L.; Passerini, S. The Unseen Evidence of Reduced Ionicity: The Elephant in (the) Room Temperature Ionic Liquids. *Journal of Molecular Liquids* **2021**, *324*, 115069. https://doi.org/10.1016/j.molliq.2020.115069.

(41) Lantelme, F.; Groult, H. *Molten Salts Chemistry: From Lab to Applications*, 1st. edition.; Elsevier: Amsterdam, 2013.

(42) Singh, S. K.; Savoy, A. W. Ionic Liquids Synthesis and Applications: An Overview. *Journal of Molecular Liquids* **2020**, *297*, 112038. https://doi.org/10.1016/j.molliq.2019.112038.

(43) Sood, K.; Saini, Y.; Thakur, K. K. Ionic Liquids in Catalysis: A Review. *Materials Today: Proceedings* **2021**, S221478532103145X. https://doi.org/10.1016/j.matpr.2021.04.225.

(44) Rogers, R. D.; Seddon, K. R. Ionic Liquids--Solvents of the Future? *Science* **2003**, *302* (5646), 792–793. https://doi.org/10.1126/science.1090313.

(45) Gonçalves, A. R. P.; Paredes, X.; Cristino, A. F.; Santos, F. J. V.; Queirós, C. S. G. P. Ionic Liquids—A Review of Their Toxicity to Living Organisms. *IJMS* **2021**, *22* (11), 5612. https://doi.org/10.3390/ijms22115612.

(46) Vekariya, R. L. A Review of Ionic Liquids: Applications towards Catalytic Organic Transformations. *Journal of Molecular Liquids* **2017**, *227*, 44–60. https://doi.org/10.1016/j.molliq.2016.11.123.

(47) Bates, E. D.; Mayton, R. D.; Ntai, I.; Davis, J. H. CO_2 Capture by a Task-Specific Ionic Liquid. *Journal of the American Chemical Society* **2002**, *124* (6), 926–927. https://doi.org/10.1021/ja017593d.

(48) Rizzo, C.; Marullo, S.; Tz. Dintcheva, N.; Gambarotti, C.; Billeci, F.; D'Anna, F. Ionic Liquid Gels and Antioxidant Carbon Nanotubes: Hybrid Soft Materials with Improved Radical Scavenging Activity. *Journal of Colloid and Interface Science* **2019**. https://doi.org/10.1016/j.jcis.2019.08.108.

(49) Giernoth, R. Task-Specific Ionic Liquids. *Angewandte Chemie International Edition* **2010**, *49* (16), 2834–2839. https://doi.org/10.1002/anie.200905981.

(50) Wasserscheid, P.; Welton, T. *Ionic Liquids in Synthesis*, 1st ed.; Wiley, 2007.

(51) Chiappe, C.; Pomelli, C. S. Point-Functionalization of Ionic Liquids: An Overview of Synthesis and Applications: Point-Functionalization of Ionic Liquids. *Eur. J. Org. Chem.* **2014**, *2014* (28), 6120–6139. https://doi.org/10.1002/ejoc.201402093.

(52) Lee, S. Functionalized Imidazolium Salts for Task-Specific Ionic Liquids and Their Applications. *Chem. Commun.* **2006**, No. 10, 1049. https://doi.org/10.1039/b514140k.

(53) Messadi, A.; Mohamadou, A.; Boudesocque, S.; Dupont, L.; Guillon, E. Task-Specific

Ionic Liquid with Coordinating Anion for Heavy Metal Ion Extraction: Cation Exchange versus Ion-Pair Extraction. *Separation and Purification Technology* **2013**, *107*, 172–178. https://doi.org/10.1016/j.seppur.2013.01.015.

(54) Olivier-Bourbigou, H.; Magna, L.; Morvan, D. Ionic Liquids and Catalysis: Recent Progress from Knowledge to Applications. *Applied Catalysis A: General* **2010**, *373* (1–2), 1–56. https://doi.org/10.1016/j.apcata.2009.10.008.

(55) Canongia Lopes, J. N. A.; Pádua, A. A. H. Nanostructural Organization in Ionic Liquids. *J. Phys. Chem. B* **2006**, *110* (7), 3330–3335. https://doi.org/10.1021/jp056006y.

(56) Machado, G.; Scholten, J. D.; Vargas, T. de; Teixeira, S. R.; Ronchi, L. H.; Dupont, J. Structural Aspects of Transition-Metal Nanoparticles in Imidazolium Ionic Liquids. *IJNT* **2007**, *4* (5), 541. https://doi.org/10.1504/IJNT.2007.014809.

(57) Xin, B.; Hao, J. Imidazolium-Based Ionic Liquids Grafted on Solid Surfaces. *Chem. Soc. Rev.* **2014**, *43* (20), 7171–7187. https://doi.org/10.1039/C4CS00172A.

(58) He, H.; Averick, S.; Roth, E.; Luebke, D.; Nulwala, H.; Matyjaszewski, K. Clickable Poly(Ionic Liquid)s for Modification of Glass and Silicon Surfaces. *Polymer* **2014**, *55* (16), 3330–3338. https://doi.org/10.1016/j.polymer.2014.01.045.

(59) Dong, Z.; Zhao, L. Surface Modification of Cellulose Microsphere with Imidazolium-Based Ionic Liquid as Adsorbent: Effect of Anion Variation on Adsorption Ability towards Au(III). *Cellulose* **2018**, *25* (4), 2205–2216. https://doi.org/10.1007/s10570-018-1735-1.

(60) Ilyas, A.; Muhammad, N.; Gilani, M. A.; Vankelecom, I. F. J.; Khan, A. L. Effect of Zeolite Surface Modification with Ionic Liquid [APTMS][Ac] on Gas Separation Performance of Mixed Matrix Membranes. *Separation and Purification Technology* **2018**, *205*, 176–183. https://doi.org/10.1016/j.seppur.2018.05.040.

(61) Bhandary, R.; Alauzun, J. G.; Hesemann, P.; Stocco, A.; In, M.; Mutin, P. H. Phase Transfer of TiO_2 Nanoparticles from Water to Ionic Liquid Triggered by Phosphonic Acid Grafting. *Soft Matter* **2017**, *13* (44), 8023–8026. https://doi.org/10.1039/C7SM01424D.

(62) Ni, C.; Zheng, X.; Zhang, Y.; Zhang, X.; Li, Y. Multifunctional Porous Materials with Simultaneous High Water Flux, Antifouling and Antibacterial Performances from Ionic Liquid Grafted Polyethersulfone. *Polymer* **2021**, *212*, 123183. https://doi.org/10.1016/j.polymer.2020.123183.

(63) Ye, Q.; Gao, T.; Wan, F.; Yu, B.; Pei, X.; Zhou, F.; Xue, Q. Grafting Poly(Ionic Liquid) Brushes for Anti-Bacterial and Anti-Biofouling Applications. *J. Mater. Chem.* **2012**, *22* (26), 13123. https://doi.org/10.1039/c2jm31527k.

(64) Seddon, K. R.; Stark, A.; Torres, M.-J. Influence of Chloride, Water, and Organic Solvents on the Physical Properties of Ionic Liquids. *Pure and Applied Chemistry* **2000**, *72* (12), 2275–2287. https://doi.org/10.1351/pac200072122275.

(65) Huddleston, J. G.; Visser, A. E.; Reichert, W. M.; Willauer, H. D.; Broker, G. A.; Rogers, R. D. Characterization and Comparison of Hydrophilic and Hydrophobic Room Temperature Ionic Liquids Incorporating the Imidazolium Cation. *Green Chem.* **2001**, *3* (4), 156–164. https://doi.org/10.1039/b103275p.

(66) Ngo, H. L.; LeCompte, K.; Hargens, L.; McEwen, A. B. Thermal Properties of Imidazolium Ionic Liquids. *Thermochimica Acta* **2000**, *357–358*, 97–102. https://doi.org/10.1016/S0040-6031(00)00373-7.

(67) MacFarlane, D. R.; Forsyth, S. A.; Golding, J.; Deacon, G. B. Ionic Liquids Based on Imidazolium, Ammonium and Pyrrolidinium Salts of the Dicyanamide Anion. *Green Chem.* **2002**, *4* (5), 444–448. https://doi.org/10.1039/b205641k.

(68) Bonhôte, P.; Dias, A.-P.; Papageorgiou, N.; Kalyanasundaram, K.; Grätzel, M.

Hydrophobic, Highly Conductive Ambient-Temperature Molten Salts. 11.

(69) Endres, F.; Zein El Abedin, S. Air and Water Stable Ionic Liquids in Physical Chemistry. *Phys. Chem. Chem. Phys.* **2006**, *8* (18), 2101. https://doi.org/10.1039/b600519p.

(70) Chiappe, C.; Pieraccini, D. Ionic Liquids: Solvent Properties and Organic Reactivity. *J. Phys. Org. Chem.* **2005**, *18* (4), 275–297. https://doi.org/10.1002/poc.863.

(71) Liu, S.-H.; Chen, C.-C.; Zhang, B.; Wu, J.-H. Fire and Explosion Hazards of 1-Ethyl-3-Methylimidazolium Bis(Trifluoromethylsulfonyl)Imide. *RSC Advances* **2020**, *10* (38), 22468–22479. https://doi.org/10.1039/D0RA01821J.

(72) Meine, N.; Benedito, F.; Rinaldi, R. Thermal Stability of Ionic Liquids Assessed by Potentiometric Titration. *Green Chem.* **2010**, *12* (10), 1711. https://doi.org/10.1039/c0gc00091d.

(73) Montanino, M.; Carewska, M.; Alessandrini, F.; Passerini, S.; Appetecchi, G. B. The Role of the Cation Aliphatic Side Chain Length in Piperidinium Bis(Trifluoromethansulfonyl)Imide Ionic Liquids. *Electrochimica Acta* **2011**, *57*, 153–159. https://doi.org/10.1016/j.electacta.2011.03.089.

(74) Sowmiah, S.; Srinivasadesikan, V.; Tseng, M.-C.; Chu, Y.-H. On the Chemical Stabilities of Ionic Liquids. *Molecules* **2009**, *14* (9), 3780–3813. https://doi.org/10.3390/molecules14093780.

(75) Freire, M. G.; Neves, C. M. S. S.; Marrucho, I. M.; Coutinho, J. A. P.; Fernandes, A. M. Hydrolysis of Tetrafluoroborate and Hexafluorophosphate Counter Ions in Imidazolium-Based Ionic Liquids. *J. Phys. Chem. A* **2010**, *114* (11), 3744–3749. https://doi.org/10.1021/jp903292n.

(76) Kato, H.; Nishikawa, K.; Koga, Y. Relative Hydrophobicity and Hydrophilicity of Some “Ionic Liquid” Anions Determined by the 1-Propanol Probing Methodology: A Differential Thermodynamic Approach. *J. Phys. Chem. B* **2008**, *112* (9), 2655–2660. https://doi.org/10.1021/jp710867s.

(77) Thomazeau, C.; Olivier-Bourbigou, H.; Magna, L.; Luts, S.; Gilbert, B. Determination of an Acidic Scale in Room Temperature Ionic Liquids. *J. Am. Chem. Soc.* **2003**, *125* (18), 5264–5265. https://doi.org/10.1021/ja0297382.

(78) Arduengo, A. J. Looking for Stable Carbenes: The Difficulty in Starting Anew. *Acc. Chem. Res.* **1999**, *32* (11), 913–921. https://doi.org/10.1021/ar980126p.

(79) Hunt, P. A. Why Does a Reduction in Hydrogen Bonding Lead to an Increase in Viscosity for the 1-Butyl-2,3-Dimethyl-Imidazolium-Based Ionic Liquids? *J. Phys. Chem. B* **2007**, *111* (18), 4844–4853. https://doi.org/10.1021/jp067182p.

(80) Dupont, J. On the Solid, Liquid and Solution Structural Organization of Imidazolium Ionic Liquids. *J. Braz. Chem. Soc.* **2004**, *15* (3), 341–350. https://doi.org/10.1590/S0103-50532004000300002.

(81) Dupont, J.; Suarez, P. A. Z. Physico-Chemical Processes in Imidazolium Ionic Liquids. *Phys. Chem. Chem. Phys.* **2006**, *8* (21), 2441. https://doi.org/10.1039/b602046a.

(82) Gutel, T.; Garcia-Antõn, J.; Pelzer, K.; Philippot, K.; Santini, C. C.; Chauvin, Y.; Chaudret, B.; Basset, J.-M. Influence of the Self-Organization of Ionic Liquids on the Size of Ruthenium Nanoparticles: Effect of the Temperature and Stirring. *J. Mater. Chem.* **2007**, *17* (31), 3290. https://doi.org/10.1039/b706139k.

(83) Zhang, S.; Zhang, J.; Zhang, Y.; Deng, Y. Nanoconfined Ionic Liquids. *Chem. Rev.* **2017**, *117* (10), 6755–6833. https://doi.org/10.1021/acs.chemrev.6b00509.

(84) Le Vot, S.; Dambournet, D.; Groult, H.; Ngo, A.; Petit, C.; Rizzi, C.; Salzemann, C.; Sirieix-Plenet, J.; Borkiewicz, O. J.; Raymundo-Piñero, E.; Gaillon, L. Synthesis of Tin

Nanocrystals in Room Temperature Ionic Liquids. *Dalton Trans.* **2014**, *43* (48), 18025–18034. https://doi.org/10.1039/C4DT02289K.

(85) Terra, J. C. S.; Martins, A. R.; Moura, F. C. C.; Weber, C. C.; Moores, A. Making More with Less: Confinement Effects for More Sustainable Chemical Transformations. *Green Chem.* **2022**, 10.1039.D1GC03283F. https://doi.org/10.1039/D1GC03283F.

(86) Miao, L.; Song, Z.; Zhu, D.; Li, L.; Gan, L.; Liu, M. Ionic Liquids for Supercapacitive Energy Storage: A Mini-Review. *Energy Fuels* **2021**, *35* (10), 8443–8455. https://doi.org/10.1021/acs.energyfuels.1c00321.

(87) Li, Y.; Zhang, S.; Ding, Q.; Qin, B.; Hu, L. Versatile 4, 6-Dimethyl-2-Mercaptopyrimidine Based Ionic Liquids as High-Performance Corrosion Inhibitors and Lubricants. *Journal of Molecular Liquids* **2019**, *284*, 577–585. https://doi.org/10.1016/j.molliq.2019.04.042.

(88) Guo, H.; Iglesias Victoria, P. Ionic Liquids as High-Performance Lubricants and Lubricant Additives. In *Ionic Liquids - Thermophysical Properties and Applications*; M. Sohel Murshed, S., Ed.; IntechOpen, 2021. https://doi.org/10.5772/intechopen.96428.

(89) Verma, C.; Ebenso, E. E.; Quraishi, M. A. Ionic Liquids as Green Corrosion Inhibitors for Industrial Metals and Alloys. In *Green Chemistry*; Saleh, H. E.-D. M., Koller, M., Eds.; InTech, 2018. https://doi.org/10.5772/intechopen.70421.

(90) Selvam, T.; Machoke, A.; Schwieger, W. Supported Ionic Liquids on Non-Porous and Porous Inorganic Materials—A Topical Review. *Applied Catalysis A: General* **2012**, *445–446*, 92–101. https://doi.org/10.1016/j.apcata.2012.08.007.

(91) Welton, T. Room-Temperature Ionic Liquids. Solvents for Synthesis and Catalysis. *Chem. Rev.* **1999**, *99* (8), 2071–2084. https://doi.org/10.1021/cr980032t.

(92) Rios-Vera, R. M.; Sirieix-Plénet, J.; Gaillon, L.; Rizzi, C.; Ávila-Rodríguez, M.; Cote, G.; Chagnes, A. Physicochemical Properties of Novel Cholinium Ionic Liquids for the Recovery of Silver from Nitrate Media. *RSC Adv.* **2015**, *5* (95), 78268–78277. https://doi.org/10.1039/C5RA14101J.

(93) Ayala-Cabrera, J. F.; Trujillo-Rodríguez, M. J.; Pino, V.; Hernández-Torres, Ó. M.; Afonso, A. M.; Sirieix-Plénet, J. Ionic Liquids versus Ionic Liquid-Based Surfactants in Dispersive Liquid–Liquid Microextraction for Determining Copper in Water by Flame Atomic Absorption Spectrometry. *International Journal of Environmental Analytical Chemistry* **2016**, *96* (2), 101–118. https://doi.org/10.1080/03067319.2015.1128538.

(94) Hagiwara, R.; Matsumoto, K.; Hwang, J.; Nohira, T. Sodium Ion Batteries Using Ionic Liquids as Electrolytes. *The Chemical Record* **2018**. https://doi.org/10.1002/tcr.201800119.

(95) Hirata, K.; Morita, Y.; Kawase, T.; Sumida, Y. A Carbonate-Free Electrolyte for Lithium-Ion Batteries Based on Lithium Bis(Fluorosulfonyl)Imide and 2-Methylglutaronitrile Enabling Graphite Negative Electrodes. *Electrochimica Acta* **2019**. https://doi.org/10.1016/j.electacta.2019.02.032.

(96) Basile, A.; Hollenkamp, A. F.; Bhatt, A. I.; O'Mullane, A. P. Extensive Charge–Discharge Cycling of Lithium Metal Electrodes Achieved Using Ionic Liquid Electrolytes. *Electrochemistry Communications* **2013**, *27*, 69–72. https://doi.org/10.1016/j.elecom.2012.10.030.

(97) Elia, G. A.; Ulissi, U.; Jeong, S.; Passerini, S.; Hassoun, J. Exceptional Long-Life Performance of Lithium-Ion Batteries Using Ionic Liquid-Based Electrolytes. *Energy Environ. Sci.* **2016**, *9* (10), 3210–3220. https://doi.org/10.1039/C6EE01295G.

(98) Howlett, P. C.; MacFarlane, D. R.; Hollenkamp, A. F. High Lithium Metal Cycling Efficiency in a Room-Temperature Ionic Liquid. *Electrochem. Solid-State Lett.* **2004**, *7* (5), A97. https://doi.org/10.1149/1.1664051.

(99) Javadian, S.; Salimi, P.; Gharibi, H.; Fathollahi, A.; Kowsari, E.; Kakemam, J. Effect of Imidazolium-Based Ionic Liquid as Electrolyte Additive on Electrochemical Performance of 18650 Cylindrical Li-Ion Batteries at Room and 60 °C Temperatures. *Journal of the Iranian Chemical Society* **2019**. https://doi.org/10.1007/s13738-019-01683-6.

(100) Lux, S. F.; Schmuck, M.; Appetecchi, G. B.; Passerini, S.; Winter, M.; Balducci, A. Lithium Insertion in Graphite from Ternary Ionic Liquid–Lithium Salt Electrolytes: II. Evaluation of Specific Capacity and Cycling Efficiency and Stability at Room Temperature. *Journal of Power Sources* **2009**, *192* (2), 606–611. https://doi.org/10.1016/j.jpowsour.2009.02.066.

(101) Yoon, H.; Howlett, P. C.; Best, A. S.; Forsyth, M.; MacFarlane, D. R. Fast Charge/Discharge of Li Metal Batteries Using an Ionic Liquid Electrolyte. *J. Electrochem. Soc.* **2013**, *160* (10), A1629–A1637. https://doi.org/10.1149/2.022310jes.

(102) Eftekhari, A.; Liu, Y.; Chen, P. Different Roles of Ionic Liquids in Lithium Batteries. *Journal of Power Sources* **2016**, *334*, 221–239. https://doi.org/10.1016/j.jpowsour.2016.10.025.

(103) Manna, S. S.; Bhauriyal, P.; Pathak, B. Identifying Suitable Ionic Liquid Electrolytes for Al Dual-Ion Batteries: Role of Electrochemical Window, Conductivity and Voltage. *Mater. Adv.* **2020**, *1* (5), 1354–1363. https://doi.org/10.1039/D0MA00292E.

(104) Fan, J.; Zhang, Z.; Liu, Y.; Wang, A.; Li, L.; Yuan, W. An Excellent Rechargeable PP $_{14}$ TFSI Ionic Liquid Dual-Ion Battery. *Chem. Commun.* **2017**, *53* (51), 6891–6894. https://doi.org/10.1039/C7CC02534C.

(105) Fan, J.; Xiao, Q.; Fang, Y.; Li, L.; Yuan, W. A Rechargeable Zn/Graphite Dual-Ion Battery with an Ionic Liquid-Based Electrolyte. *Ionics* **2019**, *25* (3), 1303–1313. https://doi.org/10.1007/s11581-018-2644-x.

(106) Salanne, M. Ionic Liquids for Supercapacitor Applications. *Top Curr Chem (Z)* **2017**, *375* (3), 63. https://doi.org/10.1007/s41061-017-0150-7.

(107) Zante, G.; Boltoeva, M.; Masmoudi, A.; Barillon, R.; Trébouet, D. Lithium Extraction from Complex Aqueous Solutions Using Supported Ionic Liquid Membranes. *Journal of Membrane Science* **2019**. https://doi.org/10.1016/j.memsci.2019.03.013.

(108) Soulmi, N.; Porras-Gutierrez, A.-G.; Mordvinova, N. E.; Lebedev, O. I.; Rizzi, C.; Sirieix-Plénet, J.; Groult, H.; Dambournet, D.; Gaillon, L. Sn(TFSI) $_2$ as a Suitable Salt for the Electrodeposition of Nanostructured Cu $_6$ Sn $_5$ –Sn Composites Obtained on a Cu Electrode in an Ionic Liquid. *Inorg. Chem. Front.* **2019**, *6* (1), 248–256. https://doi.org/10.1039/C8QI00982A.

(109) Soulmi, N.; Dambournet, D.; Rizzi, C.; Sirieix-Plénet, J.; Duttine, M.; Wattiaux, A.; Swiatowska, J.; Borkiewicz, O. J.; Groult, H.; Gaillon, L. Structural and Morphological Description of Sn/SnO $_x$ Core–Shell Nanoparticles Synthesized and Isolated from Ionic Liquid. *Inorganic Chemistry* **2017**, *56* (16), 10099–10106. https://doi.org/10.1021/acs.inorgchem.7b01850.

(110) Lair, V.; Sirieix-Plenet, J.; Gaillon, L.; Rizzi, C.; Ringuedé, A. Mixtures of Room Temperature Ionic Liquid/Ethanol Solutions as Electrolytic Media for Cerium Oxide Thin Layer Electrodeposition. *Electrochimica Acta* **2010**, *56* (2), 784–789. https://doi.org/10.1016/j.electacta.2010.09.102.

(111) Wu, L.-N.; Peng, J.; Sun, Y.-K.; Han, F.-M.; Wen, Y.-F.; Shi, C.-G.; Fan, J.-J.; Huang, L.; Li, J.-T.; Sun, S.-G. A High-Energy Density Li Metal Dual-Ion Battery with Lithium Nitrate-Modified Carbonate-Based Electrolyte. *ACS Appl. Mater. Interfaces* **2019**, acsami.9b05053. https://doi.org/10.1021/acsami.9b05053.

(112) Obrovac, M. N.; Chevrier, V. L. Alloy Negative Electrodes for Li-Ion Batteries. *Chem.*

Rev. **2014**, *114* (23), 11444–11502. https://doi.org/10.1021/cr500207g.

(113) Das, B.; Reddy, M. V.; Chowdari, B. V. R. SnO and SnO·CoO Nanocomposite as High Capacity Anode Materials for Lithium Ion Batteries. *Materials Research Bulletin* **2016**, *74*, 291–298. https://doi.org/10.1016/j.materresbull.2015.10.056.

(114) Hu, R.; Liu, H.; Zeng, M.; Liu, J.; Zhu, M. Progress on Sn-Based Thin-Film Anode Materials for Lithium-Ion Batteries. *Chin. Sci. Bull.* **2012**, *57* (32), 4119–4130. https://doi.org/10.1007/s11434-012-5303-z.

(115) Goward, G. R.; Taylor, N. J.; Souza, D. C. S.; Nazar, L. F. The True Crystal Structure of $Li_{17}M_4$ (M=Ge, Sn, Pb)–Revised from $Li_{22}M_5$. *Journal of Alloys and Compounds* **2001**, *329* (1–2), 82–91. https://doi.org/10.1016/S0925-8388(01)01567-5.

(116) Lupu, C.; Mao, J.-G.; Rabalais, J. W.; Guloy, A. M.; Richardson, J. W. X-Ray and Neutron Diffraction Studies on "$Li_{4.4}$ Sn." *Inorg. Chem.* **2003**, *42* (12), 3765–3771. https://doi.org/10.1021/ic026235o.

(117) Wardell, J. L. Tin: Inorganic Chemistry. In *Encyclopedia of Inorganic and Bioinorganic Chemistry*; Scott, R. A., Ed.; John Wiley & Sons, Ltd: Chichester, UK, 2011. https://doi.org/10.1002/9781119951438.eibc0227.

(118) Styrkas, A. D. Mechanisms of the Allotropic Transition of Sn. **2003**, *39* (8), 5.

(119) Shi, J.; Shi, W.; Jin, W.; Yin, G. Diffusion of Lithium in α-Sn and β-Sn as Anode Materials for Lithium Ion Batteries. *Int. J. Electrochem. Sci.* **2015**, *10*, 8.

(120) Im, H. S.; Cho, Y. J.; Lim, Y. R.; Jung, C. S.; Jang, D. M.; Park, J.; Shojaei, F.; Kang, H. S. Phase Evolution of Tin Nanocrystals in Lithium Ion Batteries. *ACS Nano* **2013**, *7* (12), 11103–11111. https://doi.org/10.1021/nn404837d.

(121) Kravchyk, K.; Protesescu, L.; Bodnarchuk, M. I.; Krumeich, F.; Yarema, M.; Walter, M.; Guntlin, C.; Kovalenko, M. V. Monodisperse and Inorganically Capped Sn and Sn/SnO_2 Nanocrystals for High-Performance Li-Ion Battery Anodes. *Journal of the American Chemical Society* **2013**, *135* (11), 4199–4202. https://doi.org/10.1021/ja312604r.

(122) Simon, P.; Gogotsi, Y. Materials for Electrochemical Capacitors. *Nature Mater* **2008**, *7* (11), 845–854. https://doi.org/10.1038/nmat2297.

(123) Navrotsky, A. Energetics of Nanoparticle Oxides: Interplay between Surface Energy and Polymorphism†. *Geochem Trans* **2003**, *4* (1), 34. https://doi.org/10.1186/1467-4866-4-34.

(124) Obrovac, M. N.; Dahn, J. R. Implications of Finite-Size and Surface Effects on Nanosize Intercalation Materials. *Phys. Rev. B* **2000**, *61* (10), 6713–6719. https://doi.org/10.1103/PhysRevB.61.6713.

(125) Oehl, N.; Hardenberg, L.; Knipper, M.; Kolny-Olesiak, J.; Parisi, J.; Plaggenborg, T. Critical Size for the β- to α-Transformation in Tin Nanoparticles after Lithium Insertion and Extraction. *CrystEngComm* **2015**, *17* (19), 3695–3700. https://doi.org/10.1039/C5CE00148J.

(126) Hörmann, N. G.; Gross, A.; Kaghazchi, P. Semiconductor–Metal Transition Induced by Nanoscale Stabilization. *Physical Chemistry Chemical Physics* **2015**, *17* (8), 5569–5573. https://doi.org/10.1039/C4CP05619A.

(127) Dong, H.; Chen, Y.-C.; Feldmann, C. Polyol Synthesis of Nanoparticles: Status and Options Regarding Metals, Oxides, Chalcogenides, and Non-Metal Elements. *Green Chemistry* **2015**, *17* (8), 4107–4132. https://doi.org/10.1039/C5GC00943J.

(128) Lidor-Shalev, O.; Zitoun, D. Reaction Mechanism of "Amine–Borane Route" towards Sn, Ni, Pd, Pt Nanoparticles. *RSC Adv.* **2014**, *4* (109), 63603–63610. https://doi.org/10.1039/C4RA11483C.

(129) Ahn, H.-J.; Park, K.-W.; Sung, Y.-E. Synthesis and Characterization of Sn Nanophases in a

Ta $_2$ O $_5$ Matrix. *Chem. Mater.* **2004**, *16* (10), 1991–1995. https://doi.org/10.1021/cm030665a.

(130) Li, Z.; Tao, X.; Cheng, Y.; Wu, Z.; Zhang, Z.; Dang, H. A Facile Way for Preparing Tin Nanoparticles from Bulk Tin via Ultrasound Dispersion. *Ultrasonics Sonochemistry* **2007**, *14* (1), 89–92. https://doi.org/10.1016/j.ultsonch.2005.11.008.

(131) Park, C.-M.; Kim, J.-H.; Kim, H.; Sohn, H.-J. Li-Alloy Based Anode Materials for Li Secondary Batteries. *Chem. Soc. Rev.* **2010**, *39* (8), 3115. https://doi.org/10.1039/b919877f.

(132) Sutter, E.; Ivars-Barcelo, F.; Sutter, P. Size-Dependent Room Temperature Oxidation of Tin Particles. *Particle & Particle Systems Characterization* **2014**, *31* (8), 879–885. https://doi.org/10.1002/ppsc.201300352.

(133) Xu, L.; Kim, C.; Shukla, A. K.; Dong, A.; Mattox, T. M.; Milliron, D. J.; Cabana, J. Monodisperse Sn Nanocrystals as a Platform for the Study of Mechanical Damage during Electrochemical Reactions with Li. *Nano Letters* **2013**, *13* (4), 1800–1805. https://doi.org/10.1021/nl400418c.

(134) Todd, A. D. W.; Mar, R. E.; Dahn, J. R. Tin–Transition Metal–Carbon Systems for Lithium-Ion Battery Negative Electrodes. *J. Electrochem. Soc.* **2007**, *154* (6), A597. https://doi.org/10.1149/1.2724741.

(135) Zhang, H.; Yang, Y.; Ren, D.; Wang, L.; He, X. Graphite as Anode Materials: Fundamental Mechanism, Recent Progress and Advances. *Energy Storage Materials* **2021**, *36*, 147–170. https://doi.org/10.1016/j.ensm.2020.12.027.

(136) Asenbauer, J.; Eisenmann, T.; Kuenzel, M.; Kazzazi, A.; Chen, Z.; Bresser, D. The Success Story of Graphite as a Lithium-Ion Anode Material – Fundamentals, Remaining Challenges, and Recent Developments Including Silicon (Oxide) Composites. *Sustainable Energy Fuels* **2020**, *4* (11), 5387–5416. https://doi.org/10.1039/D0SE00175A.

(137) Persson, K.; Sethuraman, V. A.; Hardwick, L. J.; Hinuma, Y.; Meng, Y. S.; van der Ven, A.; Srinivasan, V.; Kostecki, R.; Ceder, G. Lithium Diffusion in Graphitic Carbon. *J. Phys. Chem. Lett.* **2010**, *1* (8), 1176–1180. https://doi.org/10.1021/jz100188d.

(138) Pollak, E.; Geng, B.; Jeon, K.-J.; Lucas, I. T.; Richardson, T. J.; Wang, F.; Kostecki, R. The Interaction of Li $^+$ with Single-Layer and Few-Layer Graphene. *Nano Letters* **2010**, *10* (9), 3386–3388. https://doi.org/10.1021/nl101223k.

(139) Kühne, M.; Börrnert, F.; Fecher, S.; Ghorbani-Asl, M.; Biskupek, J.; Samuelis, D.; Krasheninnikov, A. V.; Kaiser, U.; Smet, J. H. Reversible Superdense Ordering of Lithium between Two Graphene Sheets. *Nature* **2018**. https://doi.org/10.1038/s41586-018-0754-2.

(140) Shi, L.; Pang, C.; Chen, S.; Wang, M.; Wang, K.; Tan, Z.; Gao, P.; Ren, J.; Huang, Y.; Peng, H.; Liu, Z. Vertical Graphene Growth on SiO Microparticles for Stable Lithium Ion Battery Anodes. *Nano Lett.* **2017**, *17* (6), 3681–3687. https://doi.org/10.1021/acs.nanolett.7b00906.

(141) Yang, Q.; Wu, J.; Li, S.; Zhang, L.; Fu, J.; Huang, F.; Cheng, Q. Vertically-Oriented Graphene Nanowalls: Growth and Application in Li-Ion Batteries. *Diamond and Related Materials* **2019**, *91*, 54–63. https://doi.org/10.1016/j.diamond.2018.11.007.

(142) Mu, Y.; Han, M.; Li, J.; Liang, J.; Yu, J. Growing Vertical Graphene Sheets on Natural Graphite for Fast Charging Lithium-Ion Batteries. *Carbon* **2021**, *173*, 477–484. https://doi.org/10.1016/j.carbon.2020.11.027.

(143) Li, S.; Luo, Y.; Lv, W.; Yu, W.; Wu, S.; Hou, P.; Yang, Q.; Meng, Q.; Liu, C.; Cheng, H.-M. Vertically Aligned Carbon Nanotubes Grown on Graphene Paper as Electrodes in Lithium-Ion Batteries and Dye-Sensitized Solar Cells. *Adv. Energy Mater.* **2011**, *1* (4), 486–490. https://doi.org/10.1002/aenm.201100001.

(144) Wang, X.; Wang, T.; Borovilas, J.; He, X.; Du, S.; Yang, Y. Vertically-Aligned Nanostructures for Electrochemical Energy Storage. *Nano Res.* **2019**. https://doi.org/10.1007/s12274-019-2392-x.

(145) Xu, J.; Wang, X.; Yuan, N.; Hu, B.; Ding, J.; Ge, S. Graphite-Based Lithium Ion Battery with Ultrafast Charging and Discharging and Excellent Low Temperature Performance. *Journal of Power Sources* **2019**, *430*, 74–79. https://doi.org/10.1016/j.jpowsour.2019.05.024.

(146) Zhang, C.; Ma, J.; Han, F.; Liu, H.; Zhang, F.; Fan, C.; Liu, J.; Li, X. Strong Anchoring Effect of Ferric Chloride-Graphite Intercalation Compounds ($FeCl_3$-GICs) with Tailored Epoxy Groups for High-Capacity and Stable Lithium Storage. *J. Mater. Chem. A* **2018**, *6* (37), 17982–17993. https://doi.org/10.1039/C8TA06670A.

(147) Li, Z.; Zhang, C.; Han, F.; Wang, F.; Zhang, F.; Shen, W.; Ye, C.; Li, X.; Liu, J. Towards High-Volumetric Performance of Na/Li-Ion Batteries: A Better Anode Material with Molybdenum Pentachloride–Graphite Intercalation Compounds ($MoCl_5$–GICs). *J. Mater. Chem. A* **2020**, *8* (5), 2430–2438. https://doi.org/10.1039/C9TA12651A.

(148) Yoo, E.; Kim, J.; Hosono, E.; Zhou, H.; Kudo, T.; Honma, I. Large Reversible Li Storage of Graphene Nanosheet Families for Use in Rechargeable Lithium Ion Batteries. *Nano Letters* **2008**, *8* (8), 2277–2282. https://doi.org/10.1021/nl800957b.

(149) Martin, C.; Genovese, M.; Louli, A. J.; Weber, R.; Dahn, J. R. Cycling Lithium Metal on Graphite to Form Hybrid Lithium-Ion/Lithium Metal Cells. *Joule* **2020**, *4* (6), 1296–1310. https://doi.org/10.1016/j.joule.2020.04.003.

(150) Lin, D.; Liu, Y.; Liang, Z.; Lee, H.-W.; Sun, J.; Wang, H.; Yan, K.; Xie, J.; Cui, Y. Layered Reduced Graphene Oxide with Nanoscale Interlayer Gaps as a Stable Host for Lithium Metal Anodes. *Nature Nanotech* **2016**, *11* (7), 626–632. https://doi.org/10.1038/nnano.2016.32.

(151) Lee, C.; Wei, X.; Kysar, J. W.; Hone, J. Measurement of the Elastic Properties and Intrinsic Strength of Monolayer Graphene. *Science* **2008**, *321* (5887), 385–388. https://doi.org/10.1126/science.1157996.

(152) Zhu, Y.; Murali, S.; Cai, W.; Li, X.; Suk, J. W.; Potts, J. R.; Ruoff, R. S. Graphene and Graphene Oxide: Synthesis, Properties, and Applications. *Advanced Materials* **2010**, *22* (35), 3906–3924. https://doi.org/10.1002/adma.201001068.

(153) Avouris, P.; Dimitrakopoulos, C. Graphene: Synthesis and Applications. *Materials today* **2012**, *15* (3), 86–97.

(154) Backes, C.; Abdelkader, A. M.; Alonso, C.; Andrieux-Ledier, A.; Arenal, R.; Azpeitia, J.; Balakrishnan, N.; Banszerus, L.; Barjon, J.; Bartali, R.; Bellani, S.; Berger, C.; Berger, R.; Ortega, M. M. B.; Bernard, C.; Beton, P. H.; Beyer, A.; Bianco, A.; Bøggild, P.; Bonaccorso, F.; Barin, G. B.; Botas, C.; Bueno, R. A.; Carriazo, D.; Castellanos-Gomez, A.; Christian, M.; Ciesielski, A.; Ciuk, T.; Cole, M. T.; Coleman, J.; Coletti, C.; Crema, L.; Cun, H.; Dasler, D.; De Fazio, D.; Díez, N.; Drieschner, S.; Duesberg, G. S.; Fasel, R.; Feng, X.; Fina, A.; Forti, S.; Galiotis, C.; Garberoglio, G.; García, J. M.; Garrido, J. A.; Gibertini, M.; Gölzhäuser, A.; Gómez, J.; Greber, T.; Hauke, F.; Hemmi, A.; Hernandez-Rodriguez, I.; Hirsch, A.; Hodge, S. A.; Huttel, Y.; Jepsen, P. U.; Jimenez, I.; Kaiser, U.; Kaplas, T.; Kim, H.; Kis, A.; Papagelis, K.; Kostarelos, K.; Krajewska, A.; Lee, K.; Li, C.; Lipsanen, H.; Liscio, A.; Lohe, M. R.; Loiseau, A.; Lombardi, L.; Francisca López, M.; Martin, O.; Martín, C.; Martínez, L.; Martin-Gago, J. A.; Ignacio Martínez, J.; Marzari, N.; Mayoral, Á.; McManus, J.; Melucci, M.; Méndez, J.; Merino, C.; Merino, P.; Meyer, A. P.; Miniussi, E.; Miseikis, V.; Mishra, N.; Morandi, V.; Munuera, C.; Muñoz, R.; Nolan, H.; Ortolani, L.; Ott, A. K.; Palacio, I.; Palermo, V.; Parthenios, J.; Pasternak, I.; Patane, A.;

Prato, M.; Prevost, H.; Prudkovskiy, V.; Pugno, N.; Rojo, T.; Rossi, A.; Ruffieux, P.; Samorì, P.; Schué, L.; Setijadi, E.; Seyller, T.; Speranza, G.; Stampfer, C.; Stenger, I.; Strupinski, W.; Svirko, Y.; Taioli, S.; Teo, K. B. K.; Testi, M.; Tomarchio, F.; Tortello, M.; Treossi, E.; Turchanin, A.; Vazquez, E.; Villaro, E.; Whelan, P. R.; Xia, Z.; Yakimova, R.; Yang, S.; Yazdi, G. R.; Yim, C.; Yoon, D.; Zhang, X.; Zhuang, X.; Colombo, L.; Ferrari, A. C.; Garcia-Hernandez, M. Production and Processing of Graphene and Related Materials. *2D Materials* **2020**, *7* (2), 022001. https://doi.org/10.1088/2053-1583/ab1e0a.

(155) Müllen, K. Evolution of Graphene Molecules: Structural and Functional Complexity as Driving Forces behind Nanoscience. *ACS Nano* **2014**, *8* (7), 6531–6541. https://doi.org/10.1021/nn503283d.

(156) Tang, C.; Wang, H.-F.; Huang, J.-Q.; Qian, W.; Wei, F.; Qiao, S.-Z.; Zhang, Q. 3D Hierarchical Porous Graphene-Based Energy Materials: Synthesis, Functionalization, and Application in Energy Storage and Conversion. *Electrochemical Energy Reviews* **2019**. https://doi.org/10.1007/s41918-019-00033-7.

(157) Duan, J.; Chen, S.; Jaroniec, M.; Qiao, S. Z. Heteroatom-Doped Graphene-Based Materials for Energy-Relevant Electrocatalytic Processes. *ACS Catalysis* **2015**, *5* (9), 5207–5234.

(158) Dreyer, D. R.; Park, S.; Bielawski, C. W.; Ruoff, R. S. The Chemistry of Graphene Oxide. *Chem. Soc. Rev.* **2010**, *39* (1), 228–240. https://doi.org/10.1039/B917103G.

(159) Li, Y.; Alain-Rizzo, V.; Galmiche, L.; Audebert, P.; Miomandre, F.; Louarn, G.; Bozlar, M.; Pope, M. A.; Dabbs, D. M.; Aksay, I. A. Functionalization of Graphene Oxide by Tetrazine Derivatives: A Versatile Approach toward Covalent Bridges between Graphene Sheets. *Chem. Mater.* **2015**, *27* (12), 4298–4310. https://doi.org/10.1021/acs.chemmater.5b00672.

(160) Spyrou, K.; Rudolf, P. An Introduction to Graphene. In *Functionalization of Graphene*; Georgakilas, V., Ed.; Wiley-VCH Verlag GmbH & Co. KGaA: Weinheim, Germany, 2014; pp 1–20. https://doi.org/10.1002/9783527672790.ch1.

(161) Tran, Q. T.; Phung, T. T.; Nguyen, Q. T.; Le, T. G.; Lagrost, C. Highly Sensitive and Rapid Determination of Sunset Yellow in Drinks Using a Low-Cost Carbon Material-Based Electrochemical Sensor. *Anal Bioanal Chem* **2019**, *411* (28), 7539–7549. https://doi.org/10.1007/s00216-019-02155-9.

(162) Liu, J.-Y.; Li, X.-X.; Huang, J.-R.; Li, J.-J.; Zhou, P.; Liu, J.-H.; Huang, X.-J. Three-Dimensional Graphene-Based Nanocomposites for High Energy Density Li-Ion Batteries. *Journal of Materials Chemistry A* **2017**, *5* (13), 5977–5994. https://doi.org/10.1039/C7TA00448F.

(163) Luo, B.; Zhi, L. Design and Construction of Three Dimensional Graphene-Based Composites for Lithium Ion Battery Applications. *Energy & Environmental Science* **2015**, *8* (2), 456–477. https://doi.org/10.1039/C4EE02578D.

(164) Zhang, S.; Xiao, W.; Zhang, Y.; Liu, K.; Zhang, X.; Zhao, J.; Wang, Z.; Zhang, P.; Shao, G. Construction of a Low-Defect and Highly Conductive 3D Graphene Network to Enable a High Sulphur Content Cathode for High Performance Li–S/Graphene Batteries. *Journal of Materials Chemistry A* **2018**, *6* (45), 22555–22565. https://doi.org/10.1039/C8TA06869K.

(165) Zhou, S.; Zheng, Z.; Mei, T.; Wang, X. Structural Design and Material Preparation of Carbon-Based Electrodes for High-Performance Lithium Storage Systems. *Carbon* **2018**. https://doi.org/10.1016/j.carbon.2018.11.054.

(166) Wang, L.; Han, J.; Kong, D.; Tao, Y.; Yang, Q.-H. Enhanced Roles of Carbon Architectures in High-Performance Lithium-Ion Batteries. *Nano-Micro Letters* **2019**, *11* (1). https://doi.org/10.1007/s40820-018-0233-1.

(167) Liang, M.; Zhi, L. Graphene-Based Electrode Materials for Rechargeable Lithium Batteries. *Journal of Materials Chemistry* **2009**, *19* (33), 5871.

https://doi.org/10.1039/b901551e.

(168) Li, G.; Huang, B.; Pan, Z.; Su, X.; Shao, Z.; An, L. Advances in Three-Dimensional Graphene-Based Materials: Configurations, Preparations and Applications in Secondary Metal (Li, Na, K, Mg, Al)-Ion Batteries. *Energy Environ. Sci.* **2019**. https://doi.org/10.1039/C8EE03014F.

(169) Chen, H.; Xu, H.; Wang, S.; Huang, T.; Xi, J.; Cai, S.; Guo, F.; Xu, Z.; Gao, W.; Gao, C. Ultrafast All-Climate Aluminum-Graphene Battery with Quarter-Million Cycle Life. *Sci. Adv.* **2017**, *3* (12), eaao7233. https://doi.org/10.1126/sciadv.aao7233.

(170) Islam, Md. M.; Subramaniyam, C. M.; Akhter, T.; Faisal, S. N.; Minett, A. I.; Liu, H. K.; Konstantinov, K.; Dou, S. X. Three Dimensional Cellular Architecture of Sulfur Doped Graphene: Self-Standing Electrode for Flexible Supercapacitors, Lithium Ion and Sodium Ion Batteries. *J. Mater. Chem. A* **2017**, *5* (11), 5290–5302. https://doi.org/10.1039/C6TA10933K.

(171) Wang, G.; Wang, B.; Wang, X.; Park, J.; Dou, S.; Ahn, H.; Kim, K. Sn/Graphene Nanocomposite with 3D Architecture for Enhanced Reversible Lithium Storage in Lithium Ion Batteries. *J. Mater. Chem.* **2009**, *19* (44), 8378. https://doi.org/10.1039/b914650d.

(172) Zhuiykov, S. Composite Graphene/Semiconductor Nano-Structures for Energy Storage. In *Nanostructured Semiconductors*; Elsevier, 2018; pp 295–352. https://doi.org/10.1016/B978-0-08-101919-1.00006-4.

(173) Jiang, Y.; Jiang, J.; Wang, Z.; Han, M.; Liu, X.; Yi, J.; Zhao, B.; Sun, X.; Zhang, J. $Li_{4.4}Sn$ Encapsulated in Hollow Graphene Spheres for Stable Li Metal Anodes without Dendrite Formation for Long Cycle-Life of Lithium Batteries. *Nano Energy* **2020**, *70*, 104504. https://doi.org/10.1016/j.nanoen.2020.104504.

(174) Zhao, B.; Wang, Z.; Wang, S.; Jiang, J.; Si, J.; Huang, S.; Chen, Z.; Li, W.; Jiang, Y. Sandwiched Spherical Tin Dioxide/Graphene with a Three-Dimensional Interconnected Closed Pore Structure for Lithium Storage. *Nanoscale* **2018**, *10* (34), 16116–16126. https://doi.org/10.1039/C8NR03776K.

(175) Jiang, Y.; Wang, Y.; Jiang, J.; Liu, S.; Li, W.; Huang, S.; Chen, Z.; Zhao, B. In-Situ Solvothermal Phosphorization from Nano-Sized Tetragonal-Sn to Rhombohedral-Sn_4P_3 Embedded in Hollow Graphene Sphere with High Capacity and Stability. *Electrochimica Acta* **2019**. https://doi.org/10.1016/j.electacta.2019.04.037.

(176) Liu, X.; Li, N.; Yang, C.; Liu, Z.; Feng, Y.; Dong, W.; Liu, S.; Liu, H.; Jia, Y.; Zhao, J.; Li, Y. Sn Accommodation in Tunable-Void and Porous Graphene Bumper for High-Performance Li- and Na-Ion Storage. *Journal of Alloys and Compounds* **2019**, *790*, 1043–1050. https://doi.org/10.1016/j.jallcom.2019.03.258.

(177) Hong, X.; Wang, R.; Li, S.; Fu, J.; Chen, L.; Wang, X. Hydrophilic Macroporous SnO_2/RGO Composite Prepared by Melamine Template for High Efficient Photocatalyst. *Journal of Alloys and Compounds* **2019**, 152550. https://doi.org/10.1016/j.jallcom.2019.152550.

(178) Wang, J.-F.; He, D.-N. *In Situ* Growth of Heterostructured Sn/SnO Nanospheres Embedded in Crumpled Graphene as an Anode Material for Lithium Ion Batteries. *Dalton Transactions* **2018**. https://doi.org/10.1039/C8DT02474J.

(179) Leng, J.; Wang, Z.; Li, X.; Guo, H.; Yan, G.; Hu, Q.; Peng, W.; Wang, J. A Novel Dried Plum-like Yolk–Shell Architecture of Tin Oxide Nanodots Embedded into a Carbon Matrix: Ultra-Fast Assembly and Superior Lithium Storage Properties. *J. Mater. Chem. A* **2019**. https://doi.org/10.1039/C8TA12399C.

(180) Zhan, L.; Zhou, X.; Luo, J.; Ning, X. Binder-Free Multilayered SnO_2/Graphene on Ni Foam as a High-Performance Lithium Ion Batteries Anode. *Ceramics International* **2018**.

https://doi.org/10.1016/j.ceramint.2018.12.190.

(181) Luo, B.; Qiu, T.; Ye, D.; Wang, L.; Zhi, L. Tin Nanoparticles Encapsulated in Graphene Backboned Carbonaceous Foams as High-Performance Anodes for Lithium-Ion and Sodium-Ion Storage. *Nano Energy* **2016**, *22*, 232–240. https://doi.org/10.1016/j.nanoen.2016.02.024.

(182) Li, Y.; Zhang, H.; Chen, Y.; Shi, Z.; Cao, X.; Guo, Z.; Shen, P. K. Nitrogen-Doped Carbon-Encapsulated SnO_2@Sn Nanoparticles Uniformly Grafted on Three-Dimensional Graphene-like Networks as Anode for High-Performance Lithium-Ion Batteries. *ACS Applied Materials & Interfaces* **2016**, *8* (1), 197–207. https://doi.org/10.1021/acsami.5b08340.

(183) Zhang, W.; Du, R.; Zhou, C.; Pu, S.; Han, B.; Xia, K.; Gao, Q.; Wu, J. Ultrafine SnO_2 Aggregates in Interior of Porous Carbon Nanotubes as High-Performance Anode Materials of Lithium-Ion Batteries. *Materials Today Energy* **2019**, *12*, 303–310. https://doi.org/10.1016/j.mtener.2019.02.003.

(184) Jankovič, L.; Gournis, D.; Trikalitis, P. N.; Arfaoui, I.; Cren, T.; Rudolf, P.; Sage, M.-H.; Palstra, T. T. M.; Kooi, B.; De Hosson, J.; Karakassides, M. A.; Dimos, K.; Moukarika, A.; Bakas, T. Carbon Nanotubes Encapsulating Superconducting Single-Crystalline Tin Nanowires. *Nano Lett.* **2006**, *6* (6), 1131–1135. https://doi.org/10.1021/nl0602387.

(185) Ji, J.; Zhou, H.; Xiong, L.; Li, L.; Yu, X.; Wei, L. Synthesis of Nitrogen-Doped Reduced Graphene Oxide/SnO_2 Composite Hydrogels and Characterization of Electrode Materials. *Materials Research Express* **2019**. https://doi.org/10.1088/2053-1591/ab28e9.

(186) Gu, C.; Zhang, H.; Wang, X.; Tu, J. One-Pot Synthesis of SnO_2/Reduced Graphene Oxide Nanocomposite in Ionic Liquid-Based Solution and Its Application for Lithium Ion Batteries. *Materials Research Bulletin* **2013**, *48* (10), 4112–4117. https://doi.org/10.1016/j.materresbull.2013.06.041.

(187) Yang, Y.; Pan, Z.; Wang, Y.-Y.; Ma, Y. C.; Li, C.; Lu, Y.; Wu, X.-L. Ionic-Liquid-Bifunctional Wrapping of Ultrafine SnO2 Nanocrystals into N-Doped Graphene Networks: High Pseudocapacitive Sodium Storage and High-Performance Sodium-Ion Full Cell. *Nanoscale* **2019**. https://doi.org/10.1039/C9NR02542A.

(188) Zeb, G.; Gaskell, P.; Le, X. T.; Xiao, X.; Szkopek, T.; Cerruti, M. Decoration of Graphitic Surfaces with Sn Nanoparticles through Surface Functionalization Using Diazonium Chemistry. *Langmuir* **2012**, *28* (36), 13042–13050. https://doi.org/10.1021/la302162c.

(189) Borude, R. R.; Sugiura, H.; Ishikawa, K.; Tsutsumi, T.; Kondo, H.; Ikarashi, N.; Hori, M. Single-Step, Low-Temperature Simultaneous Formations and in Situ Binding of Tin Oxide Nanoparticles to Graphene Nanosheets by In-Liquid Plasma for Potential Applications in Gas Sensing and Lithium-Ion Batteries. *ACS Applied Nano Materials* **2019**. https://doi.org/10.1021/acsanm.8b02201.

(190) Yan, X.; Fan, C.-Y.; Yang, X.; Wang, Y.-Y.; Hou, B.-H.; Pang, W.-L.; Wu, X.-L. A Cation/Anion-Dually Active Metal-Organic Complex with 2D Lamellar Structure as Anode Material for Li/Na-Ion Batteries. *Materials Today Energy* **2019**, *13*, 302–307. https://doi.org/10.1016/j.mtener.2019.06.002.

(191) Xie, M.; Sun, X.; George, S. M.; Zhou, C.; Lian, J.; Zhou, Y. Amorphous Ultrathin SnO_2 Films by Atomic Layer Deposition on Graphene Network as Highly Stable Anodes for Lithium-Ion Batteries. *ACS Applied Materials & Interfaces* **2015**, *7* (50), 27735–27742. https://doi.org/10.1021/acsami.5b08719.

(192) Huang, R.; Wang, L.; Zhang, Q.; Chen, Z.; Li, Z.; Pan, D.; Zhao, B.; Wu, M.; Wu, C. M. L.; Shek, C.-H. Irradiated Graphene Loaded with SnO_2 Quantum Dots for Energy Storage. *ACS Nano* **2015**, *9* (11), 11351–11361. https://doi.org/10.1021/acsnano.5b05146.

(193) Pan, E.; Jin, Y.; Zhao, C.; Jia, M.; Chang, Q.; Zhang, R.; Jia, M. Mesoporous Sn_4P_3-Graphene Aerogel Composite as a High-Performance Anode in Sodium Ion Batteries. *Applied Surface Science* **2019**, *475*, 12–19. https://doi.org/10.1016/j.apsusc.2018.12.259.

(194) Kim, H.; Kim, S.-W.; Park, Y.-U.; Gwon, H.; Seo, D.-H.; Kim, Y.; Kang, K. SnO_2/Graphene Composite with High Lithium Storage Capability for Lithium Rechargeable Batteries. *Nano Research* **2010**, *3* (11), 813–821. https://doi.org/10.1007/s12274-010-0050-4.

(195) Jiang, P.; Jing, J.; Wang, Y.; Li, H.; He, X.; Chen, Y.; Liu, W. Facilely Transforming Bulk Materials to SnO/Pristine Graphene 2D-2D Heterostructures for Stable and Fast Lithium Storage. *Journal of Alloys and Compounds* **2020**, *812*, 152114. https://doi.org/10.1016/j.jallcom.2019.152114.

(196) Soulmi, N. Mise au point de nouveaux procédés d'élaboration en milieu liquide ionique de nanomatériaux à base d'étain en vue de leur utilisation comme électrode négative de batterie Li-ion, Université Pierre et Marie Curie - Paris VI, 2017.

(197) Tian, J.; Yang, J.; Yang, C.; Hao, S. Compression and Reduction of Graphene Oxide Aerogels into Flexible, Porous and Functional Graphene Films. *Journal of Materials Science* **2019**. https://doi.org/10.1007/s10853-019-03828-7.

(198) Hu, H.; Zhao, Z.; Wan, W.; Gogotsi, Y.; Qiu, J. Ultralight and Highly Compressible Graphene Aerogels. *Advanced Materials* **2013**, *25* (15), 2219–2223. https://doi.org/10.1002/adma.201204530.

(199) Balaji, M.; Nithya, P.; Mayakrishnan, A.; Muthulakshmi, V.; Jegatheeswaran, S.; Jeyaraman, A. R.; Selvam, S.; Sundrarajan, M. Two Dimensional Graphene Oxides Converted to Three Dimensional P, N, F and B, N, F Tri-Doped Graphene by Ionic Liquid for Efficient Catalytic Performance. *Carbon* **2019**. https://doi.org/10.1016/j.carbon.2019.05.060.

(200) Xiao, M.; Meng, Y.; Duan, C.; Hu, Q.; Li, R.; Zhu, F.; Zhang, Y. Preparation of Co_3O_4/Nitrogen-Doped Carbon Composite by in Situ Solvothermal with Ionic Liquid and Its Electrochemical Performance as Lithium-Ion Battery Anode. *Ionics* **2018**. https://doi.org/10.1007/s11581-018-2831-9.

(201) Du, M.; Meng, Y.; Wang, C.; Duan, C.; Zhu, F.; Zhang, Y. A Simple Synthesis of Nitrogen-Sulfur Co-Doped Porous Carbon Using Ionic Liquids as Dopant for High Rate Performance Li-Ion Batteries. *Journal of Electroanalytical Chemistry* **2019**, *834*, 17–25. https://doi.org/10.1016/j.jelechem.2018.12.042.

(202) Ding, X.; Du, C.; Li, J.; Huang, X. FeS_2 Microspheres Wrapped by N-Doped RGO from an Fe-Based Ionic Liquid Precursor for Rechargeable Lithium Ion Batteries. *Sustainable Energy & Fuels* **2019**. https://doi.org/10.1039/C8SE00539G.

(203) Chang, D. W.; Lee, E. K.; Park, E. Y.; Yu, H.; Choi, H.-J.; Jeon, I.-Y.; Sohn, G.-J.; Shin, D.; Park, N.; Oh, J. H.; Dai, L.; Baek, J.-B. Nitrogen-Doped Graphene Nanoplatelets from Simple Solution Edge-Functionalization for n-Type Field-Effect Transistors. *Journal of the American Chemical Society* **2013**, *135* (24), 8981–8988. https://doi.org/10.1021/ja402555n.

(204) Xing, C.; Tan, R.; Hao, P.; Gao, M.; Yin, D.; Yin, D. Graphene Oxide Supported Chlorostannate (IV) Ionic Liquid: Brønsted-Lewis Acidic Combined Catalyst for Highly Efficient Baeyer-Villiger Oxidation in Water. *Molecular Catalysis* **2017**, *433*, 37–47. https://doi.org/10.1016/j.mcat.2016.12.003.

(205) Ravula, S.; Baker, S. N.; Kamath, G.; Baker, G. A. Ionic Liquid-Assisted Exfoliation and Dispersion: Stripping Graphene and Its Two-Dimensional Layered Inorganic Counterparts of Their Inhibitions. *Nanoscale* **2015**, *7* (10), 4338–4353.

https://doi.org/10.1039/C4NR01524J.

(206) Zhang, Y.; Park, S.-J. Imidazolium-Optimized Conductive Interfaces in Multilayer Graphene Nanoplatelet/Epoxy Composites for Thermal Management Applications and Electroactive Devices. *Polymer* **2019**. https://doi.org/10.1016/j.polymer.2019.01.086.

(207) Zhang, S.-Y.; Zhuang, Q.; Zhang, M.; Wang, H.; Gao, Z.; Sun, J.-K.; Yuan, J. Poly(Ionic Liquid) Composites. *Chemical Society Reviews* **2020**. https://doi.org/10.1039/C8CS00938D.

Chapter 2:
Preparation of a graphene-based matrix, tin nanoparticles and the functionalized ionic liquid

The objectives of this study were the design and creation of a composite Li-ion anode material, based on tin nanoparticles and making use of their interaction with the EMI^+TFSI^- ionic liquid. These two elements would be integrated into a suitable carbon-based matrix. Specific demands and roles for each component were that tin nanoparticles would function as the main storage of lithium these would be held in place by EMI cations, paired with TFSI anions, with the latter contributing to the stability of the SEI layer[1]; graphene would provide the surface on which EMI^+ would be anchored and it would be responsible for both the form of the electrode as well as the charge transfer, while also serving as an auxiliary lithium reserve. Having established the requirements our composite material should meet, we set out to prepare its individual components. Since neither tin nanoparticles nor functionalized ionic liquid nor graphene oxide were commercially available (or in the case of graphene oxide, not at the desired dimensions), we had to synthesize them ourselves. An extensive survey of the literature and the accumulated experience within our group provided a number of methods that could be employed. This project aspired to produce a proof of concept, so a further set of restrictions was, namely that the processes and techniques that would be chosen would be as simple, easy to scale up and low-cost as possible, although cost was not taken into account in the selection of the base components.

This chapter details the work carried out in order to prepare and characterize each of these components of the ternary composite material. With the specifics of Li-ion battery operation and the constraints that were set as criteria, a number of published protocols were selected and adapted to the requirements of the targeted system. It was also necessary to identify and adapt the analytical techniques, that would allow to examine and assess the effects of each process and which might also be transferable to the assembled system.

1. Graphene-based matrix

More often than not, the covalent functionalization of graphene is not straightforward. It requires its initial oxidation to graphene oxide, a material much more easy to process via solution chemistry, but which possesses markedly different properties and critically for its use in electrodes, diminished electrical conductivity[2]. Once the functionalization and any other necessary treatments have taken place, the lattice should be restored in order to regain the properties lost by oxidation, *e.g.* electrical and thermal conductivity, mechanical strength. This often poses a painful conundrum, as the reduction process might undo the desired modifications, so there is an intrinsic properties versus added functionality trade-off that needs to be made.

1.1. Graphene oxide (GO)

In broad strokes, the oxidation of graphite to graphene oxide (or graphite oxide, as it was called before the isolation of graphene) has been through three major iterations. The first published method was that of Brodie in 1859[3]. The main oxidizer used was potassium chlorate ($KClO_3$) – though Brodie experimented with other oxidizing agents as well, such as potassium dichromate ($K_2Cr_2O_7$) – which was mixed with graphite and then fuming HNO_3 was added in a water bath kept at 60°C. The process was laborious and lasted about two weeks. In 1898, Staudenmaier[4] improved upon Brodie's method and while he kept $KClO_3$ as the oxidizer, he added it over the course of one week to a mixture of graphite, concentrated H_2SO_4 and concentrated HNO_3, cutting the processing time in half. During that time though, the reactor had to be kept cool, as chlorine dioxide (ClO_2), a byproduct of the reaction, posed an explosion hazard. It wasn't until 1958 that a different oxidizer was used and as a consequence, a quicker and safer method was developed, that of Hummers and Offeman[5].

Their oxidizer of choice was $KMnO_4$, which was added to a mixture of graphite and sodium nitrate ($NaNO_3$) in concentrated H_2SO_4, kept in an ice bath. The oxidation was completed in just under two hours. These three methods and variations thereof are still being used for the production of graphene oxide, with that of Hummers and Offeman being employed in industrial settings[6] almost exclusively, because it is faster and safer. It should be noted that any synthetic method based on that of Hummers and Offeman, regardless of reagents or conditions, falls under the umbrella term "modified Hummers method", which is rather loosely defined[7]. The protocol we've followed in our synthesis is based on that of Kovtyukhova *et al.*[8], which in turn is a variation of the Hummers method, that includes a pre-oxidation step. This facilitates both the exfoliation of graphite and the oxidation, through the intercalation of sulfate and persulfate salts between the sheets. These intercalated species act as spacers, making it easier for oxidizer ions to penetrate in the interlamellar space and also as oxidizers themselves.

Because of the immense complexity of GO, the exact mechanism for Hummers' (as well as the others) oxidation method remains a topic of study and debate[9]. However, studies such as the one by Lerf and Klinowski[10] and by Dimiev and Tour[11], which have produced the eponymous models, have elucidated the structure of graphene oxide. According to their investigations, carboxyl and carbonyl groups are found exclusively on the edges of graphitic planes, whereas hydroxyl groups and epoxides are rather ubiquitous, but mostly concentrated on the inner surface of the sheets. Looking at the reaction mixture and keeping in mind what is known about the functional groups of graphene oxide, however, some safe generalized assumptions can be made as to how each chemical species came to be and where it is expected to form on the sheets of GO. First, the oxidizer transfers an oxygen atom to a double bond, forming an epoxide. The epoxide can undergo an acid-catalyzed ring-opening reaction with water, resulting in a 1,2-diol. The newly-formed alcohol groups may be further oxidized, depending on their position on the lattice (Fig. 2.1). Primary alcohols can be oxidized to aldehydes and since a strong oxidizer is used, the aldehydes will be oxidized to carboxylic acids. Secondary alcohols will yield ketones. Tertiary alcohols cannot

be oxidized. Consequently, one would expect to find carbonyl and carboxyl groups on the edges of layers (with the caveat that carboxyl groups would have to form on distal, conjugated carbons not part of aromatic rings, or where the rings might have broken open) and hydroxyl groups and any unhydrolyzed epoxides anywhere else on the faces of the sheets.

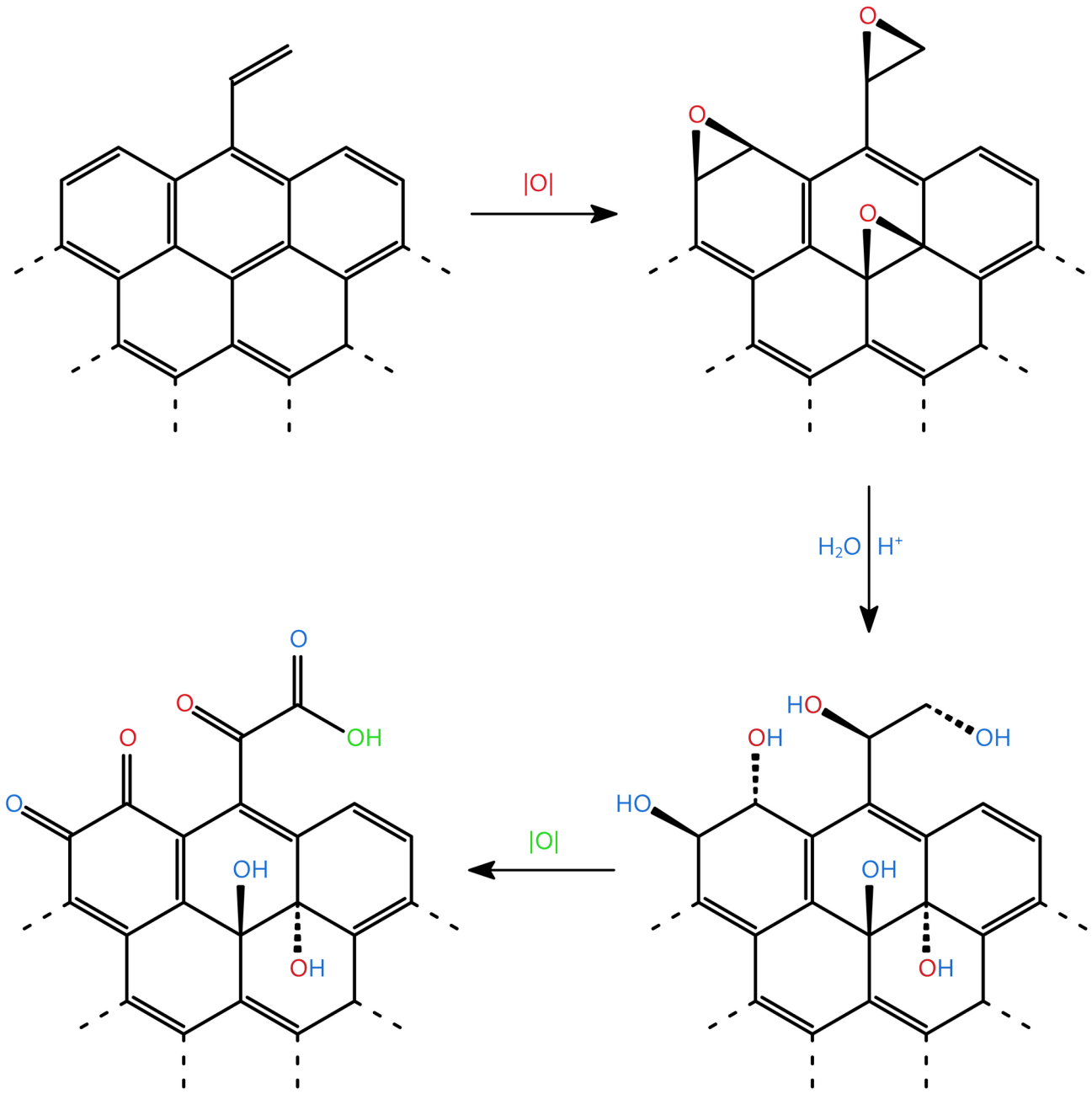

Figure 2.1: Possible reaction scheme for the oxidation of graphene to graphene oxide.

While generally true, the above summary description is a simplified representation of the

events taking place during the oxidation of graphite. For instance, the reaction conditions, in particular the use of concentrated sulfuric acid, also favor the dehydration of alcohols back to alkenes. This description fails to account for the role the extended π-systems play, the relative abundance of epoxides at the end of the reaction, or the fact that for a given combination of reagents, the degree of oxygenation reaches a plateau after a certain reaction time[9]. Furthermore, the reaction itself is exothermic and violent and can lead to the tearing of graphene lamellae, or to their being punctured, creating new reaction sites in the process. The conjugated system is divided into many smaller, unconnected sp^2 domains, which border oxygen-rich sp^3 domains. The introduction of defects leads to the wrinkling of the sheets, a hallmark of graphene oxide. The oxidized material has lost its electrical and thermal conductivity, becoming an insulator and the metallic luster of graphite has been replaced by a dark brown to black color[2,12,13].

Perhaps the most important property of graphene oxide from a chemist's point of view, is its dispersibility in water and other polar solvents, with which its polar groups interact strongly, *e.g.* via hydrogen bonding. In fact, one could even talk about the solubility of graphene oxide in polar solvents, since its polar groups can undergo dissociation and are actually solvated, not unlike other macromolecules, such as proteins. This of course is a matter of perspective and it is mentally challenging to think of something that is visible to the naked eye as a solvated particle. In any case, what is important is that this permits GO to be integrated in a wide array of "classical chemistry" synthetic routes. In contrast, pristine graphene can be suspended in a limited number of organic solvents, at moderate to low concentrations, often requiring the use of surfactants[14,15]; the range of compatible solvents and the use of additives increase the complexity and often the toxicity of resultant systems[14,16].

During oxidation, as the oxygen-bearing groups are being introduced into the lattice and the sp^3-hybridized carbon atoms bend out of plane, the sheets push each other apart. This facilitates the intercalation of solvent and oxidizer molecules, further promoting the

exfoliation of the platelets. At the end of the reaction and depending on the shearing forces (*e.g.* due to stirring), a considerable amount of material is found completely (*i.e.* as single-layer GO) or partially exfoliated. The material that remains stacked can be brought to almost complete exfoliation with little effort – compared to the exfoliation of pristine graphite[15] – by mechanical means, such as sonication or high-shear mixing.

1.2. Reduced graphene oxide (rGO)

Brodie had marveled at "the minutest state of division" he saw in "graphite oxide", but it wasn't until 1962, when Boehm[17] considered the graphene oxide route as a method to produce monolayers of graphite (graphene hadn't been isolated yet, hence the word choice), by reducing the layers he had previously oxidized. Boehm's assumption holds true and the reduction of top-down produced graphene oxide into reduced graphene oxide is widely used today, especially when production at scale or modifications to graphene's intrinsic properties are required. Unfortunately, regardless of the chosen method of reduction, the restoration cannot be complete, not unless the material is subjected to the same conditions of temperature and pressure that led to the formation of graphite in the first place. As a result, the properties of rGO will always lie somewhere between those of graphene oxide and pristine graphene. The omnipresence of this trade-off when choosing to follow the path of graphene oxide cannot be overstated enough. As detailed in the first chapter, a number of different techniques, mostly chemical and thermal are employed for the reduction of GO to rGO, with the latter yielding superior results in terms of both the removal of functional groups and the restoration of the graphitic lattice[18]. The resistivity of electrode materials is crucial to the design of a battery, as the stored energy is finite and ohmic losses consume an amount of that energy, while they can pose safety threats when the battery is being charged. For these reasons, we opted to reduce our materials thermally, tailoring the process to the stability of the other components of the targeted composite.

1.3. Synthesis of graphene oxide

The effect of the starting material, that is graphite, on the properties of GO and any resulting derivatives often goes overlooked[19]. Brodie had noticed that minerals from different regions of the world did not exhibit the same behavior during oxidation[3]; this is in part due to the different impurities in each ore (responsible for the variations in color he observed), but also due to the crystallinity that differs based on how natural graphite might have formed. Nowadays, purity is not a problem anymore, as the manufacturers process the ore in order to remove other minerals and clays that are usually found together with graphite. For instance, the graphite purchased for this work had a stated purity higher or equal to 99.9%. Furthermore, it was in the form of graphite flakes, which possess a high level of crystallinity. Also, we selected flakes of a rather large size, -10 Mesh (≤ 2 mm) and considering that graphene sheets can be found folded inside the flakes, we expected to end up with some individual sheets larger than that size. This was done with the application of the material in mind. While electrons can undergo ballistic transport on graphene, that is not the case when they need to hop from one sheet to a neighboring one[20]. We reasoned that by using larger sheets, we could minimize the hops along the conduction path and produce a material with lowered resistivity.

As it was already mentioned, during the pre-oxidation step sulfate and persulfate salts are intercalated between the sheets of graphite and this promotes both its exfoliation and its oxidation. While to the best of our knowledge, no definitive proof of a specific reaction mechanism has been demonstrated, it has been proposed that the main oxidation proceeds in three distinct stages[21]. The first two involve the intercalation of sulfates/sulfuric acid and permanganates, followed by the oxidation of the sheets. At the last stage, the covalent bonds that have formed between the oxidizing species and the graphitic lattice are hydrolyzed, inducing the exfoliation of individual sheets. The presence of some amount of water is essential for the oxidation to take place. If oleum (fuming sulfuric acid) is used instead of concentrated sulfuric acid, at the end of the process the material remains largely

unchanged, save for the intercalation of some salts between the sheets. It has been claimed that this lack of reactivity is the result of the oxidizing species being mostly found in their non-ionized forms[21], though this assumption is not backed by the cited sources. A typical synthesis, based on the protocol of Kovtyukhova *et al.* was carried out during this work, as described below.

1.3.1. Experimental method

A beaker containing 2 g of $K_2S_2O_8$ and 2 g P_2O_5 dissolved in 12 mL of concentrated (97%) H_2SO_4 was heated under stirring to 80°C. As soon as the temperature had stabilized, 4 g of graphite flakes were added to the above solution. After about 10 minutes, heating was stopped and the mixture was left to cool to room temperature while being stirred. It was then slowly diluted with 300 mL of distilled water and filtered through a PTFE membrane (450 nm pore diameter). It was washed on the membrane with approximately 4 L of distilled water, until the pH of the filtrate was ~5.5. The solid was transferred to a crystallizer, which was placed in a drying oven at 80°C for 20 h.

The pre-treated solid was placed in a beaker with 92 mL of concentrated (97%) H_2SO_4 and chilled in an ice bath, under constant stirring. 12 g of $KMnO_4$ was slowly added to the mixture, taking care not to let the temperature exceed 20°C. During the course of the addition, the color of the mixture turned dark green. When all of the $KMnO_4$ had been added, the ice bath was removed and the mixture was kept stirring at 30-35°C for 2 h. At that point, it was carefully diluted with 185 mL of distilled water (water in acid, highly exothermic) and left for 15 minutes to return to room temperature. It was further diluted with 560 mL of distilled water and 10 mL of H_2O_2 30% was added to terminate the oxidation, causing the mixture to turn bright yellow-green. The mixture was then filtered using a PTFE membrane (450 nm pore diameter) and the residue was washed in the filtering funnel with 1 L HCl 3.5% to remove metal ions and then with 300 mL distilled water. The viscous, dark

brown remainder was dispersed in distilled water to a final volume of 300-400 mL, depending on the desired final concentration and was transferred into dialysis tubes (cellulose, cut-off: 12400 Da) to be purified from metal ions and acids. The dialysis was considered complete when the pH of the eluant remained stable (typically around 5.6) after 24 h – usually after a week and up to two months, depending on concentration. The resulting GO suspension would then be either exfoliated as-prepared or after dilution with distilled water. Exfoliation was performed by 2 h of sonication in a bath sonicator in 30 min increments, taking care to maintain the temperature of the bath close to ambient. The final suspensions, which are stable up to this day, had a concentration of graphene oxide in the range of 7-16 mg/mL.

There are three modifications compared to the original protocol: First, the drying of the pre-treated graphite was carried out in a drying oven, at 80°C and not in air. While this can cut down on the processing time, it also promotes the expansion of the graphite, as the intercalated species decompose with heating. The resulting material was slightly swollen and has a more “puffed up” texture, compared to both pristine graphite flakes and air-dried pre-treated graphite flakes. Second, the final dilution prior to dialysis was adapted to the desired concentration of the suspensions. While the process of osmosis does not allow for a precise control over the molecules that diffuse through the membrane, we obtained suspensions within 2 mg/mL of the targeted concentration. This was done because we wanted to experiment with higher concentrations of GO and while dilution is easy, the opposite is not true, when our options were either to heat the suspensions at $T < 50°C$, so as not to reduce the GO, or to remove excess water by filtration. Third, the sonication time was fourfold that of the original publication. It is often difficult if not impossible to quantify the energy imparted on a system via a sonicator bath, as there are a lot of variables that can play a role. In short, satisfactory results with regard to the exfoliation of the suspended particles were obtained after 2 h of sonication, based on electron microscopy observations.

These suspensions were stable during the course of this study and they were used in all

subsequent experiments. Most characterizations were conducted on films, prepared by filling crystallizers or Petri dishes with the suspensions and evaporating the solvent at temperatures between 45-48°C either in a drying oven or on a hotplate.

Materials. *Graphite flakes (purity ≥ 99.9%, -10 Mesh), $K_2S_2O_8$ (purity ≥ 99.0%), and $KMnO_4$ (purity ≥ 99.0%) were purchased from Sigma-Aldrich, H_2SO_4 (97.0%, ACS reagent grade) from Honeywell, HCl (37%, analytical grade) from VWR Chemicals, H_2O_2 30% (w/v) in water was purchased from Fisher Scientific and P_2O_5 (purity ≥ 99%) from Carl Roth GmbH.*

1.4. Thermal reduction to rGO

Ideally, thermal reduction at temperatures where graphitization naturally occurs, would yield a nearly-defect-free material. However, we were limited by the thermal stability of the other components we wished to incorporate in the composite. EMI^+TFSI^-, our model ionic liquid, begins to decompose around 366°C[22] and tin imposed an even lower limit, as it melts at 232°C. In the past we've had to work under similar restrictions and inspired by a number of publications on the annealing of graphene oxide under vacuum[23–25], we settled for a thermal reduction protocol consisting of a ramp of ~1.5°C/min to 200°C, followed by heating at 200°C for two hours under 0.05 mbar of pressure. The slow heating rate served to avoid the explosive exfoliation[26,27] of stacked GO, though for dense samples we also had to cut them to pieces, to facilitate the escape of decomposition gases.

Experimental details. *Samples were annealed in a Medline Scientific™ Jeio Tech 665L Vacuum Oven (OV-12).*

1.5. Characterizations of GO and rGO

GO and rGO were characterized at different levels: the crystallinity using polycrystalline X-ray diffraction (PXRD), the morphology using microscopy (TEM and SEM), the chemical homogeneity using energy-dispersive X-ray spectroscopy (EDX) and the amount of defects using Raman spectroscopy. In addition, the thermal behavior was evaluated with respect to the goal of incorporating tin and the ionic liquid in the composite material. Finally the acidity and surface charge of GO in suspension were examined in order to find the best conditions for its functionalization.

1.5.1. Crystallinity of GO – rGO

Graphite and its oxides have been studied in great extent via X-Ray diffraction, almost from the invention of the technique[28–32]. The addition of oxygen-bearing groups to the lattice, the out-of-plane bending of sp^3-hybridized carbons and the adsorption and intercalation of solvent molecules lead to an increase of interlayer distance between graphene sheets. This is immediately discernible from X-ray diffraction, as the signal from the 002 planes, which is found at 26.5° in pristine graphite, corresponds to the spacing between the sheets. At the same time, the exfoliation of crystallites to few-layer graphene means that fewer planes can contribute to the constructive interference that produces the characteristic peaks of a diffractogram according to Bragg's law. Lastly, if we think of graphene sheets like sheets of paper stacked together, it is easy to visualize how they deform more easily when there are fewer of them in a stack. These are the telltale signs of the oxidation of graphite: the shift of the interlayer spacing signal to lower angles, hence greater distances, the decrease in signal intensity due to exfoliation and the broadening of the peaks, as planes bend and become distorted.

The diffraction patterns of the graphite used in our syntheses, its pre-treated form just prior to oxidation and that of graphene oxide are presented in Figure 2.2. We can observe

that the treatment with potassium persulfate in sulfuric acid induced a fair amount of exfoliation, as the intensity of the diffraction from the 002 plane has decreased significantly, which means that fewer sheets are now stacked together. The signal appears slightly shifted to lower angles, hinting at the intercalation of the salts between the sheets of graphene. Furthermore, the broadening of the peaks indicates that there is a considerable strain and deformation of the crystal planes. In the case of the oxide, the 002 signal is found at 11.16°, so the interlayer spacing, d_{002} is now ~7.9 Å, more than double that of graphite (3.35 Å). There is a remnant of the peak at 26.5°, due to the stacking of remaining sp^2 domains. The breadth of the peaks and the form of the pattern between 11.16° and 26.5° are evidence of the extensive distortion of the planes in graphene oxide.

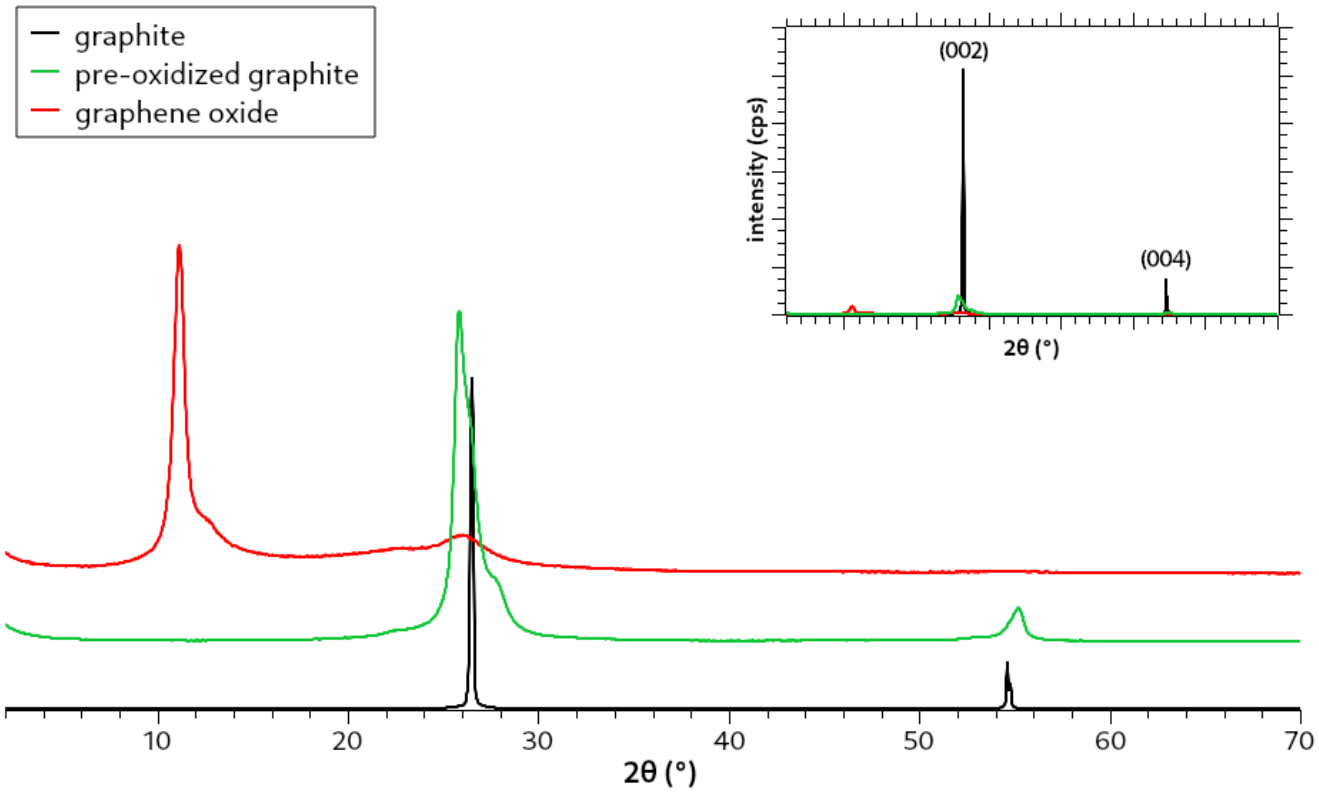

Figure 2.2: Diffractograms of graphite, pre-treated graphite before the oxidation step and graphene oxide. Peak intensities have been normalized for the sake of comparison. Inset: the same diffractograms at their actual measured intensity (in counts per second).

Experimental details. *PXRD patterns were recorded on a Rigaku Ultima IV diffractometer with a CuKα source, operating at 40 kV and 40 mA, configured in a Bragg-Brentano (2θ/θ) geometry. The patterns were typically recorded at 1°/min scanning speed, with a 0.02° step. Graphite flakes and the pre-oxidized material were measured as prepared, after being brought to level with the sample holder. Graphene oxide was measured as a film, prepared by the slow evaporation of the*

water of an aqueous suspension.

1.5.2. Morphology of the GO sheets

The synthesized material was examined under a transmission electron microscope. In the micrographs of Figure 2.3, one can clearly see the crystals of the salts from the pre-treatment of graphite, intercalated between the graphene sheets, as dark spots in a), b) and better observable in c). The edges of stacked graphene sheets are clearly visible in d). The sheets themselves are already somewhat crinkled, even though they have not been subjected to oxidation yet. Evidently, this is brought on by the treatment with potassium persulfate in sulfuric acid. The mere fact that TEM imaging is possible, reveals that considerable

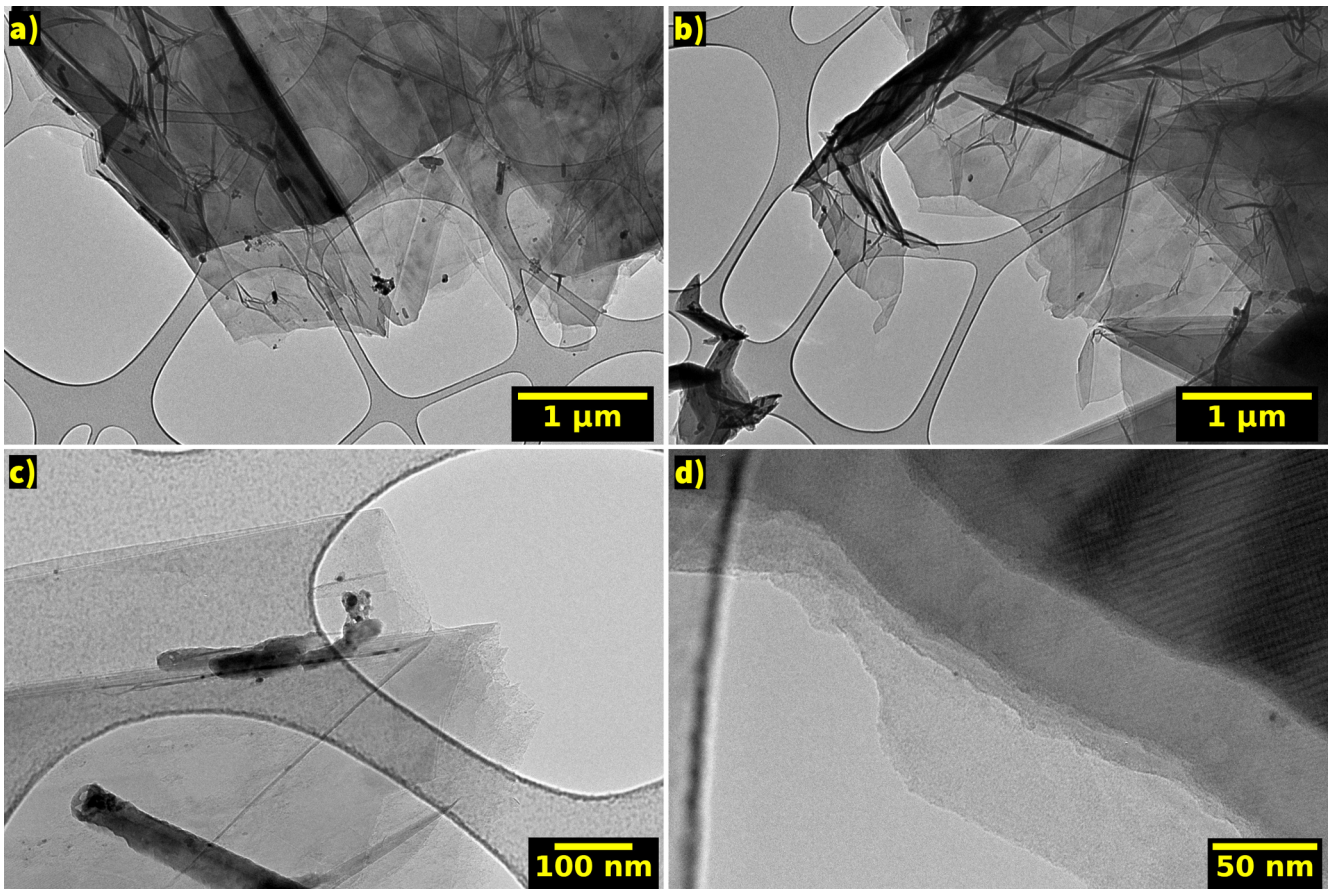

Figure 2.3: Transmission electron micrographs of the pre-treated graphite, *i.e.* the dried material just prior to oxidation.

exfoliation has taken place, notwithstanding some of it being the result of the sonication during sample preparation. Both the pre-oxidized sample and the final product were prepared in the same manner and yet only in the latter could we observe single layers of material. That should dispel any doubts as to when exfoliation takes place or to what extent.

The characteristic wrinkles of graphene oxide are clearly present in the micrographs of Figure 2.4. The fewer the sheets present, the lower the contrast between them and the carbon coating of the TEM grids. The sheets are much more distorted than those of the pre-treated material and they are mostly found as single-layer or bilayer graphene oxide, though stacks consisting of more sheets are also present. This confirmed our choice of synthetic protocol, especially with regard to the adjustment in the duration of sonication and the consequent exfoliation efficiency. As expected, we've also observed sheets large enough to cover the entire grid, which measures 3.05 mm.

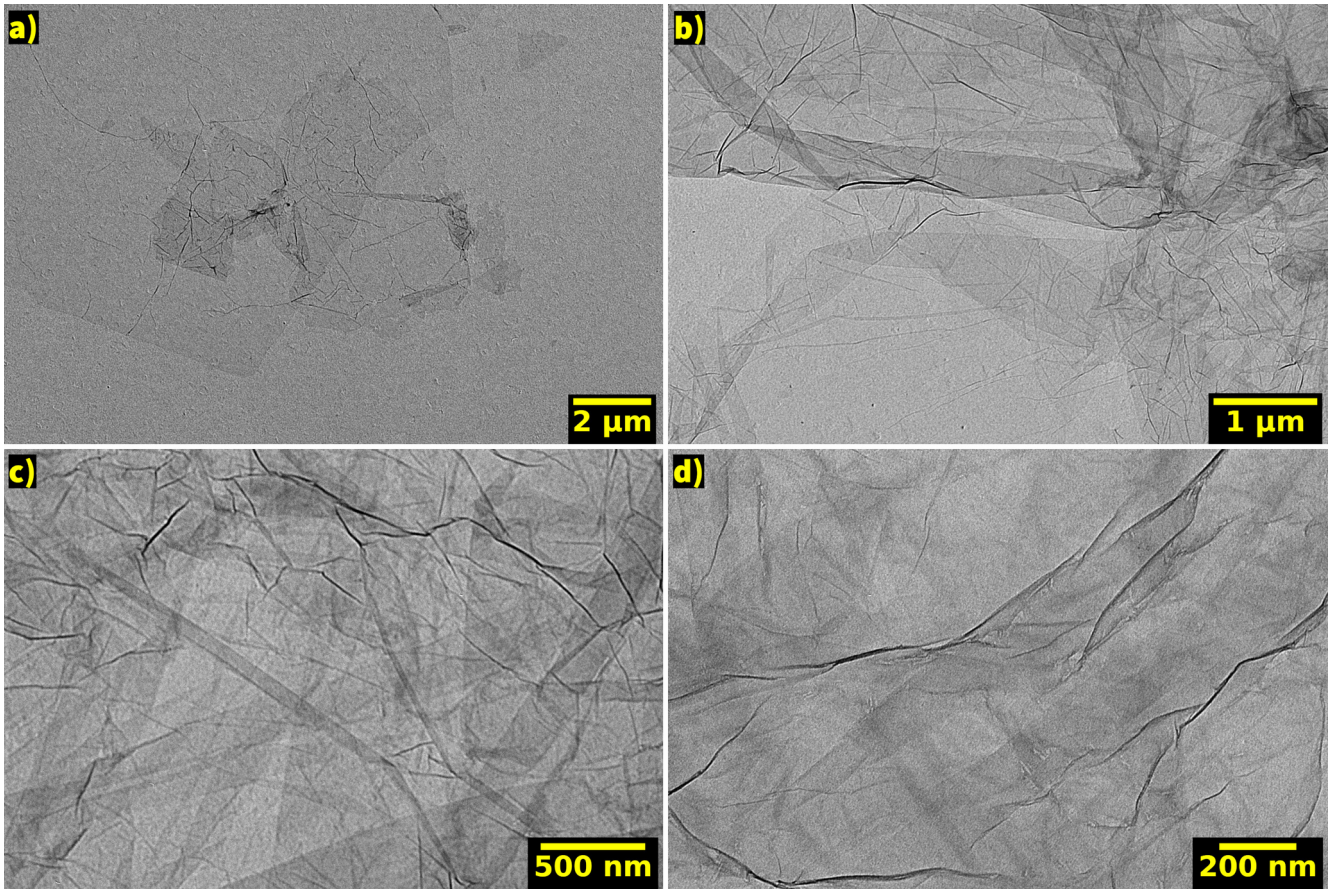

Figure 2.4: TEM images of graphene oxide supported on carbon film.

Experimental details. *Transmission electron microscopy images were recorded on a JEOL JEM 1011 microscope operating at an accelerating voltage of 100 kV. Samples were deposited on 300 mesh copper grids, coated with either a carbon film or lacy carbon film, depending on the material to be observed. The samples were prepared by diluting the suspension of GO with distilled water to the point that its color was barely perceptible and deposited a single drop on a copper grid coated with a carbon film. For the pre-oxidized graphite, in order to preserve the intercalated potassium sulfates and persulfates, a small quantity of material was dispersed via sonication for 30 minutes in ethanol, in which the salts are insoluble. Again, the suspension was diluted with ethanol until it became almost colorless and a single drop was deposited on a copper grid covered with lacy carbon, which allowed for better contrasted images.*

1.5.3. Chemical homogeneity

In order to verify the reproducibility and homogeneity of our syntheses and as a convenient and readily available technique of elemental analysis, we examined all the different batches of GO we prepared via energy-dispersive X-Ray spectroscopy (EDX).

As described earlier, we prepared films of material by slow evaporation of the water of the suspensions. Taking into account that the chemical makeup of graphene oxide varies locally, we conducted many measurements on each sample, trying to include as many

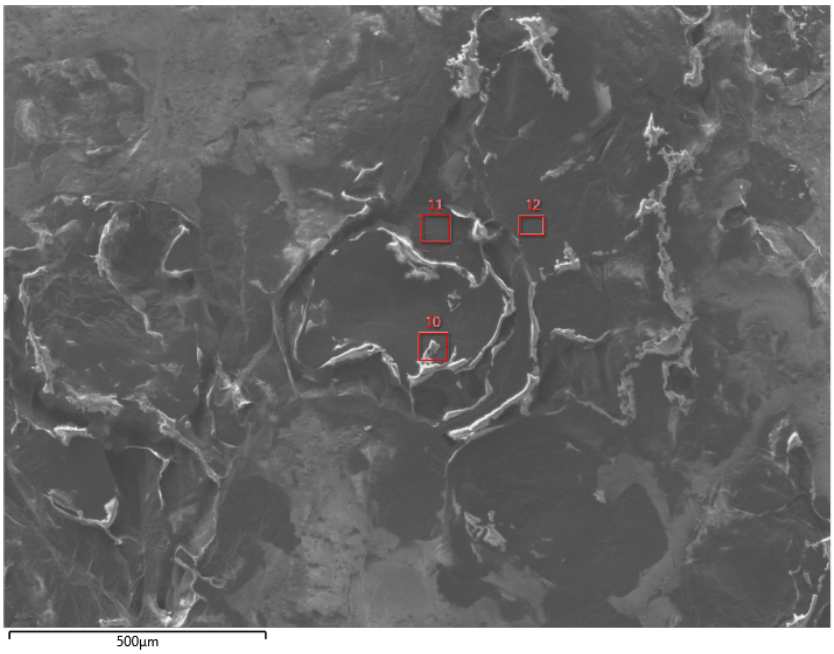

Figure 2.5: SEM image of a GO film during EDX measurements. The areas that have been selected for analysis are delimited by numbered squares.

topographic variations as possible and the results were then averaged, in order to have a representative image of the entirety of the material.

In Figure 2.5, we observe a typical SEM image of a GO film, along with three areas selected for analysis. Since the acceleration potential of the electron gun had been increased in order to extract a maximum amount of inner-shell electrons from the sample, the image is not as detailed or as fine-tuned as it would be during normal SEM observations. It mainly serves to roughly select the areas of interest. The differences in brightness are due to the local accumulation of static charges, as expected of an insulator. The brighter the area, the more charged it is and usually the higher the local oxygen content. Areas with intact sp^2 domains have a higher C:O ratio and appear darker, while the opposite is true for areas with a lot of oxygen-bearing groups. The spectrum of the area #10 of Figure 2.5 is shown in Figure 2.6. This region of the sample contains a charged edge fragment superimposed onto a more conducting surface. As a result, the estimated atomic ratios are close to the averages for the sample.

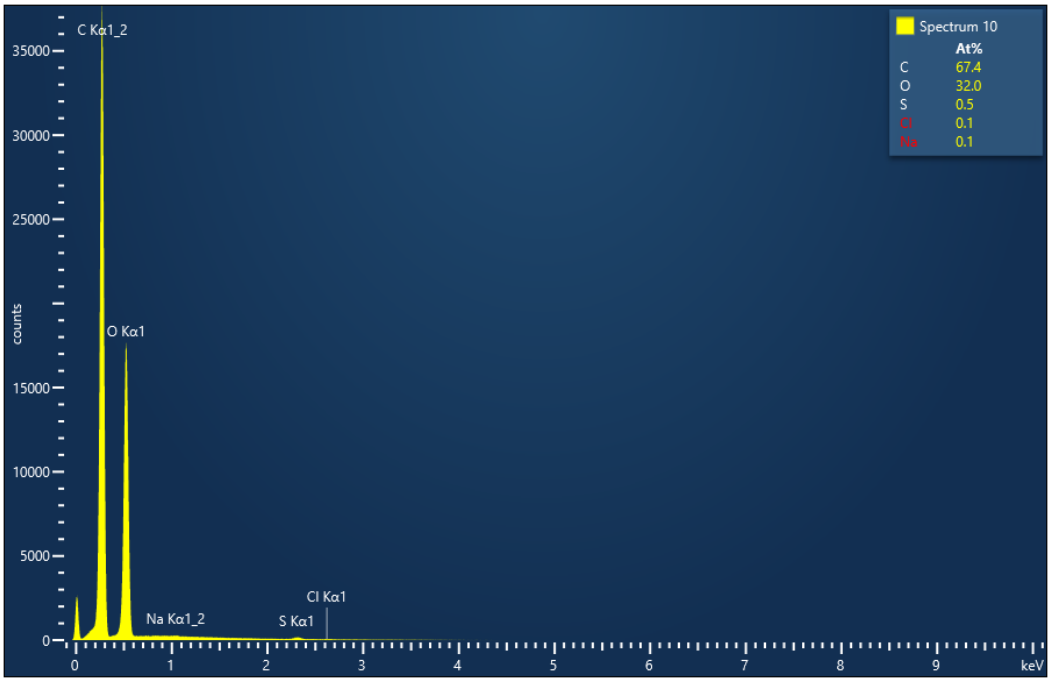

Figure 2.6: EDX spectrum of area #10 from Fig. 2.5 and extrapolated atomic percentages of elements found in it. Na and Cl are marked in red because of the very low confidence level of the analysis.

Based on the EDX measurements, the syntheses were indeed reproducible, with an

average atomic percentage of C of 66 ± 4% and 32 ± 3% for O. Besides some possible contaminants whose presence was disputable, such as Na and Cl shown in Fig. 2.6, sometimes we would encounter trace amounts of S, up to 0.5%. Although it falls within the margin of error of the technique, it could not be dismissed outright as an artifact. The average atomic percentages of C and O in rGO were found to be 83 ± 3% and 16 ± 3% respectively.

Experimental details. *EDX analyses was usually performed together with scanning electron microscopy (SEM), as both were conducted on a Hitachi SU-70 field emission scanning electron microscope, equipped with an Oxford X-Max 50 mm^2 detector for the recording of EDX spectra. The INCA and AZTEC software suites were used for EDX measurements and analyses.*

1.5.4. Defect evolution investigation via Raman spectroscopy

A surface characterization technique often employed to assess graphene-based materials, is Raman spectroscopy, which allows to distinguish graphene from graphene oxide, based on the vibrational signals of the disordered carbon lattice. A single sheet of graphene at its basal plane has one Raman-active mode, with an E_{2g} representation, which gives rise to the so-called "G band" predicted at 1582 cm^{-1} (Figure 2.7a). Stacking graphene sheets in an AB arrangement to form graphite, gives rise to a second Raman-active E_{2g} mode, with a signal predicted at 47 cm^{-1}, which however is rarely detected. A number of other bands, second order features attributed to overtones of fundamental modes and of Raman-forbidden modes are often measured in the range of 2450 and 3300 cm^{-1} [33]. Structural defects, usually found at the edges of graphene sheets and graphite crystallites produce another signal, mainly located at ~1350 cm^{-1}, the "D band" (Fig. 2.7b) as well as several possible associated second and third order features at higher wavenumbers[33,34]. In a typical modern Raman spectrometer, an area of a sample is selected for measurement through a microscope lens and then, through the same optics, a laser beam excites that area and the Stokes and anti-Stokes scattering signals are recorded by a CMOS (complementary metal-oxide-

semiconductor) detector. In Figure 2.7 is shown a simplified representation of the laser excitation process and the associated signals of pristine graphene (Fig. 2.7a) and those of overlapping edges of graphene sheets with edge defects (Fig. 2.7b). If only sp^2 carbons part of the aromatic system are in the pathway of the laser beam, the recorded spectrum between 1100 and 1700 cm^{-1} will resemble that of Fig. 2.7a. If the beam falls on defect sites, the spectrum will be more like the one shown in Fig. 2.7b.

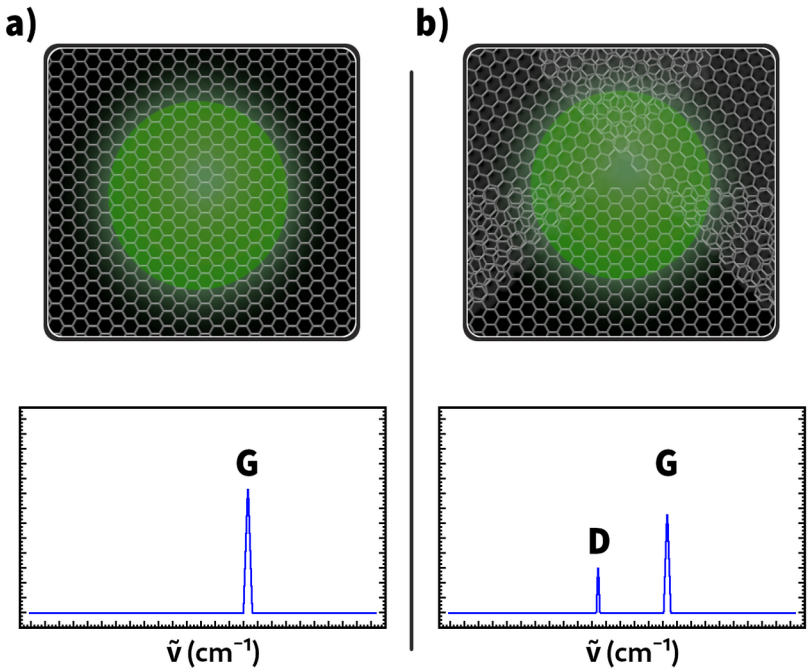

Figure 2.7: a) Laser excitation of the surface of a single sheet of pristine graphene and b) laser excitation of an area that includes overlapping borders of three graphene sheets with edge defects and the corresponding spectra below.

Over the last decades, the paradigm of the Raman analysis of graphite has been applied to a host of carbon-based materials consisting of sp^2 domains and disordered structures, *e.g.* carbon black, or completely amorphous carbons[35]. One application of this methodology with numerous examples in the literature is for the assessment of the effectiveness of the reduction of graphene oxide[36,37]. The D and G bands of the material before and after reduction are usually fitted with symmetrical functions such as Lorentzian or Gaussian curves (or more rarely asymmetrical functions such as Breit-Wigner-Fano) and the areas under each of the peaks are integrated and then divided, yielding the I_D/I_G intensity ratio – a

measure of the density of defects[38]. Counterintuitively, except for cases where the sample has been almost completely graphitized and the D band is all but extinct, that I_D/I_G ratio increases after reduction. This has been attributed to a decrease in size, but increase in number of sp^2 domains after reduction[36,38].

We too employed that methodology when examining the Raman spectra of films of graphene oxide (GO) and thermally reduced graphene oxide (rGO), annealed for 2 h at 200°C under vacuum. Their respective spectra are shown in Figure 2.8 in black and red. A small peak that appears at ~1120 cm^{-1} is from the sample holder. The two spectra appear as expected, with the G band centered at 1601 cm^{-1} for both samples. The peak of the D band of graphene oxide is found at 1350 cm^{-1} and slightly shifted, to 1358 cm^{-1} for rGO. The relative intensity of the D band is somewhat decreased in the rGO sample, which could be tied to an increase of the sp^2 character of the lattice. Following the methodology described above, for the GO sample, when fitting with Lorentzian, Gaussian and Breit-Wigner-Fano (BWF) curves, the calculated I_D/I_G intensity ratios were 1.265, 1.607 and 1.135, respectively. For the rGO sample, the I_D/I_G intensity ratios were 2.170 (Lorentzian), 2.155 (Gaussian) and 1.399 (BWF).

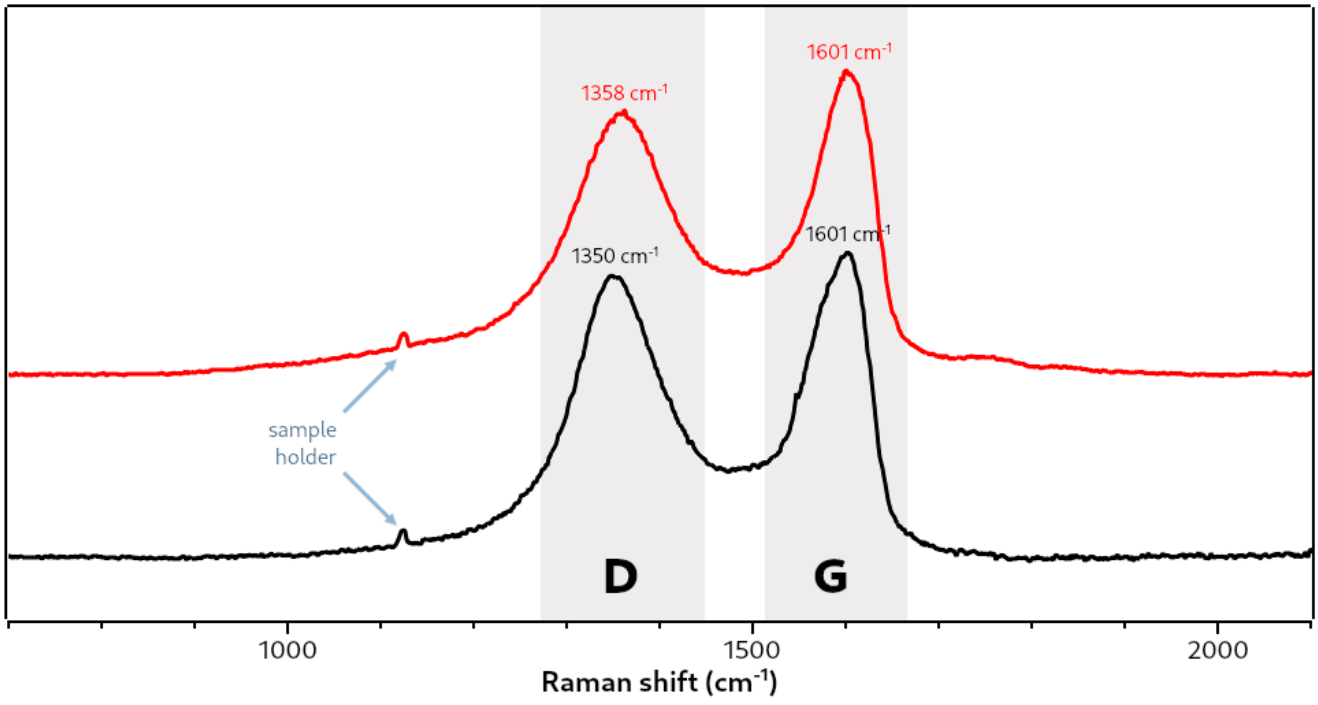

Figure 2.8: Raman spectra of graphene oxide (black curve) and thermally reduced graphene oxide (red curve). The spectra have been vertically displaced for the sake of comparison.

In terms of absolute values the ratios varied widely for the different curves used for fitting. Yet, an increase in the I_D/I_G intensity ratios after reduction, the trend discussed earlier, was apparent every time.

When fitting the spectra with any of the above functions, a satisfactory match of the recorded curve could not be obtained. In terms of shape, the BWF function gave the best result, but it severely underestimated the area between the two bands and it was impossible to simultaneously match the maxima and slope of both peaks. It started to seem that the deconvolution of the spectrum into two components was perhaps not a correct approach. Despite appearances, graphene is a complex material and its photon and phonon excitation response differs a lot when examining a single layer and multiple layers: resonant and non-resonant behaviors can take place simultaneously with both constructive and destructive interference effects, leading to drastically different measured signals, which are also highly dependent on the experimental conditions[39,40]. Oxidation of graphene to graphene oxide, so the functionalization and the introduction of defects to the lattice, only add to the complexity, with new excitation modes becoming possible and localized variation of the different signals in accordance with compositional variations[41]. Drawing from that research and taking into account these complexities, recent analyses of graphene-oxide-based materials tend to adopt a more detailed methodology, examining both the main spectral window (~1100 – 1700 cm^{-1}), which is deconvoluted to more components, as well as the signals from second-order overtones and combination modes[42–47]. It is clear that the widely practiced analysis of the Raman signal in the narrow range of the main spectral window is overly simplistic and cannot lead to sound conclusions as to the structure, *i.e.* the state of disorder of graphene oxide samples, all by itself.

For more precise structural information to be extracted, many features of the spectra have to be taken into consideration, at least the intensity ratios of the D and G bands, the presence of additional signals, the width of all bands and ideally, multiwavelength measurements should be conducted[41]. Despite the erroneous methodology, the Raman

spectra of the synthesized materials examined appeared as expected from published examples.

Experimental details. *Raman measurements were carried out at the PLASVO platform hosted by the MONARIS laboratory at Sorbonne University. The spectra were recorded using a Horiba Jobin Yvon HR800 confocal, high-resolution spectrometer, equipped with a 600 groove/mm grating. An ionized argon 514 nm laser source was used, operating at 100 μW power level, with the beam diameter set to 1 μm. Acquisition time was 600 s.*

1.5.5. Thermal analyses

In order to obtain further compositional information about the synthesized graphene oxide and estimate the effectiveness of the selected thermal treatment protocol, thermal analyses were conducted.

The thermal decomposition of the material is a multistep, complex process, as demonstrated by the typical thermogravigram of a graphene oxide sample shown in Figure 2.9. Plotting the first and second derivatives (DTG and D^2TG curves in the plot) of the TGA curve can assist in determining the onset temperatures for the different steps and in identifying overlapping segments belonging to different decomposition processes.

While most of the observable steps overlap, the thermogravigram can be approximately divided in the following segments:

- From ambient temperature up to 129°C, there is a weight loss of 7.8 wt%, with the maximum of the process taking place at 50°C. This can be attributed to the loss of weakly or strongly adsorbed water and the beginning of the decomposition of carboxyl groups[48].

- From 129°C to 151°C and with a maximum at 148°C, an abrupt weight loss of 4.5 wt% was observed. By conducting an experiment where the epoxide groups were hydrolyzed, it was possible to attribute this part to the decomposition of the hydroxyl

groups (see Chapter 3).

- The previous process overlaps with another one, equally abrupt, that continues up to 213°C and reaches its maximum at 198°C. The main process here seems to be the decomposition of epoxy groups (as evidenced by the aforementioned hydrolysis experiment) and results in a further weight loss of 21.8 wt%.

- Again, the previous process overlaps with the next one, that extends to 309°C. A maximum cannot be identified. This decomposition process is slower and results in a weight loss of 6.2 wt%.

- From 309°C onward, the decomposition rate remains almost constant and by 800°C a further weight loss of 9 wt% is recorded.

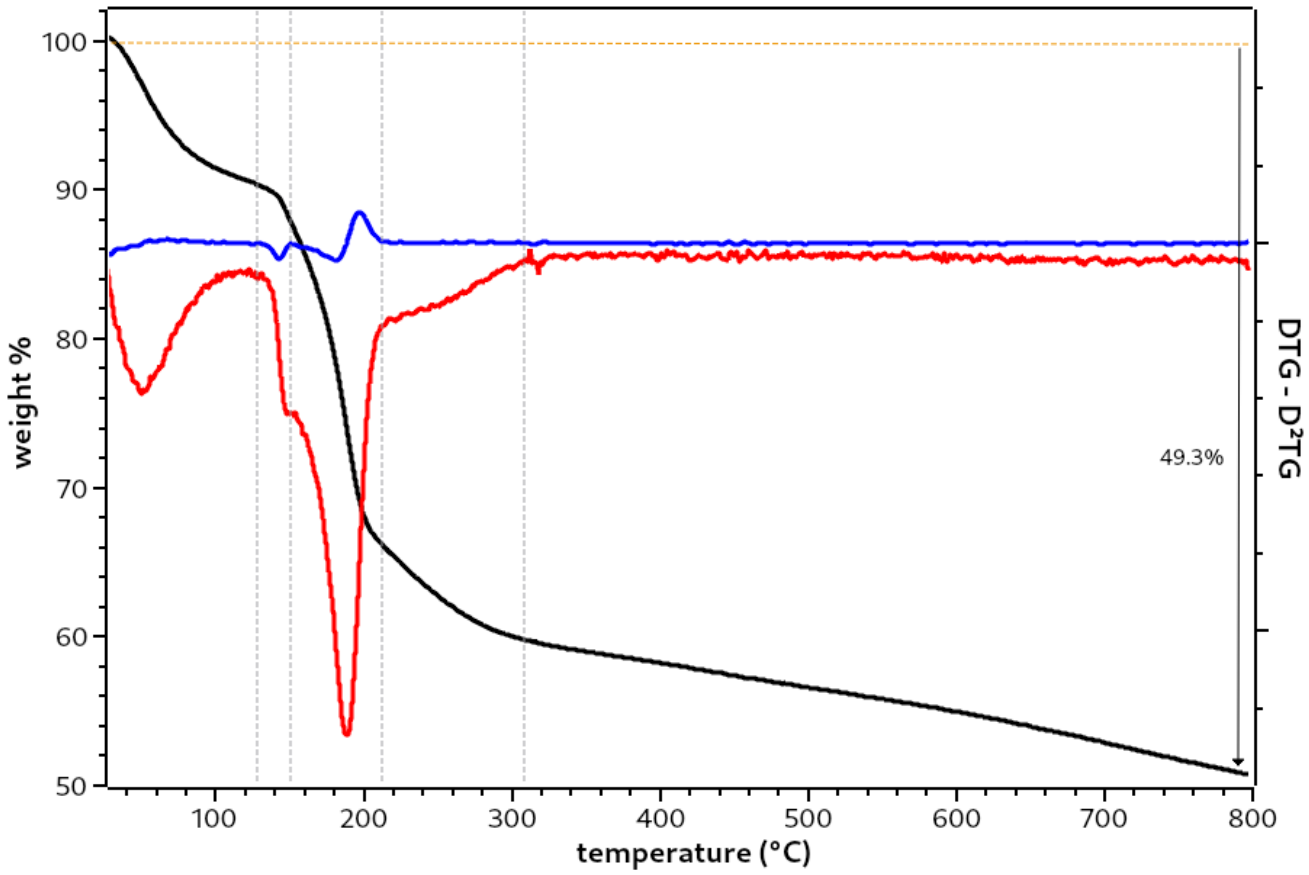

Figure 2.9: Thermogravimetric analysis of a GO sample under inert atmosphere (N_2). The first (red) and second (blue) derivatives of the TGA curve (black) have also been plotted. The dashed vertical lines indicate the onset of additional events.

The total weight loss of the sample at 800°C is 49.3 wt%. The two dominant overlapping decomposition processes taking place in the range 129°C – 213°C were attributed to hydroxyl and epoxy groups, though the simultaneous decomposition of other species cannot be excluded.

In order to get some more information about the thermal reduction process, we conducted a TGA analysis of a GO sample under N_2 flow, where the outlet of the carrier gas was connected to a mass spectrometer. This allowed us to analyze the decomposition products at the various stages of the process.

The complexity of the thermal decomposition of GO and by extension, that of its thermal reduction is further reflected in the diagram of Fig. 2.10. Before proceeding with the analysis, it should be noted that the beginning of the TGA curve in Figure 2.10 is slightly different than that of Figure 2.9. It is less steep and during the first segment up to 129°C, the weight loss is almost double than before, 15 wt%. This is due to adsorbed humidity. The sample of Fig. 2.9 was measured within minutes after drying, whereas that of Fig. 2.10 was

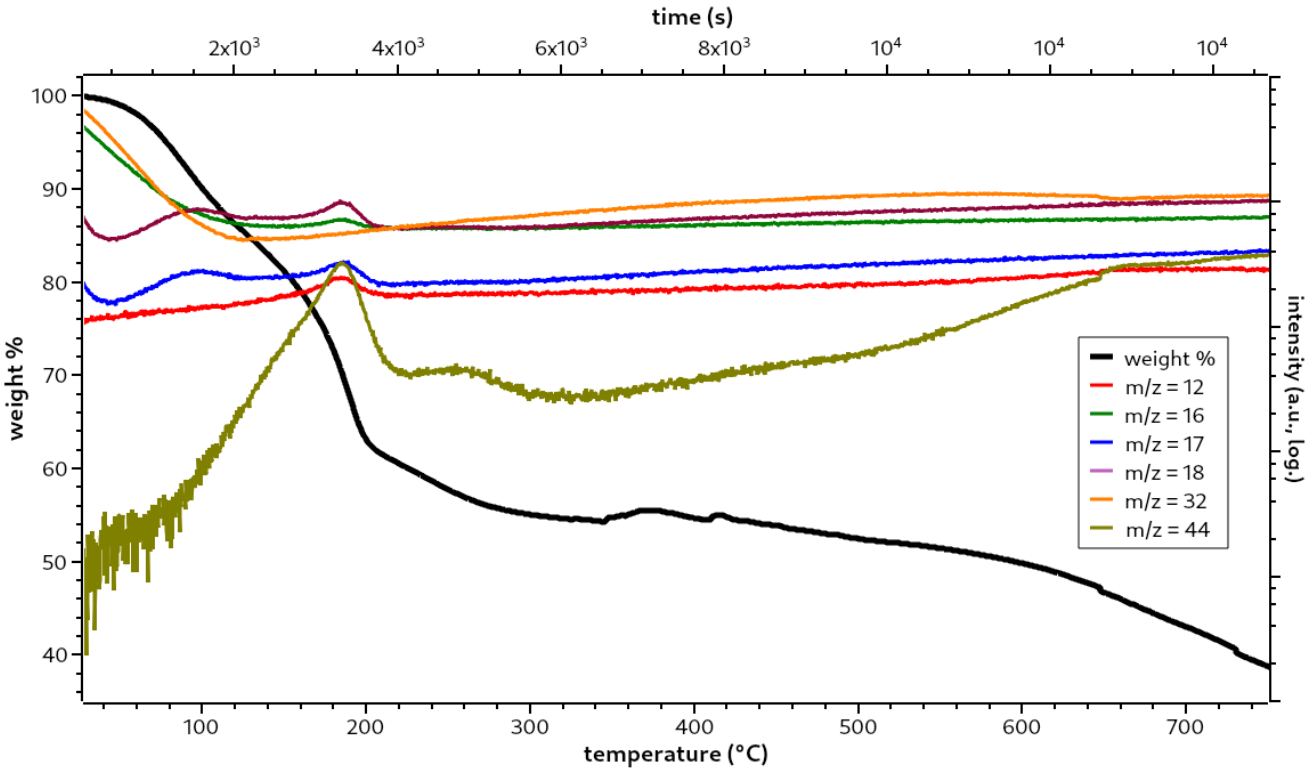

Figure 2.10: TG analysis of a GO sample under N_2 flow, coupled with mass spectrometry.

left in air for almost 24 h before it could be measured. This shows the great affinity GO has for water.

The mass spectra were measured in the range 10 < m/z < 160 for the duration of the experiment. The evolution of several gaseous decomposition products detected by MS is plotted together with the thermal decomposition of the sample. The detected signals that stood out against the background noise correspond to m/z ratios of 12, 16, 17, 18, 32 and 44. These values were attributed in that order to the following cationic species: C^+, O^+, $[OH]^+$, $[H_2O]^+$, $[O_2]^+$ and $[CO_2]^+$. While O^+ and C^+ could be fragmentation products of CO, carbon monoxide itself could not be monitored, as it shares the same molecular weight as the carrier gas, N_2.

The initial intensities of the signals of $[H_2O]^+$, $[OH]^+$, O^+ and $[O_2]^+$ suggest that a certain amount of both oxygen and water remained adsorbed on the graphene oxide sheets despite the initial purge with N_2. That does not seem to be the case for carbon dioxide, perhaps due to its size and affinity towards GO.

Both the signals of $[H_2O]^+$ and $[OH]^+$ exhibit the same pattern throughout the process, with an initial increase after the removal of the loosely adsorbed water molecules, that reaches a first maximum at ~100°C, suggesting water evaporation. They reach a second maximum at 185°C, where the decomposition of hydroxyl and epoxy groups overlaps, as mentioned previously. It is possible that the two groups react together as they decompose, with water being one of the products. The signal intensities of the two species slowly but steadily continue to increase up to the end of the measurement, hinting at the decomposition of species that involve both oxygen and hydrogen.

The $[CO_2]^+$ signal while at first difficult to separate from the background noise, constantly increases from ~57°C onward, reaching a maximum at 185°C, coinciding with the maximum of the evolution of water. As it has been reported in the literature[48], carboxyl groups start to decompose at approximately 50°C, which would confirm the source of the signal in the

sample at lower temperatures. However, the fact that it reaches a maximum at exactly the same temperature as the water ion, suggests that it also evolves as a product during the decomposition of hydroxyl and epoxy groups. The $[CO_2]^+$ signal drops immediately after, before it reaches a local maximum close to 260°C, when it slightly drops again and starts increasing after 330°C. From that point on, the signal increase changes slope several times, hinting at different processes releasing CO_2 during the pyrolysis.

The intensities of the signals from the ionic oxygen species, O^+ and $[O_2]^+$, do not exhibit the same trends. It appears that their sources are different for the most part of the measurement. The diatomic ion signal increases steadily from 125°C until ~568°C, where it starts to undergo a small decrease until 650°C, when it appears to slightly increase until the end. From 150°C to 310°C, the signal from the monatomic cation, O^+, follows the same pattern as the fragments belonging to water. After that point, its evolution remains almost constant.

Perhaps the most difficult signal to interpret is that of the C^+ cation, which is present from the beginning of the measurement, reaches a maximum at 185°C like those of $[CO_2]^+$, $[H_2O]^+$, $[OH]^+$ and O^+, drops slightly after that and then steadily increases up to 650°C, where it becomes almost constant. While the peak at 185°C could be ascribed to the fragmentation of $[CO_2]^+$, C^+ does not share any other trend with that species. Had we had access to a different carrier gas, we would have been able to follow the evolution of CO and maybe reach some conclusion.

This experiment gave us little information, most of it in hindsight. However, considering the multitude of gaseous reactive species that evolve during thermal reduction[49], it provided a further justification for the choice of conducting it under vacuum. The less time these species spent adsorbed on the surface of GO, the more oxygen-free the resulting rGO would be, compared *e.g.* to reduction under gas flow.

Finally, in order to assess the efficacy of the thermal treatment we selected, we conducted

a TGA measurement simulating the process. A GO sample was heated with a ramp of 3°C/min to 200°C, where it was kept for two hours. The evolution of the weight loss and the temperature as a function of time are presented in Figure 2.11.

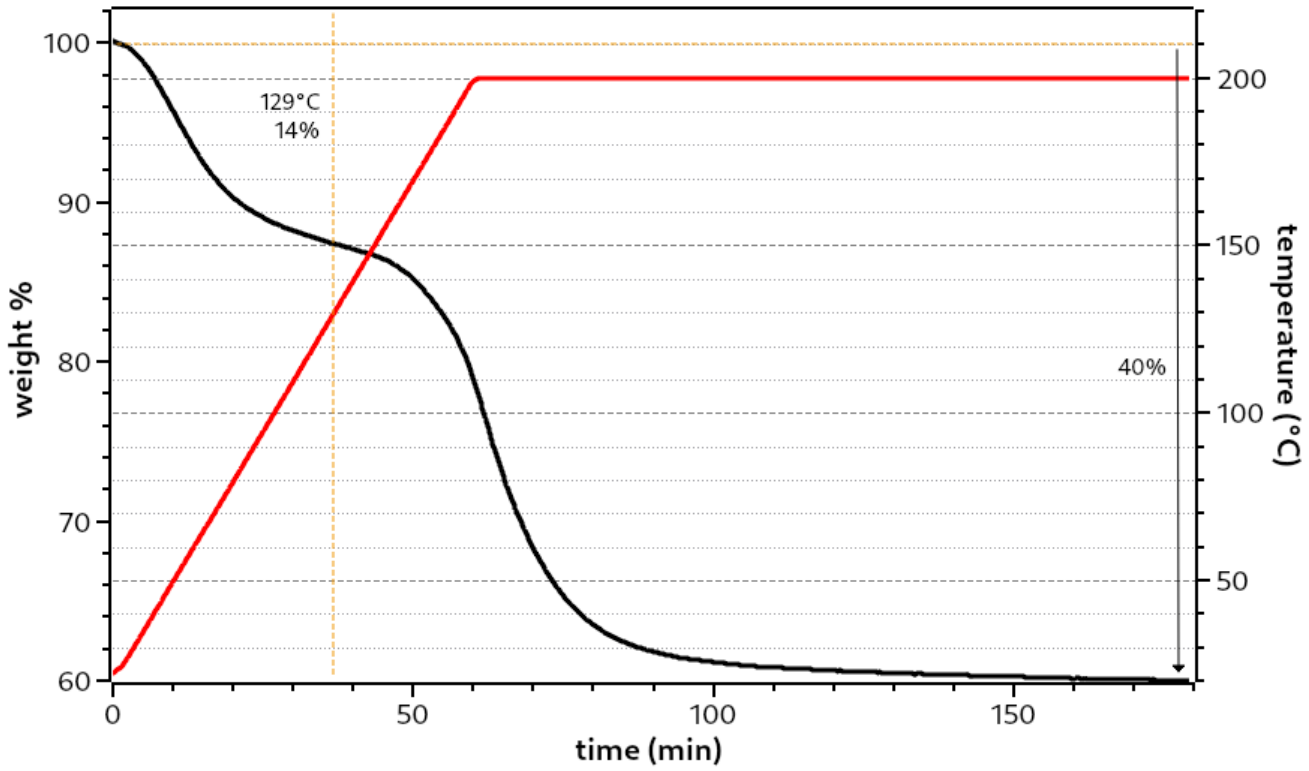

Figure 2.11: Thermogravimetric analysis (in black) of a GO sample simulating the thermal treatment protocol selected for reducing it to rGO under N_2 flow. Heating at 3°C/min up to 200°C is followed by an isotherm for 2 h (in red).

Up to 200°C, the processes resembles what was shown before. Once more, the sample had adsorbed moisture, so the weight loss after the first complex step is almost 14 wt%. By the time the temperature reached 200°C, the sample had lost ~21% of its weight. The total weight loss thirty minutes into the isotherm part of the process, was 38 wt% and further 90 minutes at 200°C added 2 wt% more, for a total weight loss of 40 wt%. The curve tapers off softly at its lowest part and we do not observe the segments with different slopes present in the previous thermogravigrams. Assuming that the adsorbed water was responsible for the 6 wt% increase of the first weight loss, the actual weight loss of GO was 30 wt%. Looking back to the thermogravigram of Fig. 2.9, a weight loss of 30 wt% coincides almost exactly with the 200°C mark. This would seem to justify the duration of the treatment; sustaining the temperature

for two hours results in almost half the weight loss of the sample and eventually leads to the same state as the one measured before.

The results of the thermal analyses of the graphene oxide samples confirmed what would be expected from the literature on the material. The added oxygen-containing functional groups almost double the weight of the graphene lattice, as evidenced by the weight loss by 800°C. The simultaneous evolution of different gaseous fragments combined with the complex decomposition profile attest to the many processes that take place during the pyrolysis. The formation of reactive gaseous species justifies performing the actual thermal reduction under vacuum. Also, simulating the annealing process in the TG analysis allowed us to determine the optimal treatment duration.

Experimental details. *Thermogravimetric analyses were carried out on a TA Instruments TGA 550 analyzer. Samples would be placed in alumina crucibles and heated under a N_2 flow, at various scanning speeds. For samples containing graphene oxide or reduced graphene oxide, a lid would be placed on the crucible, in order to avoid material loss. These samples were measured at 3°C/min, so as to prevent their explosive expansion.*

The TGA-MS measurement was conducted at the LRS laboratory at Sorbonne University. The TGA part of the experiment was carried out using a TA Instruments Q600 SDT thermal analyzer, at a heating rate of 3°C/min. The effluent of the thermal analyzer was transported by the carrier gas (N_2 flow rate: 100 mL/min) to a Pfeiffer Vacuum ThermoStar GSD 301 T quadrupolar mass spectrometer, where it was ionized by a hot filament. Before the measurement, the chamber with the sample holder was purged for 30 minutes with N_2 at ambient temperature.

1.5.6. Acidity – ζ-potential

Figure 2.12 shows how the ζ-potential of GO suspensions varies according to their pH. It is a diagram typical for an acidic material, with an isoelectric point at pH = 0.66, at which

flocculation was observed. The suspensions are very stable[50], almost over the entire pH range, with the ζ-potential value going above -30 mV for pH < 2, approximately.

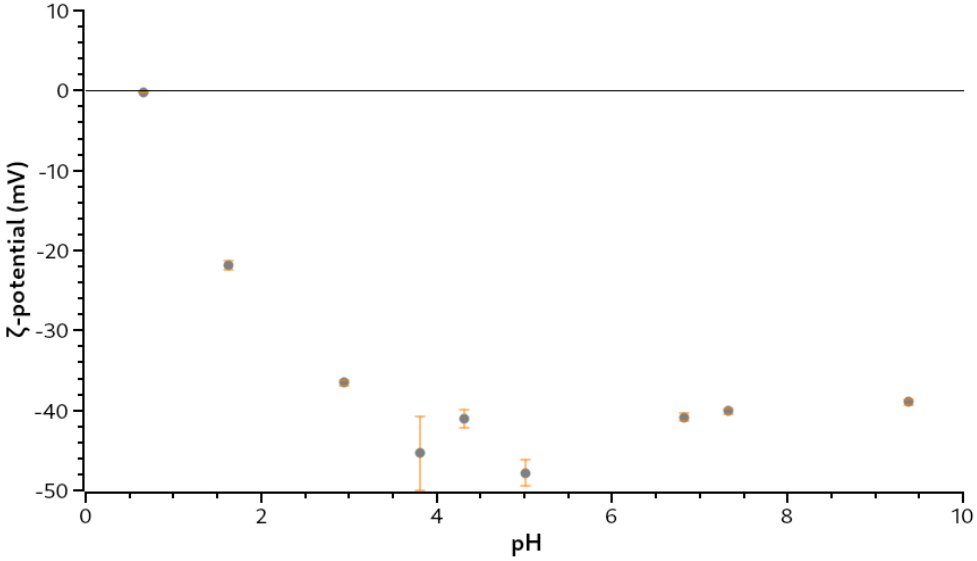

Figure 2.12: pH dependence of ζ-potential of aqueous suspensions of GO at 76.5 µg/mL.

Whereas carboxyl groups are rather few compared to other functional groups present on graphene oxide, it exhibits a very high acidity. This stems from the combination of carbonyl and hydroxyl groups connected through π systems, producing a high number of vinylogous carboxylic acids[11]. As a result, a high number of acidic groups dissociate when in contact with water and the surface of the material assumes a negative charge, as evidenced by the previous diagram. This high charge keeps the particles suspended and prevents them from aggregating. As a reminder, large graphite flakes (< 2 mm) were used as a starting material and consequently there were suspended graphene oxide sheets of comparable dimensions. In suspensions diluted to concentrations below 4 mg/mL, some of the largest particles would precipitate. Due to the size of the graphene oxide sheets, the solvation shells too extend for micrometers or millimeters. The pH gradient due to the solvation shells of GO sheets can be illustrated by depositing a drop of GO suspension onto a strip of pH indicator paper, as shown in Figure 2.13.

The areas of the pH paper in contact and immediately around the GO sheets indicate a very acidic pH, while the pH close to the solvent front is only mildly acidic. Using a pH

meter, the pH measured in the suspension is 2.3 – 2.6, whereas that of the water recovered by filtration is 5.4 – 5.6.

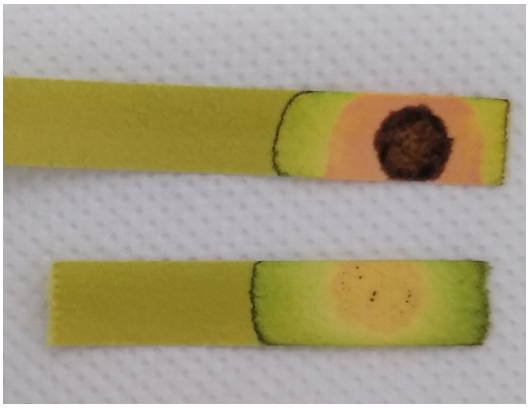

Figure 2.13: Drops of GO suspensions in water deposited onto strips of pH indicator paper. Top: [GO] = 8.5 mg/mL. Bottom: [GO] = 85 µg/mL.

The acidic character of graphene oxide and the stability of its aqueous suspensions were confirmed through the ζ-potential measurements.

Experimental details. *Measurements of ζ-potential were conducted using a Malvern Zetasizer Nano ZS apparatus. A series of samples with different pH values were prepared. In order to maintain the concentration of GO and the optical properties of the samples constant, the pH (as measured with a pH meter) was modified by the addition of 0.5 mL of aqueous solutions of acid (HCl) or base (NaOH), with varying concentrations, to 4.5 mL of an aqueous suspension of GO at a concentration of 85 µg/mL. The final concentration was always 76.5 µg/mL.*

1.6. Shaping

Having established a reproducible synthetic protocol for the production of graphene oxide and after adequately characterizing the material, we set out to explore different shaping techniques. The goal was to find a form for the GO-based matrix that would be self-supporting, capable of hosting a sufficient quantity of tin nanoparticles and which would

allow the fast diffusion of lithium ions throughout its volume. Membranes, aerogels and doughlike forms were investigated.

1.6.1. Membranes

The most straightforward shaping technique that can be applied to graphene oxide suspensions is the preparation of films. By transferring the suspension to a suitable container, leaving it undisturbed and slowly evaporating the solvent, the suspended GO sheets settle in a horizontal arrangement, in which they align and overlap. Once dry, the formed membranes can be peeled off. They are flexible, paper-like structures, that can be cut into any 2D shape.

1.6.1.1 Preparation

A quantity of graphene oxide aqueous suspension was transferred to a Petri dish or a crystallizer. The recipient was then placed on a hot plate or in a drying oven, with the temperature set to 45°C. It would be left undisturbed until the water had evaporated and the GO residue had completely dried off. Carefully separating the GO films from the container, they could be peeled off in one piece.

By varying the quantity of GO suspensions set to evaporate, the thickness of the films was controlled in the range of approximately 0.05 to 1.5 mm. The minimum surface coverage required to produce easy-to-handle films that would remain intact, was ~2.7 mg/cm^2, for our batches of graphene oxide. One of the thinnest membranes prepared is shown in Figure 2.14 (a and b). Thinner films were possible, but they were more difficult to remove without tearing and any minute imperfections in the container or if the container was not completely flat could produce observable defects in the consistency of the films. Films prepared from larger quantities at times presented small holes and imperfections due to inhomogeneous drying and they were significantly less flexible. The membranes could be reduced by

annealing without requiring any other processing (Figure 2.14c).

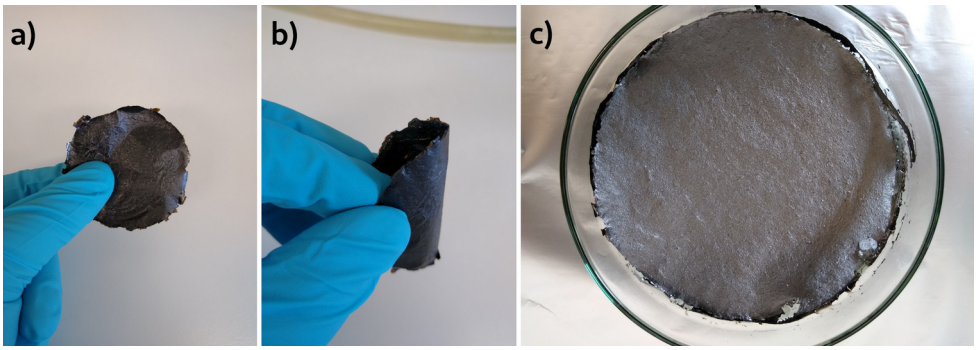

Figure 2.14: a, b) A thin, flexible GO membrane. c) Another membrane after thermal reduction at 200°C for 2 h under vacuum (c).

1.6.1.2 Scanning electron microscopy

A close look at the films reveals that the graphene oxide lamellae assemble into membranes unfolded, for the most part. The edges of the sheets might be rolled or folded, depending on the irregularity of their shape. Some localized pleats, appearing as almost straight lines, are omnipresent. The hypothesis was that this pleating results from the combination of sp^2 domain stacking, on one hand and the presence of lattice defects, on the other. It seemed plausible that a part of a sheet that cannot properly stack and align with those of its neighbors would end up deformed, in order to accommodate the parallel arrangement. Wrinkling of the sheets was also always distinguishable, even at the magnifications offered by SEM imaging.

The images in Figure 2.15 are from a film that was scraped by the forceps used to mount it on the sample holder. It was decided to focus on the damaged area, to see if there were any distinguishable differences between the outer and the inner layers. None were observed. The white wavy patterns in Fig. 2.15a are accumulations of static charges. Fig. 2.15b shows some of the pleats on the outer layer as well as the wrinkles that are due to lattice defects.

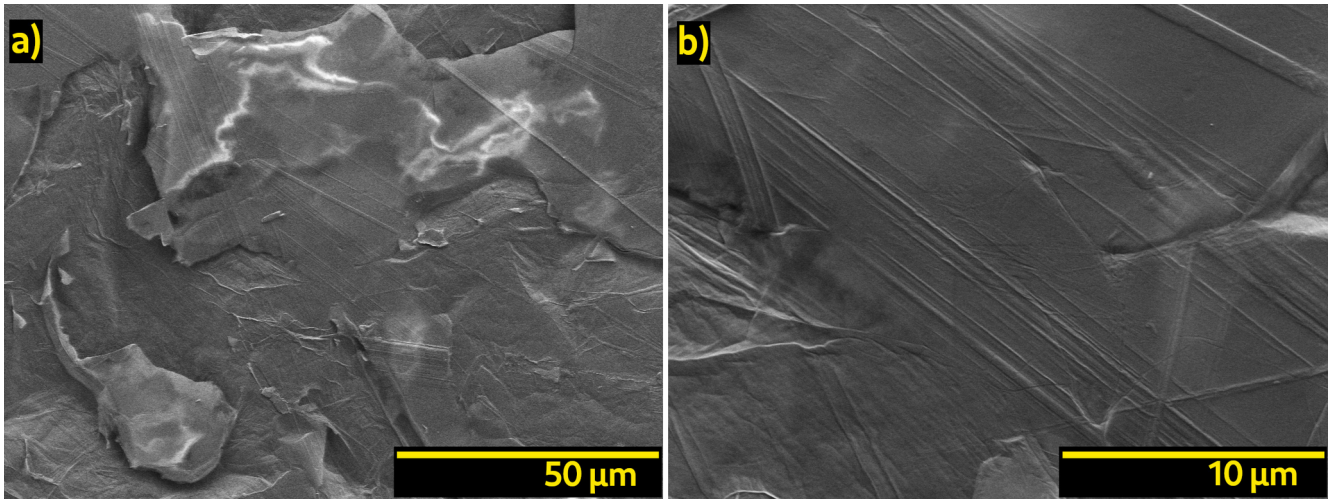

Figure 2.15: SEM images of a GO film. a) Area damaged by a pair of forceps, showing details of the inner layers. b) Higher magnification of the pleats and the wrinkles on the sheets.

Experimental details. *Same as in section 1.5.2.*

1.6.2. Aerogels

One of the most convenient methods to produce graphene-oxide-based porous structures, is via freeze-drying[51]. As suspensions – typically aqueous – of graphene oxide are frozen, the suspended sheets auto-assemble around the solidifying solvent. Subsequent sublimation of the solvent under vacuum results in a self-supporting porous structure, which can retain its shape after thermal reduction.

At first glance, aerogels might seem unsuitable for Li-ion battery electrode materials, given their low density. While a porous structure would allow the faster diffusion of Li ions and ease their intercalation into the host material, the volumetric capacity would be extremely low. Nevertheless, graphene oxide aerogels can be compressed without fracturing, due to the interactions between the sheets and can be completely flattened down to a film[52]. By tuning the compression level, a balance can be struck between fast ion diffusion and acceptable volumetric capacity.

A number of GO aerogels were prepared by submerging in liquid nitrogen plastic vials of different diameters filled with ~5 mL of graphene oxide suspensions of various concentrations, 4, 6, 8 and 16 mg/mL. These would then be placed in a lyophilizer for at least 48 hours, at a pressure of 0.01 mbar. However, once the freeze-drying process was complete and the aerogels were removed from the vials, they would all fracture. This was the result of mechanical stress at the core of the aerogels, as the suspensions froze inward and not all the GO sheets could rearrange to adapt to the forming structure. The large size of the graphene oxide sheets probably exacerbated that. In order to overcome this problem, the freeze-casting technique was employed.

1.6.2.1 Freeze-casting

Freeze-casting, or sometimes called ice-templating, when the solvent is water, is a materials processing technique. First used in 1954 to prepare refractory materials for aeronautics applications[53], it has seen increased utilization in the last couple of decades for the preparation of a wide range of materials, from metals and ceramics to biopolymers[54,55]. The main and perhaps most critical point in the evolution of the technique over the years, has been the introduction of a temperature gradient during freezing. This is the main difference from simple freeze-drying. A suspension is placed in contact with a cold surface and the nucleation of the solvent starts at the interface. The solvent crystals begin to grow in the direction perpendicular to the cold surface, oriented parallel to each other. At first, the suspended solids are expelled from the solidification front, accumulating ahead of the interface. As the crystal dendrites increase in size, they penetrate that accumulation zone and the particles are forced in the space between the crystals. This prevents the entrapment of particles in solvent crystals, which could result in residual mechanical stress, as observed with omnidirectional freezing. Once sublimated, the solvent crystals leave behind a highly directional macroporous network. This use of the solidified solvent as a template for the structure of the final material is the origin of the term “ice-templating”. The basic steps of

the process are schematized in Figure 2.16.

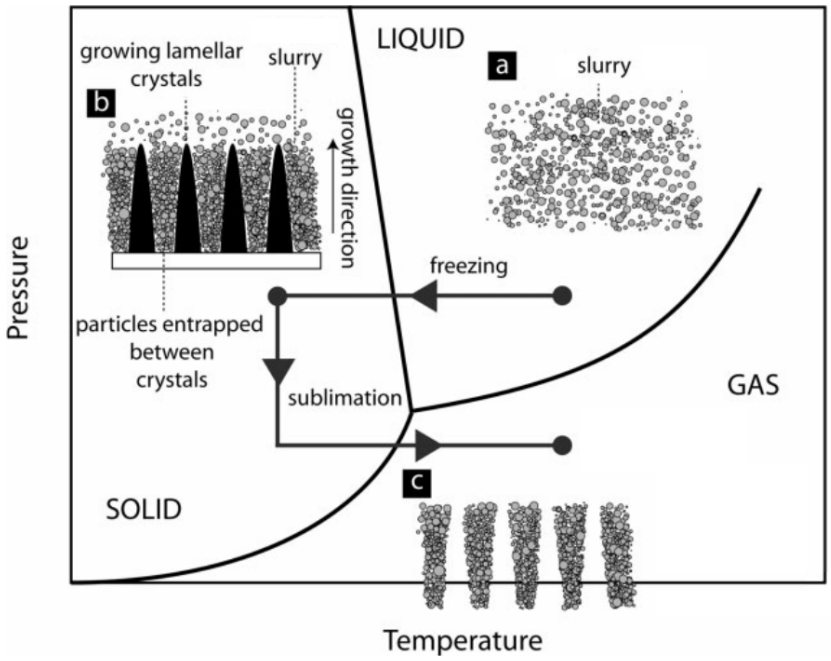

Figure 2.16: The basic steps of freeze casting: a) preparation of the suspension, b) solidification and c) sublimation. Adapted from [54].

Since the porous network can be thought of as the "negative" of the formed solvent crystals, any factor affecting their growth, will also have an effect on the porous system. A higher temperature differential will impose a faster freezing rate and will produce thinner, more oriented crystals. While pore diameters will always exhibit a certain variance, the average pore size and the pore size distribution can be shifted to lower values by increasing the freezing rate[55]. It follows that the nature of the suspended particles (shape, inter-particle interactions, lyophilicity, *etc.*), the physicochemical properties of the suspension as a whole (*e.g.* increased viscosity hinders the crystal growth), as well as the presence of species interacting with the crystallizing solvent (solutes, other solvents, *etc.*) will also influence the eventual structure of the network. For instance, higher concentrations of suspended matter will lead to narrower pore sizes, with thicker pore walls[56]. Similarly, the thermal conductivities of the suspended particles, of the solvent in both the liquid and the solid phase and the respective mass ratios of these components will play a role in how fast and how homogeneously heat can be removed from the system and will thus have an effect on how the solvent crystals will grow.

1.6.2.2 Preparation of freeze-cast aerogels

The experimental setup used to freeze-cast graphene oxide suspensions is shown in Figure 2.17a. It consisted of copper rods, partially submersed in a reservoir filled with liquid

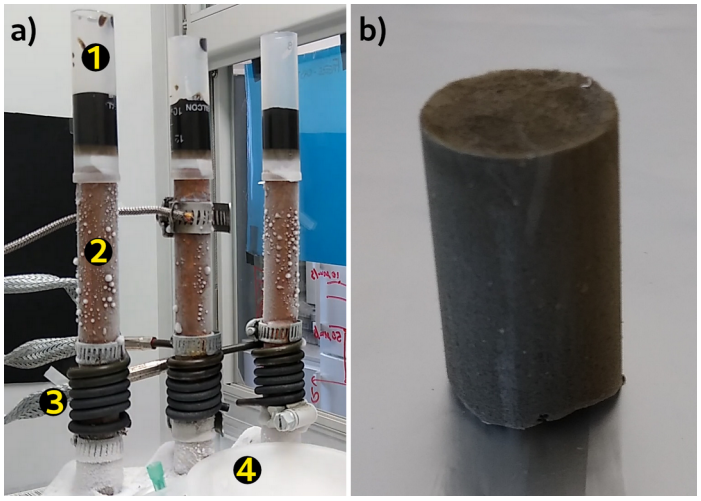

Figure 2.17: a) The experimental set up used for freeze-casting: 1. sample to be frozen, 2. copper rod ("cold finger") 3. resistor 4. N_2 reservoir. b) A close-up of a GO aerogel (height ~4 cm, diameter 1.3 cm) after lyophilization.

nitrogen, with their top surface covered with a thin PTFE film. Plastic tubes, with a diameter of 1.3 cm, were fitted on top of the rods, and the suspensions were poured in them (~5 mL). Flexible resistors were coiled around the middle part of the rods, under the tubes with the suspensions and above the liquid nitrogen reservoir. Thermocouples, to measure the temperature, were also attached to the rods. The resistors and thermocouples were connected to a programmable proportional-integral-derivative (PID) controller. Based on the input settings and the measured temperature, the PID controller would increase or decrease the current flowing through the resistors, in order to maintain the desired temperature, or impose a specific freezing rate.

Having no interest in a large pore size, the fastest achievable freezing rate was selected for all the samples, 10°C/min. The suspensions were set to equilibrate at 20°C and then they were frozen at the set rate, until they reached -80°C and they had completely solidified. The ascending cold front is visible in Figure 2.17a, presenting as a grayish zone just above the PTFE film. The frozen suspensions, still in their tubes, were stored in a container submerged

in liquid nitrogen until all the samples had been prepared and were ready to be transferred to the lyophilizer. The lyophilization process was conducted at a pressure of 0.01 mbar for at least 48 hours, without any heating applied to the samples. Once all of the water had been removed, the samples were brought to ambient pressure and the aerogel monoliths were removed from the tubes with the help of a plastic piston. A typical GO aerogel monolith is shown in Figure 2.17b.

Initially, a range of different GO concentrations (4, 6, 8, and 16 mg/mL) was freeze-cast. However, aerogels prepared from suspensions with a concentration below 8 mg/mL exhibited poor mechanical stability, buckling under the slightest pressure, making their handling and processing impossible. Subsequent experiments were conducted using only suspensions with the higher concentrations, 8 and 16 mg/mL. Suspensions at these two concentrations differed significantly in their viscosity (the more concentrated suspension being much more viscous) and the resulting aerogels possessed markedly different mechanical properties, with the denser ones producing sturdier monoliths. Since water expands as it transitions from the liquid to the solid state, the densities of the different aerogels could not be immediately deduced from the GO concentrations in the suspensions. Through weighing and physical measurements, it was determined that the aerogels made from the 16 mg/mL suspensions consisted of approximately 97% air, whereas the air content in those made from the 8 mg/mL suspensions was around 99%. We proceeded to examine their structural differences at the microscale, through electron microscopy.

1.6.2.3 Macroscopic morphology

Aerogels made from 8 mg/mL suspensions presented an ordered porous network, barely visible to the naked eye, when viewed from the top. Since the internal structure of the aerogels was of interest, to facilitate observations, the samples were examined via SEM, were sliced first perpendicularly to the crystal growth direction and the resulting disks were cut again in half along their middle, to reveal the view parallel to the temperature differential.

The cuts were made using razor blades that were discarded after each incision. This was done to avoid abrading the samples with dulled blades. The top of the aerogels was never flat, because of the expansion of water during solidification and the crystallites not all reaching exactly the same dimensions. At the bottom of the monoliths, in the zone were the nucleation of the crystallites started, there were again inhomogeneities, revealing that the crystallites formed in certain areas and then branched out, orienting themselves parallel to the freezing direction a little over one millimeter from the interface with the metal rods.

The insulating nature of graphene oxide in the 3D structures obtained by freeze-casting was an even bigger problem than with the films. While observation was possible, acquiring images, which necessitated a relatively long exposure time at increased accelerating potential, was much more difficult. The contrast was almost nonexistent, because of the accumulation of static charges. Charge accumulation was at times so high, that the resulting electric field caused distortion in the images. After examining tens of samples before and after thermal reduction (for 2 h, at 200°C, under vacuum), it was verified that the structure remained unchanged. Consequently, it was decided that for purely structural observations, only the conductive forms of the rGO monoliths would be imaged.

Figure 2.18 shows views of a sliced GO monolith, made from a suspension with a GO concentration of 16 mg/mL. The cut in Fig. 2.18a has been made parallel to the temperature

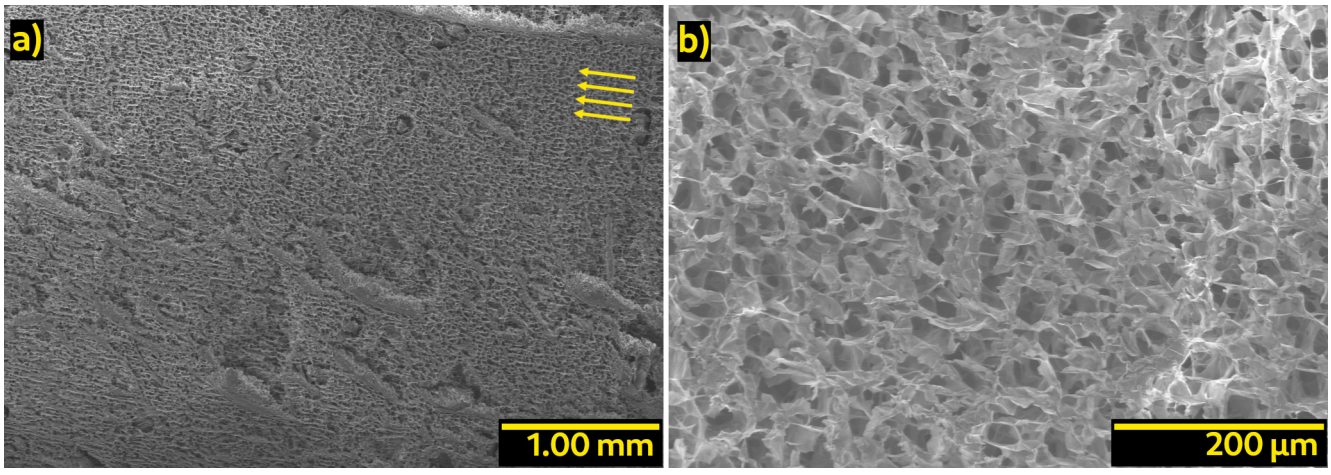

Figure 2.18: SEM images of a GO monolith made from a suspension with a GO concentration of 16 mg/mL. a) Side view of a slice made along the axis of the monolith, the arrows denote the freezing direction. b) View of a slice of the monolith perpendicular to the temperature differential.

gradient. The ice crystals grew from the right to the left, along the direction denoted by the arrows. Some deformations that are visible in the image were caused by the blade used to make the section. The view in Fig. 2.18b is perpendicular to the differential, with the ice crystals having grown towards the viewer. The lack of contrast and the accumulation of static charge (white areas) is clearly apparent in the image.

The sample exhibits a cellular structure, made up of interconnected, oblong cavities. These cavities are anisotropic, with their largest dimension – approximately 20 to 200 μm – measured along the axis of solidification, whereas a frontal view reveals a narrower size distribution, between 21 and 48 μm. While this dimensional anisotropy in general follows the direction of freezing, most of the cavities are not aligned with it, with some being at an angle of up to 23° to it. At the edges of the monolith, the external area in contact with the walls of the tube consists of compressed GO sheets, with a thickness of approximately 12 μm.

The monoliths made from the suspensions at [GO] = 8 mg/mL were too delicate to mount on the SEM sample holder without damaging them. When the aerogels were pressed against the adhesive tape, they would deform and even when they were gently deposited on it, they would break when air was blown on them with a rubber bulb, to ensure that they were stuck in place. When the monoliths where cut along the temperature gradient, these aerogels were much more anisotropic, with a striated structure clearly visible. Observation under an optical microscope revealed a porous system consisting of continuous, interconnected cylindrical pores, perfectly aligned along the freezing direction. However, it was impossible to capture the porous system in its entirety under the electron microscope, due to its fragility.

Figure 2.19 shows two fragments of a monolith after thermal reduction, made from a suspension with a GO concentration of 8 mg/mL. In the first one, the deformation of the porous network in multiple directions is visible, after its upper layer was twisted and torn off during positioning on the SEM sample holder. In Figure 2.19b, one of the fragments that had maintained the orientation of its network is shown. A number of such fragments of different

monoliths were examined and the pore widths in them were found to be in the range of 23 and 47 μm.

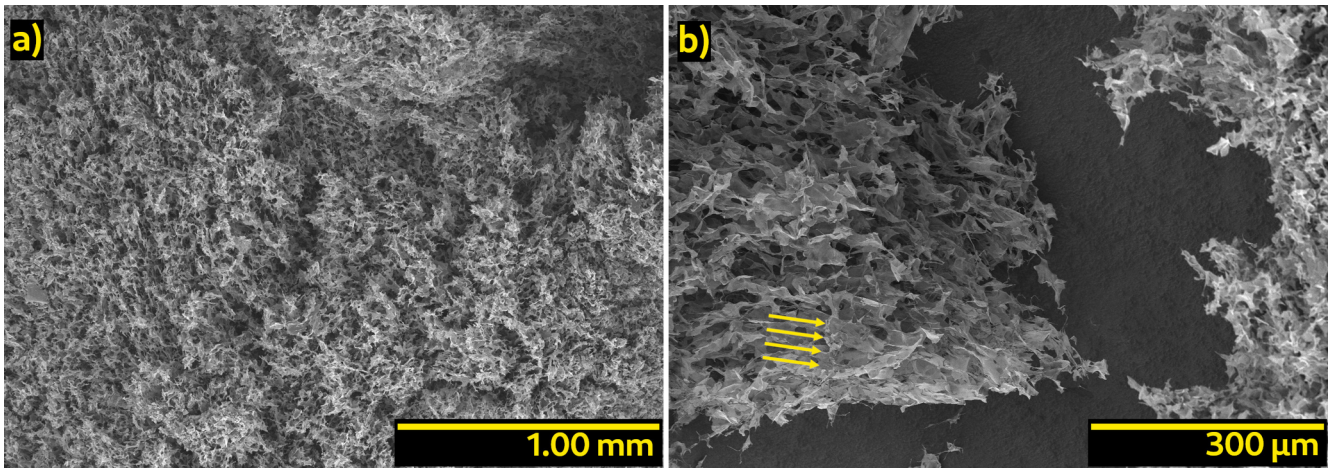

Figure 2.19: SEM images of fragments of rGO aerogel made from a suspension with [GO] = 8 mg/mL. a) Low magnification view of a piece of aerogel deformed during mounting on the sample holder. The different orientations of the pores are visible in several areas of the image. b) Close-up view of a fragment with the porous system mostly intact. The arrows denote the direction of freezing.

1.6.3. Graphene oxide dough

Near the onset of this study, a work was published detailing how it was possible to rehydrate GO foam in a controlled manner, to obtain a gel, that can best be described as a dough[57]. This dough could then be kneaded, pressed and rolled in a variety of forms, with an ordered or disordered structure. By subjecting it to different treatments, it was possible to produce different structures, ranging from porous to glassy carbons. The process is depicted in Figure 2.20.

The ease of application and the versatility of the technique presented indisputable advantages over a number of established, time and energy consuming approaches. While experimenting with the process, it was discovered that due to graphene oxide's amphiphilic nature, it was possible to produce dough with a variety of solvents besides water. Among the

solvents tested successfully were DMSO, carbonate esters used in Li-ion batteries and the $EMI^{+}TFSI^{-}$ ionic liquid.

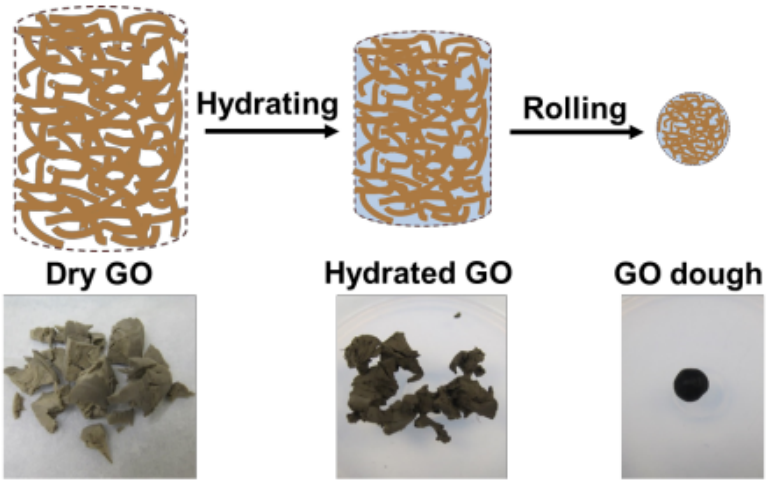

Figure 2.20: Controlled hydration and shaping of lyophilized graphene oxide into dough. Reprinted from [57].

However, the process proved problematic when combined with thermal reduction to rGO. No control could be exerted on the unavoidable shrinking of the material during calcination and the resulting structures were deformed and brittle, making it impossible to cut or machine them in a shape suitable for a battery electrode. Other issues encountered were the decomposition of the organic solvents to toxic or undesirable byproducts during the thermal treatment and the immiscibility of water and the hydrophobic ionic liquid preventing their combination with GO to produce a more structured material.

1.7. Chemical modifications

Since the isolation of graphene and the renewed interest in graphene oxide, a multitude of reactions involving the latter have been researched. Several post-synthetic modification methods were explored, with a mind to the application of the material as a Li-ion battery electrode and what might be beneficial to its properties. Of these methods, the reductive treatment with hydrazine vapors and the perforation of the GO sheets via treatment with

hydrogen peroxide were examined. The first was seen as a convenient method to improve in one stroke the mechanical properties of the matrix, its porosity and its conductivity[7,58–60]. The second could prove useful in augmenting the diffusion of lithium ions through the structure[61].

1.7.1. Treatment with hydrazine monohydrate vapors

One of the most frequently encountered reducing agents in the chemical reduction of graphene oxide is hydrazine (H_2N-NH_2), either in its pure form or as its monohydrate. While the exact reduction mechanism between hydrazine and graphene oxide remains open for debate[62–64], it proceeds through reactions with the oxygen-bearing groups of GO, as the oxygen content decreases afterwards[63]. Among the various addition products that have been suggested, are cyclic, pyrazoline-like structures, eventually converted to pyrazole rings[*] [58]. The simultaneous addition of both nitrogen atoms to the lattice could explain the increased wrinkling of the hydrazine-treated GO sheets, which has also been observed after reactions with other molecules containing two reactive nitrogen centers, such as ethylenediamine[59,65]. A number of these adducts remain on the lattice after the reaction and they can be integrated into it through thermal treatment, producing nitrogen-doped graphene oxide[66]. This N-doping of the lattice has a direct and measurable effect on the properties of the final material[67], *e.g.* the ease with which electrons can be extracted from it (work function). The reaction between hydrazine and GO can take place in solution, under solvothermal conditions, or in a heterogeneous system, with the heated hydrazine vapors directed to GO-based solids. The hydrazine-treated graphene oxide shall be labeled NGO.

*

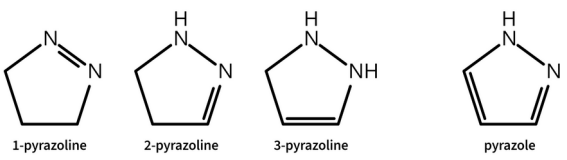

1.7.1.1 Synthesis

50 mL of hydrazine monohydrate (98%, Sigma-Aldrich) was introduced in a two-neck round-bottom flask, along with a magnetic stir bar. A compressed air inlet was connected to one of the necks of the flask and to the other, a horizontal glass cylinder containing the GO monolith. The aerogel was supported on a glass spiral, so as not to come in direct contact with condensed vapors in the tube (Fig. 2.21). The other end of the cylinder was connected to a condensation apparatus with a collection flask. The solution was heated to 110°C (b.p. of

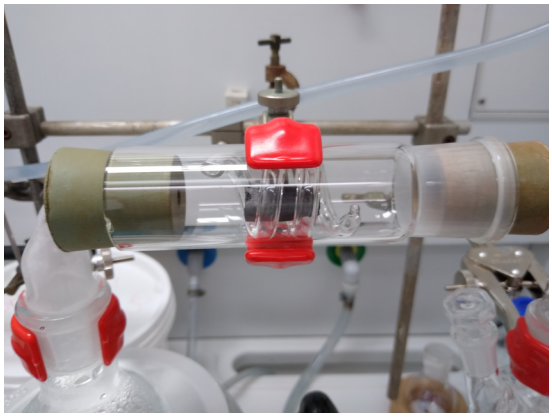

Figure 2.21: Part of the experimental setup used for reduction with N_2H_4 vapors, showing the cylinder with the aerogel mounted on a glass spiral.

hydrazine monohydrate: 119°C) while slowly being stirred and once vapors started appearing in the flask, the compressed air was turned on, to aid the vapors to course through the chamber with the aerogel. The airflow and heating were stopped after 8 hours and the sample was left to dry in air for 3 days.

After drying, the monoliths had shrunk and their color was gray-black, resembling that of thermally reduced graphene oxide. Shrinking was more pronounced in the case of the less dense aerogels, made from the 8 mg/mL GO suspensions, reaching up to 40% volume loss. At the same time, their weight increased 6-7.5 times. All the aerogels were markedly sturdier after the treatment and exhibited some elasticity.

1.7.1.2 Macroscopic morphology of NGO

After the treatment with hydrazine, even the less dense aerogels were much easier to handle and section, so it was possible to examine them in their entirety under the electron microscope. Furthermore, there was no appreciable charge accumulation during imaging, suggesting that reduction had taken place and facilitating image acquisition. The structural changes at the micron scale seemed to explain the macroscopic changes observed, that is the shrinking of the aerogels. In Figure 2.22 are shown SEM images of a monolith made from a suspension with a GO concentration of 8 mg/mL, after the treatment with hydrazine vapors and drying. The network of straight, parallel pores has been contorted and twisted (Fig. 2.22a). A close view of the sheets making up the pore walls (Fig. 2.22b) reveals excessive wrinkling, resulting in an overall rugged appearance. After these observations, the propagation of deformation can be hypothesized as starting at the individual GO sheet level, going up the pore shape, all the way to the entire structure of the monolith.

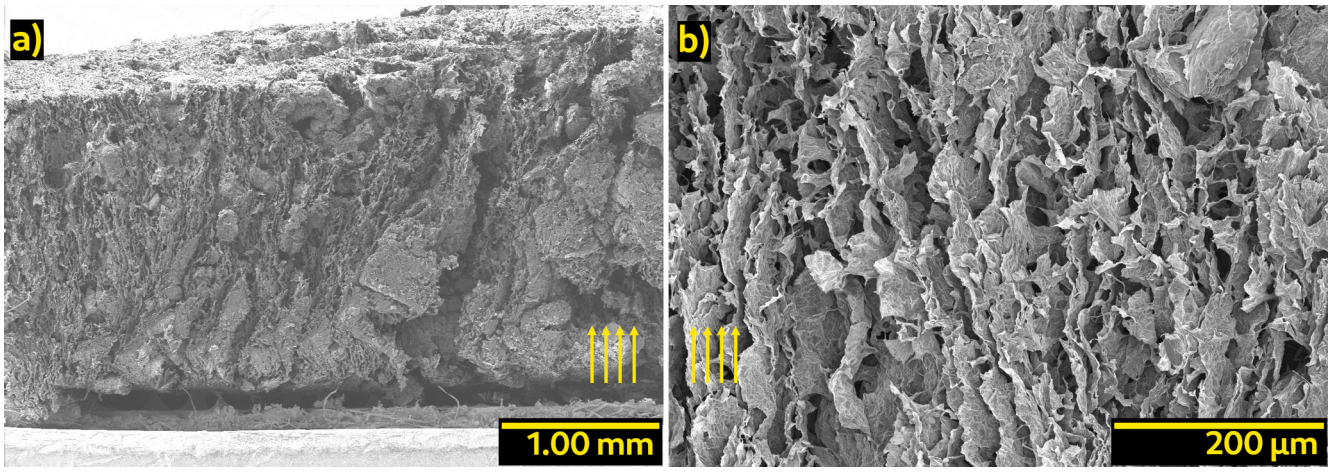

Figure 2.22: SEM cross-sectional views of an aerogel made from a 8 mg/mL GO suspension, after treatment with hydrazine vapors. The arrows denote the freezing direction.

1.7.2. Treatment with hydrogen peroxide

Combining the 2D structure of graphene with pores could prove useful in a lot of different settings where diffusion may play a role and in particular electrochemical applications. As a result, a vast number of methods to produce perforated graphene have been researched and proposed[61]. Among them, the treatment of graphene oxide with hydrogen peroxide yields what is termed holey graphene oxide (HGO). The reaction can take place under both hydrothermal[68,69] and atmospheric[70,71] conditions. Obviously, the latter method affords speed, simplicity and is easy to scale up, therefore it was selected as a candidate post-synthetic modification for graphene oxide.

1.7.2.1 Synthesis

48 mL of a suspension of graphene oxide with a concentration of 8.5 mg/mL was diluted to a final volume of 110 mL with deionized water in a round-bottom flask, equipped with a stir bar. To that, 20 mL of hydrogen peroxide 30% (Sigma-Aldrich) was added. The flask was fitted with a reflux condenser and the mixture was heated to 100°C under vigorous agitation for 6 hours. The reaction mixture was left to cool and was then separated in centrifugation tubes and was centrifuged until the supernatant was clear. The supernatant was decanted and the remaining slurry was redispersed in water and centrifuged again. After decantation of the supernatant, the slurry from each tube was recombined and dispersed in 100 mL of water by ultrasonication for 1 hour. The concentration of the resulting suspension was determined to be approximately 2.7 mg/mL.

1.7.2.2 Mesoscopic morphology of HGO

A quantity of the HGO suspension was diluted with distilled water to the point that its color was barely perceptible. Then a single drop was deposited on a copper grid coated with

a lacy carbon film. Once dry, it was examined under the transmission electron microscope.

TEM imaging revealed that the sheets of HGO had irregularly shaped tears in them. In the TEM images, these tears were perceptible as abrupt discontinuities in the contrast of the overlain graphene oxide sheets against the backdrop of the carbon coating. In the images presented in Figure 2.23, the arrows denote some of these tears or holes. From some of them, strands of material could be seen hanging, *e.g.* those marked by the red arrows in Fig. 2.23b.

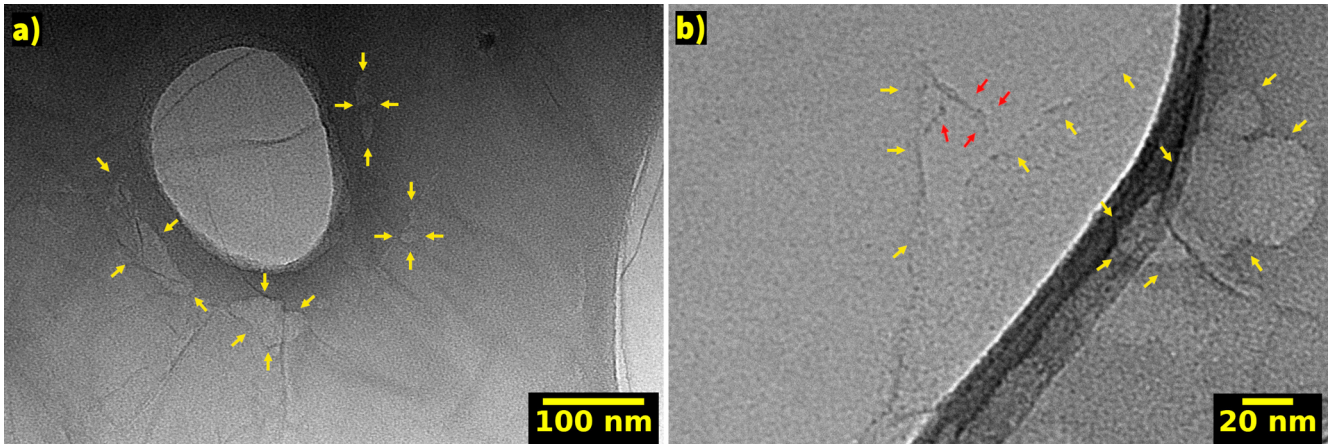

Figure 2.23: TEM images of holey graphene oxide supported on a lacy carbon substrate. The yellow arrows delineate some of the holes in the sample and the red arrows indicate strands of material.

1.7.3. Chemical state of the surface of GO and its derivatives

Since graphene oxide is not a "traditional" molecular compound, in the sense that the atomic ratios between its constituent atoms are not strictly defined and are largely dependent on the fabrication method, we needed to determine its chemical makeup, in order to estimate the stoichiometry of the epoxide ring-opening reaction and consequently, the amount of ionic liquid that could be grafted onto the oxide. We also wanted to examine the effects of the various treatments on its composition; this would allow us to assess the

effects of a treatment or to reorder the various processes within the overall fabrication scheme. X-Ray photoelectron spectroscopy (XPS), a surface-sensitive analytical technique has been used extensively for the characterization of graphene-based materials and we turned to it for answers to the above questions. The principle of the technique is presented in Appendix A.

1.7.3.1 Analyses

In order to determine the effect of the treatments of graphene oxide with hydrazine and hydrogen peroxide we prepared two samples in the form of films, so that they could be analyzed by XPS. We also examined as prepared graphene oxide and reduced graphene oxide. While we considered the hydrazine treatment for the GO aerogels, the fact that the sample, as prepared for the analysis, was shaped as a non-porous membrane necessitated a slight modification of the treatment protocol. As the vapors didn't have to course through a porous network, the reaction with the exposed surface of the membrane was much faster and after just two hours it was stopped, as it seemed to have concluded.

Some differences and similarities between the four samples are immediately apparent from the survey scan spectra (Fig. 2.24). The main body of information is provided by the high-resolution spectra, presented below. Trace amounts of nitrogen were found in all of the samples because of the chamber preparation (purged with N_2 gas) and some of it remained trapped between graphene sheets, despite the ultra-high vacuum ($\leq 10^{-9}$ mbar). Except for the NGO sample, N 1s has been omitted from the analyses for clarity.

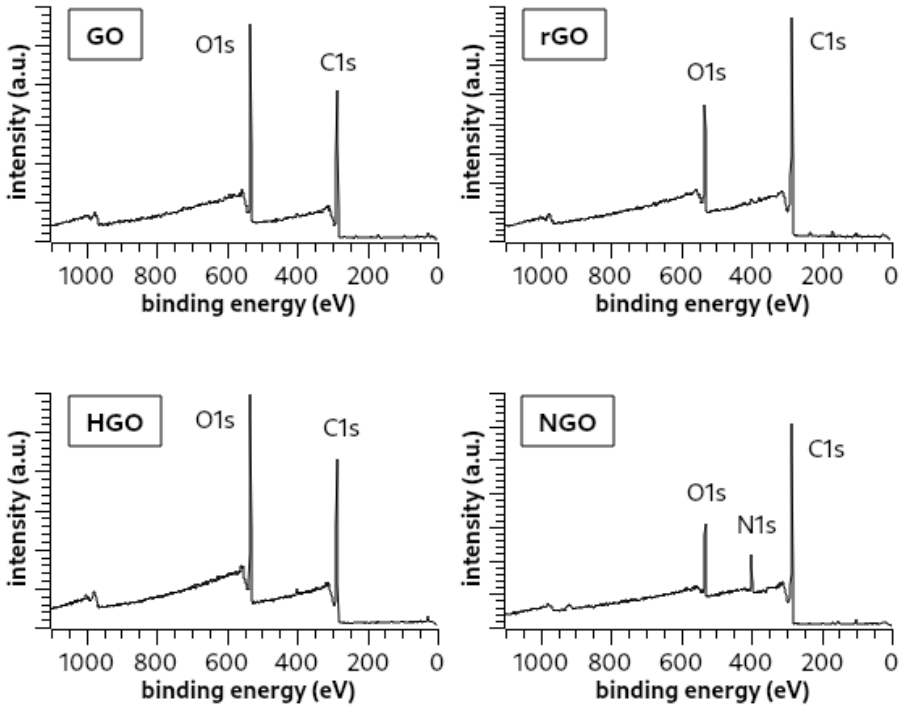

Figure 2.24: XPS survey scans of GO, rGO, HGO and NGO

Graphene oxide

High resolution scans of the C 1s and O 1s orbitals of graphene oxide are presented in Figure 2.25:

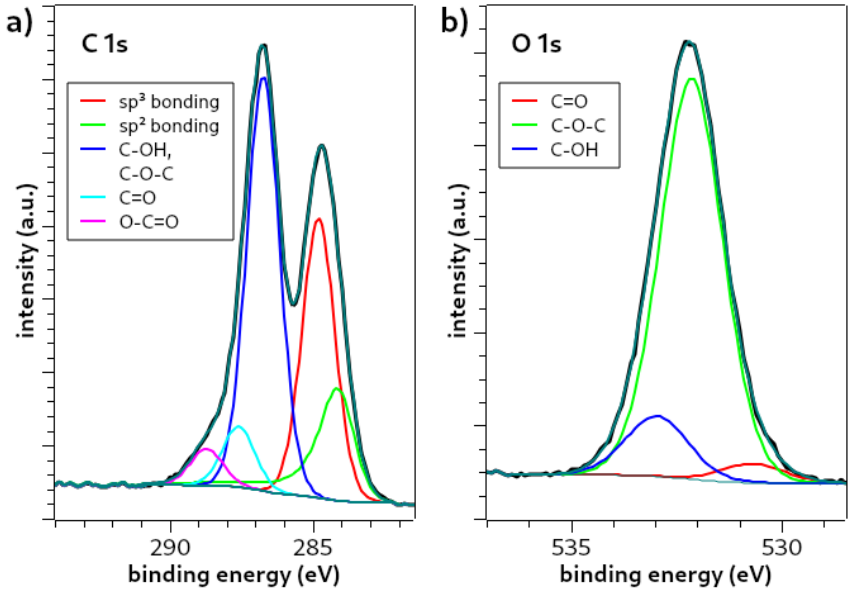

Figure 2.25: Deconvoluted XP spectra of a) C 1s and b) O 1s of the GO sample

The C 1s peak of the GO sample (Fig. 2.25a) appears split. This suggests that C atoms take part in bonds with considerable differences in polarization. The two apparent peaks, centered at binding energies 284.7 eV and 286.7 eV, were deconvoluted into five components: atoms in sp^2 C=C bonds at 284.1 eV, atoms in sp^3 C-C bonds at 284.8 eV, C-O (as in C-OH and C-O-C) bonds at 286.7 eV, carbonyl carbons at 287.6 eV and finally carbons in carboxylates (O-C=O) at 288.7 eV.

Similarly, the O 1s peak (Fig. 2.25b), centered at 532.2 eV, consists of three components: carbonyl oxygens at 530.7 eV, epoxide oxygens at 532.1 eV and atoms in hydroxyls at 533.0 eV.

It must be noted that in order to estimate the quantity of certain species, results from the analyses of both signals have to be combined. In the C 1s spectra we cannot distinguish carbon atoms that belong to hydroxyls from those belonging to epoxides and in the O 1s spectra we have no information whether the second neighbors to a carbonyl oxygen are all carbons or if another oxygen atom is present. While the percentages of atoms belonging to different functional groups from the perspective of oxygen and from that of carbon are not exactly the same, they are reasonably close and the discrepancies are well within the margin of error of the technique (up to 10%).

The sample presents an image typical for graphene oxide prepared in this manner. A little less than a third of its atoms (28.6%) are oxygen atoms, most of them appearing as epoxide adducts. Hydroxyls and carbonyls are also present at comparable levels, with the latter being either part of carboxylates or by themselves. The conjugated system is significantly diminished, with only 8.7% of atoms being carbon atoms in sp^2 bonds to other carbons, whereas sp^3 defects in the lattice make up 21.9% of the sample. The full results of the analysis are presented in Table 2.1.

Table 2.1: Atomic percentages of O and C atoms in GO, participating in different types of chemical bonds and their corresponding binding energies

species		binding energy (eV)	At%
O 1s	C-OH	533.0	3.6
	C-O-C	532.1	23.9
	C=O	530.7	1.1
C 1s	O-C=O	288.7	2.9
	C=O	287.6	4.8
	C-OH, C-O-C	286.7	32.5
	C sp^3 bonding	284.8	21.9
	C sp^2 bonding	284.1	8.7

Reduced graphene oxide (rGO)

High resolution scans of the C 1s and O 1s orbitals of reduced graphene oxide are presented in Figure 2.26:

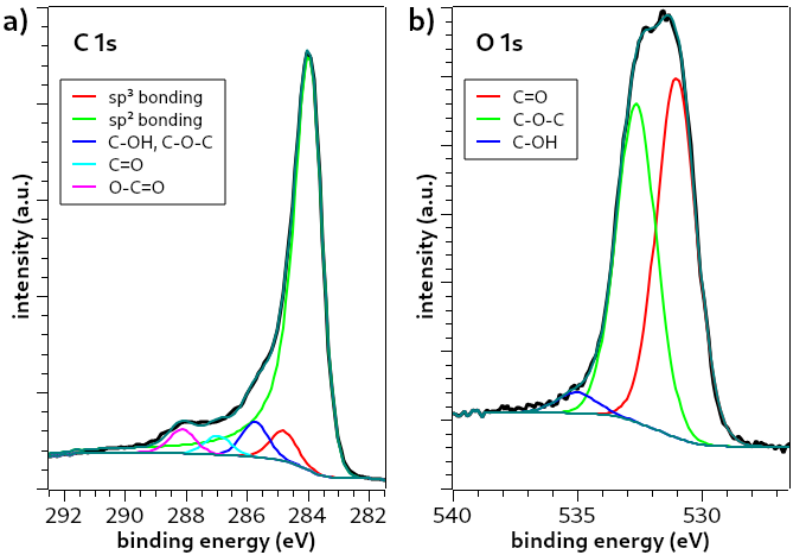

Figure 2.26: Deconvoluted XP spectra of a) C 1s and b) O 1s of the rGO sample

Looking at the C1 s high-resolution spectrum (Fig. 2.26a) of the reduced graphene oxide sample, it was immediately evident that one part of the doublet peak of GO had almost disappeared. Since it was the part at higher binding energies, we could immediately infer

that a substantial loss of C-O bonds had taken place. The signal was deconvoluted into five components: atoms in sp^2 C=C bonds at 284.0 eV (coinciding with the main parent peak), atoms in sp^3 C-C bonds at 284.8 eV, C-O (as in C-OH and C-O-C) bonds at 285.7 eV, carbonyl carbons at 287.0 eV and carbons in carboxylates (O-C=O) at 288.1 eV.

The O 1s peak (Fig. 2.26b), centered at binding energy 531.8 eV, was deconvoluted into three components: carbonyl oxygens at 531.0 eV, oxygens attributed to epoxides at 532.6 eV and atoms in hydroxyls at 535.0 eV.

The results summarized in Table 2.2 paint a picture typical for graphene oxide annealed at 200°C under vacuum. Oxygen atoms make up now about a fifth (20.3%) of the sample and half of them are found as carbonyls – a potential byproduct of the partial thermal decomposition of other oxygen-bearing groups. The graphitic lattice has been extensively restored, with 62.1% of the atoms in the sample taking part in sp^2 bonds, while the sp^3 defects amount to 4.5%. What is a bit odd and probably an artifact of the deconvolution of the spectrum is the amount of carbon atoms in carboxylates, which appear to have increased compared to those in GO. Arithmetic error aside (which can be up to 10%), the thermal reduction of graphene oxide entails the loss of functional groups as CO and CO_2 gasses, so the relative abundance of certain groups might indeed fluctuate.

Table 2.2: Atomic percentages of O and C atoms in rGO, participating in different types of chemical bonds and their corresponding binding energies

species		binding energy (eV)	At%
O 1s	C-OH	535.0	0.6
	C-O-C	532.6	9.3
	C=O	531.0	10.4
C 1s	O-C=O	288.1	3.6
	C=O	287.0	2.9
	C-OH, C-O-C	285.7	5.4
	C sp^3 bonding	284.8	4.5
	C sp^2 bonding	284.0	62.1

Holey graphene oxide (HGO)

High resolution scans of the C 1s and O 1s orbitals of holey graphene oxide are presented in Figure 2.27:

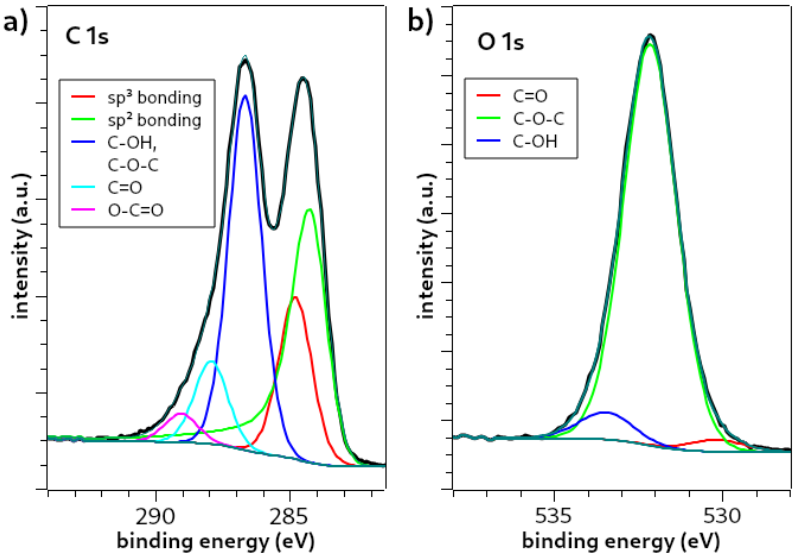

Figure 2.27: Deconvoluted XP spectra of a) C 1s and b) O 1s of the HGO sample

The C 1s spectrum of the HGO sample (Fig. 2.27a) bears some resemblance to that of the parent GO, in that there is a doublet peak present, though the relative intensities of the two peaks centered at binding energies 284.5 eV and 286.7 eV are different. The peaks consist of five components: atoms in sp^2 C=C bonds at 284.3 eV, atoms in sp^3 C-C bonds at 284.8 eV, C-O (as in C-OH and C-O-C) bonds at 286.7 eV, carbonyl carbons at 287.9 eV and carbons in carboxylates (O-C=O) at 289.0 eV.

The O 1s peak (Fig. 2.27b), centered at binding energy 532.2 eV, was deconvoluted into three components attributed to carbonyl oxygens at 530.2 eV, epoxide oxygens at 532.1 eV and atoms in hydroxyls at 533.5 eV.

Holey graphene oxide appears to have a composition quite close to that of untreated graphene oxide. There is a small decrease of oxygen content (24.8%) and all types of preexisting oxygen atoms appear affected. A small restoration of the sp^2 character of the material has taken place with a simultaneous reduction of sp^3 defects. Both of these changes,

the loss of oxygen and the partial reduction of the carbon skeleton, could be due to the energy input to the system during the reaction, as the mixture was kept in reflux at 100°C for 6 h, so no useful conclusions could be drawn as to a possible reaction mechanism with hydrogen peroxide. The complete analysis is presented in Table 2.3.

Table 2.3: Atomic percentages of O and C atoms in HGO, participating in different types of chemical bonds and their corresponding binding energies

species		binding energy (eV)	At%
O 1s	C-OH	533.5	1.5
	C-O-C	532.1	22.6
	C=O	530.2	0.7
C 1s	O-C=O	289.0	2.4
	C=O	287.9	7.0
	C-OH, C-O-C	286.7	30.0
	C sp^3 bonding	284.8	13.7
	C sp^2 bonding	284.3	21.2

Hydrazine-treated graphene oxide (NGO)

High resolution scans of the C 1s, N 1s and O 1s orbitals of hydrazine-treated graphene oxide are presented in Figure 2.28:

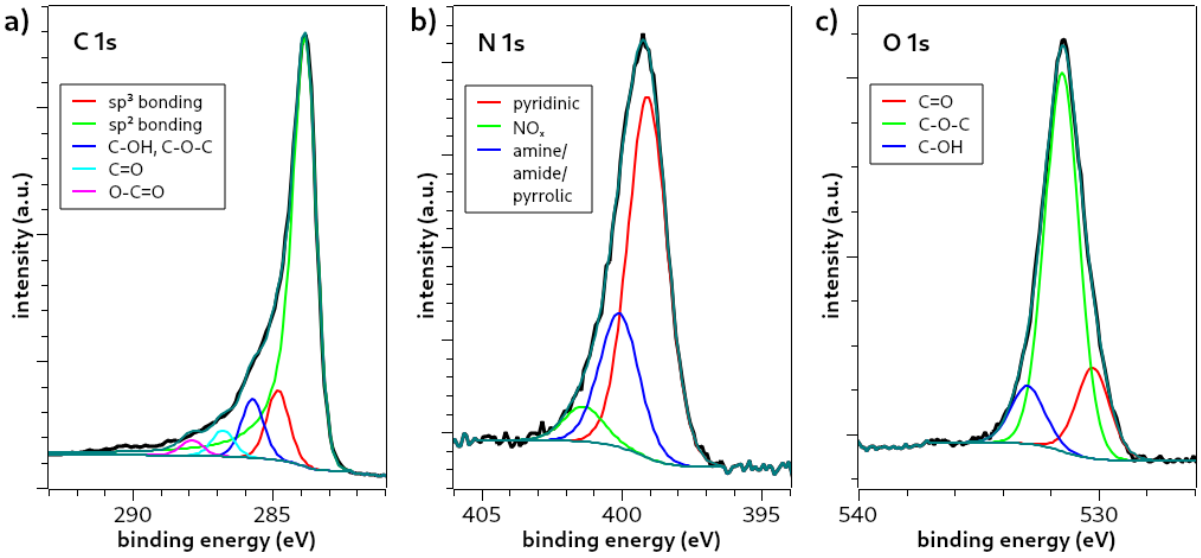

Figure 2.28: Deconvoluted XP spectra of a) C 1s, b) N 1s and c) O 1s of the NGO sample

The C 1s high-resolution spectrum of NGO (Fig. 2.28a) appears more similar to that of thermally reduced graphene oxide than that of the starting material. The peak centered at binding energy 283.8 eV was deconvoluted into five components, attributed to atoms in sp^2 C=C bonds at 283.8 eV, atoms in sp^3 C-C bonds at 284.8 eV, C-O bonds at 285.7 eV, carbonyl carbons at 286.8 eV and carbons in carboxylates (O-C=O) at 287.9 eV. It must be noted that C-O bonds are virtually indistinguishable from C-N bonds in terms of binding energy, so the component at 285.7 eV certainly contains an amount of nitrogen-bonded carbons. That amount can only be estimated after the analyses of the N 1s and the O 1s spectra.

The N 1s peak (Fig. 2.28b), centered at 399.2 eV was deconvoluted into three components: pyridine-like nitrogen atoms at 399.1 eV, nitrogen atoms bonded with one or more oxygen atoms at 401.4 eV and finally nitrogen atoms that could be part of amine-, amide- or pyrrole-like formations [*]at 400.1 eV.

The O 1s peak (Fig. 2.28c), which is centered at binding energy 531.5 eV consists of three components, attributed to carbonyl oxygens at 530.2 eV, epoxide oxygens at 531.5 eV and atoms in hydroxyls at 532.9 eV.

It turns out that the resemblance to the rGO sample is not just visual; more than half of the atoms present in NGO are sp^2-bonded carbons and there are half as much sp^3 defects as in the GO sample. The loss of oxygen atoms is considerable and given the relative percentages, at least some of them must have been displaced by nitrogen atoms. Unfortunately, the analyses of the N 1s and O 1s spectra do not provide much information on the amount of C-N bonds present in the sample, as some components might have been underestimated or others overestimated, or both. The detailed breakdown of atomic ratios is presented in Table 2.4.

---

* 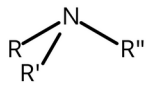

amine

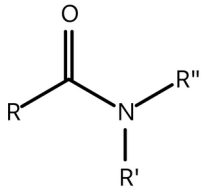

amide

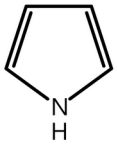

pyrrole

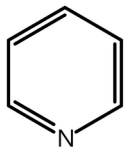

pyridine

Table 2.4: Atomic percentages of O, N and C atoms in NGO, participating in different types of chemical bonds and their corresponding binding energies

species		binding energy (eV)	At%
O 1s	C-OH	532.9	1.4
	C-O-C	531.5	9.2
	C=O	530.2	2.2
N 1s	amine/amide/pyrrolic	400.1	2.4
	NO_x	401.4	0.6
	pyridinic	399.1	6.6
C 1s	O-C=O	287.9	2.0
	C=O	286.8	3.4
	C-OH, C-O-C	285.7	7.6
	C sp^3 bonding	284.8	9.1
	C sp^2 bonding	283.8	55.4

Conclusions

The results of the analyses of the four materials presented so far are perhaps better summarized in Figure 2.29 (the adsorbed N_2 has been included in the plot so that all bars stack up to 100%). Atomic percentages for all samples are given in Table 2.5.

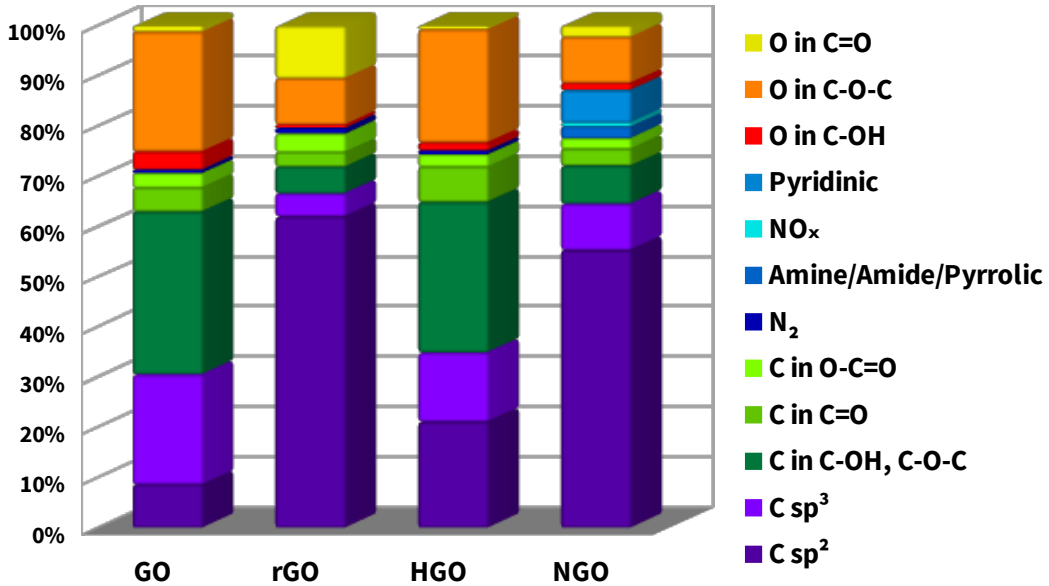

Figure 2.29: Atomic composition of GO, rGO, HGO and NGO. The different nitrogen atom types are represented by shades of blue, between the C and O stacks – adsorbed N_2 in dark blue.

Table 2.5: Atomic percentages of O, N and C atoms in GO, rGO, HGO and NGO

species		GO	rGO	HGO	NGO
		At%	At%	At%	At%
O 1s	C-OH	3.6	0.6	1.5	1.4
	C-O-C	23.9	9.3	22.6	9.2
	C=O	1.1	10.4	0.7	2.2
N 1s	amine/amide/pyrrolic	0.6 (adsorbed N_2)	1.2 (adsorbed N_2)	0.9 (adsorbed N_2)	2.4
	NO_x				0.6
	pyridinic				6.6
C 1s	O-C=O	2.9	3.6	2.4	2.0
	C=O	4.8	2.9	7.0	3.4
	C-OH, C-O-C	32.5	5.4	30.0	7.6
	C sp^3 bonding	21.9	4.5	13.7	9.1
	C sp^2 bonding	8.7	62.1	21.2	55.4

Graphene oxide and reduced graphene oxide have been studied extensively[72–76] in the last couple of decades and the XPS analyses confirm what we expected for both of them, given the oxidation and reduction methods and reaffirmed the results obtained from EDX analyses. If we consider GO and rGO as the starting and the end point respectively in the envisioned assembly process of the composite material, holey graphene oxide is near the beginning, while hydrazine-treated graphene oxide towards the end. HGO has an atomic composition which is very close to that of GO, despite the slight reduction of the lattice and the small loss of oxygen atoms. Epoxide content – the anchoring point for the cation of the ionic liquid – remains almost unchanged. The atomic ratios reported by XPS can be converted to mass ratios, based on the molecular weights of every atom in the sample and from there, molar quantities per mass of material can be deduced. According to the analysis, GO contains 18.16 mmol/g of epoxides and the treatment with H_2O_2 lowers their amount to 17.36 mmol/g. In contrast, epoxide content is 7.21 mmol/g for GO and 7.22 mmol/g for NGO. As a first conclusion, we can say that GO and HGO are equally suitable to be functionalized by the modified EMI^+, so if a purely GO-based structure proves inadequate for the application, HGO can be used in its stead.

We already knew that the thermal reduction would be the final step in the process. Similarly, as the treatment with hydrazine vapors "locks into place" the 3D structures, it wouldn't be possible to graft them with EMI^+ post-treatment. What we did not know, was the extent of the reduction in NGO. Looking at just the carbon content of the four samples in Figure 2.30, it appears that chemical reduction with hydrazine is almost as good as thermal reduction. If the process proves compatible with the grafted GO (or HGO), the subsequent annealing would have much less defects to eliminate, potentially yielding a better-conducting material, with the added benefit of electron-rich nitrogen atoms doped into the lattice.

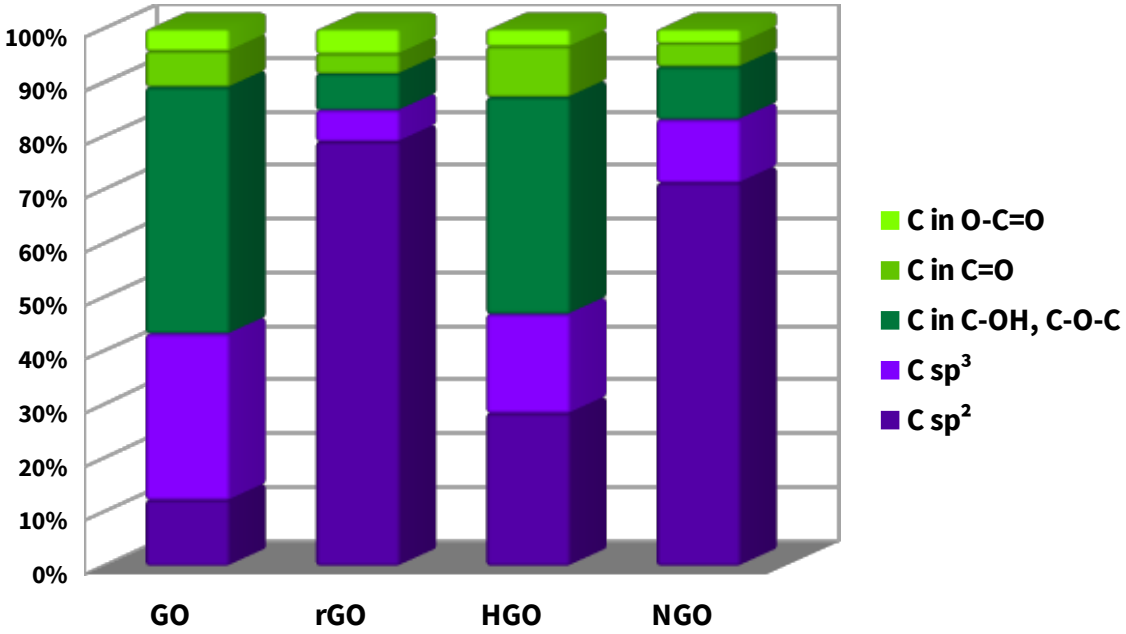

Figure 2.30: Normalized C content in GO, rGO, HGO and NGO samples.

Experimental details. *XPS measurements were made at the IMPC at Sorbonne University, using an Omicron Nanotechnology spectrometer, equipped with a monochromated Al Kα X-ray source. Survey scans were recorded at 100 eV energy pass. High-resolution spectra, were recorded at 20 eV energy pass. All spectra were recorded at a takeoff angle of 45° relative to the sample surface (90° between source and collector). Trace amounts of nitrogen were found in all of the samples because the instrument's preparation chamber was purged with N_2 gas before the measurements and some of it remained trapped between graphene sheets, despite the ultra-high vacuum (≤10^{-9} mbar) in the measurement chamber.*

1.8. Conclusions

Graphene oxide is a truly versatile material, capable of being shaped in radically different structures and of being chemically modified in a multitude of ways. The two last decades of intensive research into the family of graphene-based materials have produced an arsenal of methodologies one can choose form, to create a host of forms and fine tune their functional, morphological and physicochemical aspects. From this plethora of options, several were selected and tested, based on the criteria set forth during the bibliographic stage of this study.

Following an established synthetic protocol, with small adaptations tailored to the fabrication of a Li-ion battery electrode, graphene oxide was produced repeatably and in quantities. The main adaptation was the choice to use large graphite flakes as a starting material, to ensure a higher degree of overlapping between sheets in a 3D structure and to provide longer conductive pathways for electrons. The synthesized graphene oxide was adequately characterized and its composition and morphology were found to conform with what was expected from the literature.

Graphene oxide membranes are very easy to make and they should be capable of hosting tin nanoparticles among the stacked sheets. The flexibility of the films means that they have the potential to adapt to volumetric changes as tin expands to accommodate lithium in its structure. These layered films can be produced from graphene oxide subjected to chemical modifications, as long as the sheets remain dispersible in a solvent. The wrinkling of GO sheets, which persists even after reduction, results in an increase of the interlayer spacing, which should give GO membranes an advantage over graphite, in terms of speed of lithium ions diffusion and perhaps, the amount of lithium ions that can be hosted by the structure. However, for purely practical geometric reasons, the films would have to be placed perpendicular to the path of lithium ions in an assembled battery and this could severely impact the speed of lithiation of the material. On the other hand, perforating the layers, as

was done during the treatment with hydrogen peroxide, might be able to alleviate this issue.

Graphene oxide foams are very interesting because of their inherent porosity, which can be tuned via simple compression, to achieve the right balance between the gravimetric and volumetric capacities of the electrode material. At the same time, compression should increase their electrical conductivity, as the contact surface between sheets also increases. The freeze-casting technique, already used in manufacturing, produces aerogels, that are mechanically more stable than what could be obtained by simple freezing and lyophilization. The anisotropy induced by the temperature gradient conveniently creates interconnected paths throughout the structure for the lithium ions to follow, even though these paths are rather wide. Between the ordered and more disordered forms – the result of the difference in viscosity of the two starting GO suspensions, 8 mg/mL and 16 mg/mL respectively – the latter would seem as the one capable of hosting a higher quantity of lithium ions. Besides its higher carbon content in a given volume, it presents more surface immediately available to host lithium. The cellular structure of the disordered foams could also prove useful in preventing the migration of tin during the operation of a battery.

Graphene oxide dough seemed promising at first, because it presented the possibility to fashion the material directly into the form of the final electrode. However, it proved incompatible with the thermal treatment protocol, precluding any precise control over the form and dimensions of the annealed material, which would become too brittle to process. For these reasons, GO dough was deemed an unsuitable choice for shaping and was abandoned.

The selected thermal reduction regime, conducted for 2 hours under vacuum, at 200°C, a temperature well below the decomposition temperature of the pure ionic liquid and the melting point of bulk tin, even though it could not remove all of the oxygen-bearing functional groups of GO, it was sufficient to eliminate close to two thirds of them, according to thermal analyses. Based on secondary observations during SEM imaging, the resulting materials were adequately conductive so as to never exhibit any accumulation of static

charges, even when bombarded with electrons at a close distance.

Treatment of the matrix with hydrazine could impart simultaneously a number of useful properties to the material. First of all, it improves the cohesiveness and the mechanical properties of the 3D structures, facilitating their handling and processing. It can decrease the pore size of the graphene oxide foams and expose more of the lattice to lithium ions, through the increase in wrinkling. The chemical reduction induced by hydrazine might be able to complement that of the thermal treatment, which is mainly limited by the melting point of tin. It is an established fact that thermal reduction of graphene oxide, previously treated with hydrazine, results in the doping of the graphitic lattice with nitrogen atoms. This could enhance the properties of a matrix intended to conduct electrons, with low ohmic losses.

Through experimentation and analysis, all of the synthetic and preparative processes examined were evaluated as to the properties conferred upon the candidate electrode material. These processes were then ordered in the eventual overall protocol, based on the modifications they brought about and how these would affect the chemical and structural capabilities of graphene oxide at each step and in particular in relation with the other two components.

2. Sn nanoparticles

The synthetic route initially chosen for the preparation of tin nanoparticles (NPs) in the EMI^+TFSI^- ionic liquid was developed in our lab and optimized by N. Soulmi[77,78]. This synthesis is highly attractive for its simplicity and the precise control exerted on the size of the particles – a narrow size distribution, with the majority of the particles having a diameter of ~10 nm (Fig. 2.31). The ionic liquid functions as both the viscous medium and

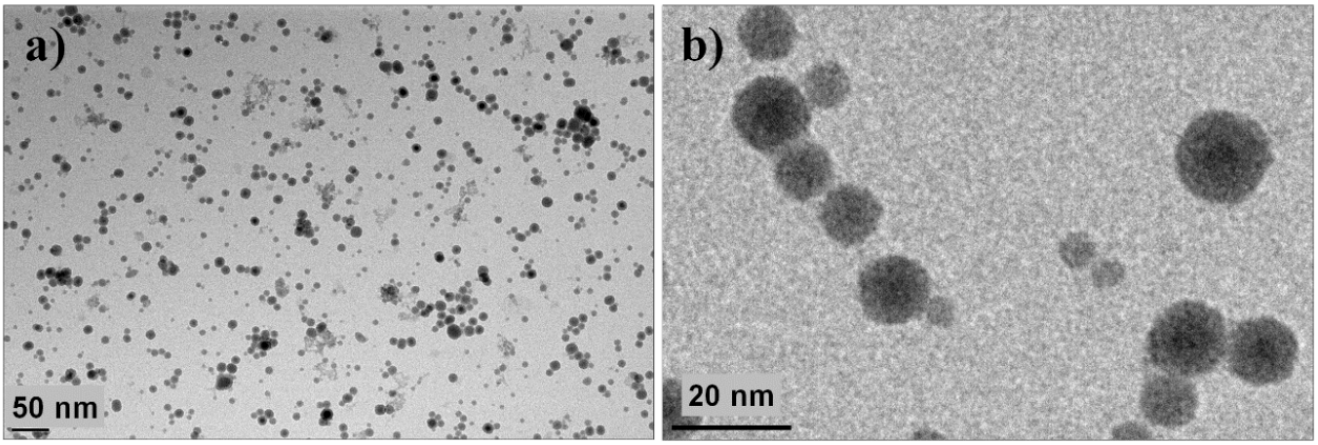

Figure 2.31: TEM images of Sn nanoparticles synthesized in EMI^+TFSI^-. Reprinted from the doctoral thesis of N. Soulmi[78].

the capping agent that contains the growth of forming metal nanoparticles. Tin(II) chloride is dissolved in the ionic liquid, as is an excess of sodium borohydride (a reducing agent), in a separate container. Once the dissolution is complete, the two solutions are combined and the reduction of tin cations to metallic tin begins instantly. The interactions between the ionic species of the IL are largely responsible for its viscosity, which, for the purposes of the process, serves to keep nucleation sites well-dispersed, avoiding aggregation. NMR relaxometry analyses have shown that the surface of the isolated nanoparticles is covered with the cation of the IL (EMI^+), hence the postulation that it assumes the role of a capping agent, further hindering accretion, while simultaneously stabilizing the nanoparticles. The reaction is sensitive to the presence of humidity and once the metal nanoparticles have formed, they readily oxidize upon contact with oxygen. For these reasons, the synthesis is

conducted within a high purity inert argon atmosphere (in a glovebox). The full synthetic protocol is presented in Appendix B. This process bears some similarities with the polyol synthesis[79], in which polyols also function as the viscous medium and the capping agent and simultaneously they are capable of reducing noble metals from their precursors without the use of a reducing agent. The use of a reducing agent is however necessary for other metal salts, such as tin. Unlike the synthesis in polyols, the synthesis in the IL requires no heating.

While trying to master the synthesis of tin nanoparticles in $EMI^{+}TFSI^{-}$, the preparation of the carbon scaffolds had advanced and estimates had been made of the amounts of each component that would be used in the final composite material: the freeze cast matrices were frozen in tubes with a diameter of 1.3 cm, work had been done with suspensions of GO with concentrations of up to 16 mg/mL and the resulting aerogel monoliths were 3 to 5 cm in height. Considering the fabrication methods that had been chosen for the matrices, a loading of up to 80 wt% in tin seemed feasible. Given these dimensions and quantities, that translated to at least 200 mg of tin nanoparticles, almost 100 times the amount produced in a single batch. It quickly became evident that the aforementioned preparation method could not be employed to produce sufficient quantities of Sn NPs. Combining multiple batches would pose problems to quality control and ascertaining the exact composition of the final materials would be difficult. Scaling up the process or adapting it to a continuous flow scheme was ruled out, as it would be very time-consuming and also, very expensive. Isolating the nanoparticles is a rather involved process, entailing 13 consecutive washing steps, carried out under a nitrogen flow, which again added to the cost. For these reasons, alternative methods were sought in the literature.

2.1. Researching alternative preparative methods

There exist a number of synthetic approaches, many utilizing the polyol synthesis[80–82] or closely related variations[83,84] thereof, while others employed the so-called “amine-borane

route"[85]. Amine-borane adducts are themselves strong reducing agents, but also suitable capping agents towards the forming metal nanoparticles, sometimes even alleviating the need for a solvent[86]. A top-down method, involving the sonication of molten tin in paraffin oil has also been described[87]. Unfortunately, none of these methods seemed able to produce tin NPs of comparable size and dispersity and also – more importantly – free from any contaminants. A lecture by Carsten Bolm on mechanochemistry[88] pointed towards another top-down approach: size reduction via ball milling. Materials with low melting points such as waxy substances are usually ground in cooled grinders[89]. Given tin's low melting point and the fact that the ball mill that was available could not be cooled during operation, ball-milling tin by itself was not an option, as it would melt and fuse back together. During that lecture, a series of syntheses had been presented in which some of the reagents were added to the ball mill sealed in glass tubes. The glass casings were sacrificed, in order for the reaction to take place. A similar approach might provide the solution.

2.2. Ball milling

2.2.1. Size reduction

The terms size reduction and comminution refer to the cutting or breaking down of particles of solids into smaller pieces and as such, they encompass a host of different methods. Size reduction is achieved through external mechanical forces acting upon the solids in such a manner, that the cohesion forces keeping them together are overcome. Depending on the physicochemical properties of the materials, different types of action or combinations thereof can be applied. The hardness of the solids, their initial size, shape, their mode of fracturing, their elasticity and their hygroscopicity – properties included in the term "grindability" of a material – ultimately dictate the method most suitable for the reduction of their size. Generally speaking, most size-reduction machines commonly may

employ compression, impact, attrition and cutting. Compression is mainly used to reduce big pieces of hard material to smaller, workable lumps and it produces very little fine particles. Impact can give coarse, medium as well as fine particles. Attrition products are typically very fine. Cutting, which is usually reserved for fibrous, elastic materials, yields particles of definite size and at times, definite shape, producing few or no fine particles.

Even though size-reduction machines such as mills have been in use from antiquity, modeling the processes involved in order to extrapolate the accompanying parameters is extremely complex as it pertains to complex systems and as a result, the theory remains incomplete. For instance, the product of size reduction always consists of a mixture of particle sizes and the ratio of the diameters of the largest and smallest particles can be in the order of 10^4. However, through observations and comparisons to ideal systems, a number of empirical equations related to equipment performance and energy requirements have been developed[89,90]. These are presented in Appendix C.

2.2.2. Ball mills

Tumbling mills are a type of grinding device consisting of a horizontally rotating cylindrical or conical shell, partially filled (⅓ to ½ of its volume) with a solid grinding medium. When these grinding elements are spherical, the grinder is called a ball mill. The shell is usually made of steel, lined with a variety of materials such as high-carbon steel, zirconia, porcelain, silica rock or rubber, depending on the intended use. The grinding medium can be made of the same material or one of a lower hardness, to decrease the wear of the shell lining. As the shell rotates, the balls are carried up its side and under the influence of gravity, they fall onto the particles underneath, a little before they reach the top of the shell. From this description it is easy to surmise that size reduction is mainly accomplished through impact. Attrition plays a smaller role, as the grinding balls slip and roll over the particles, which are also in motion and they may grind against themselves. Ball

mills can operate in either a continuous or batch mode and the grinding can be done with dry solids or suspensions in water. They are typically used to grind relatively small feed to fine or ultra-fine particles.

The faster the mill rotates, the longer the grinding balls stay in contact with the walls and the higher their momentum is when they fall back down to the impact zone. Above a certain critical speed threshold, the balls never break contact with the drum walls and they are said to be centrifuging. Depending on the solids being ground and the viscosity of the suspension (in the case of wet grinding) ball mills are run at 65 to 80% of their critical speed.

Ideally, the energy requirements of a ball mill would be computed from the mass of the rotating shell, the mass of solids (the sample), the mass of the grinding medium (the grinding balls), the speed of rotation and the maximum distance of fall. However, even if all losses external to grinding were to be ignored, it would still be extremely difficult to calculate the exact energy input required for any given system. Some particles are overground even though they are of the requisite size, the grinding balls might slip as they are being raised and they might fall without doing any grinding. In industrial settings, such calculations are done by modeling the input/output of pilot plants. In general, the capacity of a mill decreases and its energy requirement increases as the product gets finer.[89,90]

Planetary ball mills are a special kind of ball mill, where the axis of rotation is vertical and they consist of a rotating disk (the “sun”) onto which counter-rotating grinding jars or bowls are mounted (the “planets”). The speed of the bowls can be equal or higher than that of the disk and their rotations relative to one another are kept in lockstep. This dual rotation subjects the grinding balls to both centrifugal and centripetal forces and hence centrifugation is avoided. This means that the speed of the mill is practically only limited by the mechanical tolerances of the bowls and of the moving parts of the system, while the balls can attain a much higher momentum than in a similarly sized horizontal mill. Because of the high energy impacts generated during the operation of planetary ball mills and the associated material strength requirements, they are relatively smaller than their

conventional counterparts; their useful capacity rarely exceeds a few litters, whereas that of horizontal ball mills can be of several tens of cubic meters. The working principles of both types of ball mills are presented in Figure 2.32 and the planetary ball mill used in our experiments is shown in Figure 2.33.

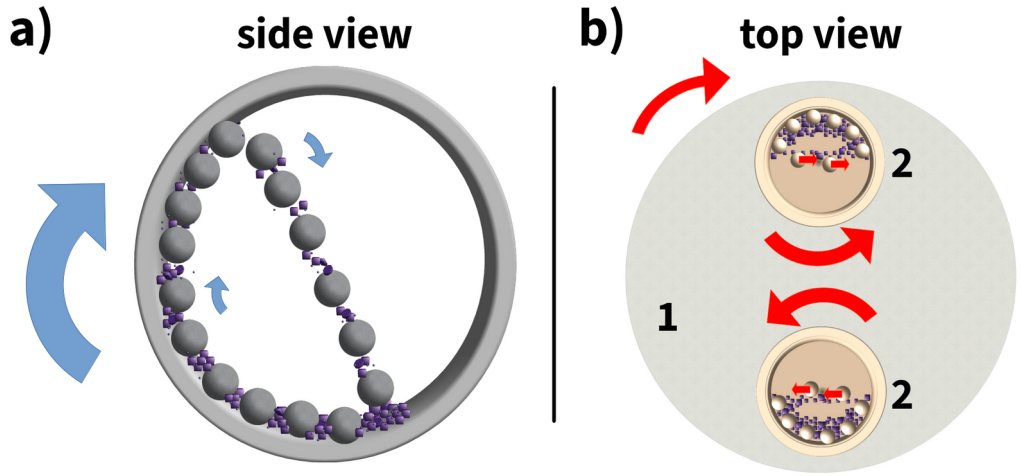

Figure 2.32: a) Side view of a horizontally-rotating ball mill and b) top view of a planetary ball mill, showing the rotational direction of the disk (1) and of the grinding bowls (2). The direction of movement of grinding balls in both systems is also indicated.

Ball mills have been a boon to the field of mechanochemistry, *i.e.* the synthesis of chemical products by mechanical action. The highly localized energy input from the impacts can bring materials in a metastable state above or near the activation energy level required for a reaction to take place and the constant moving and mixing in the mill removes the need

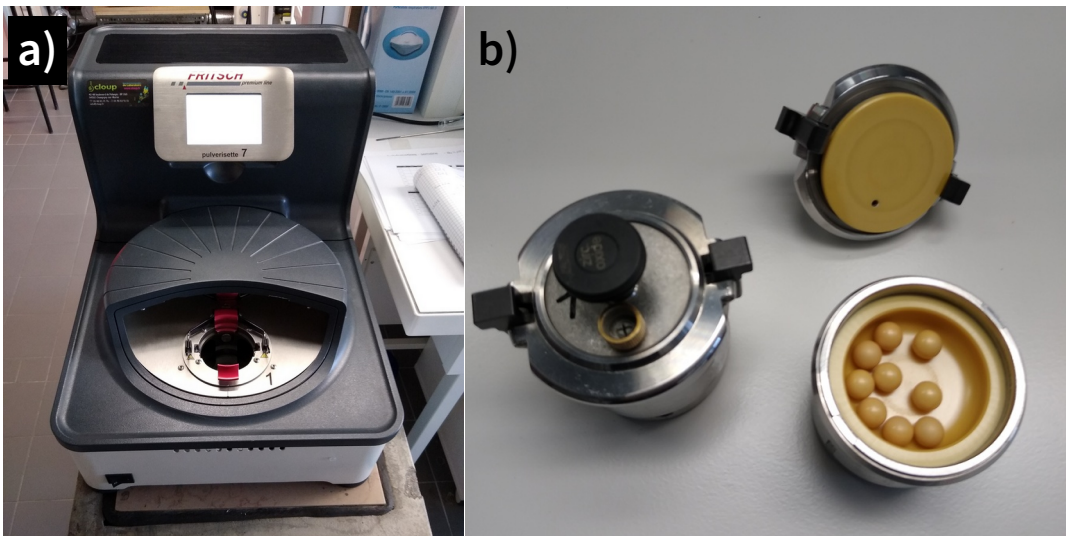

Figure 2.33: a) The planetary ball mill and b) the grinding bowls and 10 mm balls used in our experiments.

for a solvent to help the reagents reach each other[91]. Ball milling is seeing increased use in the preparation of nano-sized materials, both through size reduction and by bottom up synthesis[92–94]. This was very beautifully demonstrated in a 1993 study by Zaluski *et al.*[95], where they prepared nanocrystalline, as well as amorphous Fe-Ti alloys by ball milling micrometric powders of the intermetallic compound and elemental metals.

2.2.3. Co-milling tin with graphene oxide or graphite

The use of sacrificial glass casings that had been presented by Bolm, while not technically the same, led to the idea of co-milling tin with graphene oxide or graphite, since graphene was already part of the targeted composite material. To the best of our knowledge, this had not been tried before. Graphene's impermeability towards gases even as small as hydrogen and helium has been well established[83], so it was posited that if the Sn nanoparticles could be wrapped in it, they could be protected from oxidation from atmospheric oxygen. It also seemed reasonable that the addition of graphene oxide would help with their dispersion in aqueous media; this would be necessary, since the freeze casting process requires the dispersion of the solids in water. At the same time, a large number of publications concerning tin encased in graphene or similar carbon-based materials[84–86], clearly demonstrates that this entrapment does not prevent lithium ions from diffusing into tin, probably due to the small size of the Li^+ ions combined with the presence of defects, such as 8-membered rings, in the lattice[87].

2.2.4. Grinding parameters

The ball mill that was used was equipped with 20 mL zirconium dioxide grinding bowls. The available grinding balls – also made of ZrO_2 – came in two sizes, with diameters of 10

mm or 2 mm. When grinding with the larger balls, 10 balls would be loaded into the bowls, weighing 2.6 g on average. When grinding with the 2 mm balls, 30 g or approximately 160 balls were used.

The weight ratio of tin to graphite or graphene oxide was kept constant to 9:1, *i.e.* mixtures containing 90 wt% Sn and 10 wt% graphite or graphene oxide. This ratio was estimated based on a number of assumptions, since neither the form, nor the roughness nor the size of the particles obtained after grinding could be anticipated. The basic goals were to keep the tin content high in the mixture, while at the same time preventing the new surfaces from fusing back together. The specific surface area of one side of a graphene sheet is 1315 m^2/g[96]. Since the mass of graphene oxide is almost twice that of the graphite used to produce it, it follows that the specific surface area of GO is roughly half of that. The stable metallic allotrope of tin, β-Sn has a density of 7.265 g/cm^3. If tin were ground to spheres with a diameter of 10 nm, 100 mg of graphite would provide enough surface to cover approximately 1.592 g of tin. If tin were ground to cubes with a diagonal of 10 nm, the graphene sheets would be able to cover ~0.955 g of tin. For 50 nm spheres and cubes, those same 100 mg of graphite would cover 7.961 g and 4.596 g respectively. All of the above quantities would be halved in the case of graphene oxide. Knowing that a mixture of sizes would be obtained and aiming for the smallest attainable particle size, the 9:1 ratio seemed perfectly acceptable. Obviously, when graphite would be used instead of graphene oxide at the same mass ratio to tin, there would be 50% more surface available. However, keeping constant the mass fraction of tin in the grinding bowls was deemed more important in order to be able to make useful comparisons.

Next, the combination of parameters which would yield the most satisfactory results in terms of uniformity, size and size distribution was examined. The following were varied: grinding time, grinding speed, sample mass, and grinding ball size. Milling was conducted in 15 min increments, followed by a 15 min pause with the 10 mm balls, to allow the system to cool down to room temperature. The smaller balls possessed an increased total surface area,

compared to the larger ones, which meant higher heat generation due to friction. As a result, when grinding with them, the pause was extended to 25 minutes. Every other milling session was performed in the inverse sense of rotation to the preceding one, in order to prevent the accumulation of compacted material on the walls of the bowls. If during milling session #n the bowls rotated clockwise, during session #n+1 they would be rotated counter-clockwise and so on. After some experiments, it was noticed that grinding with graphite was less efficient and more so when grinding solely with small balls. Furthermore, when using the larger balls, regardless of grinding time, there would always remain some chunks of material several hundred nanometers in size. Following some discussions with the manufacturer and given the equipment that was at our disposal, it was decided to make the following adjustments: that the main pulverization would be performed by milling with the larger balls, followed by milling with the smaller ones, to better homogenize the samples and that grinding speed would be limited to 400 rpm for the 10 mm balls and to 600 rpm for the 2 mm ones, as exceeding these, could result in ZrO_2 being chipped off from the bowls and the balls. The bowls were always filled and emptied inside a glovebox, to prevent the oxidation of the nanoparticles. It was observed that when the bowls were opened after grinding, the oxygen levels in the glovebox would increase by 2 to 4 ppm and they would be a little higher (1 to 1.5 ppm) when graphene oxide had been used instead of graphite. This lead to the hypothesis that a certain amount of air was always trapped between graphene sheets, but in the case of graphene oxide, some thermal reduction could also have taken place, resulting in the release of oxygen. Both hypotheses were later confirmed by XPS analyses (Section 2.3.4 of this chapter).

The various samples along with the different grinding parameters used in their preparation are listed in Tables 2.6 and 2.7, which pertain to samples of Sn co-milled with GO and graphite, respectively.

Table 2.6: Sn-GO co-milled samples and the corresponding grinding parameters

sample name	Sn (mg)	GO (mg)	total solids (mg)	ball ⌀ (mm)	rpm	time (h)
SnGO01	900	100	1000	10	400	12
SnGO02	900	100	1000	10	400	24
SnGO03	900	100	1000	2	600	6
SnGO04	2700	300	3000	10	400	12
SnGO05	2700	300	3000	2	400	12
SnGO06	2700	300	3000	10 2	400 600	23 1
SnGO07	2700	300	3000	10 2	400 600	23 1
SnGO08	2700	300	3000	10 2	400 600	22 2

Table 2.7: Sn-graphite co-milled samples and the corresponding grinding parameters

sample name	Sn (mg)	graphite (mg)	total solids (mg)	ball ⌀ (mm)	rpm	time (h)
SnGR01	900	100	1000	2	400	12
SnGR02	900	100	1000	2	400	16
SnGR03	900	100	1000	2	600	6
SnGR04	2700	300	3000	2	600	6
SnGR05	2700	300	3000	2	600	8
SnGR06	2700	300	3000	2	600	12
SnGR07	2700	300	3000	2	600	20
SnGR08	2700	300	3000	10 2	400 600	12 12
SnGR09	2700	300	3000	10 2	400 600	18 6
SnGR10	2700	300	3000	10 2	400 600	23 1
SnGR11	1800	200	2000	10 2	400 600	23 1
SnGR12	900	100	1000	10 2	400 600	23 1

The components of the grinding mixtures differed widely in both their initial dimensions and their physical properties. Tin particles were up to 63 μm in size, whereas graphite flakes and graphene oxide pieces of film measured up to 2 mm. As a result, the initial surface area of tin was much higher than that of the second component. Consequently, some aggregation of tin took place in parallel with the size reduction of graphite or graphene oxide in the early stages of milling. Mixtures of graphene oxide and tin ground at 400 rpm with either 10 mm or 2 mm balls were examined after 2 h of grinding and a black fine powder along with millimeter-sized, platelet-shaped silver particles with dark inclusions were observed. The former was probably ground GO, while the latter was by all appearances tin that had been welded into larger particles, entrapping some powdered and fragmented GO. By 8 h of milling, all the samples appeared as a fine dark powder.

Based on the above observations, it was estimated that the size reduction process could be accelerated, at least for the mixtures with graphene oxide, by incorporating the tin powder in the GO films. This way, tin particles would not fuse together before GO had been reduced to a sufficiently small size. A sample was prepared by mixing Sn powder with a suspension of GO at the same 9:1 mass ratio and after homogenization on a magnetic stirrer, the mixture was left undisturbed and the water was evaporated slowly under air, forming a film, which was then cut to millimeter-sized pieces. That composite film was harder than those of pure GO. When TEM images of that sample were compared with those of another one made using the exact same parameters (sample mass, rotation speed, grinding media used, time), but which had not been mixed before milling, similarly sized tin NPs were observed, but they were all encased in larger, strand-like aggregates of carbonaceous material. Since there were not any time gains and the complexity of the resulting system increased, this method was abandoned.

Experimental details. *Experiments were conducted using a Fritsch Pulverisette 7 Premium planetary ball mill, equipped with 20 mL zirconium dioxide grinding bowls. The ZrO_2 grinding balls used had a diameter of 10 mm or 2 mm (or both, but not simultaneously). In the first case, 10 balls would be loaded into the bowls, weighing 2.6 g on average, whereas in the latter case, 30 g of the smaller ones (≃160 balls). The starting materials were micrometric Sn powder (99.75% purity,*

63 μm max. particle size, Goodfellow Cambridge Ltd.), graphite flakes (99.9% purity, -10 Mesh, Alfa Aesar) and millimeter-size pieces of graphene oxide films (their preparation is discussed in section 1.6.1 of this chapter).

2.3. Characterizations of the Sn-graphene composites

When size reduction exceeds the microscale, simple techniques such as sifting and weighing cannot be employed for sample analysis. The analysis of the composites was primarily done via transmission electron microscopy (TEM) imaging and small-angle X-Ray scattering (SAXS) measurements. Knowing that the ground samples would be polydisperse, it was expected to get information about the breadth of the particle size distributions in each of them from both techniques and the precise distributions through TEM observations in particular. Both techniques can yield information about the shape and morphology of the particles in such samples, with TEM providing the close-ups and SAXS a view of the whole. SAXS can further supply information about the mean size of the particles in a sample, the mean distance between them, as well as their degree of orientation (if there is indeed a particular orientation). Some of the samples were also subjected to PXRD measurements, in order to inspect the diffraction angle range not covered by SAXS, look for the presence of oxides and verify the crystallinity of the particles. Finally, XPS was employed to examine the chemical composition of the surface of the particles in two samples, one made by co-milling with GO and the other with graphite.

2.3.1. Transmission Electron Microscopy

Electron microscopy revealed early on that the co-milling strategy was indeed effective in producing nanoparticles. It also provided the information that co-milling with graphite was less efficient with the 2 mm balls and that when grinding with the 10 mm balls there would

remain large bits of unground material. Tin being denser and heavier than carbon facilitated observations; Sn particles present as dark spots in the micrographs, whereas graphene/graphene oxide sheets and fragments are barely distinguishable from the carbon film with which the TEM grids are coated. However, two problems were encountered with regard to the technique.

The first one had to do with the nature of tin itself, which has a low melting point. When reducing the size of materials, beyond a threshold, the bulk can no longer completely stabilize the surface. Surface atoms, unlike their kin in the bulk material don't share the same number of neighbors and they are more susceptible to the influence of their environment, outside the material. In the case of tin nanoparticles, this is expressed by their propensity to oxidation, whereas bulk metallic tin is used to protect other metals and alloys from corrosion. Another symptom of the increased surface-to-bulk ratio, is the decrease of the melting point temperature[97,98]. This posed a problem during TEM observations especially when the nanoparticles were found on areas of the grids where the contrast was poor, requiring a higher focus of the electron beam. In such cases, the nanoparticles would melt while surveying the grid, or while we would be trying to acquire their image.

The second problem encountered was the fact that the nanoparticles would be very easily transported by the liquid in which they were suspended. The nanoparticles were mostly accumulated on the edges of the drop deposited on the grid, much like the coffee ring effect, though they would sometimes get trapped near the ridges of the grids. Deposition of more drops would lead to the first nanoparticles being rinsed away. We tried dispersing them in ethanol, isopropanol and mixtures of the two, without any significant improvement and in order to prevent the drops from spreading out, we also tried setting the grids on a hydrophobic surface (Parafilm). In Figure 2.34, two characteristic cases are shown: the deposition of one drop of a suspension of sample SnGR06 in ethanol and the successive deposition of five drops (each one after the previous drop had dried) of sample SnGR06 in ethanol. The dark disks around the grids (indicated by the red arrows) are material that has

been carried away. Furthermore, once the grids had dried, the nanoparticles would often fall off, even though they tend to stick on almost every other surface. For these reasons, the TEM images of the samples were not representative of them and did not allow a size distribution analysis. After a certain point, the focus was put on poorly ground particles, trying to locate the biggest in each sample, as a measure of the efficiency of the combination of parameters.

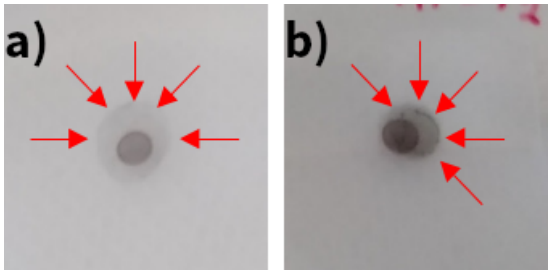

Figure 2.34: TEM grids on Parafilm left to dry after the deposition of suspensions of co-milled material. a) sample SnGR06 - deposition of a single drop, b) sample SnGR07 deposition of five drops.

Some indicative micrographs are presented in this section.

The sample shown in Figure 2.35 (sample SnGO02) was the first sample in which a large number of nanoparticles was observed . To make sure what was observed was not the result of a contamination, two more samples were prepared and analyzed, taking extra care to avoid dust and other possible contaminants. Images a) and c) show a population consisting exclusively of particles with a diameter up to 10 nm. In micrographs b) and d) we see a mix of two different populations, smaller particles like in a) and c) and particles ranging in size from 20 to 50 nm. The particles appear wrapped in graphene sheets, which have been torn to what are essentially graphene oxide nanoribbons and which connect all the particles. This hints at the mechanics of particle formation, with tin probably melting during the process, but being prevented from forming large aggregates by the graphene oxide sheets that engulf it during milling. Graphene has been shown to exhibit a fast brittle fracture in an almost straight line[99] and we would expect largely the same behavior from GO sheets. With the propagation of the fractures moving in a straight path, the successive impacts during milling could lead to regularly shaped fragments, such as ribbons.

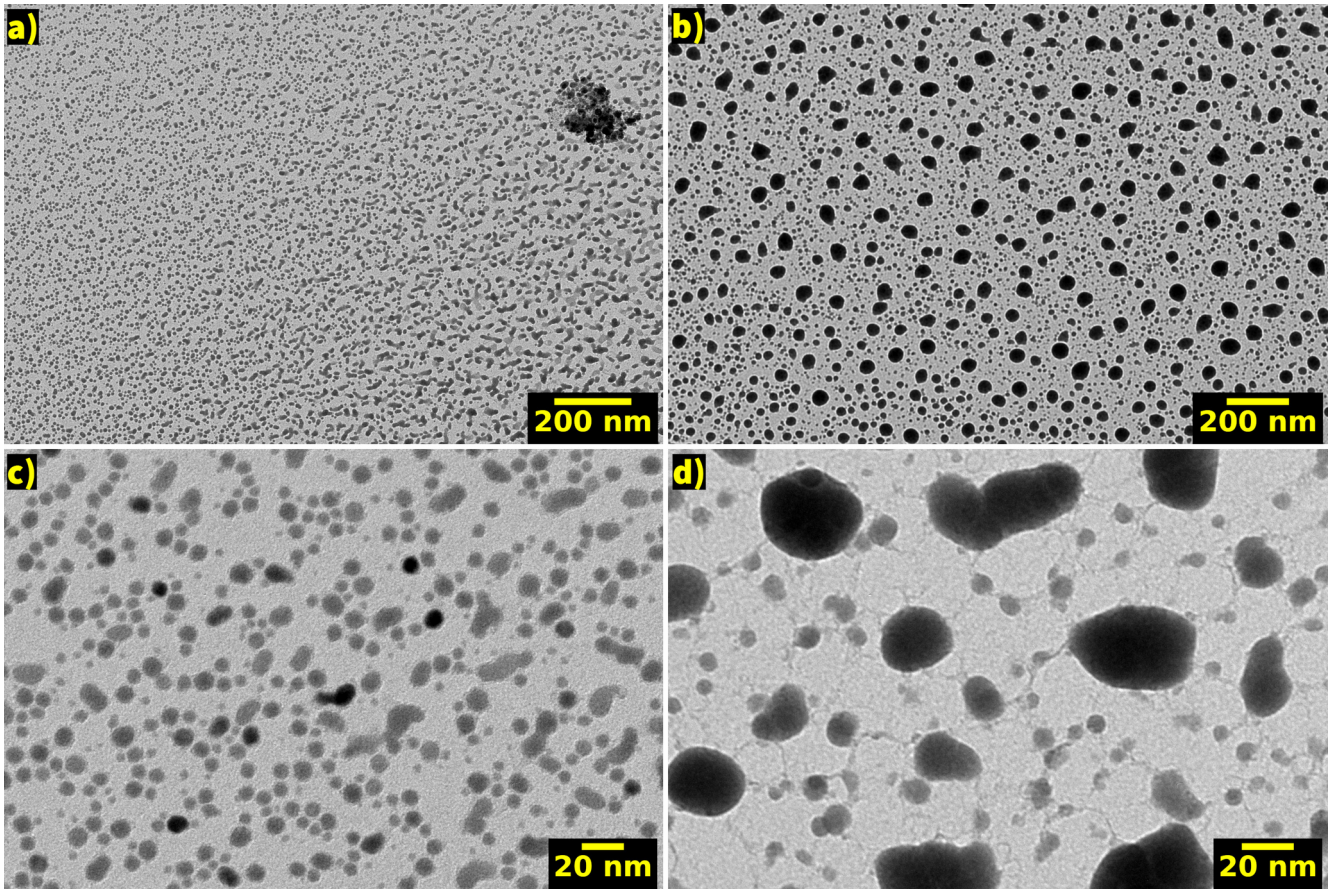

Figure 2.35: TEM images of sample SnGO02 (900 mg Sn, 100 mg GO, 24 h, 10 mm balls, 400 rpm).

Besides the above mentioned size groups, several large and irregularly-shaped particles, with sizes up to 300 nm were also observed (images not shown).

Images of sample SnGR01 are shown in Figure 2.36. The nanoparticles in a), b) and c) are all between 14 and 29 nm in size. In d) some of the larger nanoparticles with sizes ranging between 50 and 250 nm. In none of the samples prepared with graphite flakes were any nanoribbons observed, unlike in the samples ground with graphene oxide. However, almost always, the larger particles appear to be embedded in pieces of damaged, but still stacked graphite (such as in Fig. 2.36d), which on occasion was found without any Sn present. This can be explained by the fact that while the mass fraction of graphite in the mixtures was the same as that of graphene oxide, its volume fraction was roughly double that of GO. Furthermore and unlike GO, which has been subjected to exfoliation and whose layers are not as strongly bound to each other, it appears that graphite, through the Van der Waals forces holding its sheets together, can better withstand the impacts during milling.

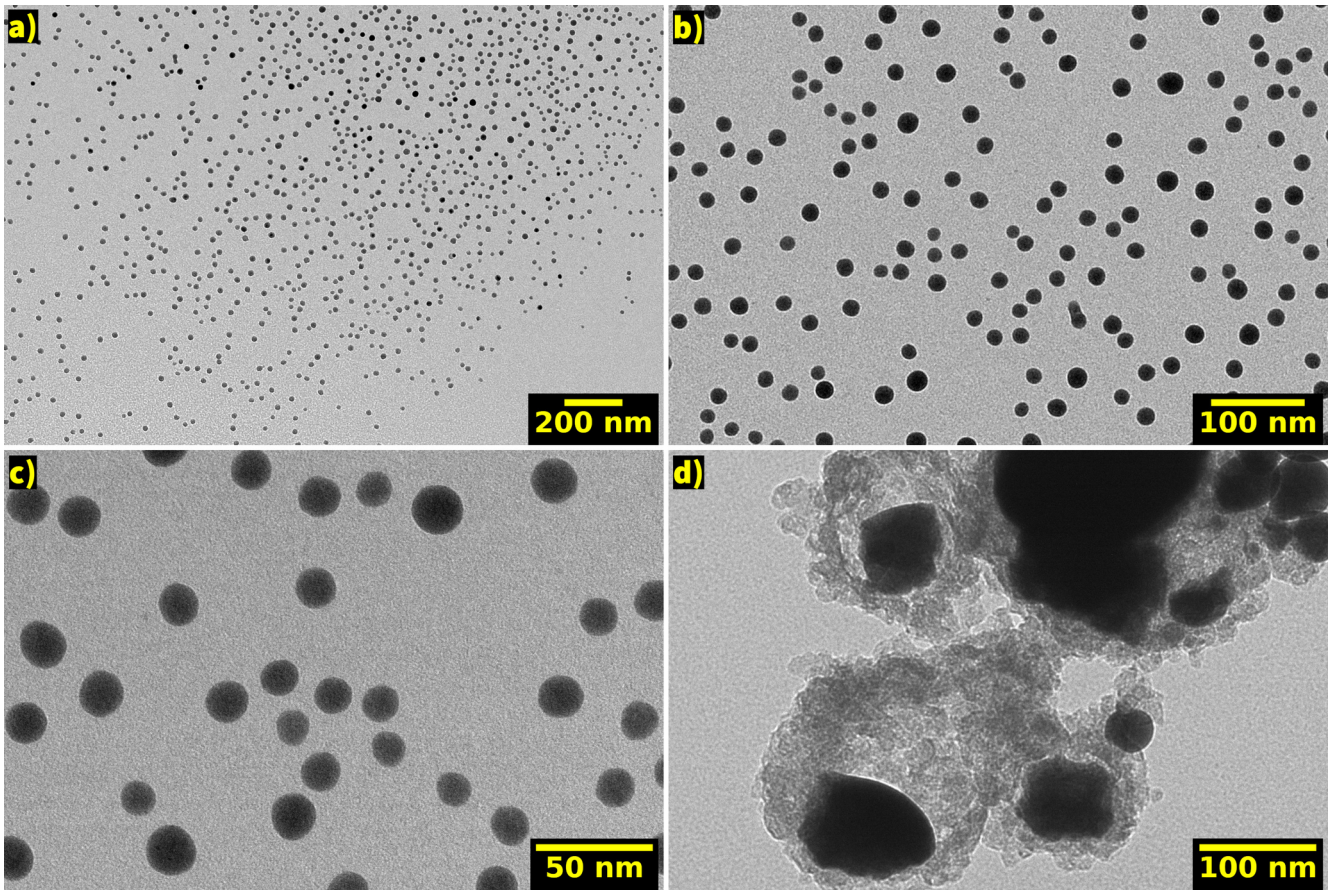

Figure 2.36: TEM images of sample SnGR01 (900 mg Sn, 100 mg graphite flakes, 12 h, 2 mm balls, 400 rpm).

The smallest nanoparticles observed in samples of tin ground with graphite, were slightly larger than those in samples ground with GO under the same conditions. This point had to be verified with an experimental technique with a more global view of the sample, such as SAXS.

Sample SnGO06, shown in Figure 2.37, was prepared by grinding pieces of the pre-mixed tin and GO composite film. It was ground for 23 h, using 10 mm balls, with a rotation speed of 400 rpm and then for another hour using 2 mm balls, with a rotation speed of 600 rpm. While once more the smallest particles didn't stay on the TEM grid, the pieces of material observed were bigger than expected. It appears that the incorporation of tin between the sheets of GO resulted in a reinforced structure, something also observed at the macroscale, when cutting the film. Despite that, a closer inspection of the aggregates (Fig. 2.37b) revealed that they contained large numbers of tin nanoparticles, ranging in size from 4.5 to 20 nm.

While in itself this finding was interesting, it was decided to keep the two materials separate before grinding, to simplify comparisons.

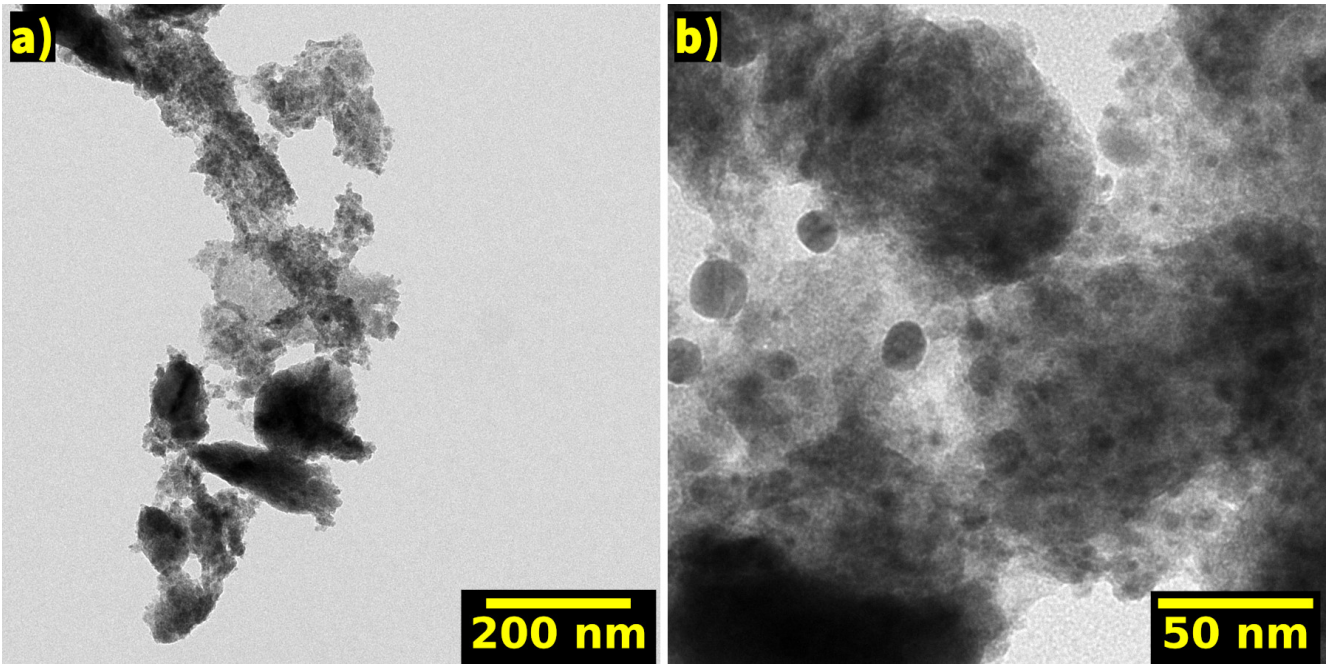

Figure 2.37: TEM images of SnGO06, prepared by milling films of pre-mixed GO and Sn.

Even though we were able to draw some conclusions about all our samples, for the reasons mentioned before (*i.e.* NPs melting under the electron beam and getting rinsed away during grid preparation), we could not get images representative or the samples and more importantly, we could not get size distributions for them.

At that point, it was suggested to embed the samples in epoxy resin, so as to keep all the particles in place. We could not repeat the analysis of all the samples we had already studied, so we decided to target samples we considered the most well-ground, based on the data we had so far, namely 3 g samples ground for 22 + 2 h and 23 + 1 h. We also selected samples that had been ground for less time (8 h and 12 h), to see if any differences would be apparent.

Unfortunately, neither that technique proved suitable for our polydisperse samples. The particles were packed together as the cuts were made, aggregating the samples even more. The addition of a thick carbon layer (the resin) decreased the contrast and as a result the smaller metal nanoparticles or the graphene oxide nanoribbons observed before, were no

longer distinguishable. For these reasons it was impossible to get a particle count which would have allowed to calculate the size distribution in the samples. However, it was possible to determine the upper bound of the particle size distribution in the samples examined, with a higher degree of confidence.

For instance, after closely examining hundreds of particles in tens of slices, it was concluded that the largest particles in sample SnGO08 (Figure 2.38) did not exceed 200 nm in size. At low magnifications (Figure 2.38a), the sample appears rather dense and gives the

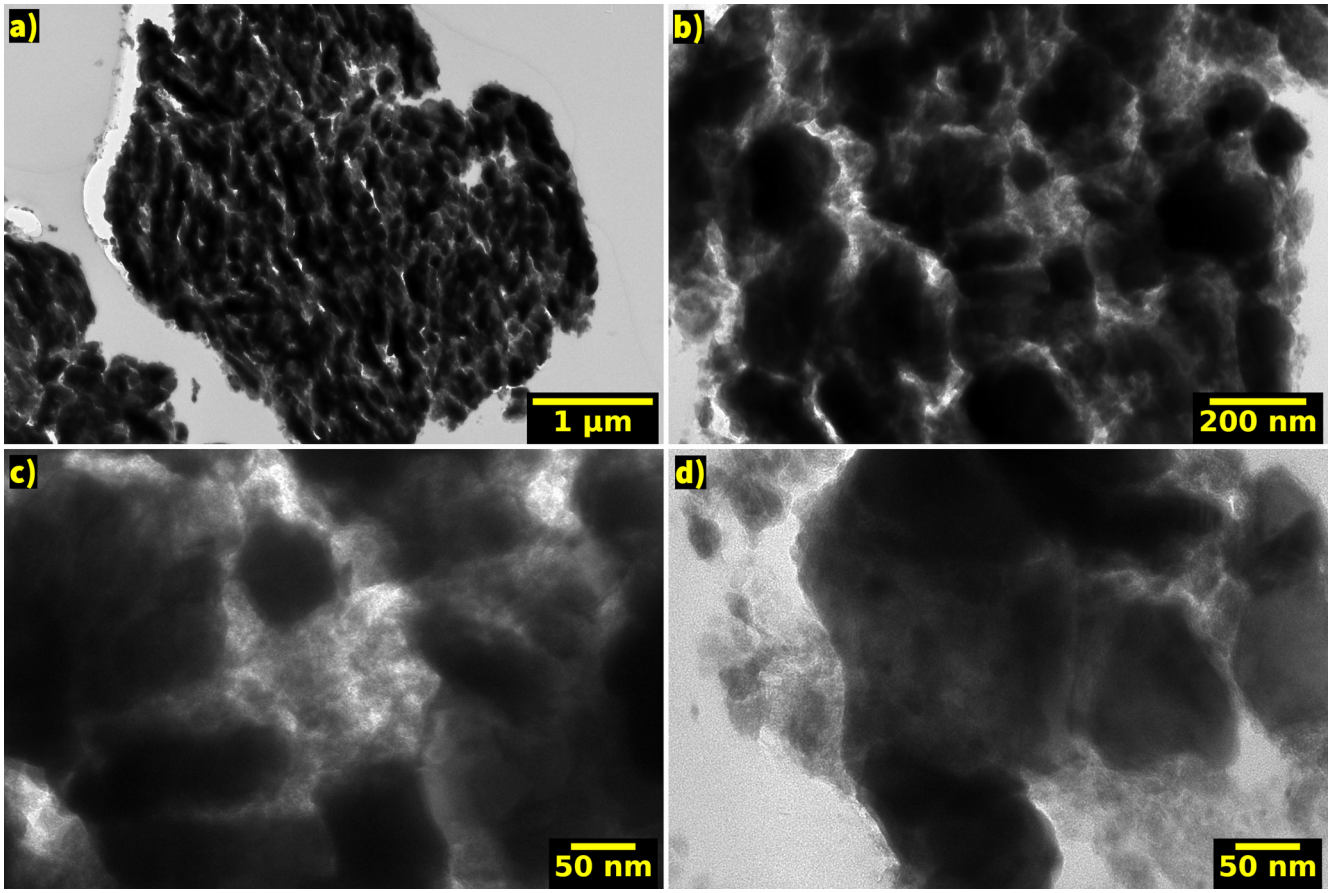

Figure 2.38: TEM images of sample SnGO08 (2700 mg Sn, 300 mg GO; 22 h, 10 mm, 400 rpm, followed by 2 h, 2 mm, 600 rpm) embedded in resin.

impression that it contains µm-sized particles. At higher magnifications it is revealed that these are actually aggregates of smaller particles and at times, even some very small (< 25 nm) particles are visible (Figure 2.38d). However, a comparison with sample SnGO07 was not feasible; the two samples appeared identical at the observable level of detail. Again, no particles larger than 200 nm were discerned, but we could not estimate if there were more or

less of them in each sample. Any other differences were too small to be noticed.

One of the other samples examined, SnGO04, with Sn and GO milled for 12 h at 400 rpm with 10 mm balls is presented in Figure 2.39 for the sake of comparison. At low magnification (images a and b), the sample appears more dense compared to the one shown above. In those same images, some pieces of material can be seen protruding from the sample, well above the other particles. Their observable dimension reaches up to 2.5 µm in some instances. Based on their flat shape, they appear to be fragments of something platelet-like and so they are very likely to have been ground off from the fused particles observed

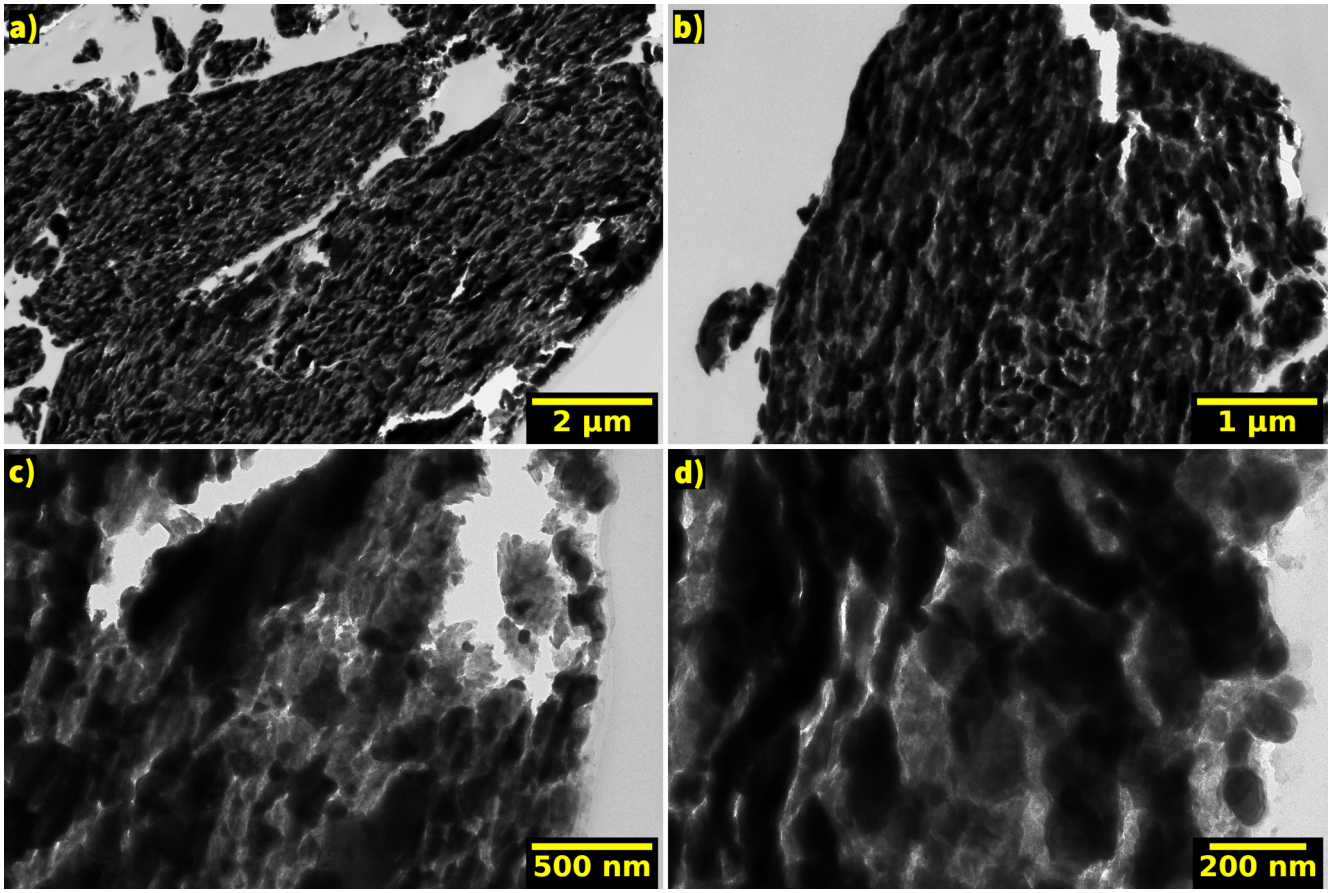

Figure 2.39: TEM images of sample SnGO04, ground for 12 h with 10 mm balls at 400 rpm.

after 2 h of milling. Again, at higher magnification (images c and d) aggregates of particles of every size can be seen. The big fragments render observations more difficult, but still, some nanoparticles in a range of sizes down to ~10 nm could be seen along the edges of the less occupied areas between the sample and the resin.

Experimental details. *Sample preparation, sample grids and operating conditions were the same as in section 1.5.2. For the encapsulation of samples in a resin, a quantity of sample was added to capsule-shaped molds filled with Agar 100 epoxy resin (purchased from Agar Scientific Ltd). Once the solids had precipitated, the resin was polymerized/cured at 70°C for two days. When the resin had fully solidified, it was cut in 70-nm-thin sections using a Leica Ultracut UCT ultramicrotome apparatus. These sections were then transferred onto TEM grids, to be studied under the transmission electron microscope.*

2.3.2. Small-angle X-Ray Scattering

The nanometric organization of the samples of nanoparticles was examined via small-angle X-Ray scattering, which is a characterization technique that enables the study of the structural properties of materials, typically in the scale of 1-100 nm. The basic principles of the technique are reported in Appendix D.

Typical diffractograms are displayed in Figure 2.40. Several regions can be distinguished: a) 10^{-3} - ~10^{-2} $Å^{-1}$, b) ~10^{-2} - ~10^{-1} $Å^{-1}$, c) above $2 \cdot 10^{-1}$ $Å^{-1}$. While these zones appear similar, the exact point at which the slope changes, differs between samples. The value of the slope at lower q values, at intermediate q values and the distance at which the slope changes in each sample are reported in the tables as “slope 1”, “slope 2” and “crossover distance”, respectively. “Intensity” refers to the measured intensity of the (200) plane at 30.7°. The scattering vector q has reciprocal space dimensions which can be converted to real-world dimensions d, via $d = \pi/q$. The results of the SAXS analysis are summarized in Table 2.8 for samples of Sn co-milled with graphene oxide and in Table 2.9 for those co-milled with graphite.

The first region, 10^{-3} – ~10^{-2} $Å^{-1}$, can hence be linked to the aggregates of nanoparticles within GO or graphite sheets. The slope, roughly equal to -2.5 in log-log scale, does not give much detail on the form and distribution of the aggregates. Nevertheless, the absence of

clear form factor confirms their polydispersity. The interesting point is the crossover between the first and the second region, that gives information on their size. For GO samples, it spans from 400 Å to 800 Å approximately, though most of the ball milling conditions yield aggregates of 600 Å. For graphite samples, the mean size of the aggregates is much smaller in most cases, as it spans from 100 to 500 Å approximately. If one compares these sizes to the TEM images in section 2.3.1, it appears that the scattering objects are not the same in both cases: in GO samples, it is the dense aggregates of Sn nanoparticles within larger and looser aggregates, while for graphite, it is the biggest tin nanoparticles (scattering techniques are particularly sensitive to large size objects).

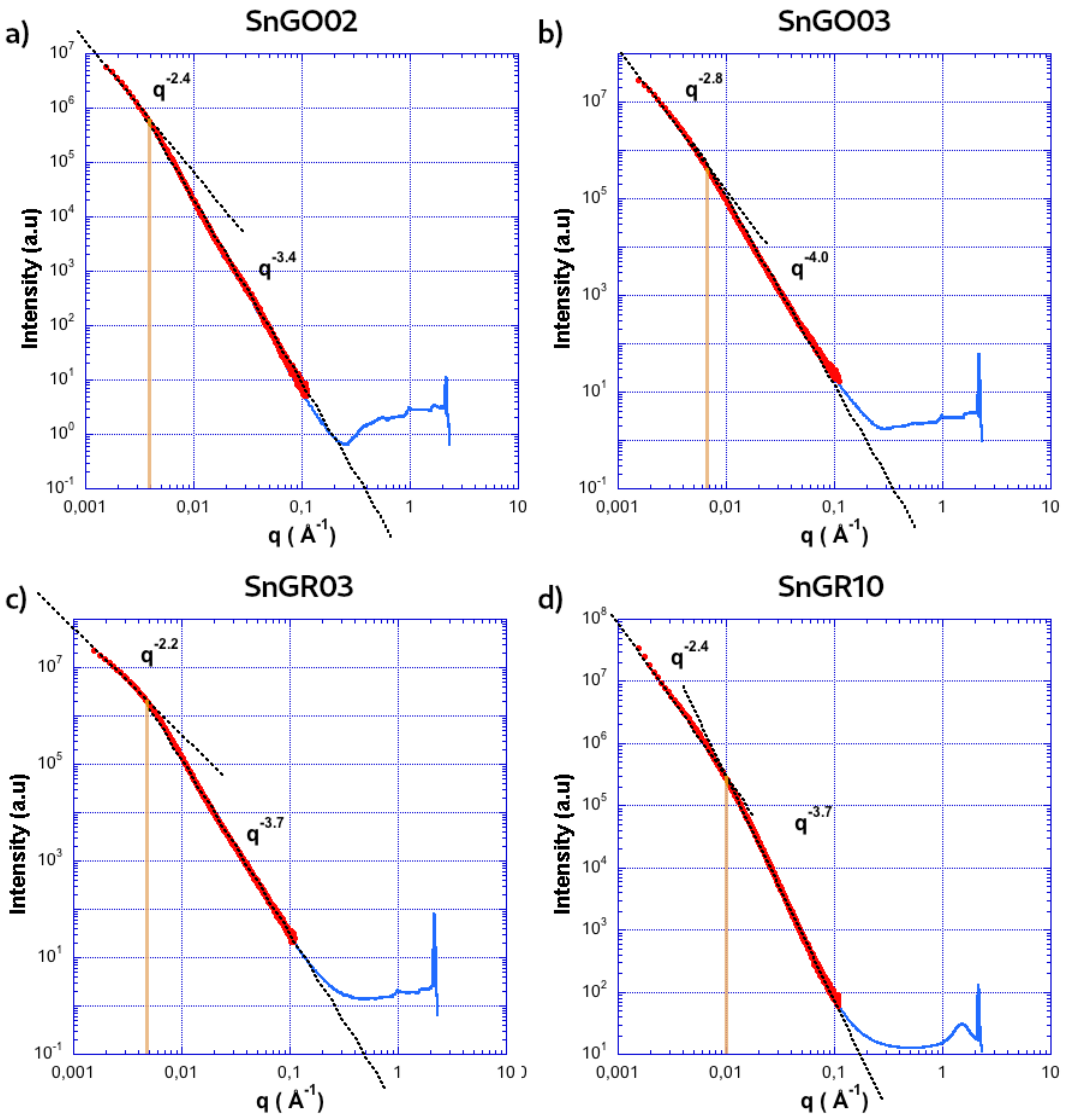

Figure 2.40: Intensity - scattering vector plots (logarithmic scales) of samples of Sn co-milled with graphene oxide (a, b) and graphite (c, d). The orange lines denote the crossover distance. The spike after q=2 is the diffraction signal from β-Sn.

Table 2.8: Sn-GO co-milled samples with corresponding grinding parameters and data from SAXS measurements.

sample name	Sn (mg)	GO (mg)	total solids (mg)	ball ⌀ (mm)	rpm	time (h)	slope 1	slope 2	crossover distance (Å)	intensity (a.u.)	crystallite size (nm)
SnGO01	900	100	1000	10	400	12	-2.2	-3.7	630	58	28.3
SnGO02	900	100	1000	10	400	24	-2.4	-3.4	630	11	26.2
SnGO03	900	100	1000	2	600	6	-2.0	-4.0	400	60	27.7
SnGO04	2700	300	3000	10	400	12	-2.7	-3.7	520	48	22.2
SnGO05	2700	300	3000	2	400	12	-2.7	-3.8	520	12	26.6
SnGO06	2700	300	3000	10 2	400 600	23 1	-2.6	-3.7	800	120	24.8
SnGO07	2700	300	3000	10 2	400 600	23 1	-3.0	-3.7	630	115	26.0
SnGO08	2700	300	3000	10 2	400 600	22 2	-2.9	-3.7	630	15	25.0

Table 2.9: Sn-graphite co-milled samples with corresponding grinding parameters and data from SAXS measurements.

sample name	Sn (mg)	graphite (mg)	total solids (mg)	ball ⌀ (mm)	rpm	time (h)	slope 1	slope 2	crossover distance (Å)	intensity (a.u.)	crystallite size (nm)
SnGR01	900	100	1000	2	400	12	-2.2	-3.9	520	105	28.7
SnGR02	900	100	1000	2	400	16	-2.7	-3.7	315	36	18.8
SnGR03	900	100	1000	2	600	6	-2.2	-3.7	520	78	26.0
SnGR04	2700	300	3000	2	600	6	-2.8	-3.7	160	23	24.1
SnGR05	2700	300	3000	2	600	8	-2.8	-3.9	100	17	25.4
SnGR06	2700	300	3000	2	600	12	-2.6	-3.8	315	11	23.3
SnGR07	2700	300	3000	2	600	20	-2.6	-4.0	800	85	35.7
SnGR08	2700	300	3000	10 2	400 600	12 12	-2.6	-4.0	160	7	21.1
SnGR09	2700	300	3000	10 2	400 600	18 6	-2.4	-3.7	160	600	21.2
SnGR10	2700	300	3000	10 2	400 600	23 1	-2.4	-3.7	450	130	19.1
SnGR11	1800	200	2000	10 2	400 600	23 1	-2.2	-3.9	160	26	24.0
SnGR12	900	100	1000	10 2	400 600	23 1	-2.5	-3.7	350	95	24.6

In the second zone, the slope in log-log scale is or approaches the value of -4, characteristic of Porod's law[100], which predicts that the scattering intensity from flat surfaces is proportional to q^{-4}, $I(q) \sim Sq^{-4}$, with S the surface area of the particles. Two important points arise from this q^{-4} dependence. First, it shows that the scattering object (i.e. the sample at the probed scale) is dense from the point of view of the scatterers, *i.e.* Sn nanoparticles. Second, the surface of the aggregates is relatively smooth with some rugosity with respect to size of the scattering object (slope < -4).

The third zone, observed using the "large angles" configuration, signals up to a 2θ angle of ~35° were recorded. In this range lie also the strongest diffraction signals of β-Sn; its main diffraction peak from the (200) family of planes, at 2θ = 30.7° and that of the (101) family, at 2θ = 32.1°. The recorded signal stops right after the first two diffraction peaks of β-Sn, which are seen as a spike in intensity at the end of the log-log plots of Figure 2.40. and magnified in Figure 2.41. This q range allowed us to get a comparative estimate of the number of the coherent crystalline domains in each sample, tied directly to the measured intensity, as well as the average crystallite size, as calculated through the Scherrer equation.

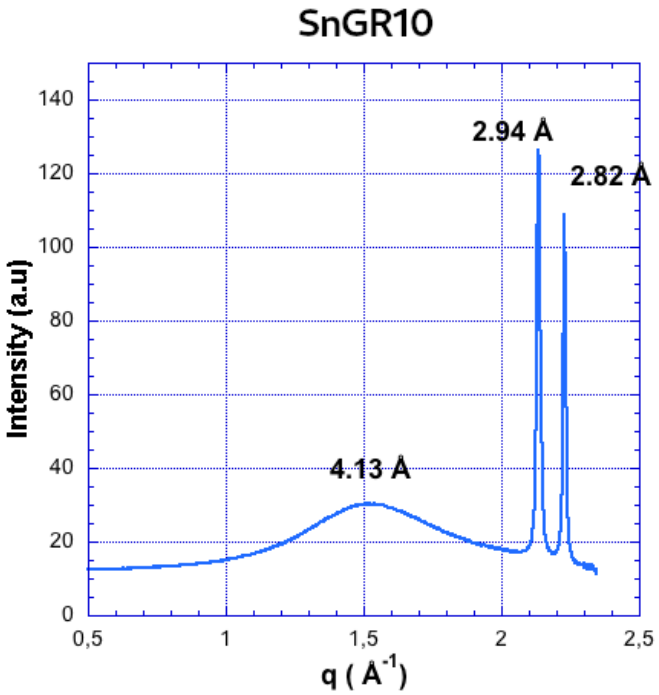

Figure 2.41: Diffraction signals from graphite and tin in sample SnGR10.

Despite part of the difference in intensity between samples could be the experimental shortcomings (*i.e.* variable capillary tube width and sample packing) it could indicate the amorphization of a larger or smaller fraction of the metallic nanoparticles. It has already been stated that during ball milling, some particles might be overground. If they become sufficiently small, they will no longer produce a detectable signal in either scattering or diffraction. As a final note, a small, broad peak found in some samples, mainly samples of tin and graphite, immediately left to the peaks of tin, is the (002) reflection of graphite. It is clearly visible in the plot of Figure 2.40d and shown magnified in Figure 2.41.

The calculation of the crystallite size has been performed using the Scherrer equation. Of course, with the samples being polydisperse and prepared by grinding, the calculated size refers to the average of all the particles in a sample, excluding particles too small to be detected, amorphous particles and particles belonging to populations with too small a volume fraction in each sample. This value carries no information about the width of the size distribution in a sample, so a sample may present a small mean crystallite size, but still contain very large particles and vice versa. We attempted to correlate these mean sizes with the grinding parameters that were varied in the course of our experiments, trying to draw conclusions about the milling process. The difference between the crystallite size and the size of the scattering Sn particles previously determined using the cross-over may indicate that the Sn particles are polycrystalline in graphite samples. This should be confirmed by HRTEM. We grouped together samples that shared some parameters and compared them with regard to the calculated crystallite size. Some of these comparisons are presented below. It should be noted, that any conclusions pertain to the specific system of grinder and materials with their initial sizes and cannot be expected to apply as they are to different setups.

In Figure 2.42, the three samples (SnGR10, SnGR11, SnGR12) differ only in the amount of solids in the grinding bowl. They were all ground for 23 h using 10 mm balls, followed by 1 h with 2 mm balls. It appears that as the solid mass increases, the mean crystallite size gets

smaller, also observed in samples with GO. This can be attributed to self attrition, with the coarser part of the solids grinding itself and the smaller fractions in the course of milling.

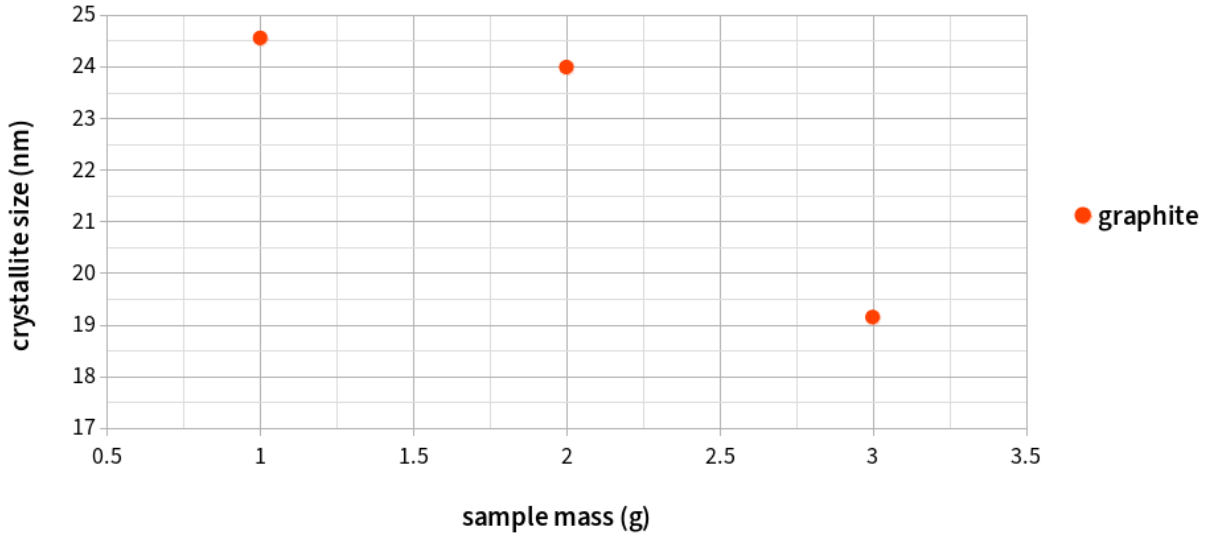

Figure 2.42: Sn-graphite samples co-milled for 23 h at 400 rpm with 10 mm balls, then 1 h at 600 rpm with 2 mm balls.

Grouped together in Figure 2.43 are graphite samples (SnGR01-SnGR07) that were ground with a single ball size (2 mm), for different amounts of time. The two bubble sizes in the plot refer to grinding at either 400 rpm (smaller bubbles) or 600 rpm (larger bubbles). All the samples we prepared had crystallite sizes in the range of 19-29 nm. Sample SnGR07 was the

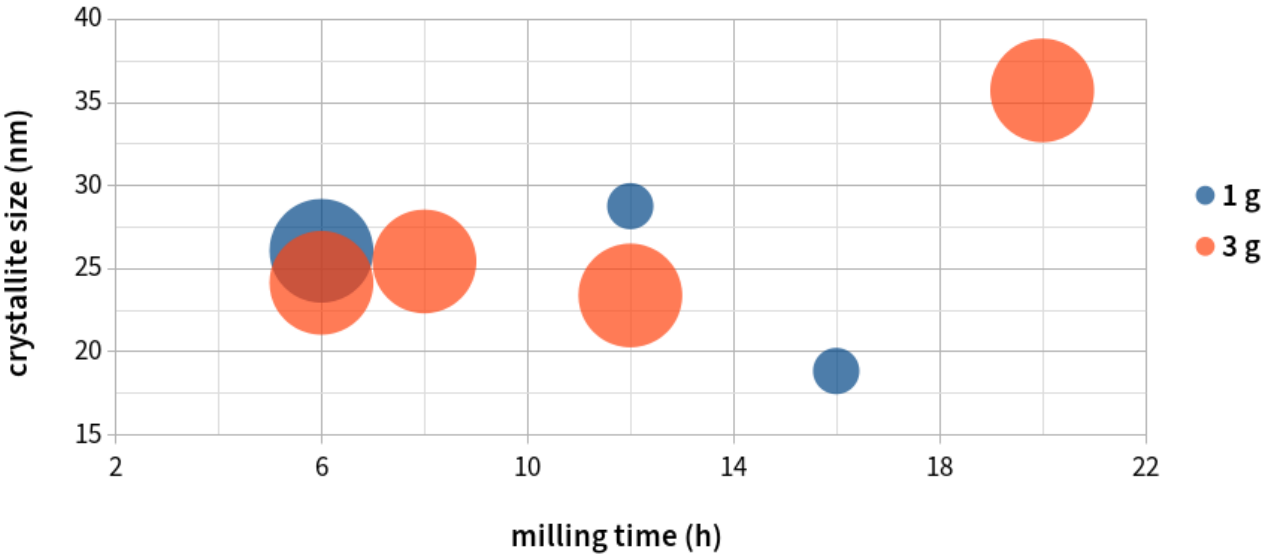

Figure 2.43: Co-milled Sn-graphite samples. The grinding speed is represented by bubble size: 400 rpm (small bubbles) or 600 rpm (big bubbles).

only exception, with a crystallite size of 35.7 nm. Since this figure does not follow the trend exhibited by the other samples, the result has to dismissed as an experimental error. The other samples with a solid mass fraction of 3 g, are in accordance to the general points of the laws describing milling (sample SnGR05, ground for 8 h is slightly off, but still close), *i.e.* that as time and so energy input increased, the crystallite size decreases. However, the difference in the trend line after 6 h is less than 1 nm, which could hint that grinding with the small balls and a high mass fraction of solids is not very effective. For a mass fraction of 1 g (samples SnGR01 – SnGR03), we can observe that a speed increase of 200 rpm (from 400 to 600 rpm) can shave off more than 6 h of milling. Samples SnGR01 and SnGR06 differ in both grinding speed and solid mass fraction, but they were milled for the same amount of time. Their difference in size is a little over 5 nm, which could be due both to an effect of self attrition and higher energy input (faster rotation and higher mass).

In general, the same conclusions hold true for the samples ground with graphene oxide. There is an effect of self attrition that leads to smaller average crystallite sizes when the mass fraction of GO in the bowls is higher. Even though it is difficult to compare the energy expenditure when a sample is ground with 2 mm balls at 600 rpm and with 10 mm balls at 400 rpm, it appears that for milling times at least up to 12 hours, the crystallite size is always smaller in the samples milled with the fewer, but heavier 10 mm balls. When comparing samples SnGO07 and SnGO08, ground for 23 h at 400 rpm with 10 mm balls, followed by 1 h at 600 rpm with 2 mm balls and 22 h at 400 rpm with 10 mm balls, followed by 2 h at 600 rpm with 2 mm balls, we observe that the latter sample exhibits an average crystallite size smaller by 1 nm and an 8-fold weaker diffraction intensity. While not very safe from a statistical point of view, it wouldn't seem fallacious to infer that the efficiency of grinding with the larger balls has significantly decreased before the 22 hour mark and that the average particle size of the sample is such, that it is more efficient to continue the size reduction with the smaller balls. Besides, that is what happens in continuous flow, industrial ball mills with segments: each segment holds grinding balls of progressively smaller size and the sample moves to the next segment once it has been reduced to a sufficiently small size. The ball

milling yields different composite morphology with graphene and graphite: dense aggregates of small Sn particles within looser and larger objects for graphene, larger polycrystalline Sn particles embedded in the carbon sheets for graphite.

Experimental details. *SAXS experiments were conducted at the SWING beamline of the SOLEIL synchrotron (Orsay, France), using a fixed energy of 16 keV. The measurements were carried out in two configurations: "small angles", corresponding to a sample-detector distance of 0.5 m and "large angles", with the distance set to 6.2 m. The samples were compacted and then sealed in borosilicate glass capillary tubes, with an external diameter of 1.5 mm and wall thickness of 0.1 mm. The capillary tubes were kept under an argon atmosphere until they were sealed, so as to avoid any oxidation from exposure to air. Owing to variations in capillary tube thickness it is not possible to have absolute intensity (cm^{-1}) and all the diffraction curves are in arbitrary units. Nevertheless, all the curves are normalized by their X-ray transmission.*

2.3.3. Polycrystalline X-Ray Diffraction

In order to verify that the nanoparticles were indeed metallic tin (β-Sn) their X-ray diffraction pattern was examined and compared to that of the micrometric powder, as well as to the pattern of bulk metallic tin. The sample was loaded into a special airtight sample holder, to avoid the exposure of the nanoparticles to atmospheric air. A slot on the upper half of the sample holder, covered with a polymer film allowed the X-rays to pass through the sample.

Indeed, as it is shown in Figure 2.44, there were no peaks in the diffractogram indicative of the formation of oxides, which of course, would not rule out the formation of a thin layer of amorphous oxide on the surface of the nanoparticles. However, we were able to verify that the nanoparticles retained their crystallinity. The presence of the polymeric window of the sample holder does not suffice to explain the depression of the intensity of the diffraction peaks, given that the measurement settings between the two samples were kept the same. We assume that a fraction of the material has been reduced to sizes not detectable by the instrument, effectively lessening the number of crystallites contributing to diffraction.

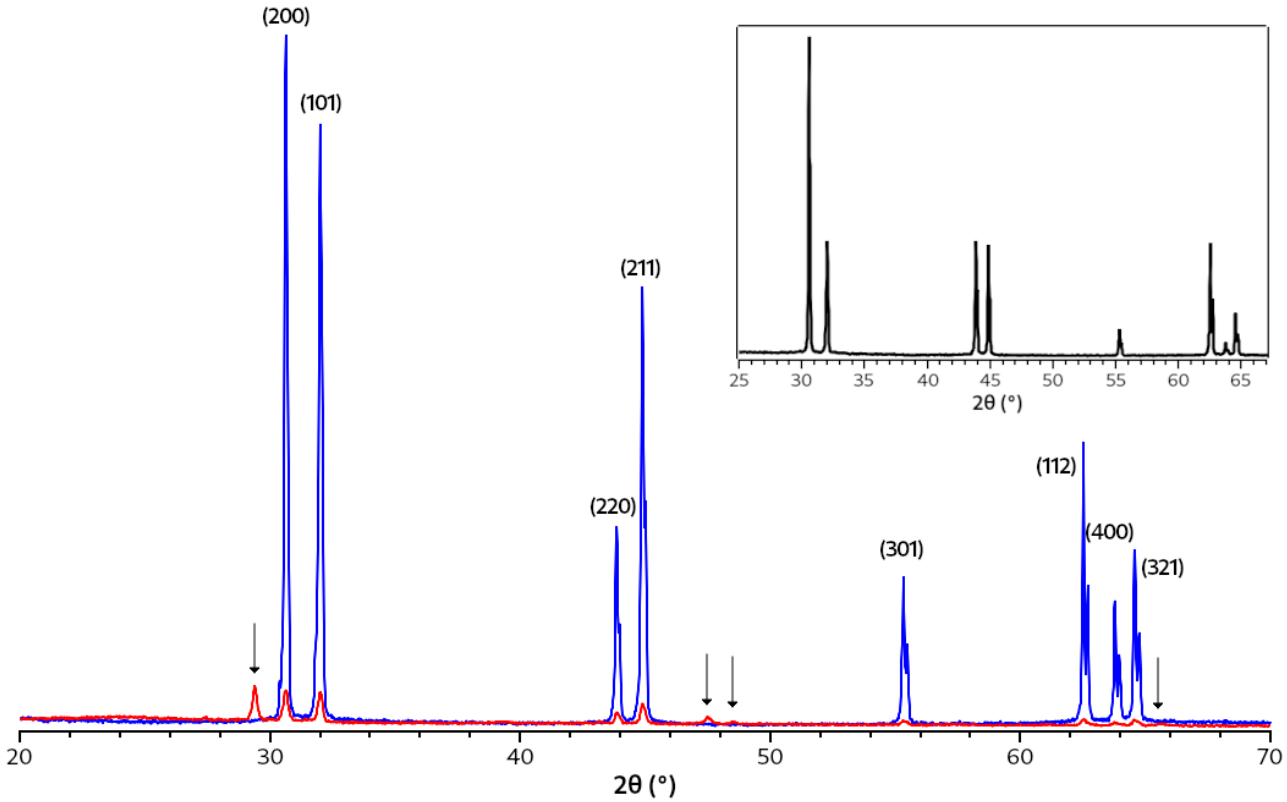

Figure 2.44: Diffraction patterns of the commercial micrometric tin powder (blue), of sample SnGO07 (red, sealed in an airtight sample holder) and bulk metallic β-Sn (inset). The arrows denote the diffraction peaks of the polymeric film on the sample holder. Peaks beyond ~40° appear split because of poor filtering of the Cu K_β radiation.

In the course of our experiments, a quantity of a sample prepared in the same manner as SnGO08 (3g, 22 + 2 h) was left exposed in air for 3.5 months. Assuming that it would have been oxidized, it was decided to examine it through X-Ray diffraction, in order to see the extent of the oxidation and which of tin's oxides, SnO or SnO_2, had formed. The diffraction pattern is presented in Figure 2.45. Besides the signals belonging to β-Sn, no other peaks are present in the diffractogram. It appears that the layer of GO does indeed have a protective effect, since it has been shown that pure tin nanoparticles readily oxidize in air[78].

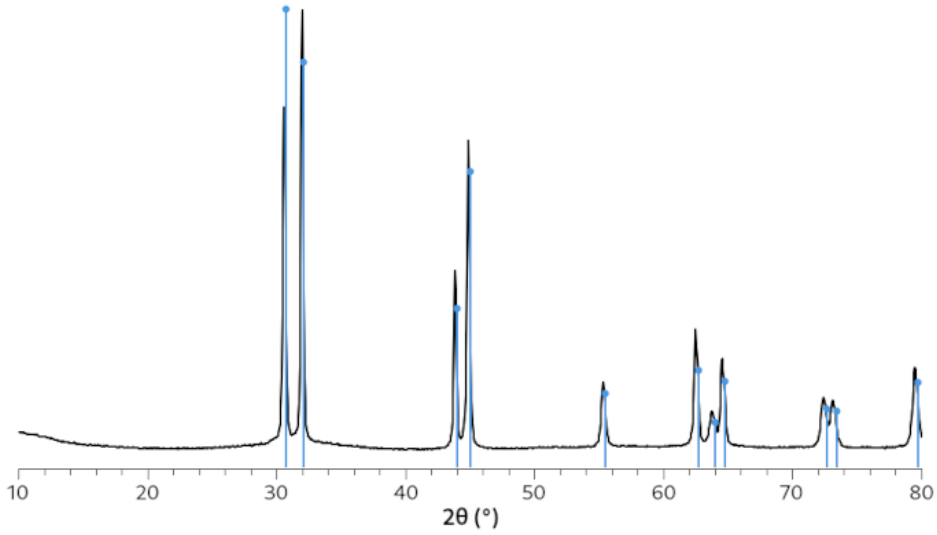

Figure 2.45: Diffraction pattern of a sample of Sn co-milled with GO, left in air for 3.5 months. In blue, the powder diffraction file (PDF) of β-Sn from the ICDD.

Experimental details. *Same as in section 1.5.1.*

2.3.4. X-Ray Photoelectron Spectroscopy

While size reduction processes are rarely connected to chemical transformations, the fact is that ball milling is routinely used in mechanochemical applications. From TEM images of the samples it was apparent that tin was indeed reduced in size and that it was wrapped in sheets of graphene or graphene oxide, but there was also the possibility that some reaction might had taken place between them. In order to verify or refute this supposition, we turned to XPS analysis. Two samples were analyzed, one with co-milled GO and Sn, the other with graphite and Sn. Both were prepared by milling first with 10 mm balls for 22 h at 400 rpm, followed by a 2 h session at 600 rpm with 2 mm balls. The samples were kept in airtight containers filled with Ar gas until the moment of the analysis, when they were exposed to air. They were mounted on a Si sample holder with the help of conductive carbon tape. Survey scan spectra were recorded at 100 eV energy pass. High-resolution spectra were recorded at 20 eV energy pass. All spectra were recorded at a takeoff angle of 45° relative to the sample surface (90° between source and collector).

The graphene-oxide-based films presented earlier had the same chemical composition throughout the material and a layered structure of stacked sheets. Furthermore, because carbon atoms are small and the material is not very dense, the ejected photoelectrons can travel along a longer mean free path, resulting in a greater probing depth of the material. In contrast to that, the polydisperse nanoparticle samples presented a rugged surface to the incoming beam and because tin's atoms are larger and the material denser, the mean free path of the photoelectrons is limited and consequently, so is the probing depth. For these reasons, the results presented here refer to the composition of the surface of the nanoparticles and the bulk of the smallest NPs probed by the beam.

In the survey scans of Figure 2.46 the main recorded signals and the corresponding orbitals have been noted. Orbitals with an angular spatial distribution (*i.e.* all except s orbitals) exhibit spin-orbit splitting and appear as doublets, with each of the two possible states having a different binding energy. The nomenclature used to describe them takes the form kl_i, with k the principal quantum number, l the angular momentum quantum number and j = l + s, where s is the electron spin angular momentum (s = ± ½). Case in point, in the

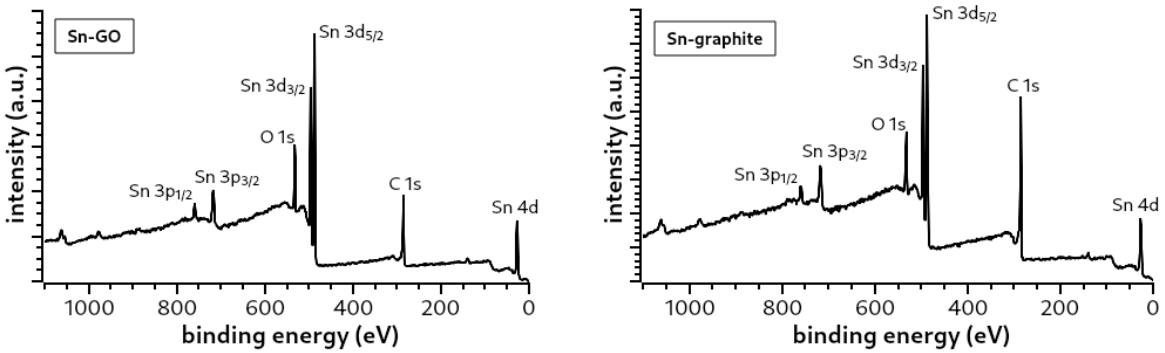

Figure 2.46: Survey scans of co-milled Sn-GO and Sn-graphite nanoparticle samples.

survey scans below, tin's 3p and 3d orbitals give two contributions each, $3p_{1/2}$, $3p_{3/2}$ and $3d_{3/2}$, $3d_{5/2}$, respectively. The areas of each peak of a doublet have specific areas based on the different spin combinations that produce the total i. It follows that for any given orbital (p, d, f) the ratios of the areas are fixed, regardless of the nucleus probed. In the case of the $3d_{3/2}$ and $3d_{5/2}$ orbitals, that ratio is 2:3.

Both scans appear rather similar, with the only notable difference being the intensity of the signal from the C 1s orbital, which is higher in the sample of Sn with graphite. Both samples have a comparable oxygen content, with that of the Sn-GO sample being higher. The source of oxygen is obvious in the case of graphene oxide, but not so much for graphite. It was posited that a certain amount of oxidation occurred during handling; taking into account the stability of the particles in air, revealed by X-Ray diffraction, we tend to conclude that this may contribute to a lesser extent, if at all, and that the oxygen comes primarily from molecules trapped between the graphite sheets prior to milling.

2.3.4.1 Sn – GO

High-resolution scans of the Sn $3d_{5/2}$, C 1s and O 1s orbitals found in the sample are presented in Figure 2.47. Sn $3d_{3/2}$ and $3d_{5/2}$ yield the same information, so the strongest signal of the $3d_{5/2}$ part of the doublet was chosen for the analysis.

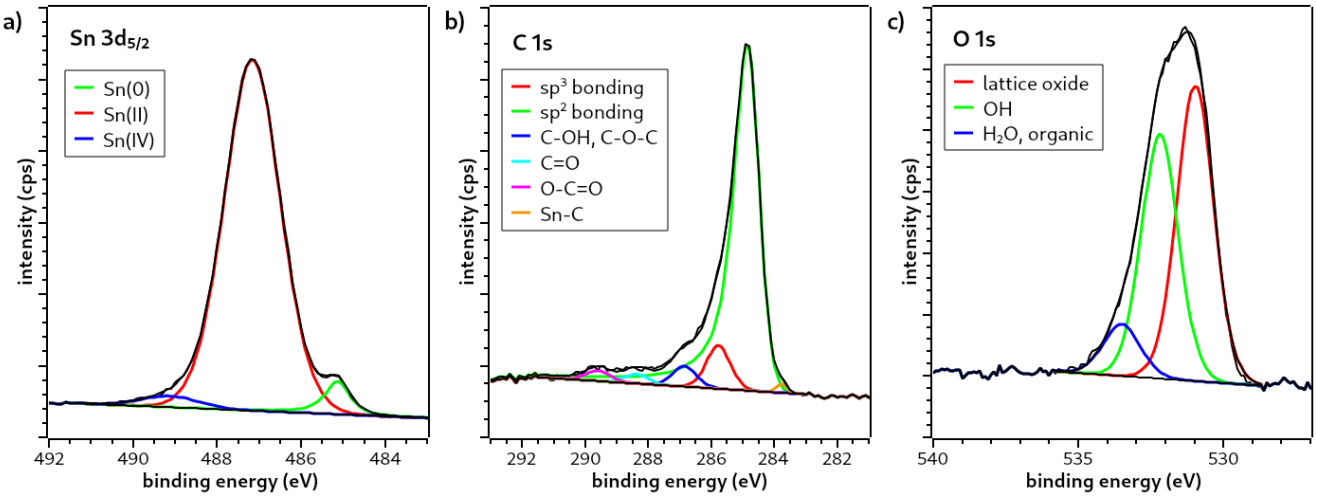

Figure 2.47: Deconvoluted XP spectra of a) Sn $3d_{5/2}$, b) C 1s and c) O 1s signals of the Sn-GO sample (co-milled with 10 mm balls at 400 rpm for 22 h, then for 2 h with 2 mm balls at 600 rpm).

The Sn $3d_{5/2}$ peak (Fig. 2.47a) appears to consist of two components, the major one centered at a binding energy of 487.2 eV, belonging to Sn(II) and the smaller one centered at 485.1 eV, belonging to metallic tin – Sn(0). Deconvolution of the spectrum gives a third component, centered at 489.1 eV, attributed to Sn(IV), albeit with too small a contribution to

the signal. Clearly, the part of the sample probed by the beam is mainly oxidized tin.

The C 1s peak (Fig. 2.47b), centered at 284.9 eV resembles a lot that of reduced graphene oxide presented earlier, both in terms of shape as well as components, after deconvolution. This and the calculated composition confirmed that during the course of milling GO does get reduced. The spectrum was deconvoluted into six components: atoms in carboxylates at 289.6 eV, carbonyl carbons at 288.4 eV, carbon atoms in C-O bonds such as C-OH and C-O-C at 286.9 eV, atoms in sp^3 C-C bonds at 285.8 eV, atoms in sp^2 C=C bonds at 284.9 eV and the final component at 283.8 eV attributed to Sn-C bonds.

Deconvolution of the O 1s peak (Fig. 2.47c), centered at a binding energy of 531.2 eV, gave three components: oxygen atoms part of lattice oxides at 531.0 eV, atoms belonging to terminal hydroxides, such as those found on metal surface defects at 532.2 eV and finally oxygen atoms being part of organic functional groups (or water) at 533.5 eV. The presence of metal oxides in the sample rendered impossible the attribution of the oxygen content of that last component to specific functional groups. The detailed breakdown of atomic ratios is presented in Table 2.10:

Table 2.10: Atomic percentages of Sn, O and C atoms in the Sn-GO co-milled sample, participating in different types of chemical bonds and their corresponding binding energies.

species		binding energy (eV)	At%
Sn $3d_{5/2}$	Sn(IV)	489.1	0.53
	Sn(II)	487.2	16.5
	Sn(0)	485.1	0.9
O 1s	Organic O, H_2O	533.5	2.4
	OH	532.2	11.3
	Lattice oxide	531.0	13.7
C 1s	O-C=O	289.6	1.3
	C=O	288.4	1.2
	C-OH, C-O-C	286.9	2.6
	C sp^3 bonding	285.8	5.5
	C sp^2 bonding	284.9	43.5
	Sn-C	283.8	0.5

Looking at these results, it is confirmed beyond any doubt that a redox reaction takes place between GO and Sn during milling, with the majority of the oxygen atoms getting transferred to tin, forming SnO while the composition of GO comes really close to that of thermally reduced graphene oxide. The component of the Sn $3d_{5/2}$ signal attributed to Sn(IV) appears at a level that could be an artifact of the analysis. In the scientific literature we were unable to find a single reference to tin carbide. Examples of compounds where carbon is bound to tin always contain at least a third type of atom linked to the tin atoms. For this reason, we have low confidence in the existence of Sn-C bonds, unless they are part of an oxide, *i.e.* something like C-Sn-O.

2.3.4.2 Sn – graphite

High-resolution scans of the Sn $3d_{5/2}$, C 1s and O 1s orbitals of the co-milled Sn – graphite sample are shown in Figure 2.48:

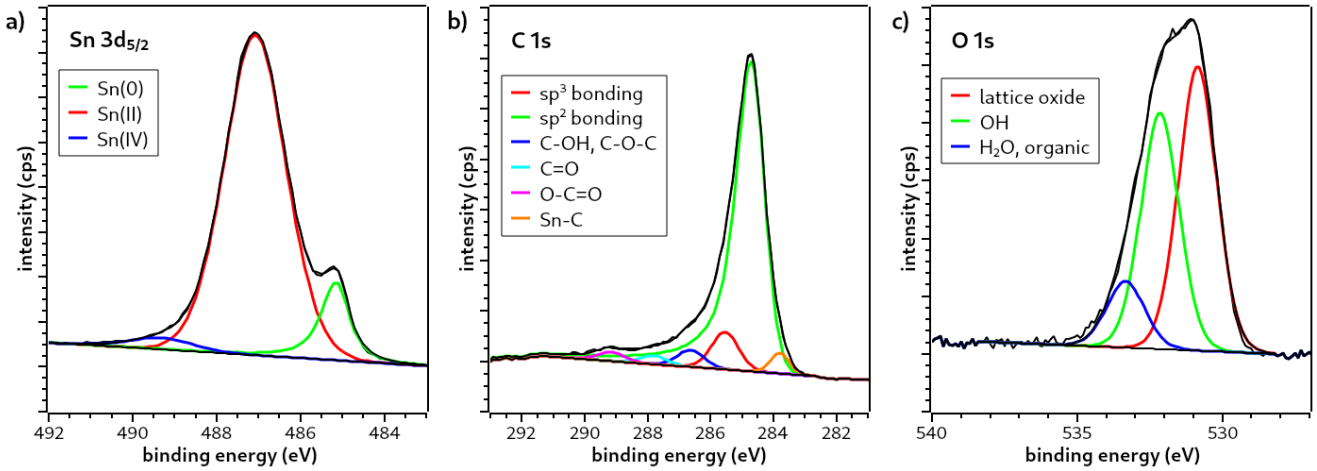

Figure 2.48: Deconvoluted XP spectra of a) Sn 3d5/2, b) C 1s and c) O 1s signals of the Sn-graphite sample (co-milled with 10 mm balls at 400 rpm for 22 h, then for 2 h with 2 mm balls at 600 rpm).

Again, the Sn $3d_{5/2}$ peak (Fig. 2.48a) appears to consist of two components, the major one centered at a binding energy of 487.1 eV, belonging to Sn(II) and the smaller one, which appears stronger than in the Sn-GO sample, centered at 485.1 eV, belonging to metallic tin. Deconvolution of the spectrum gives once more a third component with a small contribution

to the overall signal, centered at 489.3 eV, attributed to Sn(IV). While the X-Ray beam encounters more metallic tin in this sample, it interacts mainly with oxidized tin.

The C 1s peak (Fig. 2.48b), centered at 284.7 eV was deconvoluted to six components, same as before. The content of carbon atoms bound to oxygen appears low, but it is present. The deconvolution of the spectrum and attribution to specific species was as follows: atoms in carboxylates at 289.2 eV, carbonyl carbons at 287.8 eV, carbon atoms participating in C-O bonds like C-OH and C-O-C at 286.6 eV, atoms in sp^3 C-C bonds at 285.5 eV, atoms in sp^2 C=C bonds at 284.7 eV and the sixth component at 283.8 eV attributed to Sn-C bonds.

The O 1s peak (Fig. 2.48c), centered at a binding energy of 531.6 eV, was deconvoluted into three components: oxygen atoms part of lattice oxides at 530.9 eV, oxygen atoms belonging to terminal hydroxides at 532.1 eV and oxygen atoms being part of organic functional groups (or water) at 533.3 eV. The atomic ratios of all three components are lower in this sample.

The composition of the sample is summarized in Table 2.11:

Table 2.11: Atomic percentages of Sn, O and C atoms in the Sn-graphite co-milled sample, participating in different types of chemical bonds and their corresponding binding energies

species		binding energy (eV)	At%
Sn $3d_{5/2}$	Sn(IV)	489.3	0.34
	Sn(II)	487.1	9.8
	Sn(0)	485.1	1.4
O 1s	Organic O, H_2O	533.3	1.6
	OH	532.1	5.6
	Lattice oxide	530.9	6.7
C 1s	O-C=O	289.2	1.4
	C=O	287.8	1.6
	C-OH, C-O-C	286.6	3.2
	C sp^3 bonding	285.5	7.2
	C sp^2 bonding	284.7	58.3
	Sn-C	283.8	2.7

The atomic ratio of carbon appears higher in this sample, which we expected because tin was co-milled with graphite and also because the volume fraction of graphite in the grinding

bowl was higher than that of GO. There is a presence of oxygen both as metal oxide and as part of organic functional groups. This reinforces the hypothesis that the oxidation takes place mainly during milling and not after, so its source most likely is oxygen molecules adsorbed on the materials themselves. As graphite is broken down to smaller fragments, the newly formed edges will react with anything there might be in the vicinity, hence the oxygen-bearing functional groups.

Experimental details. *Same as in section 1.7.3.1.*

2.3.5. Conclusions

We have demonstrated that co-milling tin with either graphene oxide or graphite can be a successful strategy for the production of tin nanoparticles at gram scale. To the best of our knowledge, this had not been tried before. Depending on the intended application, this could be a viable strategy for the size reduction of tin, when a cooled grinder is unavailable, impractical or too costly.

None of the techniques we employed to characterize our samples could give us a full view of the particle size distribution. We considered using dynamic light scattering, but we were unable to find a medium in which the particles could be suspended as they were. However, the combination of SAXS measurements, X-Ray diffraction and microscopy showed a good complementarity, permitting us glimpses of both the whole and the finer details. This allowed us to settle on the eventual milling protocol, consisting of grinding for 22 h with the 10 mm balls at 400 rpm, followed by 2 hours of further “homogenization” with the 2 mm balls at 600 rpm. The resulting product had dimensions that would easily fit in the graphene-based matrix and the graphene (oxide) sheet coating of the particles could prove beneficial in containing the migration of tin during the functioning of an actual battery, without blocking the diffusion of lithium ions towards the nanoparticles.

It is obvious that the end product is not pure tin nanoparticles. The most plausible description would be a tin core inside a thin/amorphous shell of tin oxide, coated in a carbon layer, *i.e.* Sn@SnO@C. However, both tin and tin oxide are active towards lithiation and as mentioned above, the (reduced) graphene oxide layer could prove beneficial to the functioning of a Li-ion battery with these NPs used to increase its capacity. The NPs could be useful in other applications as well, for instance as components of conductive inks[80]. The protection against further oxidation afforded by the carbon layer alleviates any problems related to *e.g.* the storage of the material.

The process can be easily scaled up; milling is a common industrial operation and in fact, it could be performed more efficiently than in our experiments. Comparatively, we were severely limited by the equipment available at our disposal. There were a number of discussions held with colleagues working in the pharmaceutical industry on the subject of ball milling and we were made aware of several ways the process would benefit from its application in an industrial setting. For example, 20 kg of feed with average particle size of 20 μm can be reduced to particles with sizes equal to or below 1 μm in just 5 minutes, when grinding with 0.2 mm balls. For feeds with larger particle sizes, up to a few cm, continuous-flow segmented ball mills can reduce the same 20 kg of material to sub-micron sizes in a little over an hour.

Even at the scale we worked, there remain several facets of the process that could be improved, such as pinpointing the exact moment in time when it would become more efficient to switch from the 10 mm balls to the 2 mm ones. This could lead to more uniform samples, in a shorter amount of time. Cutting the GO films to the requisite size with scissors can hardly be deemed practical; however our alternative was to grind larger pieces of specific dimensions in advance and it would take a separate study to determine at which point it would be optimal to add the Sn powder and also ensure that it would get wrapped in the sheets and not just covered by small fragments of them. Eliminating the oxygen carried over by the materials to the grinding bowls, would also be a significant improvement.

3. Amino-functionalized EMI^+TFSI^-

The last component required for the composite system is the functionalized ionic liquid consisting of the $TFSI^-$ anion and an imidazolium cation, with a short ethyl side-chain and an amino group attached to its extremity. In order to graft the EMI^+ cation onto graphene oxide, the amino group appeared much more versatile compared to other functional groups that have been used for the same purpose, such as trimethoxy silane[101] or phosphonic acid[102], which can only bind to hydroxyl groups. It should be possible for it to react a) with epoxide groups, in a ring-opening reaction[103], b) with carboxyl groups to produce amides[104] and c) with carbonyl groups, yielding imines[105] (Fig. 2.49). The optimal conditions are not the same for these reactions. Epoxide ring-opening can take place under both acidic and basic conditions and requires moderate heating[106]. Amide formation requires heating to high temperatures or prior activation of the carboxyl group[107]. Imine formation necessitates mildly acidic conditions, with precise control of the pH[108]. However, the addition of the amino group presented itself as the most reasonable strategy in order to maximize the amount of grafting under a range of settings. Since an IL with an amine-terminated EMI^+ cation was not commercially available, it would have to be synthesized. To accomplish that,

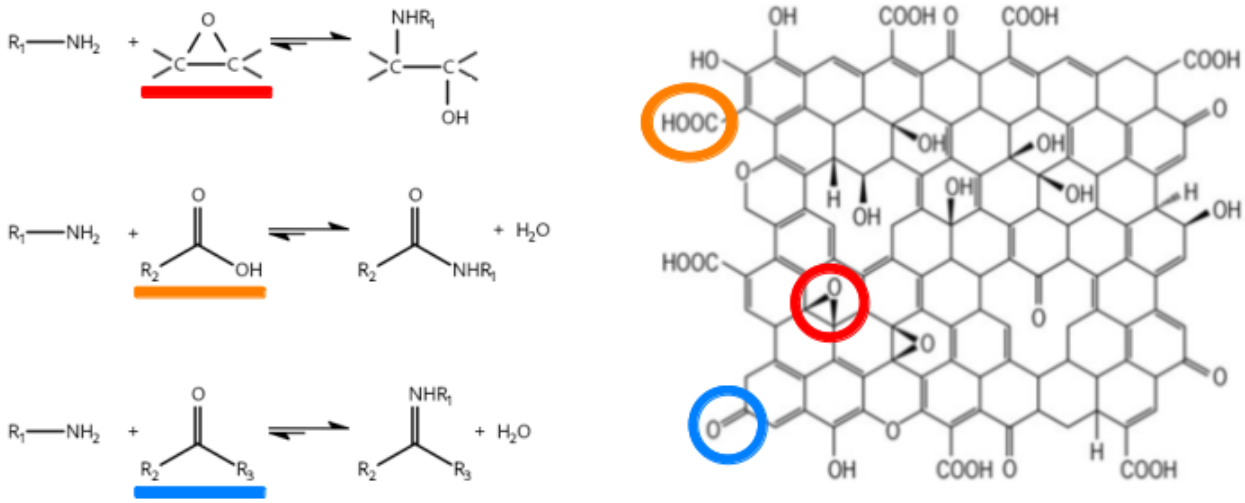

Figure 2.49: Possible grafting targets for amines on graphene oxide and the corresponding reactions.

two different synthetic approaches were tried.

3.1. First synthetic route for the amino-functionalized ionic liquid

The most cited synthesis in the literature, which often involves the grafting of graphene oxide with an imidazolium-based ionic liquid, relies on the N-alkylation of 1-methylimidazole, using 3-bromopropylamine hydrobromide, in an S_N2 reaction[109], according to Fig. 2.50. In most of the published works[103,110–112], the reaction is used to add an aminopropyl side chain to 1-methylimidazole. However, there exist a number of other studies[113–117], claiming the addition of an aminoethyl side chain in a similar fashion, using 2-bromoethylamine hydrobromide. It was decided to replicate the methodologies described in these works, as they proposed a facile and straightforward way to produce the modified EMI^+ cation.

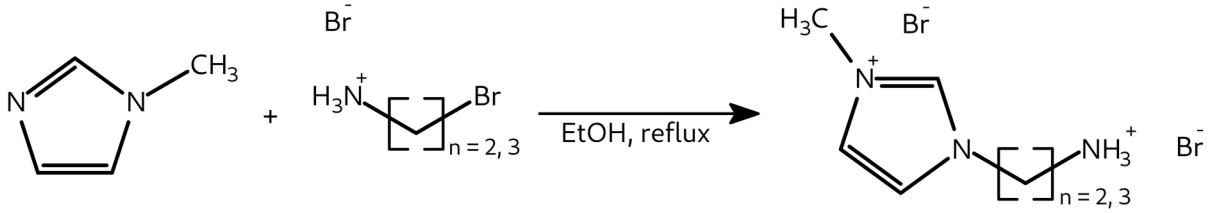

Figure 2.50: The synthesis of 1-(alkyl-n-ammonium hydrobromide)-3-methylimidazolium bromide

Several attempts were made to reproduce the synthesis as reported. The desired ionic liquid could not be obtained. The synthesis was also performed by varying several parameters such as the solvent refluxed (EtOH, CH_3CN), the reaction time (16, 20 and 24 h), the ratio of 2-bromoethylamine hydrobromide to 1-methylimidazole (1:1, 1:2) or controlling the addition of 1-methylimidazole in the course of the reaction. In every case, the result was a mixture of products. It appeared that 2-bromoethylamine may also react with itself, with the amino-functionalized imidazolium, or with 1-methylimidazole. The ^1H NMR spectra contained several methylene groups with different electronic environments, indicating polysubstitution. It should be mentioned that none of the cited works presented a characterization of the synthesized product, and different authors gave widely varying visual

descriptions of it, ranging from “yellow viscous liquid”[116,117] to “white crystalline solid”[113,114]. A more expansive investigation of the literature revealed that the reaction had already been studied in CH_3CN at 80°C for 4 h, leading to products **A** to **D** (Fig. 2.51)[118]. It yielded mostly protonated 1-methylimidazole (**A** in Fig. 2.51), which cannot react further and a mixture of substitution products with side chains of varying lengths – among them, the desired product (**B** in Fig. 2.51) as a minority product, but particularly difficult to isolate, following a simple purification process.

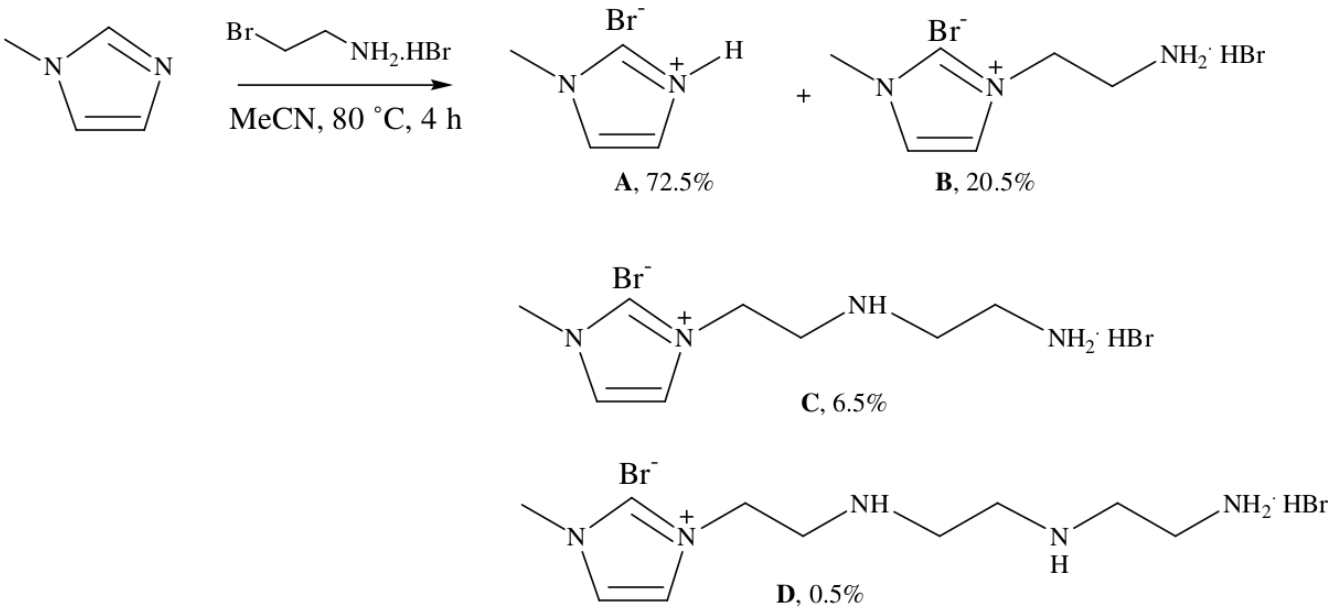

Figure 2.51: Reaction between 1-methylimidazole and 2-bromoethylamine hydrobromide. Reprinted from [118].

Interestingly, in a control experiment, the reaction of 1-methylimidazole with 3-bromopropylamine hydrobromide allowed to synthesize the respective functionalized ionic liquid. This would suggest that electronic effects over the shorter alkyl chain are the driving force behind the different outcomes of the two reactions. Consequently, a new synthetic route had to be considered.

3.2. Revised synthetic route

In order to circumvent the encountered problem during the first synthesis, the choice was made to decompose the preparation into steps. First an ethyl-functionalized imidazolium had to be prepared. Then the amino group could be introduced at the end of the ethyl chain. The precursor could be modified by using symmetric functionalized dihaloalkanes. All the steps of the synthesis we eventually employed are presented in Figure 2.52. First, an S_N2 reaction between 1-methylimidazole and 1,2-dibromoethane produces 1-(2-bromoethyl)-3-methylimidazolium bromide (Fig. 2.52-1). This undergoes another S_N2 reaction with sodium azide, yielding 1-(2-azidoethyl)-3-methylimidazolium bromide (Fig. 2.52-2). Reduction of the azide results in the formation of 1-(2-aminoethyl)-3-methylimidazolium bromide (Fig. 2.52-3). The biggest hurdle that had to be overcome in this synthetic approach was the purification of the products at the end of each step. Ionic liquids

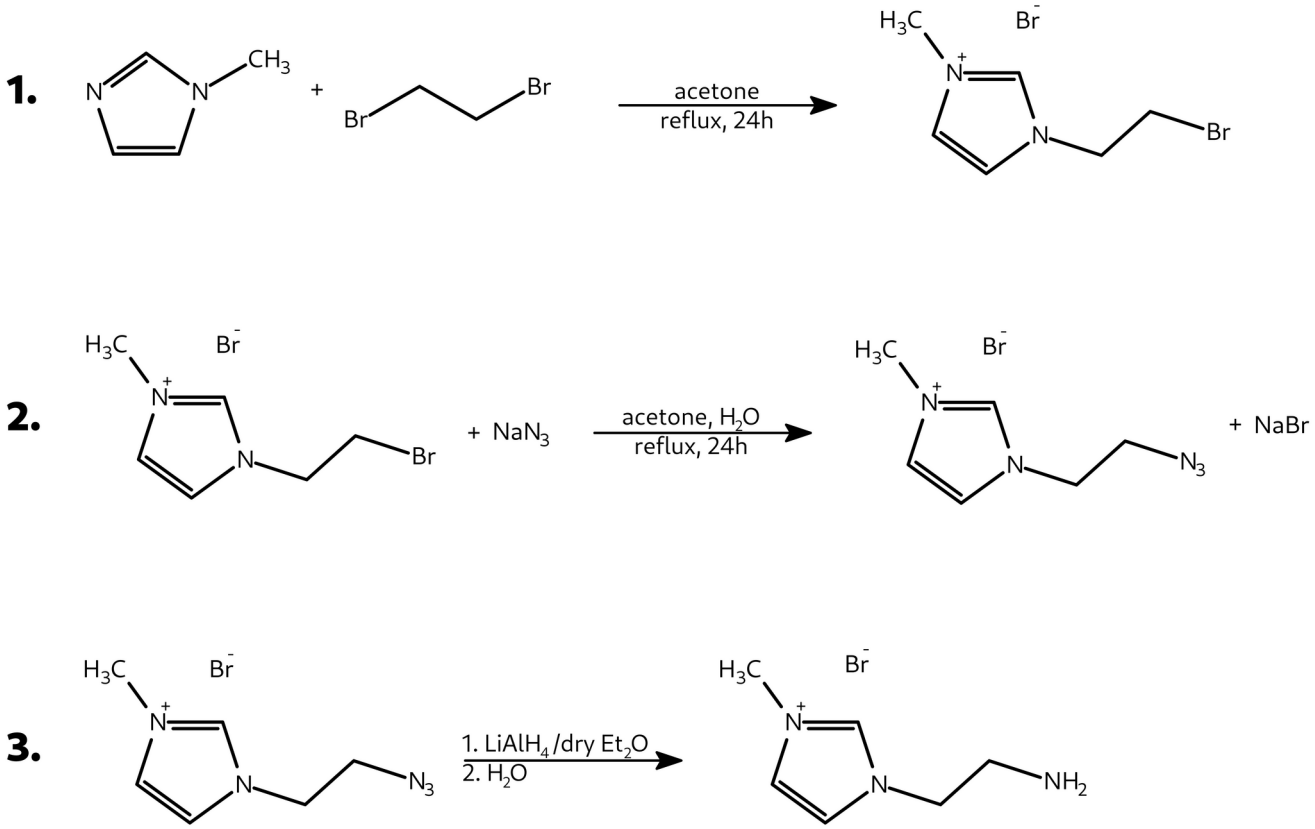

Figure 2.52: The main steps of the new synthetic route for the preparation of 1-(2-aminoethyl)-3-methylimidazolium bromide.

and especially those with short side chains are rather difficult to purify and that difficulty increases with the addition of polar groups.

Here follows an overview and a discussion of the particular details of each step.

The very first step of the synthesis consists of an alkylation of 1-methylimidazole, that follows second-order kinetics. The reaction takes place in refluxed acetone, using three equivalents of 1,2-dibromoethane. However, as the nucleophilic substitution can occur on either end of 1,2-dibromoethane, if all of the equivalents of 1-methylimidazole are added at once, a compound consisting of two methylimidazolium rings joined by an ethyl bridge forms as the major product of the reaction. The slow introduction of 1-methylimidazole by means of a syringe driver works around that problem, hinting that the desired reaction pathway is under kinetic control. The targeted, monosubstituted 1-(2-bromoethyl)-3-methylimidazolium bromide is obtained as a highly hygroscopic solid product. The same synthesis has been reported as taking place at room temperature by reacting 10 equivalents of 1,2-dibromoethane with 1 equivalent of 1-methylimidazole in diethyl ether, for 4 days[119]. This was experimentally verified, suggesting that in those conditions, only the monosubstituted product is obtained, but at lower yields and much longer reaction time.

The second step is a bimolecular nucleophilic substitution reaction of the bromide introduced in the side chain during the first step by an azide anion. The azide anion provided by the dissociation of NaN_3 in the water-acetone solvent mixture contains four lone electron pairs confined in a relatively small space and as such, it is a very good nucleophile. Despite that and the fact that the azide salt is in small excess (1.5 eq.), the reaction rate is slow, necessitating prolonged heating (24 h) to complete. When stopped at 10, 12 or 18 hours, there would always remain unreacted (2-bromoethyl)-3-methylimidazolium bromide in the mixture. The excess of NaN_3 and the produced NaBr can be easily removed, as their solubility in acetonitrile is very low, whereas 1-(2-azidoethyl)-3-methylimidazolium bromide is perfectly soluble in it.

The third step is the reduction of the azide group. Because the azide-functionalized IL is insoluble in ethers where $LiAlH_4$ can be dissolved, the reaction system is heterogeneous. Lithium aluminium hydride is pyrophoric and moisture sensitive, readily reacting with water to produce LiOH, $Al(OH)_3$ and hydrogen gas, in an exothermic reaction. For these reason, and since the azide-functionalized IL is also highly viscous, the last stage of its purification (*e.g.* lyophilization) is carried out in the reaction vessel. However, once the reaction starts, it advances rapidly and the system becomes homogeneous.

The lithium aluminium hydride used for the reduction of the azide to amine is in small excess, so as to neutralize any humidity that might find its way into the reaction mixture. Neutralization of that small excess at the end of the reaction, requires very little water, no more than a few mL. However, at that point, the reduced species is found complexed with the aluminium ($(R\text{-}NH)_4AlLi$) and requires workup with water in order for the complexes to break up and for the amine to get protonated[120], hence the large amount of water added. There is a delicate balance to be struck there, because if too little water is used, the majority of the metal hydroxides (LiOH, $Al(OH)_3$), which form a colloidal suspension, will precipitate fast, inevitably trapping some of the ionic liquid in the precipitate. On the other hand, if a large excess of water is added, a quantity of the hydroxides will remain solubilized and evade filtration, necessitating further purification. The azide α-methylene group is absent from ^1H NMR spectra of the product, so the reduction step appears to be quantitative, according to what is known about this type of reaction in the literature[120].

By acidification of the aqueous phase with a solution of HBr in water and filtration was removed $Al(OH)_3$. At this stage a small amount of Li^+ ions probably remains, most likely as LiBr, which requires confirmation by further analysis. As it cannot be separated from the ionic liquid, this prevented the determination of a yield for the reduction. These ions remain present at this point. At the same time, because of the acidic conditions, the terminal amine exists (at least in part) in ammonium form.

3.3. Synthesis of amino-functionalized EMI^+TFSI^-

The fourth step consists of exchanging the bromide anion for a bis(trifluoromethanesulfonyl)imide ($TFSI^-$) one (Fig. 2.53).

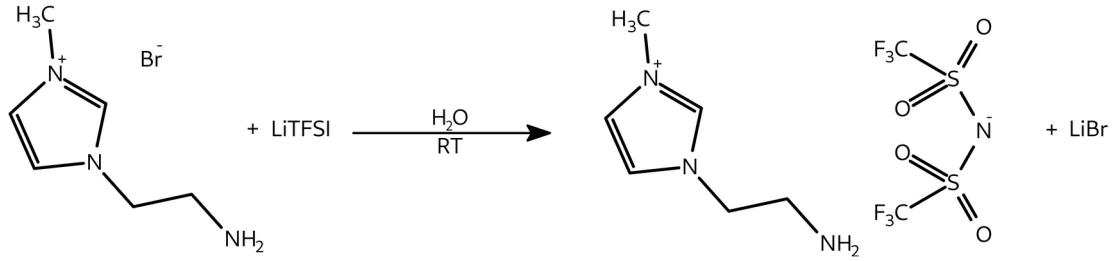

Figure 2.53: Salt metathesis reaction between 1-(2-aminoethyl)-3-methylimidazolium bromide and lithium bis(trifluoromethanesulfonyl)imide.

In order to make sure that the added functional group existed in its amine form, the protons from any ammoniums had to be removed. It was decided to deprotonate the ammonium via basification (pH ~ 10) with LiOH just before the metathesis reaction. The mixture already contained Li^+ ions and the ionic liquid was soluble in water until the anion exchange.

The final step in the protocol is classical salt metathesis reaction between 1-(2-aminoethyl)-3-methylimidazolium bromide and lithium bis(trifluoromethanesulfonyl)imide. As soon as the LiTFSI salt is added to the ionic liquid in water, a phase change occurs, with the forming H_2N-EMI^+-$TFSI^-$ ionic pairs separating from water. The IL phase is repeatedly washed with H_2O, so as to remove any bromides still present. During washing, a lot of ionic liquid leeches into the aqueous phase, as confirmed by ^1H NMR spectra.

The purification of H_2N-EMI^+TFSI^- is concluded by dissolving in acetone the quantity collected after washing. The solution is transferred into a vial for lyophilization, the acetone is evaporated under air or N_2 flow and the ionic liquid is briefly dispersed in a small amount of water before being frozen in liquid nitrogen. After lyophilization, there would be two distinct components in the vial: the very viscous ionic liquid and a small amount of solid,

cobweb-like material, formed at the level of the air-liquid interface in the vial prior to lyophilization. ^{1}H NMR analyses showed that this solid consisted of very little IL and larger amounts of water and acetone. Considering that some of the samples had been lyophilized for more than three days at a pressure below 10^{-5} bar, the presence of these solvents was attributed to hydrogen bonding between them and the ionic liquid. Several studies have examined and confirmed such interactions, between molecular solvents and ionic liquids and with the $EMI^{+}TFSI^{-}$ IL in particular[121]. A more recent study of the $EMI^{+}FSI^{-}$ system found that methanol and DMSO are capable of breaking the ionic pair, through hydrogen bonding of the cation with the electronegative oxygen atoms of the solvents, forming stable complexes[122]. Given the presence of an added charge on the cation and the polar nature of both water and acetone, strong hydrogen bonds would seem highly plausible and would justify the persistence of the solvents.

1-(2-aminoethyl)-3-methylimidazolium bis(trifluoromethanesulfonyl)imide is collected as a very viscous, dark red-brown liquid. Some trace amounts of acetone and water would always be detectable in the ^{1}H NMR spectra, along with the ionic liquid (Fig. 2.60). In the end, the product that remains is down to 20% of what was expected based on the quantity of the azide.

The yield was considerably low, because of the solubility of the ionic liquid in water, due to it having a short side chain and an added polar amine group. At the same time, this could be advantageous for the next stage, grafting the ionic liquid to graphene oxide in an aqueous suspension. However, given the low yield after the metathesis step, proceeding from there was not satisfactory.

Before the metathesis step, the mixture consists of most of the amino-functionalized IL, plus some lithium ions, probably as lithium bromide. That last point, the presence of lithium might actually prove useful in the final composite material. The pre-lithiation of electrode materials of Li-ion batteries is an increasingly researched strategy, in which the loss of active lithium during the initial cycles of the batteries is offset by the inclusion of lithium metal or

lithium sources in the electrodes, before the battery is assembled and operated[123]. If the Li "contamination" does get carried over to the anode material, it could be beneficial to its performance. Because of this, it was decided to stop the purification after the removal of aluminium hydroxide. Unpurified 1-(2-aminoethyl)-3-methylimidazolium bromide, along with the Li^+ impurities will be used as-is, to be grafted onto graphene oxide. The anion exchange will be performed with the ionic liquid grafted on GO (see Chapter 3).

3.4. Experimental method

3.4.1. Synthesis of 1-(2-bromoethyl)-3-methylimidazolium bromide

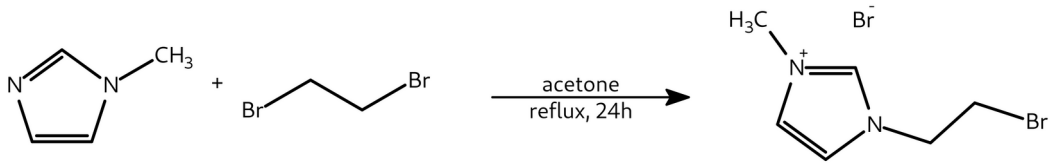

Figure 2.54: Synthesis of 1-(2-bromoethyl)-3-methylimidazolium bromide.

In a 100 mL three-neck round-bottom flask 11 mL (~128 mmol) of 1,2-dibromoethane is mixed with 8.3 mL of acetone. The flask is connected to a vertical condenser and heated to reflux (60°C), while stirring at 500 rpm. With the help of a syringe driver, 3.3 mL (~41 mmol) of 1-methylimidazole is added to the above mixture at a speed of 0.7 mL/h. The mixture is left under reflux overnight. Heating is then stopped and the mixture is left to cool down to room temperature, while still being stirred. The majority of the solvent is decanted while the solid is kept submerged in the remainder. The product is washed 4 times with ~15 mL of acetone under vigorous stirring for at least 30 min at room temperature, to break up the aggregates that may form and liberate any remaining entrapped precursors. After the last

wash, the acetone that is left is removed in a rotary evaporator. The highly hygroscopic white solid is dried either in a vacuum oven at 60°C for ~12 h or by lyophilization for at least 24 h. Yield: > 98 %.

^{1}H NMR spectrum of Br-EMI^{+}Br^{-} (300 MHz, DMSO-d$_6$): δ = 9.30 ppm 1H (s) C^{2}-H; δ = 7.88 ppm 1H (dd), J_{54} = 2.06 Hz, J_{52} = 1.77 Hz C^{5}-H; δ = 7.79 ppm 1H (dd), J_{45} = 2.10 Hz, J_{42} = 1.75 Hz C^{4}-H; δ = 4.65 ppm 2H (t), J = 5.84 Hz NC$\underline{H_2}$CH$_2$; δ = 3.97 ppm 2H (t), J = 5.84 Hz CH$_2$Br; δ = 3.91 ppm 3H (s) CH$_3$N^{+} (Fig. 2.55)

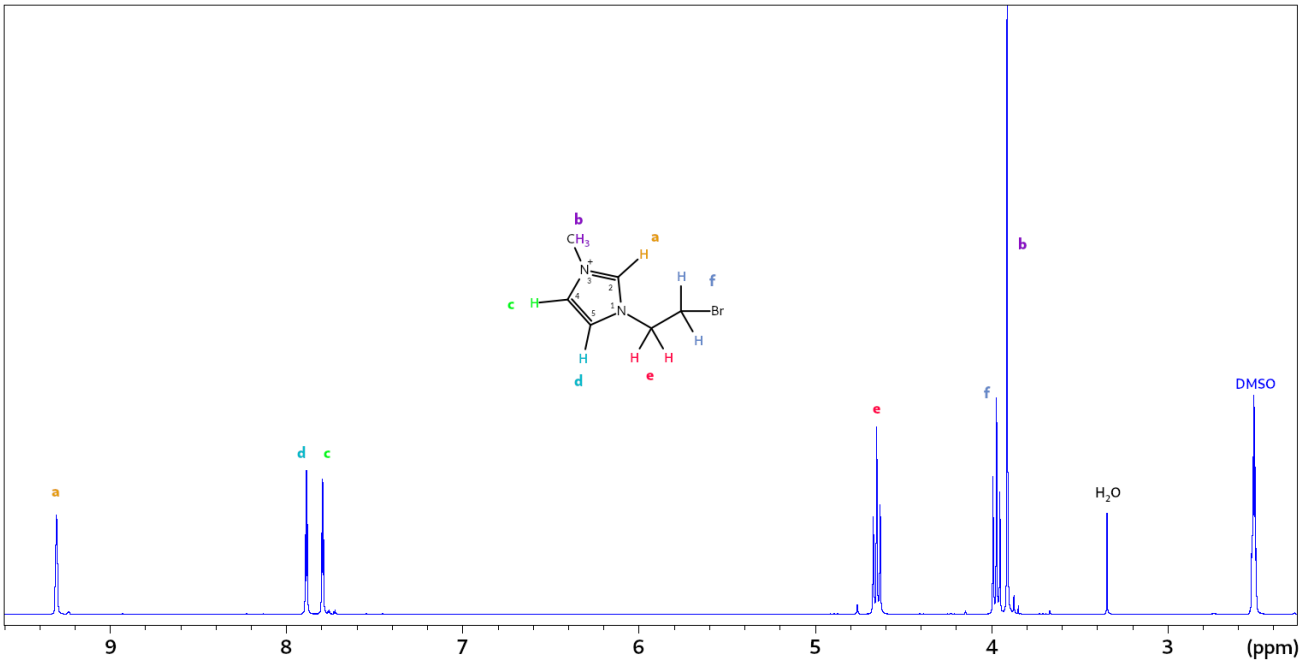

Figure 2.55: ^{1}H NMR spectrum of 1-(2-bromoethyl)-3-methylimidazolium bromide DMSO-d$_6$ (300 MHz)

3.4.2. Synthesis of 1-(2-azidoethyl)-3-methylimidazolium bromide

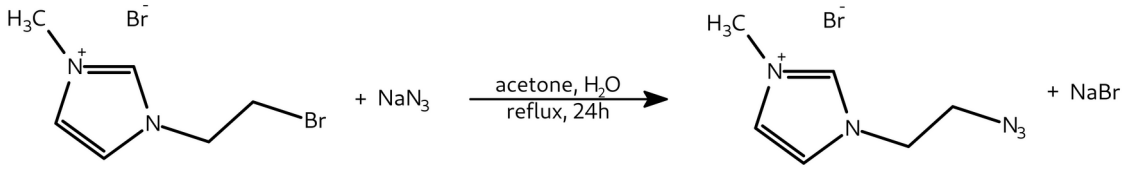

Figure 2.56: Synthesis of 1-(2-azidoethyl)-3-methylimidazolium bromide.

In a 100 mL round-bottom flask 2.6 g (~10 mmol) of 1-(2-bromoethyl)-3-methylimidazolium bromide is dissolved in 5 mL of H_2O and 20 mL of acetone. 0.95 g (~15 mmol) of NaN_3 is added to the solution. The flask is then connected to a vertical condenser and heated to reflux (60°C) for 24 h, while stirring at 500 rpm. It is then left to cool down to room temperature and condensed in a rotary evaporator. The residue is then redispersed in acetonitrile (~10 mL) at which point the insoluble salts (NaBr, NaN_3) precipitate and are removed by vacuum filtration, while the filtrate is subsequently condensed in a rotary evaporator. This is repeated once more. The resulting yellow viscous liquid is dissolved in ~25 mL H_2O, to facilitate the removal of CH_3CN traces during lyophilization (at least 24 h). If the next step is to be carried out in dry ether, the solution should ideally be lyophilized directly in the reaction vessel, *e.g.* three-neck flask. Yield: > 98 %.

^{1}H NMR spectrum of N_3-EMI$^+$Br$^-$ (300 MHz, DMSO-d_6): δ = 9.27 ppm 1H (s) C^2-H; δ = 7.85 ppm 1H (dd), J_{54} = 2.11 Hz, J_{52} = 1.78 Hz C^5-H; δ = 7.78 ppm 1H (dd), J_{45} = 2.12 Hz, J_{42} = 1.72 Hz C^4-H; δ = 4.39 ppm 2H (t), J = 5.47 Hz NCH_2CH_2; δ = 3.89 ppm 3H (s) CH_3N^+; δ = 3.88 ppm 2H (t), J = 5.50 Hz CH_2N_3 (Fig. 2.57)

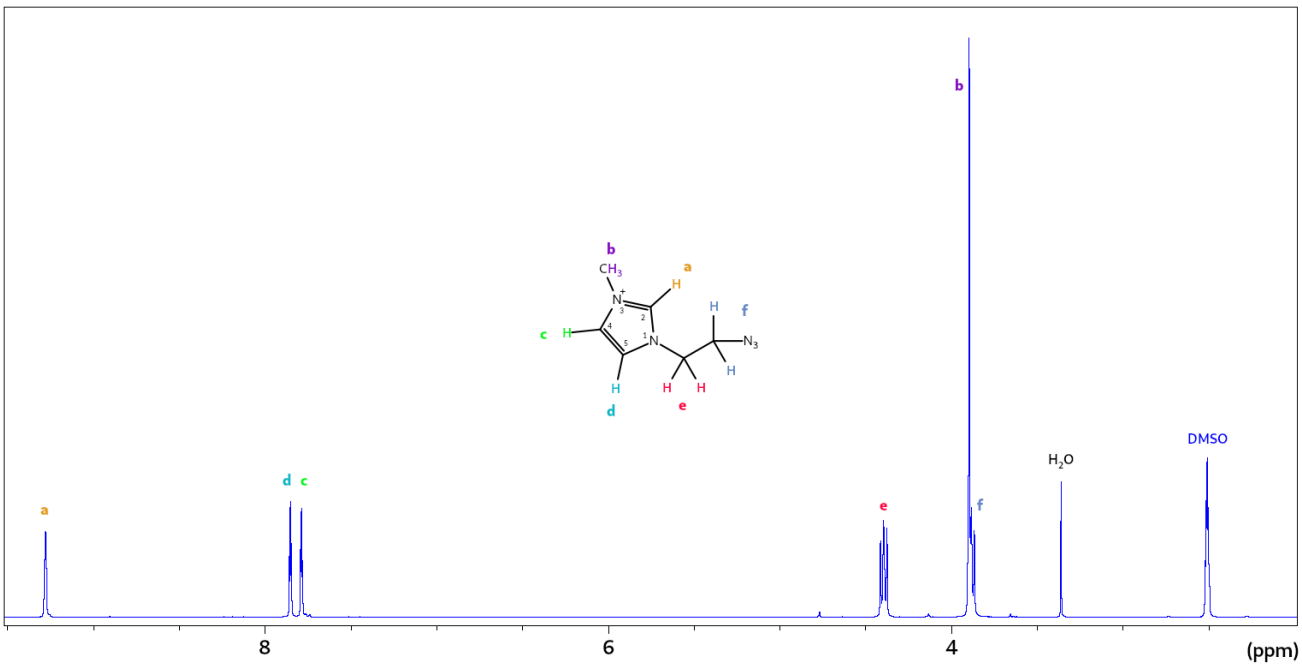

Figure 2.57: ^{1}H NMR spectrum of 1-(2-azidoethyl)-3-methylimidazolium bromide in DMSO-d_6 (300 MHz)

3.4.3. Synthesis of 1-(2-aminoethyl)-3-methylimidazolium bromide

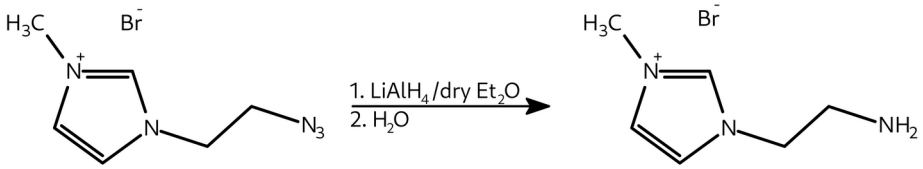

Figure 2.58: Synthesis of 1-(2-aminoethyl)-3-methylimidazolium bromide.

The azide synthesized in the previous step is lyophilized in a 500 mL flask for at least 48 h. Once the liquid is free of water, 150 mL of anhydrous diethyl ether and 0.43 g (~11 mmol) of $LiAlH_4$ are quickly added to the flask, which is then connected to a vertical condenser fitted with a drying tube, filled with $CaCl_2$, for the purpose of keeping the reaction system free of moisture. The system is brought to reflux while stirring and the reaction is left for 4 h. The reaction mixture turns from dark to light gray. The flask is then placed in an ice bath and a large excess of water (≥ 100 mL) is added to it to neutralize any unreacted $LiAlH_4$ and to

break up the metal-organic complexes. The mixture immediately turns white, as LiOH and $Al(OH)_3$ form. The aminated ionic liquid is insoluble in ether, but soluble in water.

The mixture is then filtered through cotton to remove the LiOH and $Al(OH)_3$ precipitate and the ethereal phase is discarded. The aqueous phase contains the desired product along with dissolved metal hydroxides. Water is removed in a rotary evaporator and the yellow residue is washed twice with 40 mL of isopropanol and filtered through paper, to remove any precipitate that forms. The solvent is removed in a rotary evaporator and the residue is redispersed in 30 mL of H_2O. The pH is adjusted between 5 and 6 by the addition of HBr (aq. solution), so as to force any remaining $Al(OH)_3$ to precipitate; this is removed by filtration. The filtrate is once again condensed in a rotary evaporator and the resulting dark red-orange viscous liquid is dispersed in 30 mL of ethanol and refluxed for 1 h. It is left to cool to room temperature and filtered to remove the white precipitate that forms. The filtrate is condensed in a rotary evaporator. According to ^{27}Al and ^{7}Li NMR analysis, the resulting mixture still contains a considerable amount of Li (δ: -0.39 ppm), but no detectable quantity of Al. Yield: indeterminable. Note: After Li atomic absorption measurements conducted on two batches and under the assumptions that all of the lithium bromide is found as its monohydrate, $LiBr{\cdot}H_2O$ (determined by TGA) and all of the aminated ionic liquid is found in its protonated form, the yield was determined to be 76 and 79% for the first batch and 85 to 87% for the other. This variance is probably due to the entrapment of IL in the precipitate.

3.4.4. Anion exchange

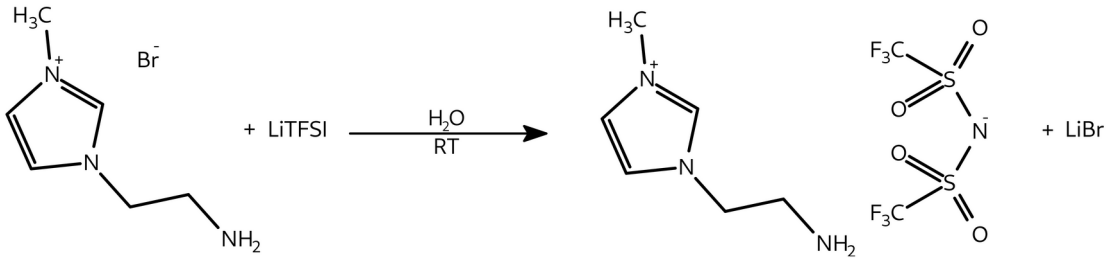

Figure 2.59: Anion exchange between 1-(2-aminoethyl)-3-methylimidazolium bromide and lithium bis(trifluoromethanesulfonyl)imide.

The lyophilized mixture from the previous step is dissolved in 5 mL of H_2O and the pH is adjusted to ~10 by the addition of an aqueous solution of LiOH. Then, 2.87 g (~10 mmol) of LiTFSI salt is added to the solution which immediately separates into two phases. The system is left stirring overnight. The aqueous phase is then carefully removed and the remainder is washed repeatedly with 3 mL of water until a negative test for Br^- is obtained with $AgNO_3$. The dark red-orange ionic liquid is dissolved in 7 mL of acetone, which is then transferred to a vial and left to dry in air. The remaining liquid is further purified by lyophilization. The presence of the amine group is also verified through a nitrous acid test (Appendix E). While the yield from the previous step could not be determined, assuming 100% conversion of the azide and product recovery at that point, the yield at this step is 20%.

^{1}H NMR spectrum of H_2N-EMI$^+$TFSI$^-$ (300 MHz, DMSO-d_6): δ = 9.15 ppm 1H (s) C^2-H; δ = 7.78 ppm 1H (dd), J_{54} = 2.15 Hz, J_{52} = 1.74 Hz C^5-H; δ = 7.73 ppm 1H (dd), J_{45} = 2.16 Hz, J_{42} = 1.76 Hz C^4-H; δ = 4.37 ppm 2H (t), J = 5.50 Hz NC$\underline{H}_2$$CH_2$; δ = 3.88 ppm 3H (s) CH_3N^+; δ = 3.86 ppm 2H (t), J = 5.50 Hz C$\underline{H}_2$$NH_2$ (Fig. 2.60)

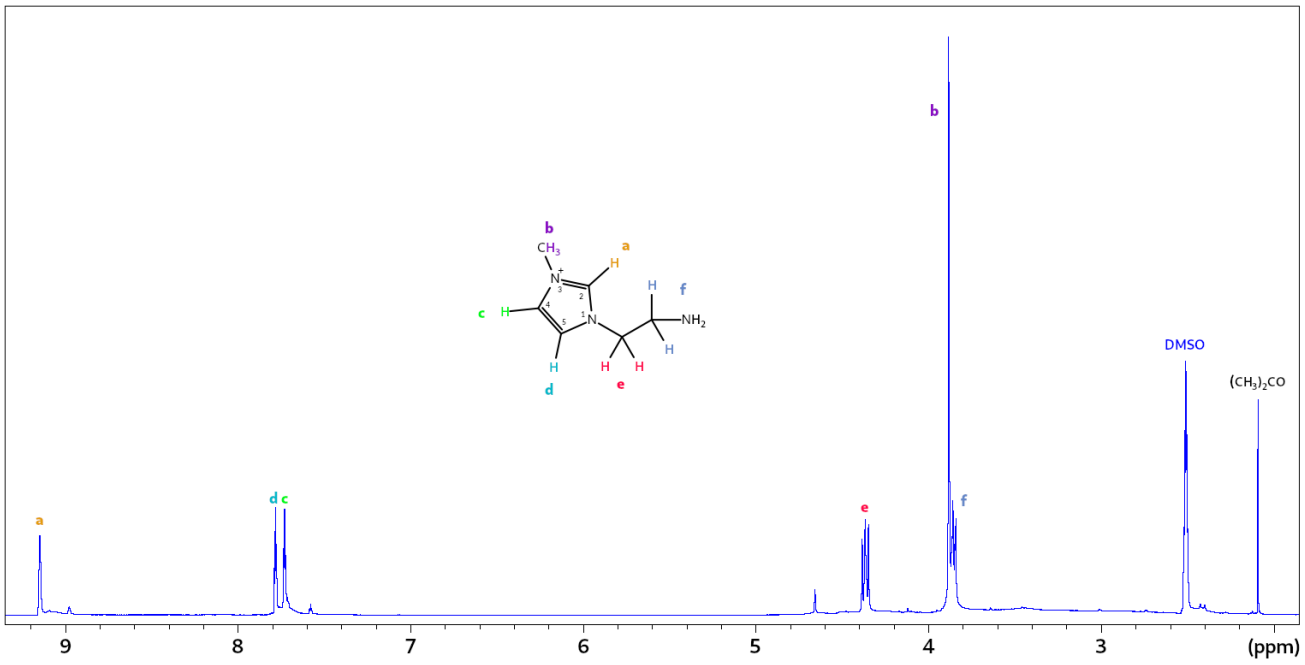

Figure 2.60: ^{1}H NMR spectrum of 1-(2-aminoethyl)-3-methylimidazolium bis(trifluoromethanesulfonyl)imide in DMSO-d6 (300 MHz)

Because of the overlap of several peaks in the spectrum, we were unable to integrate them in order to locate the amine protons, whose chemical shift is typically expected in the range of 0.5-5 ppm. Depending on the pH, the concentration of the solution in the NMR tube and the presence of other solvents, we would sometimes find a very broad peak centered at 3.4-3.8 ppm.

Experimental details and materials. *1) Materials: 1-methylimidazole (purity 99%), 1,2-dibromoethane (purity ≥ 99%), sodium azide (purity ≥ 99.5%), lithium aluminum hydride (purity 95%), lithium hydroxide monohydrate (purity ≥ 98%) and hydrobromic acid aqueous 48%, were purchased from Sigma-Aldrich. Acetone (purity ≥ 99.8), acetonitrile (purity ≥ 99.8) and diethyl ether (purity ≥ 99%) were purchased from Merck. Lithium bis(trifluoromethanesulfonyl)imide (purity > 99%) was purchased from Solvionic. 2) Nuclear Magnetic Resonance (NMR) spectroscopy: the purity of the products at the various steps of the synthesis was verified through ^{1}H, ^{7}Li, ^{27}Al and ^{13}C NMR spectroscopy. The measurements were carried out using two Bruker Avance III narrow bore spectrometers, operating at 7.05 and 11.7 T, with BBFO probes, equipped with gradient coils (55 G/cm).*

3.5. Thermal analyses of the amino-functionalized ionic liquids

3.5.1. Thermogravimetric analyses

In order to verify the thermal stability of the functionalized ionic liquid (H_2N-EMI^+TFSI^-) and hoping to gain some insights into the unpurified mixture of H_2N-EMI^+Br^- with lithium compounds we intended to use for grafting to graphene oxide, we subjected them to thermogravimetric analyses. In Figure 2.61 the thermogravigram of the H_2N-EMI^+TFSI^- ionic liquid and in Figure 2.62 that of the unpurified H_2N-EMI^+Br^- ionic liquid are presented. It should be noted that the amine group of the purified IL should not be protonated, whereas the IL of the mixture could be, at least partially, in ammonium form, since it was recovered after acidification to a pH of 5.5 (for the sake of convenience, it shall be denoted as H_2N-EMI^+Br^- with the caveat that, at least in part, it could actually exist as $Br^-{}^+H_3N$-EMI^+Br^-). Furthermore, the anion is different ($TFSI^-$ for the purified IL and Br^- for the IL in the mixture), which is known to affect thermal stability[124].

The pure ionic liquid has a thermal decomposition profile that resembles a lot that reported for pristine EMI^+TFSI^-[22]. The first difference is a slow weight loss with an onset temperature of approximately 132°C, which accelerates around 194°C and reaches its maximum at 238°C. The total weight loss at that point is 5.5 wt%. The amino group amounts to ~4% of the molar mass of the ionic liquid, so in all likelihood it is the decomposition of the amino group that takes place at that point. The onset temperature is also in the range reported for the thermal decomposition of amines[125].

The main decomposition of the H_2N-EMI^+TFSI^- ionic liquid is complex and has an onset temperature of approximately 275°C, reaching its maximum at 379°C. These temperatures are lower than those of pristine EMI^+TFSI^-, 300°C and 450°C respectively. The weight loss at the end of the process is 81.5 wt%, with the total weight loss reaching 87.0 wt% at the end of the measurement.

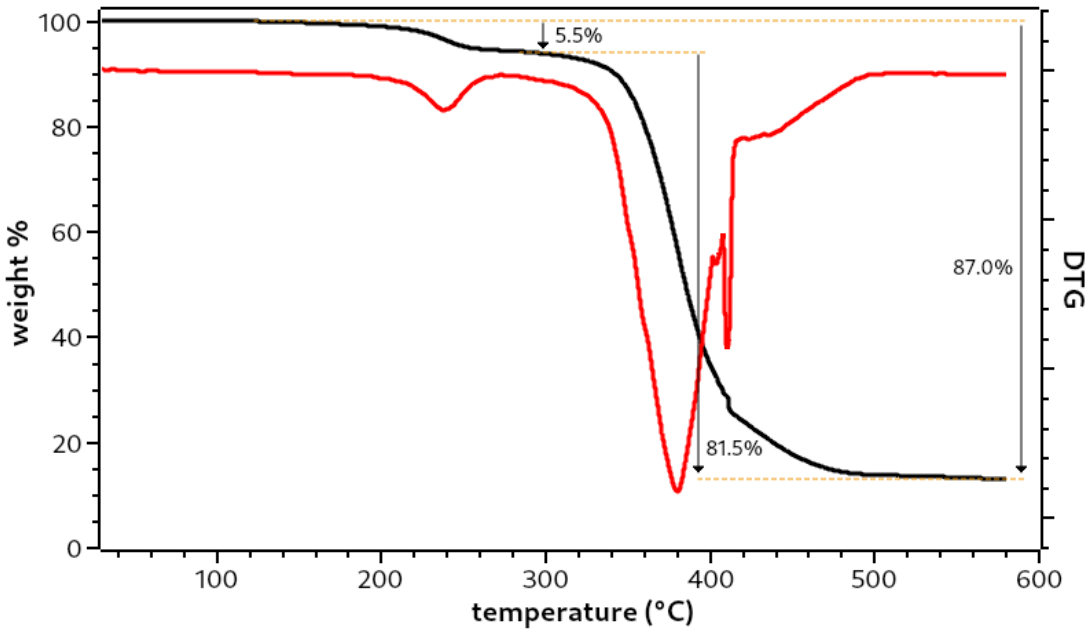

Figure 2.61: Thermogravigram of the H_2N-EMI^+TFSI^- ionic liquid under inert atmosphere (N_2). The first derivative of the TGA curve has been plotted in red.

The unpurified H_2N-EMI^+Br^- ionic liquid has a more complex decomposition profile, with more steps present (Fig. 2.62).

A first weight loss starts at 50°C and continues up to approximately 198°C, where it overlaps with another process. The decomposition rate seems to fluctuate, exhibiting several local maxima between 130°C and 153°C. The weight loss at the point of overlapping is approximately 25.2 wt%. Given the low onset temperature and the amount of weight loss, this process was attributed to water trapped in the mixture. The fluctuations of its rate could be due to water molecules bound to different species in the mixture departing at different times.

The second process continues up to 232°C, exhibiting two maxima at 211°C and 224°C approximately. The accompanying weight loss is 2.8 wt%, though that estimate could be off because of the overlapping with the previous step. Based on the weight loss and when it occurs, it could be attributed to the amino group, while the two maxima in the derivative of the curve could point to the coexistence of the protonated and deprotonated forms of the group.

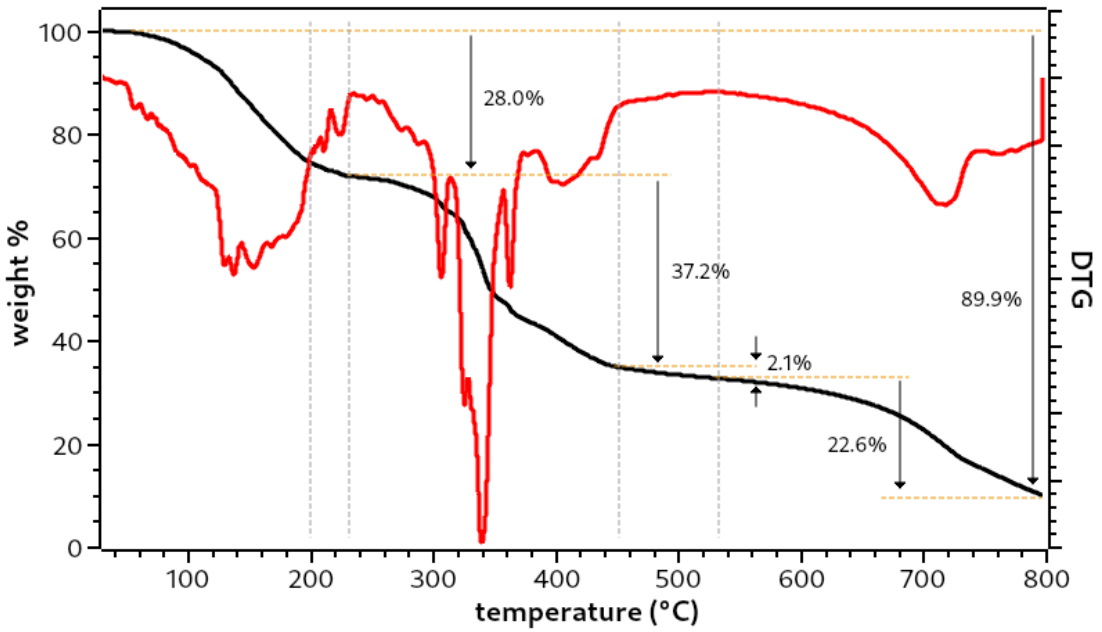

Figure 2.62: Thermogravigram of the unpurified H_2N-EMI^+Br^- ionic liquid under inert atmosphere (N_2). The first derivative of the TGA curve has been plotted in red. The dashed vertical lines indicate the onset of additional events.

The main decomposition of the unpurified H_2N-EMI^+Br^- ionic liquid begins at 259°C, reaches a maximum at 340°C and almost stabilizes at 455°C. It is accompanied by a weight loss of 37.2 wt%.

Based on the derivative, a residual, slow decomposition takes place between 455°C and 537°C, corresponding to a weight loss of ~2.1 wt%.

It is followed by yet another decomposition step, beginning at 537°C, reaching a maximum at 716°C and continuing until the end of the measurement at 800°C. The weight loss at this segment is 22.6 wt%, while the total weight loss of the sample at that point is 89.9 wt%.

While the decomposition of the sample does not appear to be complete at 800°C – a temperature that could not be exceeded because of experimental limitations – the weight ratios of the two last segments would seem to suggest that the decomposition of an EMI^+ fragment takes place first, followed by the evolution of bromine gas. The coexistence of several different ions and water in the mixture appears to have an effect on the stability of

each decomposing or evaporating species and accordingly, to influence the temperatures at which the different processes occur. Based on the literature[126–129] and experiments conducted with lithium bromide hydrates (Appendix F), the first complex decomposition (50°C – 198°C) is attributed to water released from a mixture of LiBr hydrates.

3.5.2. Differential scanning calorimetry

Differential scanning calorimetry was employed primarily to determine the melting point of the purified aminated ionic liquid – H_2N-EMI$^+$TFSI$^-$. The measurement is presented in Figure 2.63.

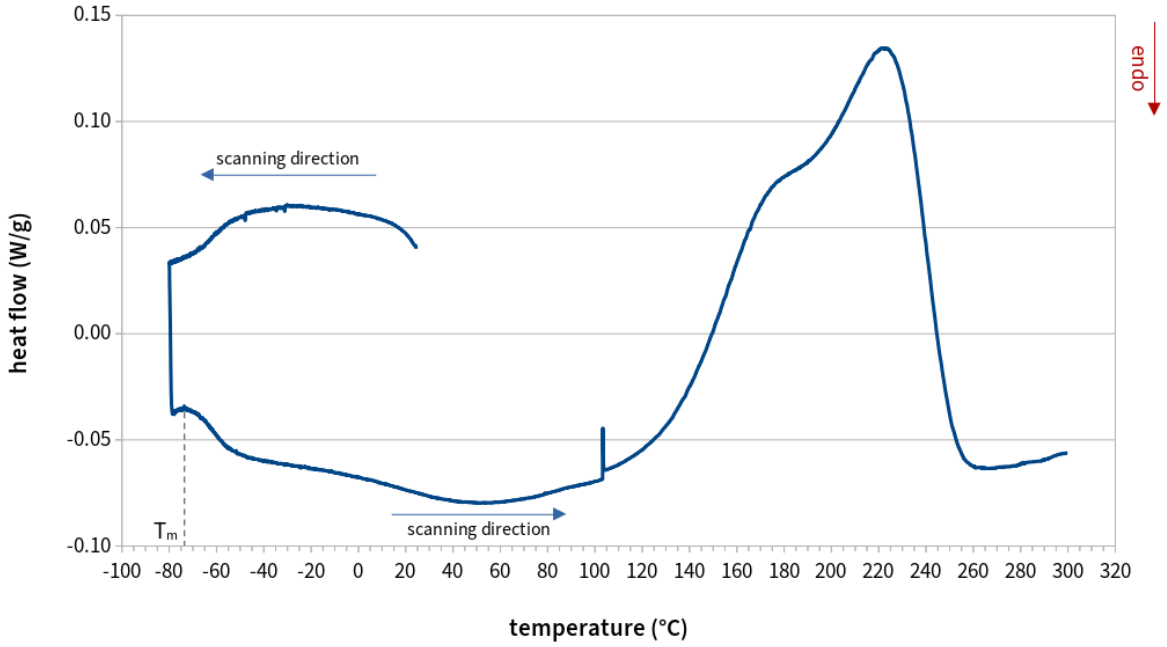

Figure 2.63: DSC thermogram of the H_2N-EMI$^+$TFSI$^-$ ionic liquid. Endothermic processes are downward.

The melting point of the ionic liquid was near the lower operating limit of the device (-80°C). It is not very clear during freezing, but it appears as the maximum of the exothermic peak after heating starts, at -74°C.

According to the ^{1}H NMR analysis, the ionic liquid already contained some traces of

water. Furthermore, condensation of moisture inside the measurement chamber took place during the cooling cycle. Some of the condensate entered the crucible from the perforation in the cover once the temperature was again above 0°C. The small, sharp exothermic peak at 100°C is due to the water.

Two overlapping exothermic events take place in the range between 120°C and 260°C and coincide with the first weight loss measured in the TG analysis, attributed to the decomposition of the amino group. The first process has a maximum at 180°C, close to where the temperature at which the slow decomposition seems to accelerate in the thermogravigram of Fig. 2.61. The second process reaches its maximum around 222°C. According to simulations of the thermal decomposition of primary amines, the bimodal decomposition of the amino group could be attributed to different decomposition pathways[130,131], but also to interactions of the IL with the aluminum crucible[132]. The thermal decomposition of 1-(2-aminoethyl)-3-methylimidazolium imidazolide has also been reported in the literature[133] and a comparable weight loss as the one observed in the thermogravigram of Fig. 2.61 occurs at ~145°C, accompanied by an exothermic event, but the researchers did not comment on it.

Experimental details. *The measurement was conducted on a Mettler Toledo DSC 3 STAR^e calorimeter. The sample was spread evenly on the bottom of an aluminium crucible, in order to facilitate heat transfer and achieve homogeneous heating and cooling of the entirety of its mass. The crucible was sealed with a perforated cover and the sample was first cooled from ambient temperature to -80°C and then heated to 300°C. The temperature ramp was 3°C/min.*

3.6. Conclusions

At the core of this study were the favorable interactions between tin nanoparticles and the EMI^+TFSI^- ionic liquid and how these could be put to use in the context of lithium ion batteries. The immobilization of the ionic liquid–tin nanoparticle system on a suitable matrix could help alleviate the problems associated with tin as an additive to Li-ion anodes,

by containing its volume expansion and preventing the migration of tin atoms during cycling. Once the matrix was selected and its chemistry explored, the next step was the elaboration of the appropriate anchor for the ionic liquid.

The amino group was deemed the most compatible choice for grafting the cation of the ionic liquid to graphene oxide. To that end, a rational, reproducible synthetic protocol had to be devised and applied. The physicochemical properties of the EMI^+ cation coupled with the interactions induced by the introduction of a polar and at times charged functional group necessitated the adaptation of established methodologies, both for the synthesis and the purification of the products at every step. The final synthetic pathway consists of four distinct stages all with excellent yields, up to the point of the metathesis reaction, which was however necessary in order to produce and investigate the properties of the envisaged ionic liquid.

Once the final form of the aminated ionic liquid had been prepared and analyzed, the synthetic protocol was revisited. On one hand, the anion exchange proved wasteful, as the majority of the ionic liquid leeched away and on the other, the hydrophobicity of the purified product would pose problems to its grafting to graphene oxide. Then came the realization that the synthesis could be stopped after the reduction of the azide to an amine and the removal of the aluminium hydroxide impurities. A combination of NMR spectroscopy, and thermogravimetric analyses elucidated the composition of that mixture: it consists of hydrated lithium bromide mixed with the brominated ionic liquid. The ionic liquid is water-soluble at that stage and thus, easy to integrate with the graphene oxide matrix. Of the remaining impurities, the bromide anions and the lithium cations, the latter do not pose a problem, in view of the intended application. Once the ionic liquid was grafted to the substrate, the metathesis could take place then and there and subsequently, the bromide ions would too be removed.

These conclusions bode well also for the possibility of scaling up the synthesis, which would benefit from being conducted on a larger scale. While not all the materials and

methods selected are cost-effective, they were the best available options while working at the laboratory scale. Possible improvements would be for instance, to perform the reduction of the azide in a solvent in which it is soluble, under milder conditions and forgoing the use of $LiAlH_4$, *e.g.* by catalytic hydrogenation. This would eliminate the variability in the final composition of the mixture brought about by the entrapment of the ionic liquid in the precipitating metal hydroxides. Similarly, the synthesis of the azide from the bromide, could perhaps be achieved by supported catalysts, minimizing the work and cost required for purification.

4. References

(1) Pointon, A. I.; Grant, N. E.; Bonilla, R. S.; Wheeler-Jones, E. C.; Walker, M.; Wilshaw, P.; Dancer, C. E. J.; Murphy, J. D. Exceptional Surface Passivation Arising from Bis(Trifluoromethanesulfonyl)-Based Solutions. *ACS Applied Electronic Materials* **2019**. https://doi.org/10.1021/acsaelm.9b00251.

(2) Dreyer, D. R.; Park, S.; Bielawski, C. W.; Ruoff, R. S. The Chemistry of Graphene Oxide. *Chem. Soc. Rev.* **2010**, *39* (1), 228–240. https://doi.org/10.1039/B917103G.

(3) Brodie, B. C. On the Atomic Weight of Graphite. *Philosophical Transactions of the Royal Society of London* **1859**, *149*, 249–259.

(4) Staudenmaier, L. Verfahren Zur Darstellung Der Graphitsäure. *European Journal of Inorganic Chemistry* **1898**, *31* (2), 1481–1487.

(5) Hummers Jr, W. S.; Offeman, R. E. Preparation of Graphitic Oxide. *Journal of the American Chemical Society* **1958**, *80* (6), 1339–1339.

(6) Zurutuza Elorza, A.; Alonso Rodrihuez, B. Method For Obtaining Graphene Oxide. US 2016/0272499 A1, September 22, 2016.

(7) Smith, A. T.; LaChance, A. M.; Zeng, S.; Liu, B.; Sun, L. Synthesis, Properties, and Applications of Graphene Oxide/Reduced Graphene Oxide and Their Nanocomposites. *Nano Materials Science* **2019**. https://doi.org/10.1016/j.nanoms.2019.02.004.

(8) Kovtyukhova, N. I.; Ollivier, P. J.; Martin, B. R.; Mallouk, T. E.; Chizhik, S. A.; Buzaneva, E. V.; Gorchinskiy, A. D. Layer-by-Layer Assembly of Ultrathin Composite Films from Micron-Sized Graphite Oxide Sheets and Polycations. *Chemistry of Materials* **1999**, *11* (3), 771–778. https://doi.org/10.1021/cm981085u.

(9) Li, C.; Chen, X.; Shen, L.; Bao, N. Revisiting the Oxidation of Graphite: Reaction Mechanism, Chemical Stability, and Structure Self-Regulation. *ACS Omega* **2020**, *5* (7), 3397–3404. https://doi.org/10.1021/acsomega.9b03633.

(10) Lerf, A.; He, H.; Forster, M.; Klinowski, J. Structure of Graphite Oxide Revisited. *The Journal of Physical Chemistry B* **1998**, *102* (23), 4477–4482. https://doi.org/10.1021/jp9731821.

(11) Dimiev, A. M.; Alemany, L. B.; Tour, J. M. Graphene Oxide. Origin of Acidity, Its Instability in Water, and a New Dynamic Structural Model. *ACS Nano* **2013**, *7* (1), 576–588. https://doi.org/10.1021/nn3047378.

(12) Zhu, Y.; Murali, S.; Cai, W.; Li, X.; Suk, J. W.; Potts, J. R.; Ruoff, R. S. Graphene and Graphene Oxide: Synthesis, Properties, and Applications. *Advanced Materials* **2010**, *22* (35), 3906–3924. https://doi.org/10.1002/adma.201001068.

(13) Eda, G.; Chhowalla, M. Chemically Derived Graphene Oxide: Towards Large-Area Thin-Film Electronics and Optoelectronics. *Advanced Materials* **2010**, *22* (22), 2392–2415. https://doi.org/10.1002/adma.200903689.

(14) Haar, S.; Ciesielski, A.; Clough, J.; Yang, H.; Mazzaro, R.; Richard, F.; Conti, S.; Merstorf, N.; Cecchini, M.; Morandi, V.; Casiraghi, C.; Samorì, P. A Supramolecular Strategy to Leverage the Liquid-Phase Exfoliation of Graphene in the Presence of Surfactants: Unraveling the Role of the Length of Fatty Acids. *Small* **2015**, *11* (14), 1691–1702. https://doi.org/10.1002/smll.201402745.

(15) Xu, Y.; Cao, H.; Xue, Y.; Li, B.; Cai, W. Liquid-Phase Exfoliation of Graphene: An Overview on Exfoliation Media, Techniques, and Challenges. *Nanomaterials* **2018**, *8* (11),

942. https://doi.org/10.3390/nano8110942.

(16) Varrla, E.; Paton, K. R.; Backes, C.; Harvey, A.; Smith, R. J.; McCauley, J.; Coleman, J. N. Turbulence-Assisted Shear Exfoliation of Graphene Using Household Detergent and a Kitchen Blender. *Nanoscale* **2014**, *6* (20), 11810–11819. https://doi.org/10.1039/C4NR03560G.

(17) Boehm., H. P.; Clauss, A.; Fischer, G. O.; Hofmann, U. Dünnste Kohlenstoff-Folien. *Zeitschrift für Naturforschung B* **1962**, *17* (3), 150–153. https://doi.org/10.1515/znb-1962-0302.

(18) Backes, C.; Abdelkader, A. M.; Alonso, C.; Andrieux-Ledier, A.; Arenal, R.; Azpeitia, J.; Balakrishnan, N.; Banszerus, L.; Barjon, J.; Bartali, R.; Bellani, S.; Berger, C.; Berger, R.; Ortega, M. M. B.; Bernard, C.; Beton, P. H.; Beyer, A.; Bianco, A.; Bøggild, P.; Bonaccorso, F.; Barin, G. B.; Botas, C.; Bueno, R. A.; Carriazo, D.; Castellanos-Gomez, A.; Christian, M.; Ciesielski, A.; Ciuk, T.; Cole, M. T.; Coleman, J.; Coletti, C.; Crema, L.; Cun, H.; Dasler, D.; De Fazio, D.; Díez, N.; Drieschner, S.; Duesberg, G. S.; Fasel, R.; Feng, X.; Fina, A.; Forti, S.; Galiotis, C.; Garberoglio, G.; García, J. M.; Garrido, J. A.; Gibertini, M.; Gölzhäuser, A.; Gómez, J.; Greber, T.; Hauke, F.; Hemmi, A.; Hernandez-Rodriguez, I.; Hirsch, A.; Hodge, S. A.; Huttel, Y.; Jepsen, P. U.; Jimenez, I.; Kaiser, U.; Kaplas, T.; Kim, H.; Kis, A.; Papagelis, K.; Kostarelos, K.; Krajewska, A.; Lee, K.; Li, C.; Lipsanen, H.; Liscio, A.; Lohe, M. R.; Loiseau, A.; Lombardi, L.; Francisca López, M.; Martin, O.; Martín, C.; Martínez, L.; Martin-Gago, J. A.; Ignacio Martínez, J.; Marzari, N.; Mayoral, Á.; McManus, J.; Melucci, M.; Méndez, J.; Merino, C.; Merino, P.; Meyer, A. P.; Miniussi, E.; Miseikis, V.; Mishra, N.; Morandi, V.; Munuera, C.; Muñoz, R.; Nolan, H.; Ortolani, L.; Ott, A. K.; Palacio, I.; Palermo, V.; Parthenios, J.; Pasternak, I.; Patane, A.; Prato, M.; Prevost, H.; Prudkovskiy, V.; Pugno, N.; Rojo, T.; Rossi, A.; Ruffieux, P.; Samorì, P.; Schué, L.; Setijadi, E.; Seyller, T.; Speranza, G.; Stampfer, C.; Stenger, I.; Strupinski, W.; Svirko, Y.; Taioli, S.; Teo, K. B. K.; Testi, M.; Tomarchio, F.; Tortello, M.; Treossi, E.; Turchanin, A.; Vazquez, E.; Villaro, E.; Whelan, P. R.; Xia, Z.; Yakimova, R.; Yang, S.; Yazdi, G. R.; Yim, C.; Yoon, D.; Zhang, X.; Zhuang, X.; Colombo, L.; Ferrari, A. C.; Garcia-Hernandez, M. Production and Processing of Graphene and Related Materials. *2D Materials* **2020**, *7* (2), 022001. https://doi.org/10.1088/2053-1583/ab1e0a.

(19) Kauling, A. P.; Seefeldt, A. T.; Pisoni, D. P.; Pradeep, R. C.; Bentini, R.; Oliveira, R. V. B.; Novoselov, K. S.; Castro Neto, A. H. The Worldwide Graphene Flake Production. *Advanced Materials* **2018**, *30* (44), 1803784. https://doi.org/10.1002/adma.201803784.

(20) Koshino, M. Stacking-Dependent Optical Absorption in Multilayer Graphene. *New Journal of Physics* **2013**, *15* (1), 015010. https://doi.org/10.1088/1367-2630/15/1/015010.

(21) Dimiev, A. M.; Tour, J. M. Mechanism of Graphene Oxide Formation. *ACS Nano* **2014**, *8* (3), 3060–3068. https://doi.org/10.1021/nn500606a.

(22) Liu, S.-H.; Chen, C.-C.; Zhang, B.; Wu, J.-H. Fire and Explosion Hazards of 1-Ethyl-3-Methylimidazolium Bis(Trifluoromethylsulfonyl)Imide. *RSC Advances* **2020**, *10* (38), 22468–22479. https://doi.org/10.1039/D0RA01821J.

(23) Zhang, C.; Lv, W.; Xie, X.; Tang, D.; Liu, C.; Yang, Q.-H. Towards Low Temperature Thermal Exfoliation of Graphite Oxide for Graphene Production. *Carbon* **2013**, *62*, 11–24. https://doi.org/10.1016/j.carbon.2013.05.033.

(24) Feng, H.; Cheng, R.; Zhao, X.; Duan, X.; Li, J. A Low-Temperature Method to Produce Highly Reduced Graphene Oxide. *Nature Communications* **2013**, *4*, 1539. https://doi.org/10.1038/ncomms2555.

(25) Acik, M.; Lee, G.; Mattevi, C.; Pirkle, A.; Wallace, R. M.; Chhowalla, M.; Cho, K.; Chabal, Y. The Role of Oxygen during Thermal Reduction of Graphene Oxide Studied by

Infrared Absorption Spectroscopy. *The Journal of Physical Chemistry C* **2011**, *115* (40), 19761–19781. https://doi.org/10.1021/jp2052618.

(26) Qiu, Y.; Guo, F.; Hurt, R.; Külaots, I. Explosive Thermal Reduction of Graphene Oxide-Based Materials: Mechanism and Safety Implications. *Carbon* **2014**, *72*, 215–223. https://doi.org/10.1016/j.carbon.2014.02.005.

(27) Zhang, H.-B.; Wang, J.-W.; Yan, Q.; Zheng, W.-G.; Chen, C.; Yu, Z.-Z. Vacuum-Assisted Synthesis of Graphene from Thermal Exfoliation and Reduction of Graphite Oxide. *Journal of Materials Chemistry* **2011**, *21* (14), 5392. https://doi.org/10.1039/c1jm10099h.

(28) Hull., A. W. A New Method of X-Ray Crystal Analysis. *Physical Review* **1917**, *10* (6), 661–696. https://doi.org/10.1103/PhysRev.10.661.

(29) Bernal, J. D.; Bragg, W. L. The Structure of Graphite. *Proceedings of the Royal Society of London. Series A, Containing Papers of a Mathematical and Physical Character* **1924**, *106* (740), 749–773. https://doi.org/10.1098/rspa.1924.0101.

(30) Zhou, Z.; Bouwman, W. G.; Schut, H.; Pappas, C. Interpretation of X-Ray Diffraction Patterns of (Nuclear) Graphite. *Carbon* **2014**, *69*, 17–24. https://doi.org/10.1016/j.carbon.2013.11.032.

(31) Li, Z. Q.; Lu, C. J.; Xia, Z. P.; Zhou, Y.; Luo, Z. X-Ray Diffraction Patterns of Graphite and Turbostratic Carbon. *Carbon* **2007**, *45* (8), 1686–1695. https://doi.org/10.1016/j.carbon.2007.03.038.

(32) Jeong, H.-K.; Lee, Y. P.; Lahaye, R. J. W. E.; Park, M.-H.; An, K. H.; Kim, I. J.; Yang, C.-W.; Park, C. Y.; Ruoff, R. S.; Lee, Y. H. Evidence of Graphitic AB Stacking Order of Graphite Oxides. *Journal of the American Chemical Society* **2008**, *130* (4), 1362–1366. https://doi.org/10.1021/ja076473o.

(33) Wang, Y.; Alsmeyer, D. C.; McCreery, R. L. Raman Spectroscopy of Carbon Materials: Structural Basis of Observed Spectra. *Chemistry of Materials* **1990**, *2* (5), 557–563.

(34) Ten, G.; Gerasimenko, A.; Savelyev, M.; Kuksin, A.; Vasilevsky, P.; Kitsyuk, E.; Baranov, V. Influence of Edge Defects on Raman Spectra of Graphene. *Lett. Mater.* **2020**, *10* (1), 89–93. https://doi.org/10.22226/2410-3535-2020-1-89-93.

(35) Adelhelm, C.; Balden, M.; Rinke, M.; Stueber, M. Influence of Doping (Ti, V, Zr, W) and Annealing on the sp^2 Carbon Structure of Amorphous Carbon Films. *Journal of Applied Physics* **2009**, *105* (3), 033522. https://doi.org/10.1063/1.3075843.

(36) Yang, D.; Velamakanni, A.; Bozoklu, G.; Park, S.; Stoller, M.; Piner, R. D.; Stankovich, S.; Jung, I.; Field, D. A.; Ventrice, C. A.; Ruoff, R. S. Chemical Analysis of Graphene Oxide Films after Heat and Chemical Treatments by X-Ray Photoelectron and Micro-Raman Spectroscopy. *Carbon* **2009**, *47* (1), 145–152. https://doi.org/10.1016/j.carbon.2008.09.045.

(37) Nikolakopoulou, A.; Tasis, D.; Sygellou, L.; Dracopoulos, V.; Galiotis, C.; Lianos, P. Study of the Thermal Reduction of Graphene Oxide and of Its Application as Electrocatalyst in Quasi-Solid State Dye-Sensitized Solar Cells in Combination with PEDOT. *Electrochimica Acta* **2013**, *111*, 698–706. https://doi.org/10.1016/j.electacta.2013.08.064.

(38) Tene, T.; Tubon Usca, G.; Guevara, M.; Molina, R.; Veltri, F.; Arias, M.; Caputi, L. S.; Vacacela Gomez, C. Toward Large-Scale Production of Oxidized Graphene. *Nanomaterials* **2020**, *10* (2), 279. https://doi.org/10.3390/nano10020279.

(39) Yoon, D.; Jeong, D.; Lee, H.-J.; Saito, R.; Son, Y.-W.; Lee, H. C.; Cheong, H. Fano Resonance in Raman Scattering of Graphene. *Carbon* **2013**, *61*, 373–378. https://doi.org/10.1016/j.carbon.2013.05.019.

(40) Hasdeo, E. H.; Nugraha, A. R. T.; Dresselhaus, M. S.; Saito, R. Breit-Wigner-Fano Line

Shapes in Raman Spectra of Graphene. *Phys. Rev. B* **2014**, *90* (24), 245140. https://doi.org/10.1103/PhysRevB.90.245140.

(41) Merlen, A.; Buijnsters, J.; Pardanaud, C. A Guide to and Review of the Use of Multiwavelength Raman Spectroscopy for Characterizing Defective Aromatic Carbon Solids: From Graphene to Amorphous Carbons. *Coatings* **2017**, *7* (10), 153. https://doi.org/10.3390/coatings7100153.

(42) Couzi, M.; Bruneel, J.-L.; Talaga, D.; Bokobza, L. A Multi Wavelength Raman Scattering Study of Defective Graphitic Carbon Materials: The First Order Raman Spectra Revisited. *Carbon* **2016**, *107*, 388–394. https://doi.org/10.1016/j.carbon.2016.06.017.

(43) Vecera, P.; Chacón-Torres, J. C.; Pichler, T.; Reich, S.; Soni, H. R.; Görling, A.; Edelthalhammer, K.; Peterlik, H.; Hauke, F.; Hirsch, A. Precise Determination of Graphene Functionalization by in Situ Raman Spectroscopy. *Nat Commun* **2017**, *8* (1), 15192. https://doi.org/10.1038/ncomms15192.

(44) López-Díaz, D.; López Holgado, M.; García-Fierro, J. L.; Velázquez, M. M. Evolution of the Raman Spectrum with the Chemical Composition of Graphene Oxide. *J. Phys. Chem. C* **2017**, *121* (37), 20489–20497. https://doi.org/10.1021/acs.jpcc.7b06236.

(45) Ma, B.; Rodriguez, R. D.; Ruban, A.; Pavlov, S.; Sheremet, E. The Correlation between Electrical Conductivity and Second-Order Raman Modes of Laser-Reduced Graphene Oxide. *Phys. Chem. Chem. Phys.* **2019**, *21* (19), 10125–10134. https://doi.org/10.1039/C9CP00093C.

(46) Lee, A. Y.; Yang, K.; Anh, N. D.; Park, C.; Lee, S. M.; Lee, T. G.; Jeong, M. S. Raman Study of D* Band in Graphene Oxide and Its Correlation with Reduction. *Applied Surface Science* **2021**, *536*, 147990. https://doi.org/10.1016/j.apsusc.2020.147990.

(47) Liu, W.; Speranza, G. Tuning the Oxygen Content of Reduced Graphene Oxide and Effects on Its Properties. *ACS Omega* **2021**, *6* (9), 6195–6205. https://doi.org/10.1021/acsomega.0c05578.

(48) Eigler, S.; Dotzer, C.; Hirsch, A.; Enzelberger, M.; Müller, P. Formation and Decomposition of CO_2 Intercalated Graphene Oxide. *Chemistry of Materials* **2012**, *24* (7), 1276–1282. https://doi.org/10.1021/cm203223z.

(49) Pei, S.; Cheng, H.-M. The Reduction of Graphene Oxide. *Carbon* **2012**, *50* (9), 3210–3228. https://doi.org/10.1016/j.carbon.2011.11.010.

(50) Kumar, A.; Dixit, C. K. Methods for Characterization of Nanoparticles. In *Advances in Nanomedicine for the Delivery of Therapeutic Nucleic Acids*; Elsevier, 2017; pp 43–58. https://doi.org/10.1016/B978-0-08-100557-6.00003-1.

(51) Ham, H.; Van Khai, T.; Park, N.-H.; So, D. S.; Lee, J.-W.; Gil Na, H.; Jung Kwon, Y.; Yeon Cho, H.; Woo Kim, H. Freeze-Drying-Induced Changes in the Properties of Graphene Oxides. *Nanotechnology* **2014**, *25* (23), 235601. https://doi.org/10.1088/0957-4484/25/23/235601.

(52) Tian, J.; Yang, J.; Yang, C.; Hao, S. Compression and Reduction of Graphene Oxide Aerogels into Flexible, Porous and Functional Graphene Films. *Journal of Materials Science* **2019**. https://doi.org/10.1007/s10853-019-03828-7.

(53) Maxwell, W. A.; Gurnick, R. S.; Francisco, A. C. *Preliminary Investigation of the "freeze-Casting" Method for Forming Refractory Powders*; Lewis Flight Propulsion Laboratory: Cleveland, Ohio, 1954.

(54) Deville, S. Freeze-Casting of Porous Ceramics: A Review of Current Achievements and Issues. *Adv. Eng. Mater.* **2008**, *10* (3), 155–169. https://doi.org/10.1002/adem.200700270.

(55) Christoph, S.; Kwiatoszynski, J.; Coradin, T.; Fernandes, F. M. Cellularized Cellular Solids

via Freeze-Casting: Cellularized Cellular Solids via Freeze-Casting. *Macromolecular Bioscience* **2016**, *16* (2), 182–187. https://doi.org/10.1002/mabi.201500319.

(56) Christoph, S.; Hamraoui, A.; Bonnin, E.; Garnier, C.; Coradin, T.; Fernandes, F. M. Ice-Templating Beet-Root Pectin Foams: Controlling Texture, Mechanics and Capillary Properties. *Chemical Engineering Journal* **2018**, *350*, 20–28. https://doi.org/10.1016/j.cej.2018.05.160.

(57) Yeh, C.-N.; Huang, H.; Lim, A. T. O.; Jhang, R.-H.; Chen, C.-H.; Huang, J. Binder-Free Graphene Oxide Doughs. *Nature Communications* **2019**, *10* (1). https://doi.org/10.1038/s41467-019-08389-6.

(58) Park, S.; Hu, Y.; Hwang, J. O.; Lee, E.-S.; Casabianca, L. B.; Cai, W.; Potts, J. R.; Ha, H.-W.; Chen, S.; Oh, J.; Kim, S. O.; Kim, Y.-H.; Ishii, Y.; Ruoff, R. S. Chemical Structures of Hydrazine-Treated Graphene Oxide and Generation of Aromatic Nitrogen Doping. *Nat Commun* **2012**, *3* (1), 638. https://doi.org/10.1038/ncomms1643.

(59) Luan, V. H.; Tien, H. N.; Hoa, L. T.; Hien, N. T. M.; Oh, E.-S.; Chung, J.; Kim, E. J.; Choi, W. M.; Kong, B.-S.; Hur, S. H. Synthesis of a Highly Conductive and Large Surface Area Graphene Oxide Hydrogel and Its Use in a Supercapacitor. *J. Mater. Chem. A* **2013**, *1* (2), 208–211. https://doi.org/10.1039/C2TA00444E.

(60) Gholampour, A.; Valizadeh Kiamahalleh, M.; Tran, D. N. H.; Ozbakkaloglu, T.; Losic, D. From Graphene Oxide to Reduced Graphene Oxide: Impact on the Physiochemical and Mechanical Properties of Graphene–Cement Composites. *ACS Appl. Mater. Interfaces* **2017**, *9* (49), 43275–43286. https://doi.org/10.1021/acsami.7b16736.

(61) Lokhande, A. C.; Qattan, I. A.; Lokhande, C. D.; Patole, S. P. Holey Graphene: An Emerging Versatile Material. *J. Mater. Chem. A* **2020**, *8* (3), 918–977. https://doi.org/10.1039/C9TA10667G.

(62) Kim, M. C.; Hwang, G. S.; Ruoff, R. S. Epoxide Reduction with Hydrazine on Graphene: A First Principles Study. *J. Chem. Phys.* **2009**, *131* (6), 064704. https://doi.org/10.1063/1.3197007.

(63) Wang, R.; Wang, Y.; Xu, C.; Sun, J.; Gao, L. Facile One-Step Hydrazine-Assisted Solvothermal Synthesis of Nitrogen-Doped Reduced Graphene Oxide: Reduction Effect and Mechanisms. *RSC Adv.* **2013**, *3* (4), 1194–1200. https://doi.org/10.1039/C2RA21825A.

(64) Chua, C. K.; Pumera, M. The Reduction of Graphene Oxide with Hydrazine: Elucidating Its Reductive Capability Based on a Reaction-Model Approach. *Chem. Commun.* **2016**, *52* (1), 72–75. https://doi.org/10.1039/C5CC08170J.

(65) Che, J.; Shen, L.; Xiao, Y. A New Approach to Fabricate Graphene Nanosheets in Organic Medium: Combination of Reduction and Dispersion. *J. Mater. Chem.* **2010**, *20* (9), 1722. https://doi.org/10.1039/b922667b.

(66) Some, S.; Bhunia, P.; Hwang, E.; Lee, K.; Yoon, Y.; Seo, S.; Lee, H. Can Commonly Used Hydrazine Produce N-Type Graphene? *Chem. Eur. J.* **2012**, 6.

(67) Sygellou, L.; Paterakis, G.; Galiotis, C.; Tasis, D. Work Function Tuning of Reduced Graphene Oxide Thin Films. *The Journal of Physical Chemistry C* **2016**, *120* (1), 281–290. https://doi.org/10.1021/acs.jpcc.5b09234.

(68) Xu, Y.; Lin, Z.; Zhong, X.; Huang, X.; Weiss, N. O.; Huang, Y.; Duan, X. Holey Graphene Frameworks for Highly Efficient Capacitive Energy Storage. *Nat Commun* **2014**, *5* (1), 4554. https://doi.org/10.1038/ncomms5554.

(69) Bai, Y.; Yang, X.; He, Y.; Zhang, J.; Kang, L.; Xu, H.; Shi, F.; Lei, Z.; Liu, Z.-H. Formation Process of Holey Graphene and Its Assembled Binder-Free Film Electrode with High Volumetric Capacitance. *Electrochimica Acta* **2016**, *187*, 543–551.

https://doi.org/10.1016/j.electacta.2015.11.090.

(70) Li, J.; Ji, B.; Jiang, R.; Zhang, P.; Chen, N.; Zhang, G.; Qu, L. Hierarchical Hole-Enhanced 3D Graphene Assembly for Highly Efficient Capacitive Deionization. *Carbon* **2018**, *129*, 95–103. https://doi.org/10.1016/j.carbon.2017.11.095.

(71) Chen, X.; Feng, Z.; Gohil, J.; Stafford, C. M.; Dai, N.; Huang, L.; Lin, H. Reduced Holey Graphene Oxide Membranes for Desalination with Improved Water Permeance. *ACS Appl. Mater. Interfaces* **2020**, *12* (1), 1387–1394. https://doi.org/10.1021/acsami.9b19255.

(72) Siokou, A.; Ravani, F.; Karakalos, S.; Frank, O.; Kalbac, M.; Galiotis, C. Surface Refinement and Electronic Properties of Graphene Layers Grown on Copper Substrate: An XPS, UPS and EELS Study. *Applied Surface Science* **2011**, *257* (23), 9785–9790. https://doi.org/10.1016/j.apsusc.2011.06.017.

(73) Sygellou, L.; Viskadouros, G.; Petridis, C.; Kymakis, E.; Galiotis, C.; Tasis, D.; Stratakis, E. Effect of the Reduction Process on the Field Emission Performance of Reduced Graphene Oxide Cathodes. *RSC Adv.* **2015**, *5* (66), 53604–53610. https://doi.org/10.1039/C5RA08633G.

(74) Al-Gaashani, R.; Najjar, A.; Zakaria, Y.; Mansour, S.; Atieh, M. A. XPS and Structural Studies of High Quality Graphene Oxide and Reduced Graphene Oxide Prepared by Different Chemical Oxidation Methods. *Ceramics International* **2019**, *45* (11), 14439–14448. https://doi.org/10.1016/j.ceramint.2019.04.165.

(75) Kovtun, A.; Jones, D.; Dell'Elce, S.; Treossi, E.; Liscio, A.; Palermo, V. Accurate Chemical Analysis of Oxygenated Graphene-Based Materials Using X-Ray Photoelectron Spectroscopy. *Carbon* **2019**, *143*, 268–275. https://doi.org/10.1016/j.carbon.2018.11.012.

(76) Morgan, D. J. Comments on the XPS Analysis of Carbon Materials. *C* **2021**, *7* (3), 51. https://doi.org/10.3390/c7030051.

(77) Soulmi, N.; Dambournet, D.; Rizzi, C.; Sirieix-Plénet, J.; Duttine, M.; Wattiaux, A.; Swiatowska, J.; Borkiewicz, O. J.; Groult, H.; Gaillon, L. Structural and Morphological Description of Sn/SnO_x Core–Shell Nanoparticles Synthesized and Isolated from Ionic Liquid. *Inorganic Chemistry* **2017**, *56* (16), 10099–10106. https://doi.org/10.1021/acs.inorgchem.7b01850.

(78) Soulmi, N. Mise au point de nouveaux procédés d'élaboration en milieu liquide ionique de nanomatériaux à base d'étain en vue de leur utilisation comme électrode négative de batterie Li-ion, Université Pierre et Marie Curie - Paris VI, 2017.

(79) Dong, H.; Chen, Y.-C.; Feldmann, C. Polyol Synthesis of Nanoparticles: Status and Options Regarding Metals, Oxides, Chalcogenides, and Non-Metal Elements. *Green Chemistry* **2015**, *17* (8), 4107–4132. https://doi.org/10.1039/C5GC00943J.

(80) Jo, Y. H.; Jung, I.; Choi, C. S.; Kim, I.; Lee, H. M. Synthesis and Characterization of Low Temperature Sn Nanoparticles for the Fabrication of Highly Conductive Ink. *Nanotechnology* **2011**, *22* (22), 225701. https://doi.org/10.1088/0957-4484/22/22/225701.

(81) Chee, S.-S.; Lee, J.-H. Synthesis of Sub-10-nm Sn Nanoparticles from Sn(II) 2-Ethylhexanoate by a Modified Polyol Process and Preparation of AgSn Film by Melting of the Sn Nanoparticles. *Thin Solid Films* **2014**, *562*, 211–217. https://doi.org/10.1016/j.tsf.2014.04.061.

(82) Sharma, S.; Das, S.; Khosla, R.; Shrimali, H.; Sharma, S. K. Highly UV Sensitive Sn Nanoparticles Blended with Polyaniline onto Micro-Interdigitated Electrode Array for UV-C Detection Applications. *Journal of Materials Science: Materials in Electronics* **2019**, *30* (8), 7534–7542. https://doi.org/10.1007/s10854-019-01067-9.

(83) Egeberg, A.; Seifert, T. P.; Roesky, P. W.; Gerthsen, D.; Feldmann, C. One-Pot Synthesis of

Reactive Base Metal Nanoparticles in Multifunctional Pyridine. *ACS Omega* **2019**, *4* (4), 7096–7102. https://doi.org/10.1021/acsomega.9b00136.

(84) Riedel, O.; Düttmann, A.; Dühnen, S.; Kolny-Olesiak, J.; Gutsche, C.; Parisi, J.; Winter, M.; Knipper, M.; Placke, T. Surface-Modified Tin Nanoparticles and Their Electrochemical Performance in Lithium Ion Battery Cells. *ACS Applied Nano Materials* **2019**. https://doi.org/10.1021/acsanm.9b00544.

(85) Lidor-Shalev, O.; Zitoun, D. Reaction Mechanism of "Amine–Borane Route" towards Sn, Ni, Pd, Pt Nanoparticles. *RSC Adv.* **2014**, *4* (109), 63603–63610. https://doi.org/10.1039/C4RA11483C.

(86) Sanyal, U.; Jagirdar, B. R. Metal and Alloy Nanoparticles by Amine-Borane Reduction of Metal Salts by Solid-Phase Synthesis: Atom Economy and Green Process. *Inorg. Chem.* **2012**, *51* (23), 13023–13033. https://doi.org/10.1021/ic3021436.

(87) Li, Z.; Tao, X.; Cheng, Y.; Wu, Z.; Zhang, Z.; Dang, H. A Facile Way for Preparing Tin Nanoparticles from Bulk Tin via Ultrasound Dispersion. *Ultrasonics Sonochemistry* **2007**, *14* (1), 89–92. https://doi.org/10.1016/j.ultsonch.2005.11.008.

(88) Bolm, C. Mechanochemistry - an Enabling Technique for Synthesis and Catalysis, 2019.

(89) McCabe, W. L.; Smith, J. C.; Harriott, P. *Unit Operations of Chemical Engineering*, 5th ed.; McGraw-Hill: New York, 1993.

(90) Σδούκος, Α. Θ. *Φυσικές Διεργασίες της Χημικής Τεχνολογίας*, 1st ed.; Πανεπιστήμιο Ιωαννίνων: Ιωάννινα, 1982; Vol. 1. (Sdoukos, A. T. Physical Processes of Chemical Technology, 1st ed.; University of Ioannina: Ioannina, 1982; Vol. 1 – text in Greek)

(91) Colombo, I.; Grassi, G.; Grassi, M. Drug Mechanochemical Activation. *Journal of Pharmaceutical Sciences* **2009**, *98* (11), 3961–3986. https://doi.org/10.1002/jps.21733.

(92) Peltonen, L.; Hirvonen, J. Pharmaceutical Nanocrystals by Nanomilling: Critical Process Parameters, Particle Fracturing and Stabilization Methods. *Journal of Pharmacy and Pharmacology* **2010**, *62* (11), 1569–1579. https://doi.org/10.1111/j.2042-7158.2010.01022.x.

(93) Koch, C. C.; Cho, Y. S. Nanocrystals by High Energy Ball Milling. *Nanostructured Materials* **1992**, *1* (3), 207–212. https://doi.org/10.1016/0965-9773(92)90096-G.

(94) Jeon, I.-Y.; Shin, Y.-R.; Sohn, G.-J.; Choi, H.-J.; Bae, S.-Y.; Mahmood, J.; Jung, S.-M.; Seo, J.-M.; Kim, M.-J.; Wook Chang, D.; Dai, L.; Baek, J.-B. Edge-Carboxylated Graphene Nanosheets via Ball Milling. *Proceedings of the National Academy of Sciences* **2012**, *109* (15), 5588–5593. https://doi.org/10.1073/pnas.1116897109.

(95) Zaluski, L.; Tessier, P.; Ryan, D. H.; Doner, C. B.; Zaluska, A.; Ström-Olsen, J. O.; Trudeau, M. L.; Schulz, R. Amorphous and Nanocrystalline Fe–Ti Prepared by Ball Milling. *J. Mater. Res.* **1993**, *8* (12), 3059–3068. https://doi.org/10.1557/JMR.1993.3059.

(96) Peigney, A.; Laurent, Ch.; Flahaut, E.; Bacsa, R. R.; Rousset, A. Specific Surface Area of Carbon Nanotubes and Bundles of Carbon Nanotubes. *Carbon* **2001**, *39* (4), 507–514. https://doi.org/10.1016/S0008-6223(00)00155-X.

(97) Allen, G. L.; Bayles, R. A.; Gile, W. W.; Jesser, W. A. Small Particle Melting of Pure Metals. *Thin Solid Films* **1986**, *144* (2), 297–308. https://doi.org/10.1016/0040-6090(86)90422-0.

(98) Sun, P.-L.; Wu, S.-P.; Chin, T.-S. Melting Point Depression of Tin Nanoparticles Embedded in a Stable Alpha-Alumina Matrix Fabricated by Ball Milling. *Materials Letters* **2015**, *144*, 142–145. https://doi.org/10.1016/j.matlet.2015.01.027.

(99) Zhang, P.; Ma, L.; Fan, F.; Zeng, Z.; Peng, C.; Loya, P. E.; Liu, Z.; Gong, Y.; Zhang, J.; Zhang, X.; Ajayan, P. M.; Zhu, T.; Lou, J. Fracture Toughness of Graphene. *Nature*

Communications **2014**, *5* (1). https://doi.org/10.1038/ncomms4782.

(100) Sinha, S. K.; Sirota, E. B.; Garoff, S.; Stanley, H. B. X-Ray and Neutron Scattering from Rough Surfaces. *Phys. Rev. B* **1988**, *38* (4), 2297–2311. https://doi.org/10.1103/PhysRevB.38.2297.

(101) Tang, W.; Lou, H.; Li, Y.; Kong, X.; Wu, Y.; Gu, X. Ionic Liquid Modified Graphene Oxide-PEBA Mixed Matrix Membrane for Pervaporation of Butanol Aqueous Solutions. *Journal of Membrane Science* **2019**, *581*, 93–104. https://doi.org/10.1016/j.memsci.2019.03.049.

(102) Mu, L.; Shi, Y.; Guo, X.; Zhuang, W.; Chen, L.; Ji, T.; Hua, J.; Wang, H.; Zhu, J. Grafting Heteroelement-Rich Groups on Graphene Oxide: Tuning Polarity and Molecular Interaction with Bio-Ionic Liquid for Enhanced Lubrication. *Journal of Colloid and Interface Science* **2017**, *498*, 47–54. https://doi.org/10.1016/j.jcis.2017.03.044.

(103) Yang, H.; Shan, C.; Li, F.; Han, D.; Zhang, Q.; Niu, L. Covalent Functionalization of Polydisperse Chemically-Converted Graphene Sheets with Amine-Terminated Ionic Liquid. *Chemical Communications* **2009**, No. 26, 3880. https://doi.org/10.1039/b905085j.

(104) Karousis, N.; Economopoulos, S. P.; Sarantopoulou, E.; Tagmatarchis, N. Porphyrin Counter Anion in Imidazolium-Modified Graphene-Oxide. *Carbon* **2010**, *48* (3), 854–860. https://doi.org/10.1016/j.carbon.2009.10.039.

(105) Zhang, X.; Hou, L.; Richard, F.; Samorì, P. Modular Preparation of Graphene-Based Functional Architectures through Two-Step Organic Reactions: Towards High-Performance Energy Storage. *Chem. Eur. J.* **2018**, *24* (69), 18518–18528. https://doi.org/10.1002/chem.201803184.

(106) Bonollo, S.; Lanari, D.; Vaccaro, L. Ring-Opening of Epoxides in Water. *Eur. J. Org. Chem.* **2011**, *2011* (14), 2587–2598. https://doi.org/10.1002/ejoc.201001693.

(107) Montalbetti, C. A. G. N.; Falque, V. Amide Bond Formation and Peptide Coupling. *Tetrahedron* **2005**, *61* (46), 10827–10852. https://doi.org/10.1016/j.tet.2005.08.031.

(108) *Nucleophilic Addition of Amines- Imine and Enamine Formation*. https://chem.libretexts.org/@go/page/36388 (accessed 2021-12-01).

(109) Zhang, Y.; Shen, Y.; Yuan, J.; Han, D.; Wang, Z.; Zhang, Q.; Niu, L. Design and Synthesis of Multifunctional Materials Based on an Ionic-Liquid Backbone. *Angewandte Chemie International Edition* **2006**, *45* (35), 5867–5870. https://doi.org/10.1002/anie.200600120.

(110) Wang, Z.; Zhang, Q.; Kuehner, D.; Xu, X.; Ivaska, A.; Niu, L. The Synthesis of Ionic-Liquid-Functionalized Multiwalled Carbon Nanotubes Decorated with Highly Dispersed Au Nanoparticles and Their Use in Oxygen Reduction by Electrocatalysis. *Carbon* **2008**, *46* (13), 1687–1692. https://doi.org/10.1016/j.carbon.2008.07.020.

(111) Zhang, Y.; Shen, Y.; Han, D.; Wang, Z.; Song, J.; Li, F.; Niu, L. Carbon Nanotubes and Glucose Oxidase Bionanocomposite Bridged by Ionic Liquid-like Unit: Preparation and Electrochemical Properties. *Biosensors and Bioelectronics* **2007**, *23* (3), 438–443. https://doi.org/10.1016/j.bios.2007.06.010.

(112) Bhunia, P.; Hwang, E.; Min, M.; Lee, J.; Seo, S.; Some, S.; Lee, H. A Non-Volatile Memory Device Consisting of Graphene Oxide Covalently Functionalized with Ionic Liquid. *Chem. Commun.* **2012**, *48* (6), 913–915. https://doi.org/10.1039/C1CC16225J.

(113) Song, G.; Cai, Y.; Peng, Y. Amino-Functionalized Ionic Liquid as A Nucleophilic Scavenger in Solution Phase Combinatorial Synthesis. *Journal of Combinatorial Chemistry* **2005**, *7* (4), 561–566. https://doi.org/10.1021/cc049844v.

(114) Hu, Y.; Hua, S.; Li, F.; Jiang, Y.; Bai, X.; Li, D.; Niu, L. Green-Synthesized Gold Nanoparticles Decorated Graphene Sheets for Label-Free Electrochemical Impedance

DNA Hybridization Biosensing. *Biosensors and Bioelectronics* **2011**, *26* (11), 4355–4361. https://doi.org/10.1016/j.bios.2011.04.037.

(115) Zhuang, X.; Wang, H.; He, T.; Chen, L. Enhanced Voltammetric Determination of Dopamine Using a Glassy Carbon Electrode Modified with Ionic Liquid-Functionalized Graphene and Carbon Dots. *Microchim Acta* **2016**, *183* (12), 3177–3182. https://doi.org/10.1007/s00604-016-1971-8.

(116) Saha, S.; Das, A.; Acharjee, K.; Sinha, B. Synthesis, Characterization and Antibacterial Studies of Mn(II) and Co(II) Complexes of an Ionic Liquid Tagged Schiff Base. *J Serb Chem Soc* **2016**, *81* (10), 1151–1159. https://doi.org/10.2298/JSC160425065S.

(117) Sun, Y.; Huang, H.; Vardhan, H.; Aguila, B.; Zhong, C.; Perman, J. A.; Al-Enizi, A. M.; Nafady, A.; Ma, S. Facile Approach to Graft Ionic Liquid into MOF for Improving the Efficiency of CO_2 Chemical Fixation. *ACS Appl. Mater. Interfaces* **2018**, *10* (32), 27124–27130. https://doi.org/10.1021/acsami.8b08914.

(118) Busetto, L.; Cristina Cassani, M.; Femoni, C.; Macchioni, A.; Mazzoni, R.; Zuccaccia, D. Synthesis, Molecular Structures and Solution NMR Studies of N-Heterocyclic Carbene–Amine Silver Complexes. *Journal of Organometallic Chemistry* **2008**, *693* (15), 2579–2591. https://doi.org/10.1016/j.jorganchem.2008.04.030.

(119) Matiello, G. I.; Pazini, A.; da Silva, K. I. M.; da Costa, R. G. M.; Ebeling, G.; Dupont, J.; Limberger, J.; Scholten, J. D. Isothiouronium Salts as Useful and Odorless Intermediates for the Synthesis of Thiaalkylimidazolium Ionic Liquids. *Tetrahedron Letters* **2019**, *60* (11), 780–784. https://doi.org/10.1016/j.tetlet.2019.02.013.

(120) Boyer, J. H. Reduction of Organic Azides to Primary Amines with Lithium Aluminum Hydride. *J. Am. Chem. Soc.* **1951**, *73* (12), 5865–5866. https://doi.org/10.1021/ja01156a507.

(121) Takamuku, T.; Hoke, H.; Idrissi, A.; Marekha, B. A.; Moreau, M.; Honda, Y.; Umecky, T.; Shimomura, T. Microscopic Interactions of the Imidazolium-Based Ionic Liquid with Molecular Liquids Depending on Their Electron-Donicity. *Phys. Chem. Chem. Phys.* **2014**, *16* (43), 23627–23638. https://doi.org/10.1039/C4CP03565H.

(122) Zhou, Y.; Gong, S.; Xu, X.; Yu, Z.; Kiefer, J.; Wang, Z. The Interactions between Polar Solvents (Methanol, Acetonitrile, Dimethylsulfoxide) and the Ionic Liquid 1-Ethyl-3-Methylimidazolium Bis(Fluorosulfonyl)Imide. *Journal of Molecular Liquids* **2020**, *299*, 112159. https://doi.org/10.1016/j.molliq.2019.112159.

(123) Holtstiege, F.; Bärmann, P.; Nölle, R.; Winter, M.; Placke, T. Pre-Lithiation Strategies for Rechargeable Energy Storage Technologies: Concepts, Promises and Challenges. *Batteries* **2018**, *4* (1), 4. https://doi.org/10.3390/batteries4010004.

(124) Cao, Y.; Mu, T. Comprehensive Investigation on the Thermal Stability of 66 Ionic Liquids by Thermogravimetric Analysis. *Ind. Eng. Chem. Res.* **2014**, *53* (20), 8651–8664. https://doi.org/10.1021/ie5009597.

(125) Rochelle, G. T. Thermal Degradation of Amines for CO2 Capture. *Current Opinion in Chemical Engineering* **2012**, *1* (2), 183–190. https://doi.org/10.1016/j.coche.2012.02.004.

(126) Khandkar, A. C.; Wagner, J. B. On the Thermodynamics of $LiBr{\cdot}xH_2O$(X=0, 1/2, 1) and Electrical Conductivity of $LiBr{\cdot}xH_2O(Al_2O_3)$ Composites. *Solid State Ionics* **1986**, *20* (4), 9. https://doi.org/10.1016/0167-2738(86)90045-7.

(127) Apelblat, A.; Tamir, A. Enthalpy of Solution of Lithium Bromide, Lithium Bromide Monohydrate, and Lithium Bromide Dihydrate, in Water at 298.15 K. *The Journal of Chemical Thermodynamics* **1986**, *18* (3), 201–212. https://doi.org/10.1016/0021-9614(86)90048-0.

(128) Lefebvre, E.; Bennici, S.; Gagnière, E.; Mangin, D.; Auroux, A. Hydration Characteristics of Lithium, Zinc, Potassium and Sodium Salts. *MATEC Web of Conferences* **2013**, *3*, 01003. https://doi.org/10.1051/matecconf/20130301003.

(129) Herold, K. E.; Radermacher, R.; Klein, S. A. *Absorption Chillers and Heat Pumps*, 2nd ed.; CRC Press, 2016.

(130) Almatarneh, M. H.; Altarawneh, M.; Poirier, R. A.; Saraireh, I. A. High Level Ab Initio, DFT, and RRKM Calculations for the Unimolecular Decomposition Reaction of Ethylamine. *Journal of Computational Science* **2014**, *5* (4), 568–575. https://doi.org/10.1016/j.jocs.2014.02.003.

(131) Cho, J.; Choi, C. H. Thermal Decomposition Mechanisms of Methylamine, Ethylamine, and 1-Propylamine on Si(100)-2 × 1 Surface. *The Journal of Chemical Physics* **2011**, *134* (19), 194701. https://doi.org/10.1063/1.3589362.

(132) Fogarty, W. D. Preparation and Characterisation of Ionic Liquids and Investigations into Their Potential Use in the Absorption and Sequestration of Carbon Dioxide, 2013.

(133) Dou, H.; Gao, S.-Y.; Fu, Z.-L.; Liu, S.-Z. Improved Synthesis of Substituted 2-Amino-4H-Chromene Derivatives Catalyzed by a New Amino-Functionalized Basic Ionic Liquid 1-(2-Aminoethyl)-3-Methylimidazolium Imidazolide. *Chinese Journal of Organic Chemistry* **2011**, *31* (07), 1056.

Chapter 3:
Assembly of composite materials

The goal was to prepare a self-supporting material with a high lithiation capacity, based on its tin content, with a form capable of adapting to the structural changes during cycling, that would also maintain a high electrical conductivity. Up to this point, the focus had been placed on establishing and optimizing the preparative methods and the various treatments for the three components of the ternary composite material: the graphene-based matrix, the tin nanoparticles and the functionalized EMI^+TFSI^- ionic liquid. In order to assemble the composite material to be used as a Li-ion battery anode, the first step consisted in preparing the ionic-liquid-functionalized graphene oxide matrix and the second step in incorporating the tin nanoparticles. For the first step, the aminated ionic liquid in its brominated form would be grafted onto graphene oxide. The bromide counter-ions would then be exchanged for $TFSI^-$ *in situ*, in order to obtain a system close to that in which the favorable interactions of the IL and the tin nanoparticles had been observed. For the second step, the tin nanoparticles would be mixed at several loading percentages with the IL-modified GO suspension, which would then be freeze-cast and afterwards annealed to produce the basic form of the electrode. Accordingly, tin content could allow a high lithiation capacity, and the graphene scaffolds should be able to buffer the structural modification during cycling as well as meet the high conductivity requirements. Subsequent improvements would have comprised grafting the aminated IL onto holey graphene oxide in order to enhance the diffusion of lithium ions, the treatment of the aerogels with hydrazine vapors to modify the structure and potentially increase the conductivity and/or a combination of the two. Identifying the degree of compression of the material that would give the best balance between gravimetric capacity, volumetric capacity and adequate charge-discharge rates would be an integral part of the optimization process. Finally, a preparation of GO dough, made from the ionic-liquid-functionalized graphene oxide could also be attempted.

From the onset, a number of questions regarding the nature of the final material would be difficult to answer. The ionic liquid actually can be grafted, but it can also remain adsorbed via π-π interactions. A few similar systems, where an imidazolium-based ionic species has been grafted onto graphene oxide have been described in the literature[1–3], yet

they presented no evidence that the imidazolium cation was indeed grafted and not adsorbed. The exact amount of grafted IL would have to be determined. At last, the ternary material could retain its functionality after annealing, but the thermal treatment could also destroy the organic molecules and cause the tin to melt away.

Besides presenting the synthetic and experimental procedures employed in the preparation and characterization of ternary materials, this chapter attempts to provide answers to the above points.

1. GO – EMI^+TFSI^- binary systems

Several experiments were conducted using mixtures of graphene oxide with the EMI^+TFSI^- ionic liquid. This was done in an attempt to anticipate the properties of the functionalized graphene oxide. These mixtures were used to prepare membranes and aerogels. For these experiments, the mixtures contained 10 wt% IL.

EMI^+TFSI^- is immiscible with water. When it was added to aqueous suspensions of GO at [GO] ≥ 8 mg/mL and after homogenization by shaking vigorously for a few seconds, emulsions[4] formed. It would appear that the coexistence of polar groups and sp^2 domains on the graphene oxide sheets enabled it to play the role of an emulsifier, with the water molecules attracted to the oxygen-bearing functional groups and the EMI^+ cation probably adsorbed on the conjugated systems. The amphiphilic character of GO has been reported in similar studies[5]. Upon addition of the IL at a 9:1 GO:IL mass ratio, suspensions of GO with a concentration of 8 mg/mL became much more viscous and suspensions with a concentration of 16 mg/mL nearly gelled. As a test, a series of GO suspensions at 8 mg/mL, but with higher mass loadings of IL, 30 wt%, 60 wt% and 80 wt% was also prepared. These mixtures were homogenized in a bath sonicator and within seconds, they all formed thick gels.

After freeze-casting the IL and GO mixtures with initial concentrations of GO of 8 and 16 mg/mL, the obtained aerogel monoliths exhibited noticeably enhanced mechanical properties. They were less fragile and easier to handle and process. Aerogels made solely from GO had a gray-brown or gray-black color, depending on initial GO concentration, with the less concentrated suspensions producing lighter colored monoliths. Even though $EMI^{+}TFSI^{-}$ itself is colorless, the aerogels made from the IL and GO mixtures had a green-gray hue.

The mixed aerogels were subjected to thermal annealing at 200°C for 2 h under vacuum. Samples of the aerogels before and after annealing were examined via several spectroscopic techniques (ATR-IR, Raman, solid state ^{1}H NMR), in order to confirm the presence of the $EMI^{+}TFSI^{-}$ ionic liquid in the structures. However, that was not possible, as only the signals from graphene oxide were apparent and not those from the IL. The existence of S, N and F from the IL ions in the same samples was verified by EDX analyses of the monoliths, but the loose nature of the aerogels precluded obtaining accurate atomic counts, with the amounts of each element and the proportions between them varying widely in each of the targeted areas, so no meaningful conclusions could be reached. However, in samples that were thermally annealed at temperatures higher than 400°C, there would always be dark stains around the monoliths, which never happened for monoliths of pure GO. Also, the quartz tubes in which the samples were heated would always exhibit signs of hydrogen fluoride attack. Since neither was ever observed for samples reduced at 200°C, a temperature well below the reported decomposition threshold[6] for $EMI^{+}TFSI^{-}$, it was deduced that the selected thermal treatment did not affect the ionic liquid.

In order to make membranes, the same protocol as before was employed (Chapter 2, section 1.6.1), *i.e.* placing the suspensions of various GO concentrations (4 to 20 mg/mL) and 10 wt% IL in a wide container and heating them at a controlled temperature of 45°C under air, to evaporate the water. However, when most of the water had evaporated, the GO mixed with the IL begun to reorganize into uneven lumps, preventing the formation of membranes

(Figure 3.1). The same results were obtained for various GO concentrations (4 to 20 mg/mL) and also when trying to obtain films by filtration of the suspensions[7] (which can accelerate the assembly of the membranes, compared to evaporation) onto PTFE or cellulose membranes.

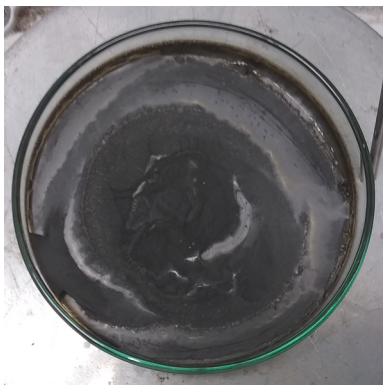

Figure 3.1: An almost dried 8 mg/mL aqueous suspension of GO with 10 wt% EMI^+TFSI^-, set to evaporate in a Petri dish, placed on a hotplate at 45°C.

Graphene oxide aerogels were also moistened with EMI^+TFSI^- until they could be worked into a dough. The resulting malleable, disordered structures could be given virtually any form, but they exhibited no porosity, as revealed by SEM imaging. Furthermore, the simultaneous addition of water and ionic liquid, that could lead to an eventual porosity after drying or thermal reduction, was not possible. GO aerogels that had been wet with ionic liquid did not allow water to permeate their structure. Kneading them resulted in a friable dried-gel-like texture. The same result was obtained if the aerogels were wet first with water and then with the IL. It appeared that the ionic liquid, rendered the GO sheets waterproof as it prevented the incorporation of water into the dough.

1.1. Preparation of EMI^+TFSI^- IL and GO suspensions

In a typical preparation, 5.9 µL or 11.7 µL of EMI^+TFSI^- (density: 1.52 g/cm^3) was added to 10 mL of a GO suspension of 8 mg/mL or 16 mg/mL, respectively. The mixtures were placed in vials, which were sealed and shaken vigorously by hand for a few seconds. The resulting

suspensions had a mass ratio of GO:EMI^+TFSI^- of 9:1.

1.2. Preparation of aerogels from EMI^+TFSI^- IL and GO suspensions

The freeze-casting apparatus presented in Chapter 2.1 was used for the unidirectional freezing of the samples. The suspensions were set to equilibrate at 20°C and then they were frozen at a rate of 10°C/min, until they reached - 80°C and they had completely solidified. The frozen suspensions were stored in containers submerged in liquid N_2 until they were lyophilized at a pressure of 0.01 mbar for at least 48 hours. Once all of the water had been removed, the samples were brought to ambient pressure and the aerogel monoliths were removed from the tubes with the help of a plastic piston.

Samples made from the 8 mg/mL suspensions that were to be thermally reduced, were placed as they were in Petri dishes and brought to the vacuum oven. Samples made from the 16 mg/mL suspensions were first sliced into approximately 2-mm-thick disks, in order to avoid explosive exfoliation during the treatment.

Materials. *EMI^+TFSI^- (purity 99.9%) was purchased from Solvionic, aqueous suspensions of graphene oxide at concentrations of 8 mg/mL and 16 mg/mL were prepared as described in Chapter 2.1.*

1.3. Structural investigations

To examine what effect – if any – the addition of the ionic liquid had to the microstructure of the aerogels, they were observed under a scanning electron microscope, after thermal reduction, to facilitate image acquisition.

1.3.1. Scanning electron microscopy

Aerogels made from GO suspensions with concentrations of 8 and 16 mg/mL with 10 wt% EMI^+TFSI^- were sliced after thermal reduction with a razor blade into disks, perpendicularly to the ice growth axis. The disks were then cut along their diameter, in order to reveal the development of the porous network. Images of samples made from both groups of suspensions are presented in Figure 3.2.

Samples of rGO made from suspensions with [GO] = 8 mg/mL with 10 wt% EMI^+TFSI^- are highly anisotropic and present an ordered network structure (Fig. 3.2a, 3.2b), much like the samples made just with GO at the same concentration (Chapter 2, Fig. 2.19). While the pure GO aerogels were fragile and very few structures were observed under the microscope

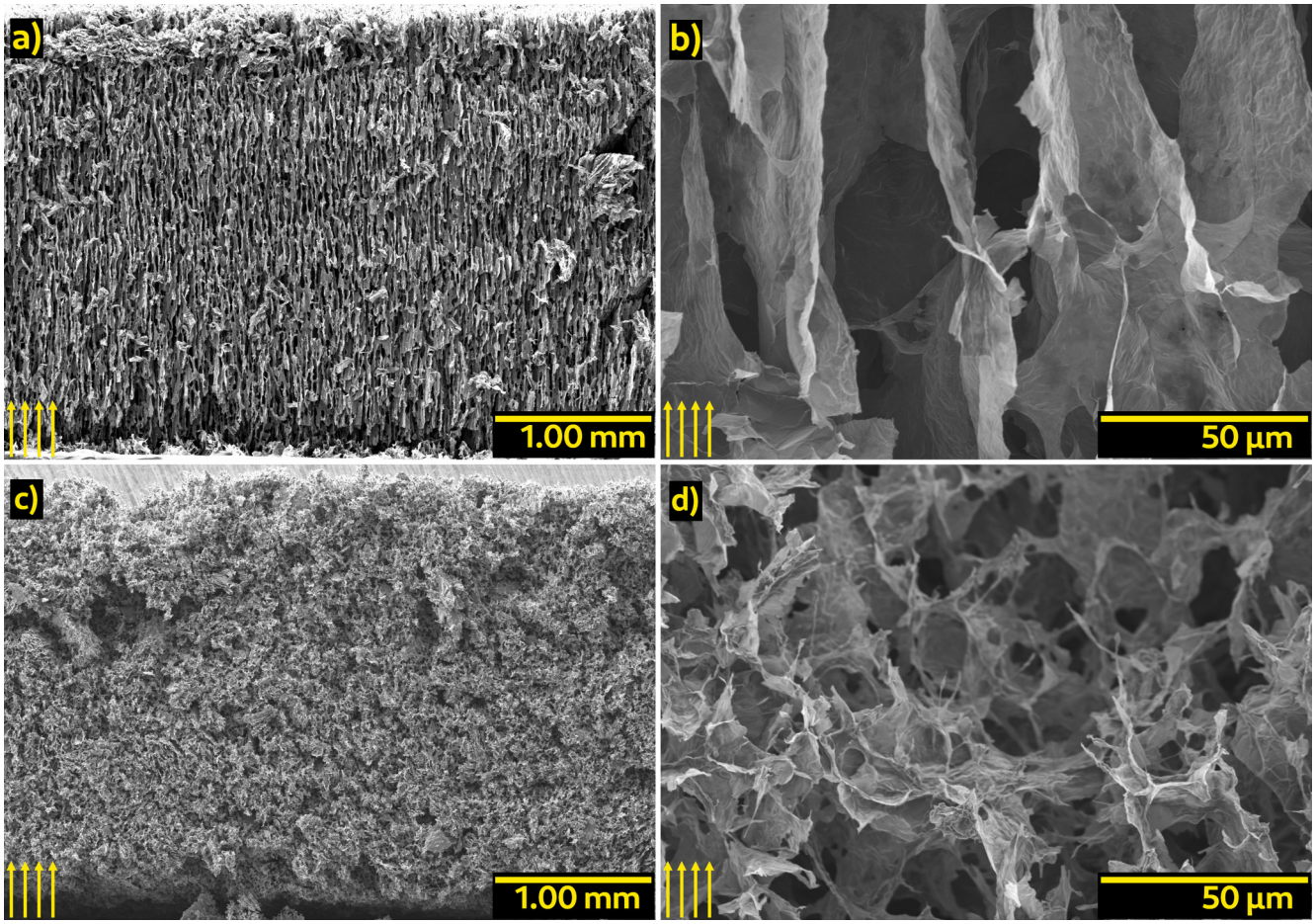

Figure 3.2: SEM images of rGO aerogels made from (a, b) 8 mg/mL and (c, d) 16 mg/mL GO suspensions in water with 10 wt% EMI^+TFSI^-. The arrows mark the direction of the ice crystal growth.

intact, the pore widths appear to be in almost the same range, between 21 and 48 μm. The pores, that have a rather oval cross section, are perfectly aligned with the applied temperature gradient. In all of the observed samples, almost all the pores run the entire length of the section. Again, the pores are interconnected through the lateral growth of the ice crystals at various points.

The rGO aerogels made from suspensions with [GO] = 16 mg/mL with 10 wt% $EMI^{+}TFSI^{-}$ (Fig. 3.2c, 3.2d) exhibit the same "cellular" structure as their counterparts made just from graphene oxide at the same concentration (Chapter 2, Fig. 2.18). However, almost all of the anisotropy has disappeared, with the interconnected cavities being much more disordered and with similar dimensions in all directions. While the form made measurements difficult, cavity dimensions were measured in the range of 23 to 39 μm. Close inspection of the cavities reveals at times that they are only slightly elongated in the general direction of the ice crystal growth. Nevertheless, it is impossible to deduce the direction of the temperature gradient from the cross-sectional view of the structure (Fig. 3.2c).

Compared to aerogels made from GO suspensions, the sheets in the aerogels made from the IL and GO mixtures appear to be a little more wrinkled. This is true for both series of samples (8 and 16 mg/mL), regardless of concentration. Furthermore, the edges of the sheets and some of the smaller sheets appear rolled up, especially in the 16 mg/mL aerogel, where this is much more pronounced (Fig. 3.2d). A recent study on the use of binary solvent mixtures[8] with sufficiently different boiling points in the lyophilization of GO suspensions has shown that this is the result of uneven surface tension on the two sides of a layer, as one of the solvents sublimates (in this case water), while the solvent with the higher boiling point (here the ionic liquid) remains adsorbed on the sheets.

1.3.2. N_2 porosimetry

The freeze-casting processing technique is known to produce macroporous structures[9]. The porous system of the aerogels was even visible to the naked eye and much more so under the scanning electron microscope. Gas adsorption porosimetry does not provide for macroporous networks the same type of information that can be deduced for microporous and mesoporous systems (*e.g.* average pore size, pore size distribution, pore organization, *etc.*). It was nonetheless decided to analyze the disordered monoliths, *i.e.* aerogels via N_2 adsorption – desorption, in case there was some other organization at lower scales in the structure, that was not apparent in the SEM images. It should be noted that due to their kinetic diameter (3.64 Å[10]), nitrogen molecules cannot probe the sp^2 stacked surfaces that are accessible to lithium ions (0.59 Å). For this reason, the specific surface area of graphite and related materials as determined by gas adsorption[11,12] is two to three orders of magnitude lower than the calculated specific surface area of graphene[13].

The adsorption – desorption isotherms are presented in Figure 3.3.

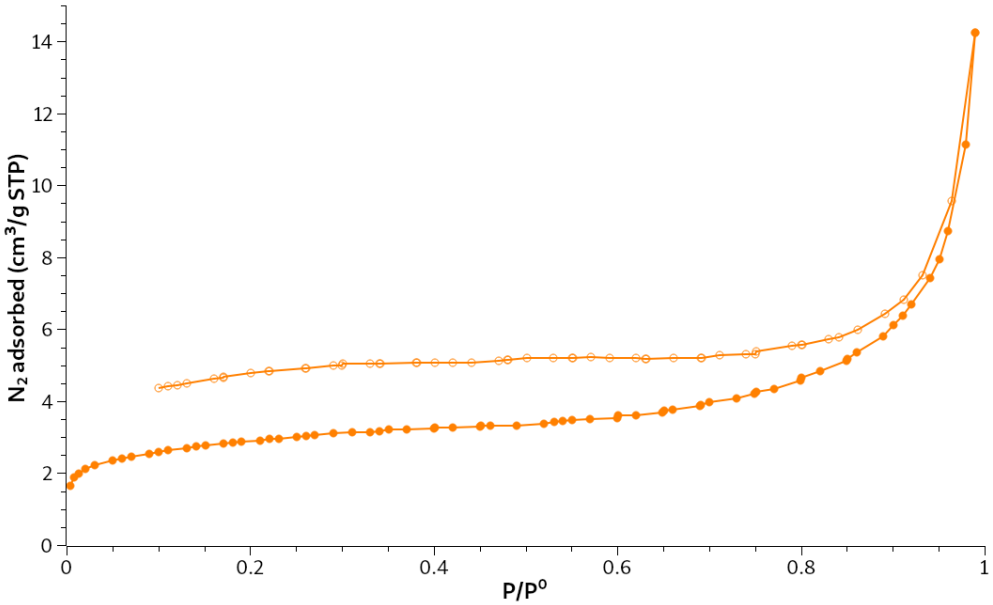

Figure 3.3: Adsorption (orange curve) – desorption (light orange curve) isotherms of an aerogel with disordered structure made from a GO and EMI^+TFSI^- mixture.

The adsorption isotherm is characteristic of the physisorption of gases on nonporous and

macroporous adsorbents (Type II according to the IUPAC classification[14]). The knee at low P/P^0 – where the slope changes before the almost linear middle section – is rather well-defined, suggesting that monolayer coverage is almost complete before multilayer adsorption begins. The sharp uptake increase close to $P/P^0 = 1$ is indicative of unrestricted multilayer adsorption.

The desorption isotherm presents a hysteresis loop characteristic of narrow slit pores, formed by flexible, plate-like particles, which perfectly describes the GO sheets (resembling an H4 Type, according to the IUPAC classification). The pronounced uptake at low P/P^0 values is associated with the filling of micropores[14,15].

According to the BET theory[16], at low pressures, typically in the range of $0.05 \leq P/P^0 \leq 0.35$, only monolayer adsorption of the adsorbate takes place, which allows to estimate the surface area of the absorbent, based on the projection of the volume of the molecule used as a probe on a surface.

The experimental points in the range of relative pressures of 0.05 to 0.35 and the corresponding linear regression are shown in Figure 3.4.

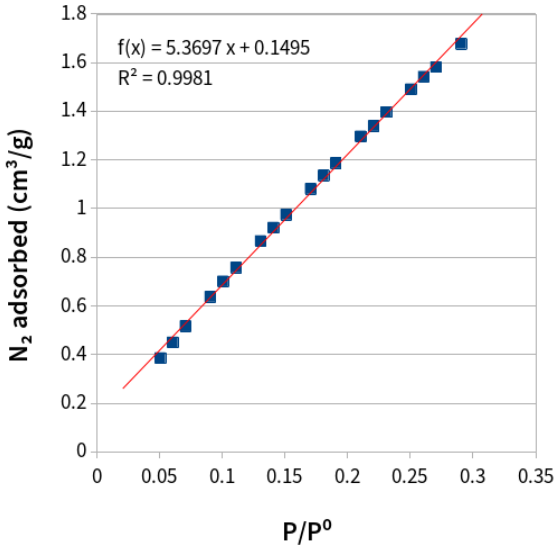

Figure 3.4: Quantity of N_2 adsorbed at relative pressures P/P^0 up to 0.35 and linear regression of the experimental points.

Using a value of 0.162 nm^2 for the cross-sectional area of the N_2 molecule[17] and based on

the linear fit of the measured values, the specific surface area of the sample is estimated to be 12.5 m^2/g, in line with what was expected for the porosity of freeze-cast materials.

Perhaps the most interesting finding of the measurement is the presence of micropores, which are responsible for the desorption hysteresis at low pressures. These could be attributed to the interlayer spacing of stacked sheets with defects, or to folds and other deformations of the GO sheets up to 20 Å, that are large enough to accommodate N_2 molecules.

Experimental details. *The porosity measurement was conducted at 77 K on a Micromeritics ASAP 2020 apparatus. After thermal reduction, a monolith that had been made from a suspension with a GO concentration of 16 mg/mL with 10 wt% ionic liquid, was cut into small (≤ 2 mm) pieces with a scalpel. These were then transferred to a sample tube. Before the measurement, the sample was degassed overnight at 110°C under high vacuum (10^{-6} bar).*

1.3.3. Conclusions

The improvement of the stability of the structures by the addition of the EMI^+TFSI^- ionic liquid was of note. A bridging effect through π-π interactions of an imidazolium-based IL on graphene sheets has already been reported[18], albeit for 1-ethyl-3-methylimidazolium chloride. Perhaps the hydrophobic character of the EMI^+TFSI^- ionic pair could play an additional role in the stabilization of the monoliths, by excluding water molecules and thus creating larger contact surfaces between the bridged sheets.

In terms of their suitability as matrices for the composite anode material, the two aerogel structures – the ordered one made from GO suspensions with a concentration of 8 mg/mL and the disordered one obtained from suspensions of GO with a concentration of 16 mg/mL – present a different trade-off between structure tortuosity and exposed surface. The ordered structure provides straight paths for the lithium ions to diffuse, but they are too wide, leaving a lot of voids. Furthermore, the walls of the pores are made up of tightly packed sheets with lengths much longer than the typical dimensions of graphite particles used in anodes. On

the other hand, the disordered cellular structure is much more tortuous. However, the available pathways are also micrometric and the cavities appear to be much more interconnected than the channels of the ordered structure. The disordered monoliths appear to have more of the sheets exposed and in thinner stacks. That could be a benefit for hosting lithium ions, as well as tin nanoparticles.

2. Grafting of 1-(2-aminoethyl)-methylimidazolium bis(trifluoromethanesulfonyl)imide onto graphene oxide

The addition of an amino group to the side chain of EMI^+ was chosen as the means to graft the cation onto graphene oxide, as it could react with several of the functional groups present on GO. The XPS analyses revealed that the oxygen atoms belonging to epoxide groups were by far the most abundant oxygen species of the synthesized graphene oxide (almost 24% atomic ratio) and validated this choice. The ionic liquid would be grafted by a reaction between its amino group and the epoxides of GO.

Nucleophilic substitution to epoxides via ring-opening results in 1,2-disubstituted products. Because of the strain on the three-membered ring, the epoxide ring-opening reaction mechanism depends on the nucleophile strength and can be both acid- and base-catalyzed, despite ether oxygens being poor leaving groups. In general, the ring opening in neutral or basic conditions usually proceeds through an S_N2 mechanism, the nucleophile attacking the least substituted position. The exact mechanism of acid-catalyzed ring opening depends on the structure of the epoxide, *i.e.* the degree of substitution of the carbon atoms, so it could undergo an S_N1 like reaction, with the nucleophile attacking the more substituted carbon[19,20]. Acid-catalyzed ring opening can take place at lower temperatures, whereas base-catalyzed ring-opening usually requires heating[20]. The hydrolysis of epoxides, whether acid- or base-catalyzed, produces anti vicinal diols (1,2-diols), also called glycols.

In the grafting reaction, the terminal amine group that has been added to the EMI^+ cation will attack the carbon atom on the least hindered side of the epoxide on GO, forming a C-N bond, effectively producing a secondary amine. The oxygen atom of the epoxide will remain attached to the other carbon atom and become protonated, producing an alcohol at position 2, with respect to the site of nucleophilic addition. The grafted species and the newly formed hydroxyl will be on opposite sides of the graphene sheet. While there are many works employing this reaction to graft amine derivatives[2,3,21–24] and in particular, aminated

imidazolium-based ionic liquids to graphene oxide there was only a single instance where the acid-catalyzed pathway was chosen[25]. Basic conditions are preferred so as to strengthen the nucleophilic character of the amine, by preventing its protonation in an acidic environment. The reaction has been carried out in both protic (usually in water[1] or ethanol[26]) and aprotic solvents, such as DMF[21].

As graphene oxide is produced in aqueous suspensions, redispersing it in another solvent would require drying it first. That in turn entails the restacking of the suspended sheets and then applying mechanical force to separate and disperse them in the new solvent, potentially damaging them in the process. Seeing no obvious advantage in that, it was decided to conduct the reaction in water. Furthermore, the amino functionalized bromide IL is soluble in water.

In the works where the reaction mixture is alkalinized by hydroxides, KOH or NaOH are used at several GO:IL:base weight ratios[2,3,21,23,24]. In the studies cited in the previous paragraphs, the reaction mixture was heated at temperatures ranging from ambient to 120°C, in open containers, under reflux or in autoclaves[21]. Reported reaction times were in the range from 2 to 24 hours.

2.1. Synthesis of bromide IL-functionalized graphene oxide

To perform the functionalization of GO, an excess of bromide amino-functionalized ionic liquid was added to an aqueous suspension of GO in a moderately basic environment, pH ≈ 10, alkalinized by the addition of LiOH, using an excess of ionic liquid. The reaction was conducted under reflux for 6 hours. The unreacted ionic liquid was removed by washing with deionized water.

As a means to verify the successful grafting of the EMI^+ cation onto GO, a control sample was also prepared, by refluxing the alkalinized GO suspension at the same dilution, for the

same amount of time, without the presence of the unpurified ionic liquid. This control sample essentially underwent basic-catalyzed hydrolysis, with the epoxide groups becoming 1,2-diols. The amino-functionalized ionic liquid was then added to the mixture once it had cooled down to room temperature. The two reaction pathways are presented in Figure 3.5.

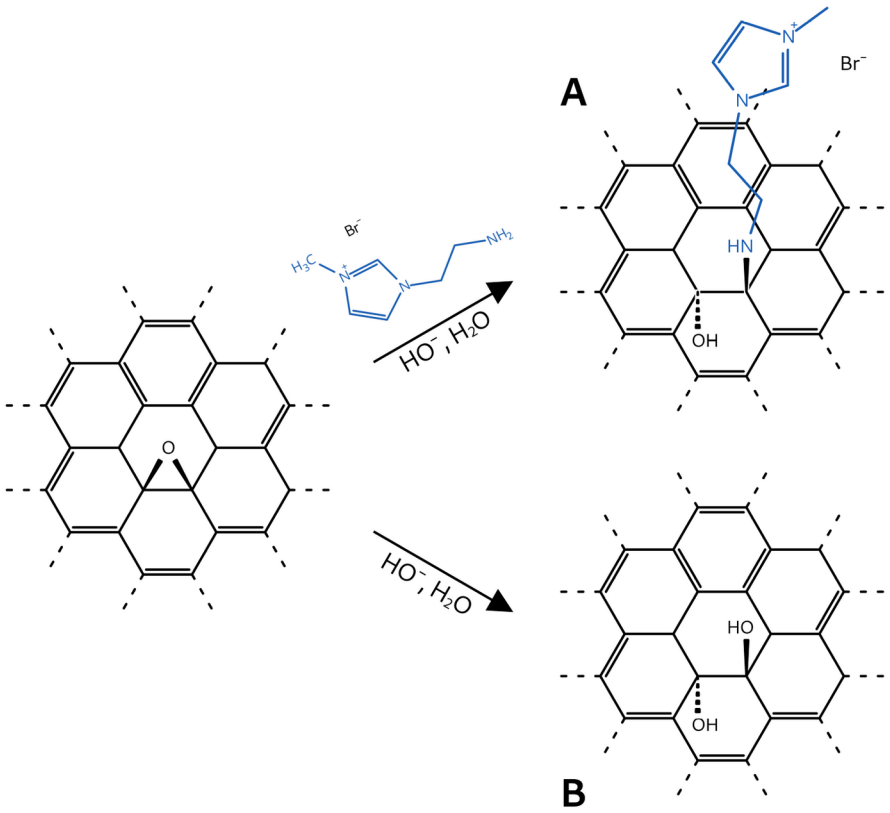

Figure 3.5: Nucleophilic substitution of the epoxide groups of GO by H_2N-EMI$^+$Br$^-$ produces the desired, functionalized product (A). Base-catalyzed hydrolysis of the epoxide groups in the control experiment produces 1,2-diols (B).

To facilitate comparisons, a third sample was prepared, that was subjected only to base-catalyzed hydrolysis, without the addition of any ionic liquid.

Synthesis of functionalized graphene oxide:

11.5 mL of a GO suspension with a concentration of 8.5 mg/mL (1.76 mmol of epoxide groups according to XPS analysis) was diluted with distilled water to 30 mL and transferred

to a 150 mL round-bottom flask, equipped with a stir bar. An excess of 3.19 mmol (determined via Li^+ AAS as discussed in Chapter 2.3) of 1-(2-aminoethyl)-methylimidazolium bromide in 35 mL of water, was added to the above. Upon addition, the mixture started to flocculate, but was homogenized by stirring vigorously. The pH of the mixture was brought to 10, by the addition of LiOH 2M solution in water. The system was brought to reflux and heating was maintained for 6 h. Then, it was left to cool to ambient temperature while being stirred. The mixture was brought to a filtering apparatus equipped with a PTFE membrane (450 nm pore diameter) where it was washed with deionized water, until the filtrate was colorless. At the end, the pH of the wash water was a little under 6. The material was kept in aqueous suspension.

Preparation of the physical mixture of hydrolyzed GO and ionic liquid (control sample):

11.5 mL of a GO suspension with a concentration of 8.5 mg/mL was diluted with distilled water to 30 mL and transferred to a 150 mL round-bottom flask, equipped with a stir bar. The pH of the suspension was brought to 10, by the addition of LiOH 2M solution in water. The system was brought to reflux and heating was maintained for 6 h. Then, it was left to cool to ambient temperature while being stirred. At that point, an excess of 3.19 mmol of 1-(2-aminoethyl)-methylimidazolium bromide in 35 mL of water with its pH also adjusted to 10 by the addition of LiOH 2M aqueous solution, was added to the above and the mixture was left stirring overnight at room temperature. The next day, it was transferred to a filtering apparatus equipped with a PTFE membrane (450 nm pore diameter) where it was washed with deionized water, until the filtrate was colorless. At that point, the pH of the filtrate was approximately 6. The material was kept in aqueous suspension.

Preparation of hydrolyzed GO:

11.5 mL of a GO suspension with a concentration of 8.5 mg/mL was diluted with distilled water to 30 mL and transferred to a 150 mL round-bottom flask, equipped with a stir bar. The pH of the suspension was brought to 10, by the addition of LiOH 2M solution in water. The system was brought to reflux and heating was maintained for 6 h. Then, it was left to cool to ambient temperature while being stirred. It was transferred to a filtering apparatus equipped with a PTFE membrane (450 nm pore diameter) where it was washed with deionized water, until the pH of the filtrate was approximately 6. The material was kept constantly in aqueous suspension.

2.2. Br^- - $TFSI^-$ anion exchange

After grafting the bromide amino functionalized ionic liquid on graphene oxide, the last step to realize was the metathesis which consisted in exchanging the bromide with the bis(trifluoromethanesulfonyl)imide anion. This was performed using an excess of LiTFSI salt in aqueous solution at room temperature. The suspension of functionalized GO was transferred to a 100 mL round-bottom flask, equipped with a stir bar. 2.032 g (7.08 mmol, 4 eq. *vs.* epoxide groups on GO) of Li^+TFSI^- salt was added to it and the mixture was diluted to a final volume of 60 mL. It was left under vigorous stirring for 48 h, at room temperature. The mixture was brought to a filtering apparatus equipped with a PTFE membrane (450 nm pore diameter) where it was washed with deionized water, until the filtrate gave a negative test for Br^- with $AgNO_3$. The functionalized material was kept in suspension throughout the metathesis reaction and washing and was recovered as such.

The exact same procedure was followed to perform the anion exchange with the control sample, using the same quantities.

For brevity, in the following sections the ionic-liquid-functionalized graphene oxide and

the physical mixture of graphene oxide with the ionic liquid, both after the anion exchange with $TFSI^-$ shall be termed IL-GO and PM respectively. Similarly, the base-treated graphene oxide shall be termed BT-GO.

Materials. *$LiOH{\cdot}H_2O$ (purity ≥ 99%) was purchased from Fluka, Li^+TFSI^- (purity ≥ 99%) was purchased from Solvionic. The preparations of the 8.5 mg/mL aqueous suspension of GO and of the unpurified H_2N-EMI^+Br^- ionic are presented in Chapter 2.1 and 2.3, respectively.*

2.3. Verification of grafting

Some differences were apparent between the functionalized sample and the physical mixture. IL-GO appeared to possess a higher surface tension than PM and it exhibited a decreased affinity towards glass. The washing and filtration of the PM sample on the PTFE membrane took almost 12 times as long as the IL-GO sample, probably due to the increase of hydrogen bonding after hydrolysis of the epoxide groups. With the nature of graphene oxide already being rather complex, the addition of another species further complicated analyses. In order to verify that the amino-functionalized ionic liquid had been covalently bonded to graphene oxide and to investigate the composition of the functionalized solid material, several techniques were combined, namely solid-state NMR spectroscopy (^{13}C, ^{19}F and ^{7}Li), thermal analyses (TGA and DSC) and EDX spectroscopy.

2.3.1. Solid-state NMR spectroscopy

^{13}C magic-angle spinning (MAS) NMR spectroscopy was used to examine the state of the GO substrate before and after functionalization. The presence of the $TFSI^-$ anion on the functionalized material was verified by ^{19}F MAS NMR spectroscopy. Finally, ^{7}Li MAS NMR spectroscopy was used to check if any Li remained in the functionalized material and if yes, in what form.

2.3.1.1 ^{13}C NMR

The solid-state ^{13}C NMR spectra of unmodified GO and that of the functionalized ionic liquid (IL-GO) are presented in Figure 3.6. The conductive sp^2 domains of the material are responsible for the "noisy" aspect of the spectra. Because of the inhomogeneity of GO, carbon atoms of the same chemical species have many different electronic environments. Due to the relative amounts of the different types of carbon atoms, it is impossible to make out a signal that could be attributed to the carbons in the structure of $H_2N\text{-}EMI^+TFSI^-$ in the spectrum.

In the GO spectrum, a number of signals of various intensities can be distinguished. According to the literature[27–30], starting from chemical shifts at low field values, the weak signals at 189.7 and 168.0 ppm are attributed to carbonyl and carboxyl groups; the strong signal at 129.7 ppm originates from sp^2-hybridized domains; the weak signal at 97.7 ppm corresponds to lactol-like structures; finally, the intense signals at 71.45 and 61.95 ppm are due to carbon atoms in alcohol and epoxy groups respectively.

In the spectrum of the ionic-liquid-functionalized GO sample, the signal from the epoxide carbons has practically disappeared (δ = 62 ppm in GO signal). Had the epoxide groups been hydrolyzed without reacting with the amino group of the ionic liquid, the signal due to C-OH groups would have increased. That does not seem to be the case. In fact, the signal due to hydroxyl groups appears to have decreased and the same is observed for the signals belonging to carbonyl and carboxyl groups, which are now very difficult to distinguish from the noise. In the IL-GO spectrum, the signal from the sp^2 carbon atoms has shifted upfield (δ = 124 ppm), compared to that in the GO spectrum. This suggests that the ^{13}C nuclei are more shielded, providing a hint as to what might have happened. This would be the result of an increase in size of the conjugated systems, brought on by a partial reduction of graphene oxide as it was heated in solution, an observation that has already been reported[31].

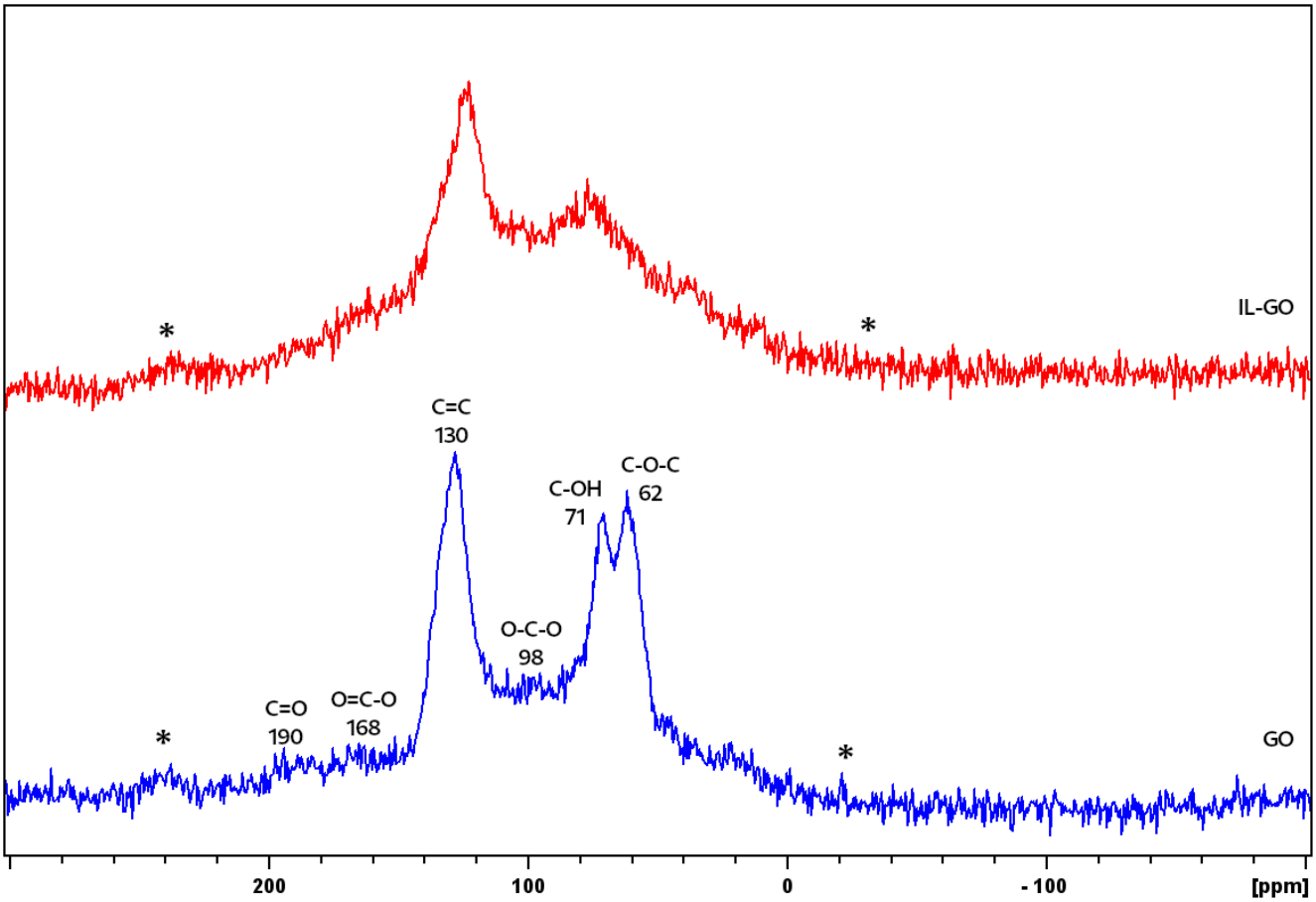

Figure 3.6: ^{13}C NMR spectra of GO (blue) and IL-GO (red). The chemical shifts of the different carbon atom types have been marked on the GO spectrum. The asterisks denote spinning sidebands.

2.3.1.2 ^{19}F NMR

A sharp intense peak is observed in the ^{19}F NMR spectrum of the functionalized material. Its chemical shift is δ = -84.65 ppm, in good agreement with what has been reported in the literature[32] corresponding to the fluorine atoms of $TFSI^-$. This confirmed the presence of the $TFSI^-$ anion in the composite.

2.3.1.3 ^{7}Li NMR

It has been reported[33] that the formation of LiOH in Li-ion batteries with $TFSI^-$ anions, results in the degradation of the latter, as the nucleophilic OH^- species react with the sulfur atoms. While the study did not conclude as to whether the SEI formed by the decomposition products of the reaction was beneficial or not to the functioning of the battery, it was

important to determine whether lithium existed in the functionalized material and if yes, in which form. As the composite material had been in contact with several lithium compounds at various steps of the synthesis of the functionalized GO: LiBr was mixed with the unpurified ionic liquid, LiOH was used to alkalinize the reaction mixture and Li^+TFSI^- was used for the anion exchange, it was quite possible that Li^+ would be present in the composite.

First, it was confirmed that some amount of lithium was present in the functionalized GO, albeit in very small concentration, as its peak (δ = 0.9928 ppm) was barely distinguishable after ~2000 scans (4800 scans were performed for the spectrum shown in Fig. 3.7). Then, a series of lithium-containing standards was prepared and measured, in order to compare the ^7Li spectrum of the IL-GO sample to them. The standards prepared, were: LiBr (δ = -1.1154

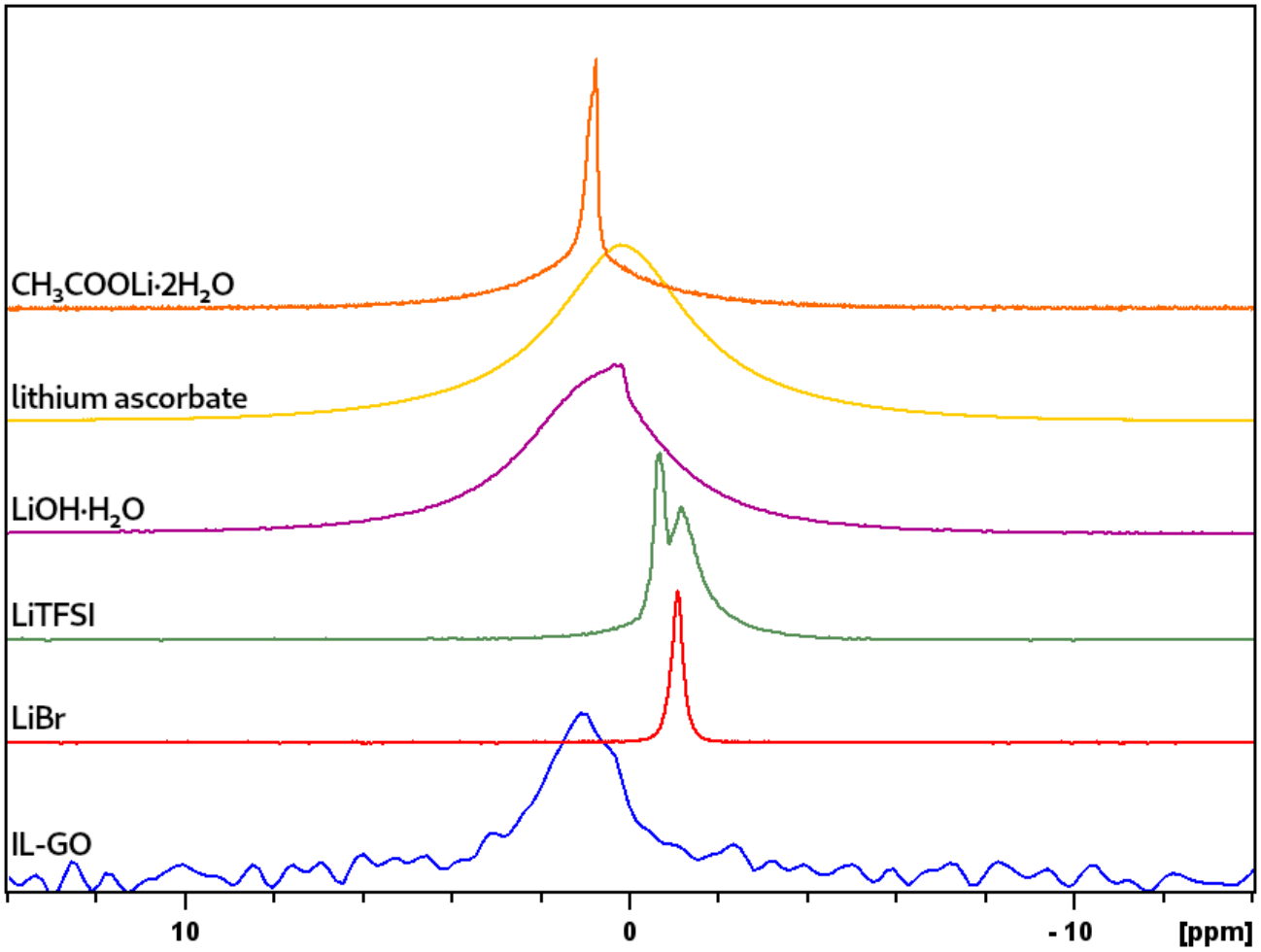

Figure 3.7: ^7Li NMR spectra of the functionalized binary material and the standards used for comparison (LiBr, LiTFSI, $LiOH·H_2O$, lithium ascorbate and $CH_3COOLi·2H_2O$). The intensities of the signals have been normalized for the sake of comparison.

ppm), LiTFSI (two peaks at -0.7043 and -1.1980 ppm), $LiOH{\cdot}H_2O$ (convoluted signal with two peaks at 0.1501 and 0.3129 ppm), lithium acetate dihydrate (convoluted signal, peak centered at δ = 0.8020 ppm) and lithium ascorbate (δ = 0.1765 ppm). Because of the vinylogous acids present on graphene oxide, it was reasoned that ascorbic acid would provide a reasonable approximation of such a system. All the spectra are presented in Figure 3.7.

From the chemical shift of the observed peaks, it can be immediately inferred that the lithium present in the IL-GO sample is neither in LiBr nor in LiTFSI form. The temperature at which the sample was dried would not be sufficient to dehydrate $LiOH{\cdot}H_2O$, the signal of which is contorted due to the asymmetry of the interactions. Since the signal from the sample is rather symmetrical, the presence of LiOH can probably be excluded.

Peak broadening can be induced by the ^1H neighbouring around ^7Li. Indeed, the linewidth is inversely proportional to the relaxation time T_2^*, which is driven for ^7Li by the quadrupolar interaction and by the dipolar coupling with ^1H. Large peaks are hence observed for lithium hydroxide and ascorbate. Given that and the proximity of the chemical shift of the IL-GO sample to that of $CH_3COOLi{\cdot}H_2O$, it was surmised that the lithium in the IL-GO sample was bound to oxygen. In all likelihood it is bound to alkoxy groups and the difference in shift (compared to the ascorbate) is due to the influence of conjugated systems in graphene oxide, without excluding the possibility that some of it is bound to carboxylates on the edges of graphene oxide.

Experimental details. *Magic angle spinning (MAS) NMR spectra were collected on a Bruker 500WB (500.07 MHz) – Avance III spectrometer, operating at 11.7 T, equipped with 2.5 mm or 4 mm H-X MAS probes, operating at a frequency of 194.51 MHz (^7Li), 125.85 MHz (^{13}C) and 470.94 MHz (^{19}F). For the ^{13}C and ^{19}F measurements, a rotor with an outer diameter of 4 mm was used, while for the ^7Li measurements the samples were inserted in a 2.5 mm rotor. The rotors were spun at 14 kHz for the ^{13}C measurements and at 20 kHz for the ^{19}F and ^7Li measurements. Adamantane (δ = 37.77 ppm), LiF (δ = -203 ppm) and LiCl (δ = 0 ppm) were used as external references for the ^{13}C, ^{19}F and ^7Li spectra, respectively. Acquisition and processing were performed through the TopSpin software suite. Finely cut pieces of film, made by drying a quantity of the suspension of the GO*

grafted with IL (and a suspension of GO) at 45°C in a drying oven, were tightly packed in zirconia rotors. The salts used for comparison in ^{7}Li measurements were finely ground in an agate mortar before being loaded into the rotors.

2.3.2. Thermal analyses

In order to obtain further indications that the covalent functionalization of GO with the amino-functionalized ionic liquid was successful, the thermal decomposition of the functionalized material was examined through TGA and DSC. Because of the complexity of the system, it was compared with the physical mixture, the base-treated GO sample and pristine GO. Additionally, three batches of functionalized material, prepared under different synthetic conditions, were compared with each other. Moreover, thermal analyses were also crucial in verifying that the functionalized material would be stable during the thermal reduction treatment.

2.3.2.1 Thermogravimetric analyses

BT-GO sample vs. GO

First was analyzed the base-treated GO sample, to examine the effect of basic hydrolysis on GO. In Figure 3.8, its thermal decomposition profile is contrasted to that of pristine GO. The decomposition profiles of both materials are rather similar up to 151°C, at which point GO exhibited a thermal event that overlapped with the previous one, which had started at 129°C. No such segment exists in the thermogravigram of BT-GO, with the step that begins at 129°C seemingly reaching a point of completion around 196°C where the rate of weight loss changes. This allowed the attribution of the first event (129°C – 196°C) to the decomposition of hydroxyl groups and the second event (151°C – 213°C), observed only for GO, to the decomposition of epoxide groups.

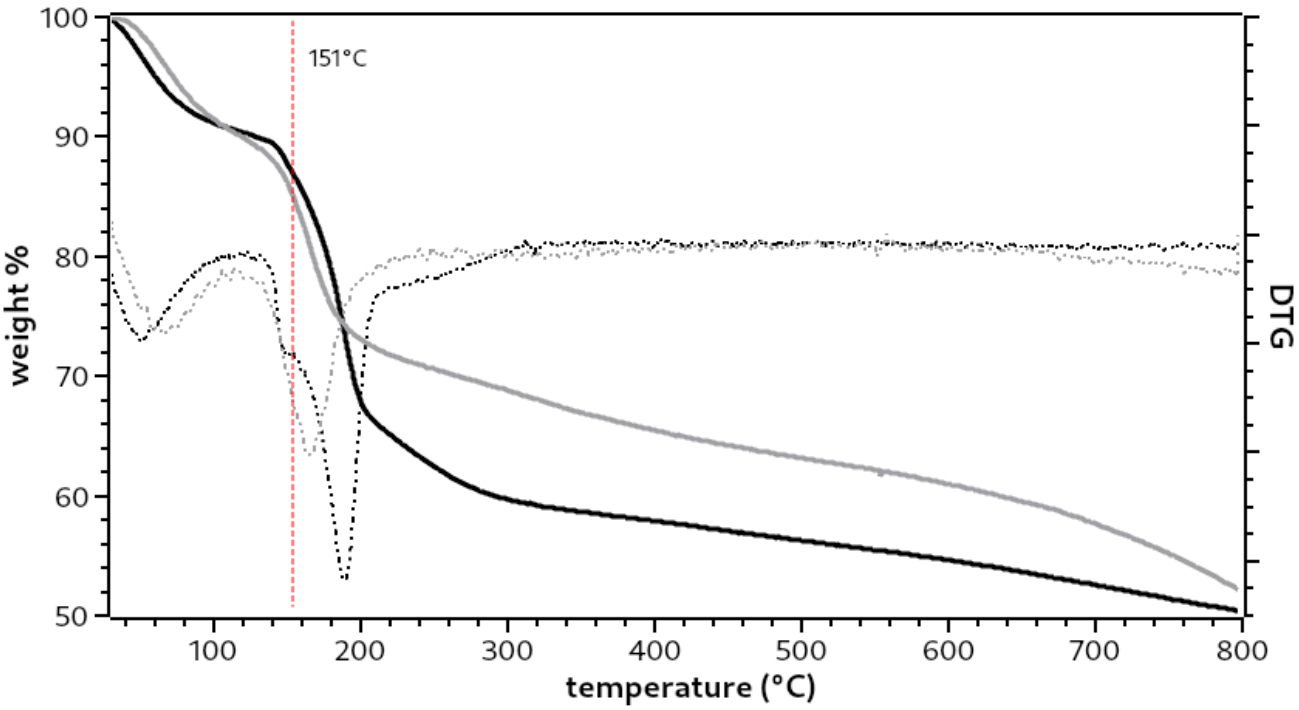

Figure 3.8: Thermogravigrams of BT-GO (in gray) and GO (in black) and the corresponding DTG curves (dotted lines). The red dashed line marks the onset of the decomposition of epoxide groups in GO. Analyses were conducted under inert atmosphere (N_2).

After 196°C, the decomposition rate of the BT-GO sample stabilizes and remains almost constant. That was not the case for GO, which exhibited a different rate between 213°C and 309°C. Perhaps this could be attributed to further reactions of the initial epoxide fragments.

Between approximately 387°C and 588°C, the decomposition of both materials proceeds at the exact same rate.

From 588°C onward, the decomposition of BT-GO accelerates and its total weight loss approaches that of GO. It could be posited that some of the reactive species that form as the epoxide groups are pyrolyzed, are responsible for the degradation of other moieties, that by themselves would decompose at higher temperatures.

At the end of the measurement, the weight loss of BT-GO is slightly smaller, with the weight difference between the two materials being 1.8 wt%. Taking into account the adsorbed water content, it can be estimated that the treatment of GO with base under reflux induced a weight loss of approximately 3 wt%.

IL-GO and PM samples

Thermogravigrams of the ionic-liquid-functionalized GO (IL-GO) and the physical mixture of the ionic liquid with GO (PM), contrasted with the base-treated GO are presented in Figure 3.9.

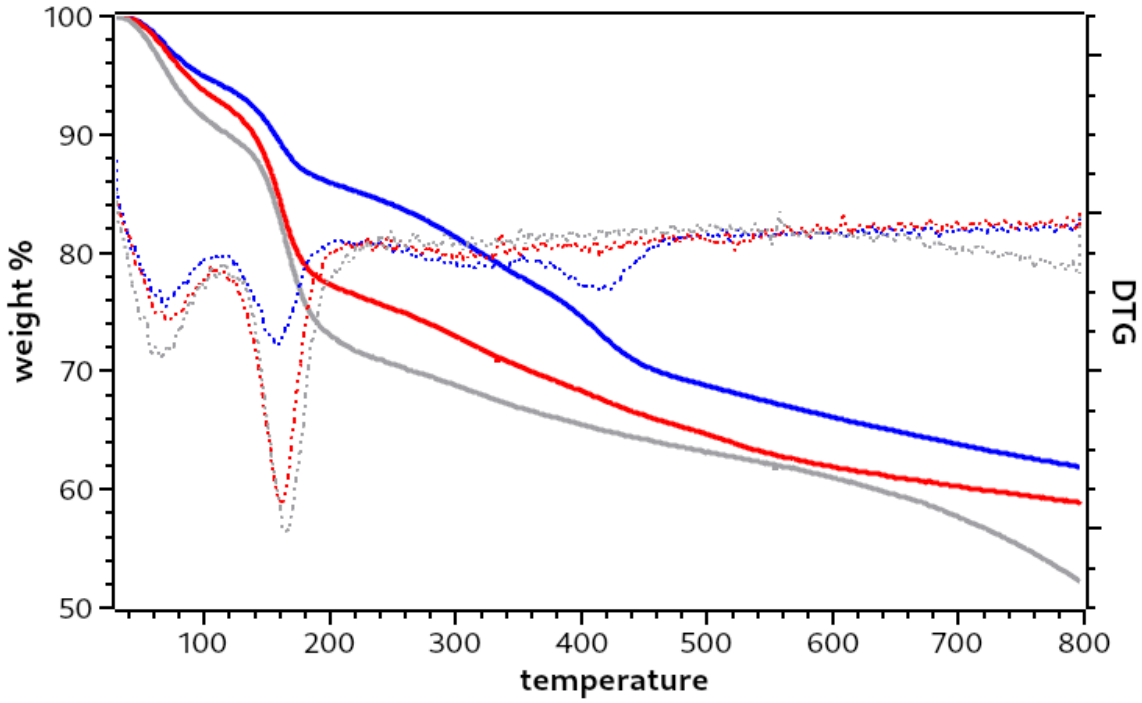

Figure 3.9: Thermogravigrams of IL-GO (in blue), PM (in red) and BT-GO (in gray) and the corresponding DTG curves (dotted lines). Analyses were conducted under inert atmosphere (N_2).

Up to 227°C, the general shape of all three thermogravigrams appears similar, with the evolution of IL-GO and PM being identical until ~110°C. However, there is a notable difference in the segment between 129°C and 227°C, which corresponds to the decomposition of the hydroxyl groups. The weight loss of the functionalized material is 8.4 wt%, whereas those of the physical mixture and the base-treated GO are 15.2 wt% and 17.13 wt% respectively. This is a direct indication that half the hydroxyl groups that formed during the hydrolysis of the BT-GO sample, are not found in the IL-GO sample, while almost all of them are measured in the physical mixture. This would be the expected result if during the epoxide ring-opening reaction a nucleophile other than the hydroxyl anion was added to one of the epoxide carbon atoms.

In conclusion, a first, perhaps encouraging, indication that the functionalization was completed successfully, is the different decomposition profile exhibited by IL-GO and PM.

Compared to the base-treated GO, both the functionalized sample and the physical mixture start showing an accelerated weight loss at around 230°C and the derivatives of the TG curves show two consecutive events, with their maxima at approximately 315°C and 415°C, reaching completion at 478°C. The weight loss of the IL-GO sample for that segment is 15.37 wt%, whereas that of the PM is 10.61 wt%. The decomposition rate of the functionalized sample remains steady from there on until the end of the measurement. The physical mixture exhibits another event, from 478°C to 565°C, before its rate stabilizes, that could not be identified, corresponding to a weight loss of 2.76 wt%.

In comparison with the base-treated GO, if it is assumed that all of the amino-functionalized ionic liquid (grafted or adsorbed) is broken down to gaseous products in the segment from 230°C to 478°C, then the loading in IL of the functionalized material would be 7.7 wt%. Similarly, the adsorbed IL in the physical mixture would be 3.0 wt% of its mass. Comparing the weight loss of the two materials with that of pristine GO in that same segment, the results are almost the same, with 7.9 wt% loading for IL-GO and 3.2 wt% for PM.

Because both the matrix (GO) and the graft (IL) are organic and their thermal evolution is constant, it is difficult to precisely determine the ratio of the one to the other. Moreover, the decomposition products of the ionic liquid, be it grafted or adsorbed, have an effect on the course of the pyrolysis, they do not just depart the system “cleanly”. Otherwise, the weight evolution of the physical mixture for example, would follow the same trend as that of base-treated graphene oxide after the decomposition of the ionic liquid. This is clearly not the case. The weight losses of the two materials differ by 2.5 wt% in the segment corresponding to the decomposition of the hydroxyl groups, but at the end of the measurement, their difference is 6.7 wt%. Their difference cannot be correlated to the IL content of the mixture.

The pure H_2N-EMI^+TFSI^- ionic liquid exhibited two decomposition events (Chapter 2.3.5). The first one, which was attributed to the decomposition of the amino group and which was accompanied by a weight loss of 5.5 wt%, took place between 132°C and 238°C. This was not observed in either the functionalized material nor the physical mixture. One hypothesis was that the event was masked by the decomposition of the hydroxyl groups. However, as the weight loss rate in that segment does not indicate the presence of a separate event, another hypothesis was that the GO matrix had a stabilizing effect on the amino group, either through the covalent bond, or via electrostatic interactions with the polar groups of GO. The second, complex decomposition event in the thermogravigram of the pure H_2N-EMI^+TFSI^- IL, with a weight loss of 81.5 wt%, had an onset temperature of 275°C, reaching completion around 490°C. This is more or less in line with the observations made with both the physical mixture and the functionalized material, with the onset temperature appearing earlier, at 230°C. Evidently, the ionic liquid species adsorbed or grafted on GO did not exhibit the same stabilizing interactions as in the mass of pure IL.

IL-GO1, IL-GO2 and IL-GO3

Finally, three different batches of functionalized material were compared. The functionalized sample already presented, IL-GO1, is compared in Figure 3.10 to IL-GO synthesized in a more concentrated, viscous suspension, IL-GO2 and to IL-GO3, an IL-GO synthesized using equimolar quantities of IL and GO and not an excess of IL as in IL-GO1. All the other parameters of the three syntheses were the same.

Besides the more pronounced initial weight loss of sample IL-GO3, due to adsorbed humidity, the three thermogravigrams present almost exactly the same profile. Their comparison was made while trying to correlate the amount of decomposing hydroxyl groups to the amount of grafted ionic liquid. Unfortunately, that was not as straightforward as it was thought at first. The weight losses during decomposition of hydroxyl groups were 8.4 wt%, 11.6 wt% and 5.9 wt% for IL-GO1, IL-GO2 and IL-GO3 respectively. In the segment attributed

to the decomposition of the ionic liquid, the respective weight losses were, 15.4 wt%, 13.4 wt % and 15.2 wt%. While a higher hydroxyl group content was accompanied by a lower ionic liquid loading, there does not appear to be a linear correlation of the two. Furthermore, all three samples converge to the same weight towards the end of the measurement, with 61.9 wt%, 61.4 wt% and 61.5 wt% measured for IL-GO1, IL-GO2 and IL-GO3 respectively.

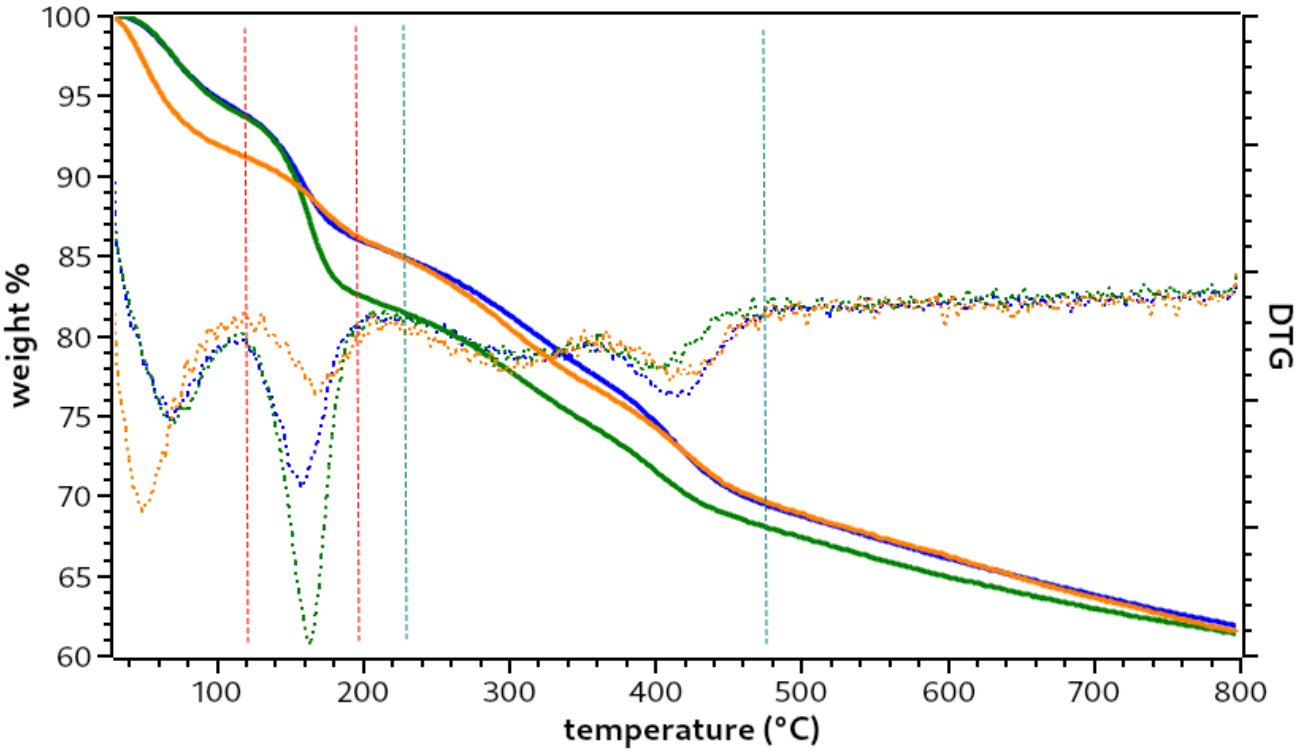

Figure 3.10: Thermogravigrams of three different IL-GO samples: IL-GO1 (in blue), IL-GO2 (in green) and IL-GO3 (in orange) and the corresponding DTG curves (dotted lines). The red vertical dashed lines delimit the decomposition of hydroxyl groups and the teal vertical lines the decomposition attributed to the IL. Analyses were conducted under inert atmosphere (N_2).

2.3.2.2 Differential scanning calorimetry

The ionic-liquid-functionalized material and the physical mixture of IL and GO were also examined via DSC. Their respective thermograms, as well as those of pristine graphene oxide and base-treated graphene oxide are presented in Figure 3.11. The measurements were

conducted on pieces of film of each material.

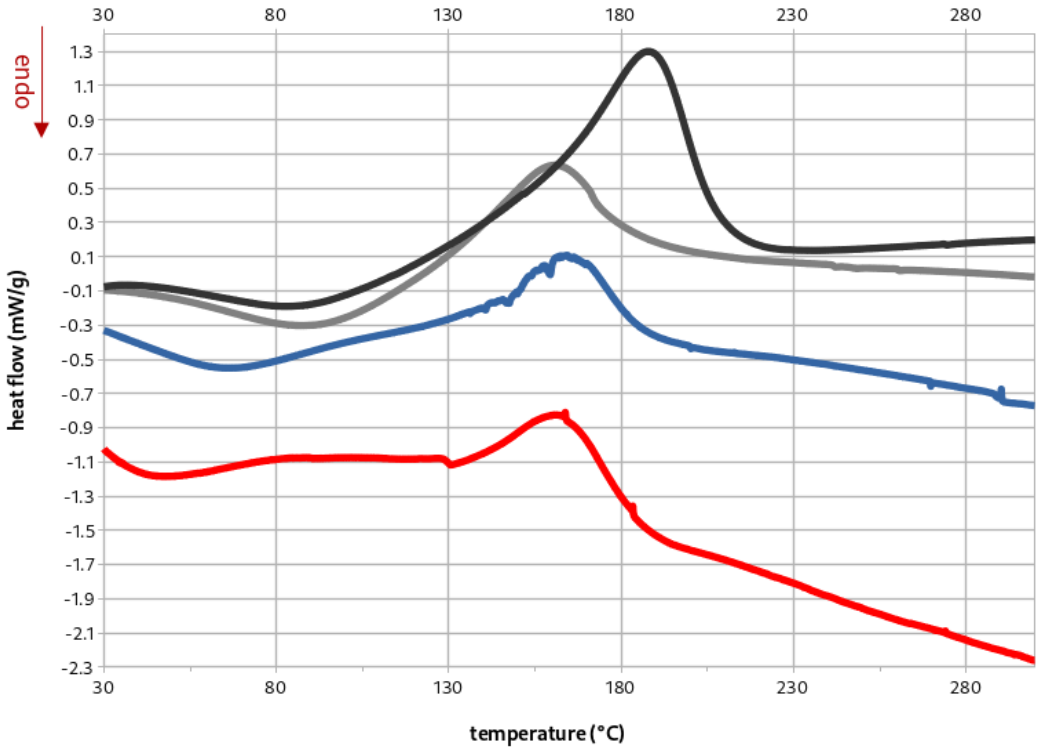

Figure 3.11: DSC thermograms of IL-GO (blue), PM (red), BT-GO (gray) and GO (black). Endothermic processes are downward. Temperature ramp 3°C/min.

All the DSC curves begin with a small endothermic process, the evaporation of adsorbed water. The main thermal event in all of the thermograms is the exothermic decomposition of the hydroxyl groups and in the case of pristine graphene oxide, that of epoxide groups as well, confirming what had been deduced for the two processes from TG analyses.

Graphene oxide and base-treated graphene oxide exhibit very similar behaviors, except for the decomposition of epoxide groups in the first and an increased heat release during the decomposition of hydroxyl groups in the second. The general aspect of the curves suggests that in terms of thermal conductivity and heat capacity, the two materials are very close. A rather important difference is that after the decomposition of hydroxyl and epoxide groups, GO continues to slowly release heat, whereas BT-GO (and the other samples) proceed to absorb heat for the rest of the measurement.

The functionalized material shows a profile that resembles that of BT-GO. The initial

offset of heat flow could indicate some hindrance in the heat transfer between the graphene oxide sheets, induced by the ionic liquid present. However, the difference between the functionalized material and GO and BT-GO in that regard, is rather small. Some very small endothermic peaks appearing towards the maximum of the thermal envelope, could not be investigated further, as the instrument lacked sufficient resolution, nor could they be attributed to a specific event.

The physical mixture of ionic liquid and graphene oxide has a markedly different behavior, starting with the amount of energy required to bring it to equilibrium and start the measurement. It is fairly probable that the mobility of the ionic liquid plays an important role in heat transfer in the system. Accompanying the exothermic decomposition of the hydroxyl groups, there appear to be two minor exothermic events at 165°C and 185°C, again too small to investigate given the instrument's resolution.

2.3.3. EDX

It was expected that EDX measurements could provide quantitative information about the composition of each sample, so films made from the ionic-liquid-functionalized graphene oxide and the physical mixture of amino-functionalized ionic liquid and GO were analyzed as prepared and after thermal reduction at 200°C, under vacuum for 2 h. Another reason to conduct the EDX measurement, was to examine the distribution of the ionic liquid on the GO sheets. The GO matrix of the sample is made of carbon and oxygen atoms and their abundance is reflected in the corresponding maps. The cation of the functionalized ionic liquid possesses three nitrogen atoms and the $TFSI^-$ anion possesses one nitrogen atom, two sulfur atoms and six fluorine atoms that could stand out against the backdrop of C and O. An elemental analysis of the samples was not carried out, because there would always be strong signals from the metal sample holder, making an accurate atom count impossible. It was however possible to perform an elemental mapping of the surface of the films. During the

analysis, it was noted that sulfur was consistently over-detected, probably because of an issue with signal to noise ratios in the sample. As a result, the image maps of S, should not be considered accurate.

2.3.3.1 IL-GO sample

Elemental mapping images of the IL-GO sample are presented in Figure 3.12, along with the layered (composite) image of the same area. At the scale examined by the scanning electron microscope, the surface of the IL-GO sample appears to be homogeneous. It has a grainy aspect, which could reflect the localized character of the disorder in graphene oxide itself. Areas where previously epoxide groups existed, should now have the cation of the ionic liquid grafted in place and in its vicinity, the anion. Conversely, in areas where mostly sp^2 domains are present, no any ionic liquid should be present, unless of course it is adsorbed. The overall uniformity of the sample is reflected in the composite image.

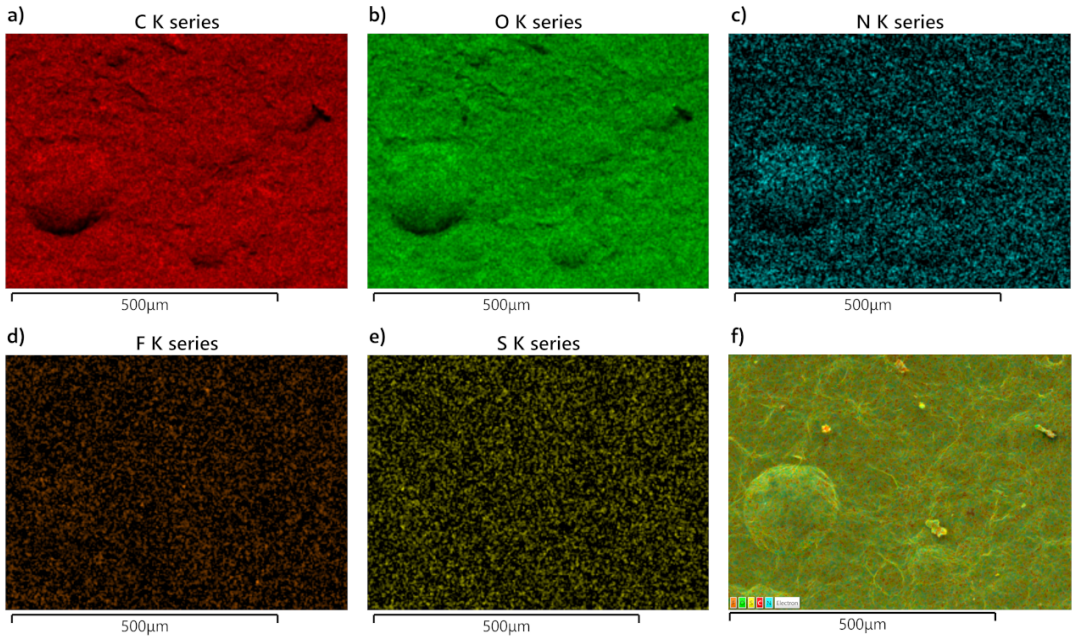

Figure 3.12: Elemental mapping images of a) C, b) O, c) N, d) F and e) S on the surface of an IL-GO film. f) composite image of all the previous elements together.

This "grainy" uniformity is for the most part maintained after thermal reduction (Figure 3.13). There are a few areas that appear almost empty of IL, *e.g.* a patch on the lower left of the composite image. This could be due to the expansion of sp^2 domains and/or increased heat transfer through certain points of contact during thermal reduction. It is also possible

that area had never been oxidized. However, the rest of the surface appears to exhibit the same coverage as before.

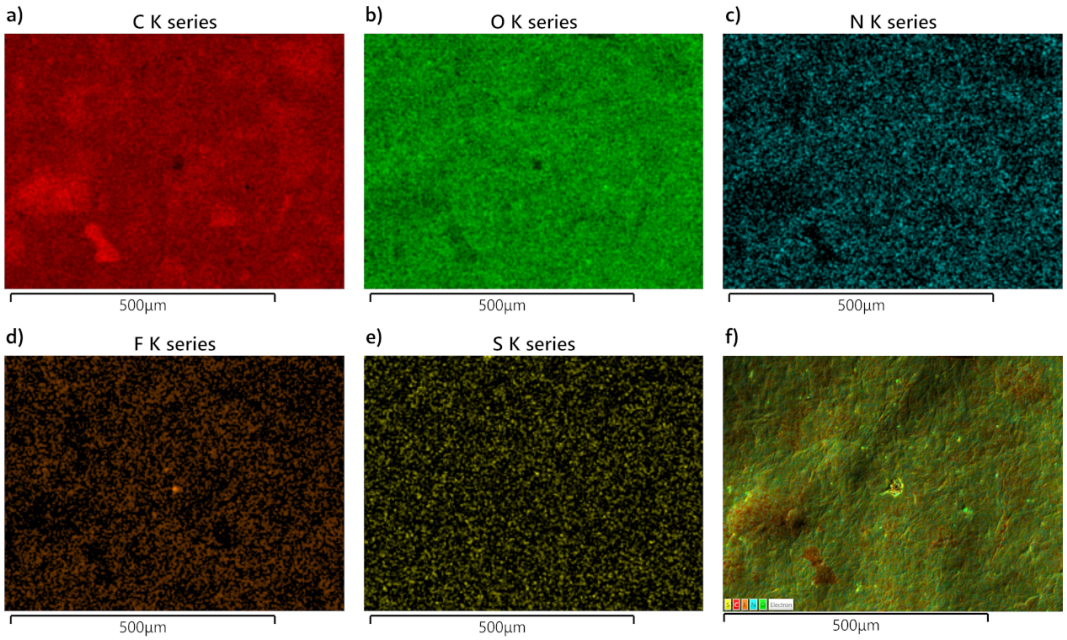

Figure 3.13: Elemental mapping images of a) C, b) O, c) N, d) F and e) S on the surface of an IL-GO film after thermal reduction. f) composite image of all the previous elements together.

2.3.3.2 PM sample

The physical mixture of graphene oxide and the amino-functionalized ionic liquid presents a different image (Figure 3.14).

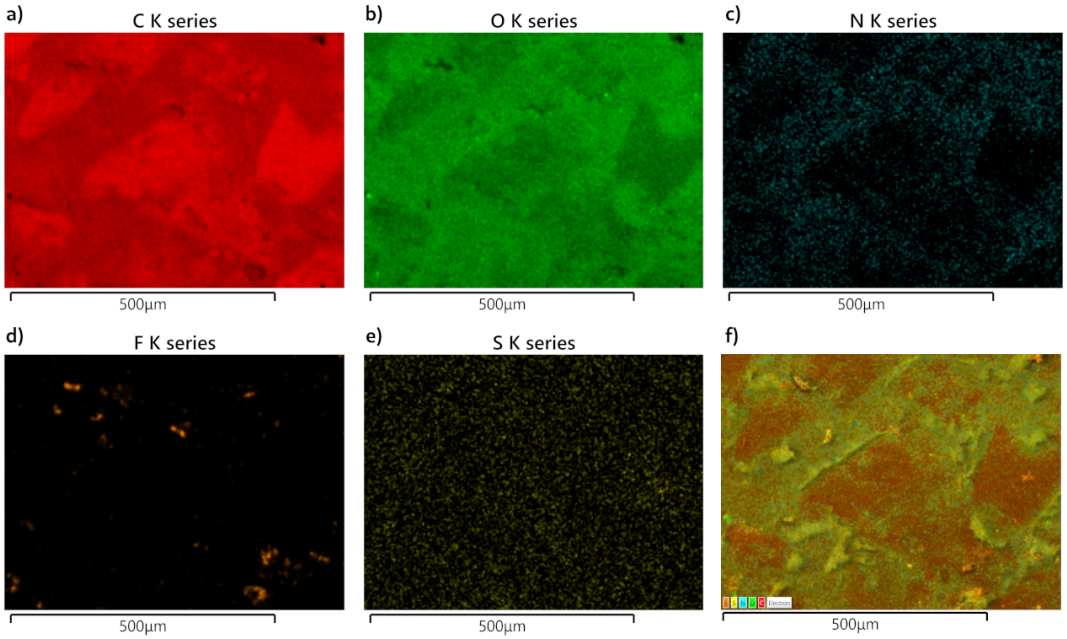

Figure 3.14: Elemental mapping images of a) C, b) O, c) N, d) F and e) S on the surface of an PM film. f) composite image of all the previous elements together.

First, the amount of heteroatoms appears to be lower, compared to the IL-GO sample. This was not unexpected, considering the results of the thermogravimetric analyses. Second, large parts of the surface of the sample have little to no ionic liquid present. This is more striking in the composite image. Compared to the nitrogen atom signals, fluorine atom signals from the $TFSI^-$ anion appear less dispersed and more aggregated in certain locations. This could indicate a separation of the ionic pair on the surface of the sheets.

After thermal reduction (Figure 3.15), the inhomogeneity is maintained. In addition to the aggregation of fluorine signals, some aggregation can also be observed for the signals from the nitrogen atoms as well. This could be attributed to the mobility of the ionic liquid, which should have increased during the thermal treatment.

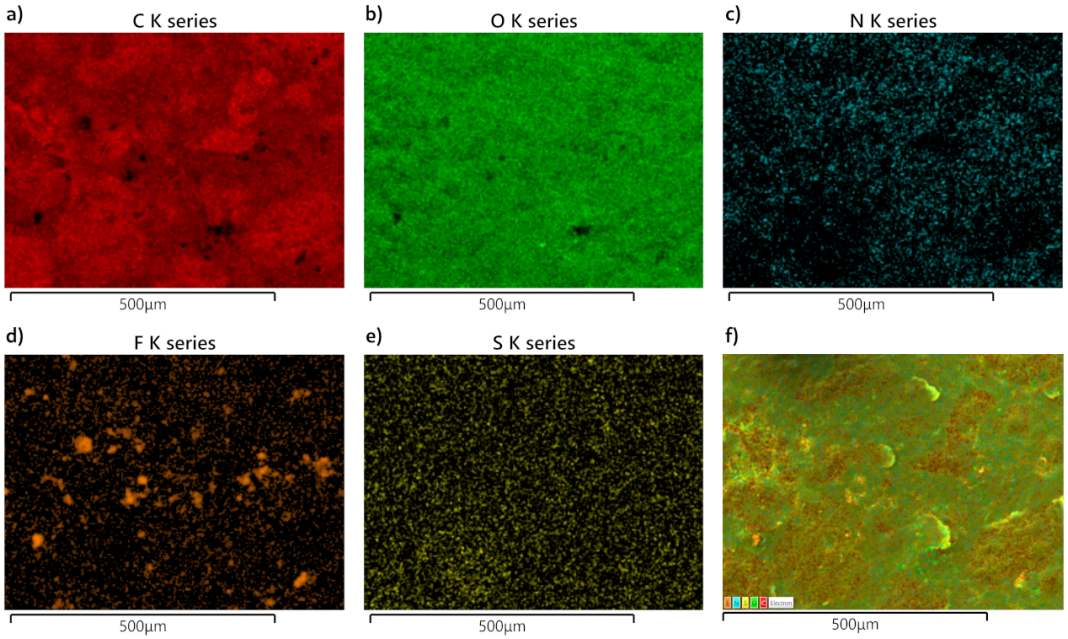

Figure 3.15: Elemental mapping images of a) C, b) O, c) N, d) F and e) S on the surface of an PM film after thermal reduction. f) composite image of all the previous elements together.

2.4. Conclusions

The grafting of the amino-functionalized ionic liquid onto graphene oxide via an epoxide ring-opening reaction, was carried out in basic conditions, with water as a solvent, under

reflux. The bromide anion was then replaced with a $TFSI^-$ one, to produce the targeted form of the functionalized material. Because of the complexity of the material and the challenges that the confirmation of the formation of the N-C bond presented, series of control experiments and measurements were conducted.

A sample of the functionalized material was characterized via NMR spectroscopy of ^{13}C, ^{19}F and ^{7}Li nuclei. The ^{13}C NMR analysis showed that the epoxide groups on the graphene oxide sheets had practically disappeared after the reaction, in line with what was expected from the mechanism of the nucleophilic addition of the amine to the epoxide group under these conditions. Through the same analysis, it was evident that some reduction of graphene oxide had taken place, as the reaction was carried out at 100°C for 6 h.

The ^{19}F NMR analysis confirmed the presence of the $TFSI^-$ anion in the final material. Since the metathesis reaction was followed by washing with comparatively copious amounts of deionized water until all the bromide anions had been removed, there was a question whether $TFSI^-$ too had been removed by washing.

Through the ^{7}Li NMR analysis, the presence of trace amounts of Li^+ in the final material was confirmed. By comparing the signal from the sample to that of several lithium compounds, it was deduced that the lithium ions are bound in salts with carboxylic and vinylogous acids of the GO sheets and are not hosted as separate species (*e.g.* LiBr, LiTFSI, LiOH, *etc.*).

By conducting thermal analyses on the functionalized material and control samples, it was shown that the amino-functionalized ionic liquid was grafted and not just adsorbed on the final material. While some amount of IL adsorption cannot be excluded, the very different thermal profiles of the physical mixture and the functionalized material rule out that adsorption has occurred at an appreciable degree. It would appear that the majority of the ionic liquid present on the functionalized material is indeed covalently bonded. The exact determination of the amount of IL grafted was not possible, but TGA analyses provided

a reasonable estimate, close to 8 wt%.

XPS analysis of GO had determined the atomic ratio of ether oxygens at 23.9% (Chapter 2, section 1.7.3), which – assuming they are all found as epoxides – translates to a quantity of 0.018 mmol of epoxide groups per mg of GO. If an equimolar amount of IL had been grafted, the IL content in the functionalized material would be ~88 wt%. Based on the TGA estimate, that content was 7.7 – 7.9 wt% – a full order of magnitude lower. Even if some amount of $TFSI^-$ anions had leached during washing, that would not suffice to explain the discrepancy. Furthermore, if some epoxide groups had remained unreacted, they would have shown up in the TG analysis. Similarly, if the amino-functionalized IL was in competition with the other nucleophiles in the mixture, HO^- and H_2O, there would be an increase in the quantity of decomposing hydroxyl groups. Since neither was observed, it was deduced that the interpretation of the XPS spectrum had overestimated the amount of oxygen atoms belonging to epoxide groups.

Thermal analyses also appear as a viable method to be used in the verification of the reproduction of the synthetic protocol. Finally, it was shown that the thermal reduction of the composite material at 200°C does not affect the grafted ionic liquid, as the weight losses attributed to it, do not occur before ~230°C.

3. Adding the final component

After the functionalization of graphene oxide with the ionic liquid, what remained in the preparation of the ternary composite material was the addition of the tin nanoparticles. From the different protocols studied to prepare Sn-GO co-milled nanoparticle samples (Chapter 2, section 2.2.4), one was ultimately selected, based on TEM observations and SAXS measurements. This was the sample prepared by co-milling 2700 mg of tin with 300 mg of GO for 22 h with the 10 mm balls at 400 rpm, followed by 2 h of fine grinding with the 2 mm balls at 600 rpm (sample SnGO08). The average crystallite size in the sample was 25 nm, with the largest nanoparticles reaching 200 nm. The nanoparticles would be mixed with the aqueous suspensions of GO, which would be freeze-cast and then thermally annealed, to produce the final form of the material.

3.1. Synthesis of the ternary composite material

Initially, two series of samples were prepared using suspensions of the ionic-liquid-functionalized GO in water at concentrations of 8 mg/mL and 16 mg/mL. To these, Sn-GO co-milled nanoparticles were added in such quantities as to obtain aerogels with final mass loadings in tin of approximately 40 wt%, 60 wt% and 80 wt%. The amount of nanoparticles to be added to each sample was calculated taking into account the Sn and GO content in the ground mixture. Furthermore, control samples were prepared using aqueous suspensions of GO at the same concentrations, 8 and 16 mg/mL and the same amounts of Sn-GO nanoparticles, again producing aerogels with loadings in tin of 40 wt%, 60 wt% and 80 wt%.

The series of samples based on aqueous suspensions with a concentration of GO or IL-functionalized GO of 8 mg/mL collapsed during lyophilization and were discarded. The remaining samples made from the suspensions of IL-GO and GO with concentrations of 16

mg/mL are presented in Table 3.1:

Table 3.1: Quantities of the different components used in the preparation of composite aerogels and the corresponding sample names.

Sample name	suspension volume (mL)	[IL-GO] (mg/mL)	[GO] (mg/mL)	Sn loading (wt%)	Quantity of Sn-GO NPs (mg)
IL-GOSn40	8	16		40	102
IL-GOSn60	8	16		60	256
IL-GOSn80	8	16		80	1024
GOSn40	8		16	40	102
GOSn60	8		16	60	256
GOSn80	8		16	80	1024

The samples were named based on the matrix material (IL-GO or GO) and the mass loading in tin. For example, the sample named IL-GOSn40 corresponds to a material prepared using an IL-GO suspension, with a tin loading of 40 wt%, while GOSn80 was made using a GO suspension, with a tin loading of 80 wt%. As a reminder, the IL in the name refers to the grafted aminated EMI^+ cation, paired with the $TFSI^-$ anion.

To further distinguish between samples at the stages after the formation of the aerogel and after thermal reduction, an “r” is added to the name, *e.g.* IL-GO60 and IL-rGO60 refer to the same sample, but before and after annealing respectively.

3.1.1. Preparation of the suspensions

According to the quantities reported in Table 3.1, six samples were prepared. The Sn-GO nanoparticles were transferred to 8 mL of IL-GO or GO suspensions and then they were homogenized by stirring. The addition of the nanoparticles to the already viscous suspensions resulted in the formation of dense, thixotropic gels, with those of IL-GO appearing denser. As a consequence and because of the relatively small quantities, homogenization was achieved by stirring by hand since via ultrasonication, magnetic stirring or with an overhead stirrer it was not possible. The black color of both the particles and the medium made determining that homogenization was complete difficult. After a few

hours, the nanoparticles would begin to precipitate in the GO suspensions, whereas the IL-GO suspensions with tin nanoparticles appeared stable.

3.1.2. Freeze-casting IL-GO-Sn and GO-Sn aerogels

The freeze-casting apparatus presented in Chapter 2.1 was used for the unidirectional freezing of the samples. Because of the very high viscosity of the mixtures, pipetting, or transferring them to the cold fingers of the apparatus with a syringe was not feasible. Instead, the material was transferred with a spatula and then it was compacted with the help of a syringe plunger. The samples were set to equilibrate at 20°C and then they were frozen at a rate of 10°C/min, until they reached -80°C and they had completely solidified. The frozen samples were stored in a container submerged in liquid N_2 until they were transferred to the lyophilizer, where they were exposed to a pressure of 0.01 mbar for at least 48 hours. Once all of the water had been removed, the samples were brought to ambient pressure and the monoliths were removed from the tubes with the help of a plastic piston.

3.1.3. Thermal reduction of the composite aerogels

The aerogel monoliths were cut into 2-mm-thick disks using a razor blade. The disks were placed in Petri dishes, which were then introduced into a vacuum oven. They were annealed by heating under vacuum, at a heating rate of ~1.5°C/min until a temperature of 200°C was reached, which was then maintained for 2 h. Once the oven had cooled to ambient temperature, the samples were removed and stored in sealed containers.

3.2. Characterizations of the ternary composite material

A concern in the thermal reduction of the composite material had been the melting point of tin nanoparticles, which was expected to be lower[34] than that of bulk tin, 232°C. A visual

inspection of the thermally reduced disks revealed the formation of very few sub-millimeter particles on their outer surface after annealing. However, after observing sections of the monoliths, no such particles were discernible in their internal structure. It appeared that the segmentation of the nanoparticles in the composite had prevented the aggregation of melting tin. In order to verify if that were true at scales not visible to the naked eye, samples of the annealed disks were examined via SEM. Furthermore, to confirm that the crystallinity of the metal nanoparticles in the samples had been retained, the diffraction patterns of thin slices of material were recorded before and after annealing.

3.2.1. Macroscopic morphology

Some representative SEM images of the samples are shown in Figure 3.16. The micrographs reveal the disordered, cellular structure of the aerogels that was expected. The

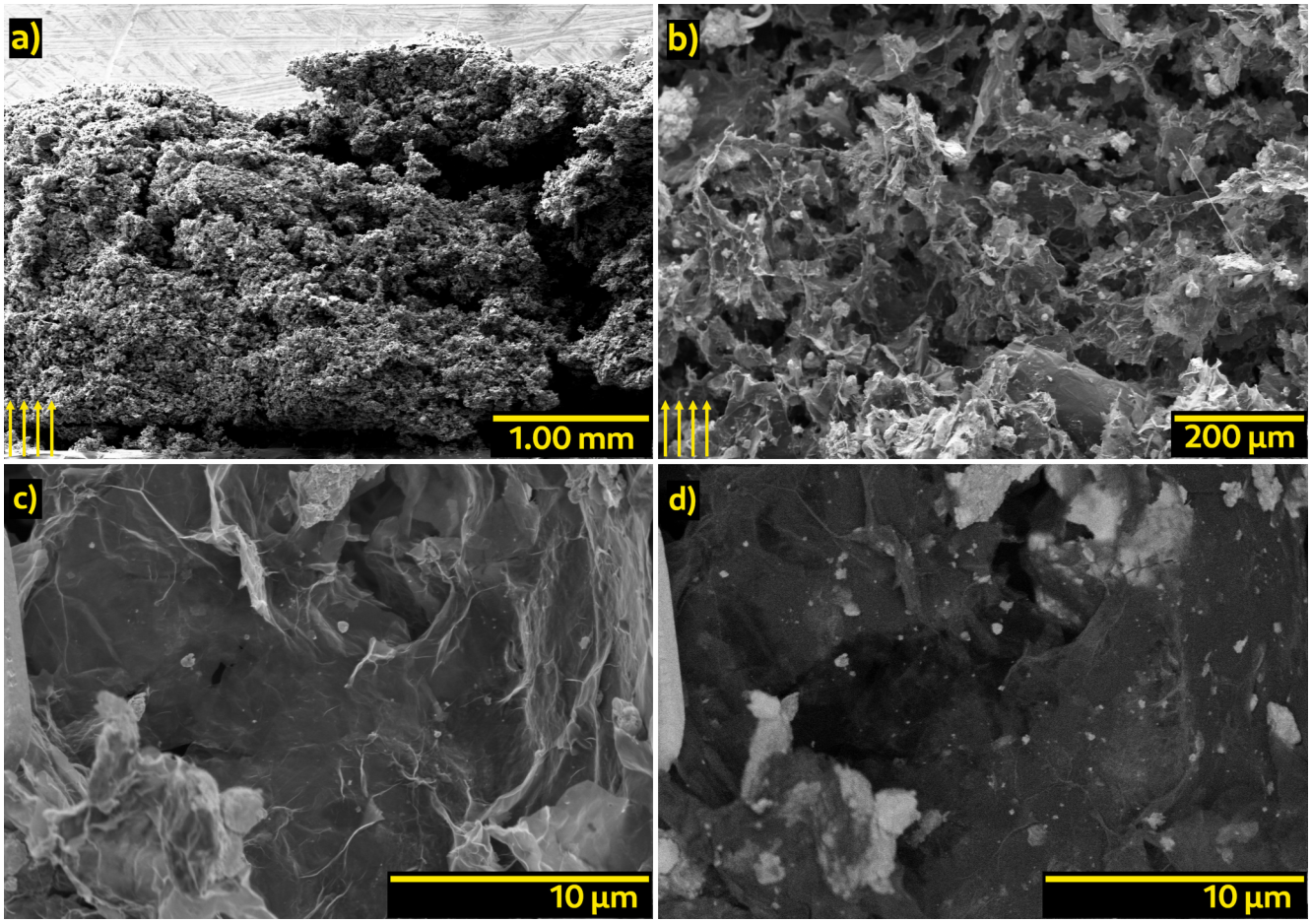

Figure 3.16: a) Side view and b) detail of a section of the IL-rGOSn80 composite aerogel. The arrows denote the direction of freezing. c) Top view of a pore and d) BSE image of the same pore.

presence of the metal nanoparticles throughout the mass of the material is also verified. The images in Fig. 3.16c and Fig. 3.16d show the view down a pore from the top of the monolith, with only backscattered electrons (BSE) collected in Fig. 3.16d, which provide information about the chemical composition in view. Dark areas correspond to material made up of lighter atoms, in this case mostly carbon, whereas the whiter areas indicate the presence of tin. One thing that is immediately apparent at higher magnifications, is that there are a lot of aggregates of nanoparticles of various sizes, larger than those observed through TEM (Chapter 2, section 2.3.1). This suggests that homogenization by hand was not optimal. In the IL-rGO80 sample, some needle-like crystals had grown from such aggregates.

Furthermore, in some of the sections examined there were voids. These were due to the entrapment of air as the viscous mixtures were transferred to the freeze-casting apparatus. In that regard, the use of a positive displacement pipette or some similar device might have prevented such defects.

3.2.2. Crystalline structural evolution

The diffraction patterns of the composite aerogel made from IL-functionalized GO with a tin loading of 80% before and after thermal reduction are compared in Figure 3.17.

In the diffractogram of the as-lyophilized aerogel, peaks belonging to diffraction from SnO are faintly visible. While the Sn-GO nanoparticles were stable in air and there was no further oxidation beyond the initial amorphous oxide layer that had formed during co-milling, it appears that their introduction into the aqueous suspensions of IL-GO induced some more oxidation.

The diffraction pattern of the same slice of material after thermal reduction shows clearly the presence of both phases, β-Sn and SnO. While metallothermic reduction reactions[35] have been employed to reduce graphene oxide, it seemed that the most plausible explanation for

the development of the SnO phase would be that as the graphene oxide matrix is reduced, the reactive oxygen-bearing species that form, oxidize the nanoparticles.

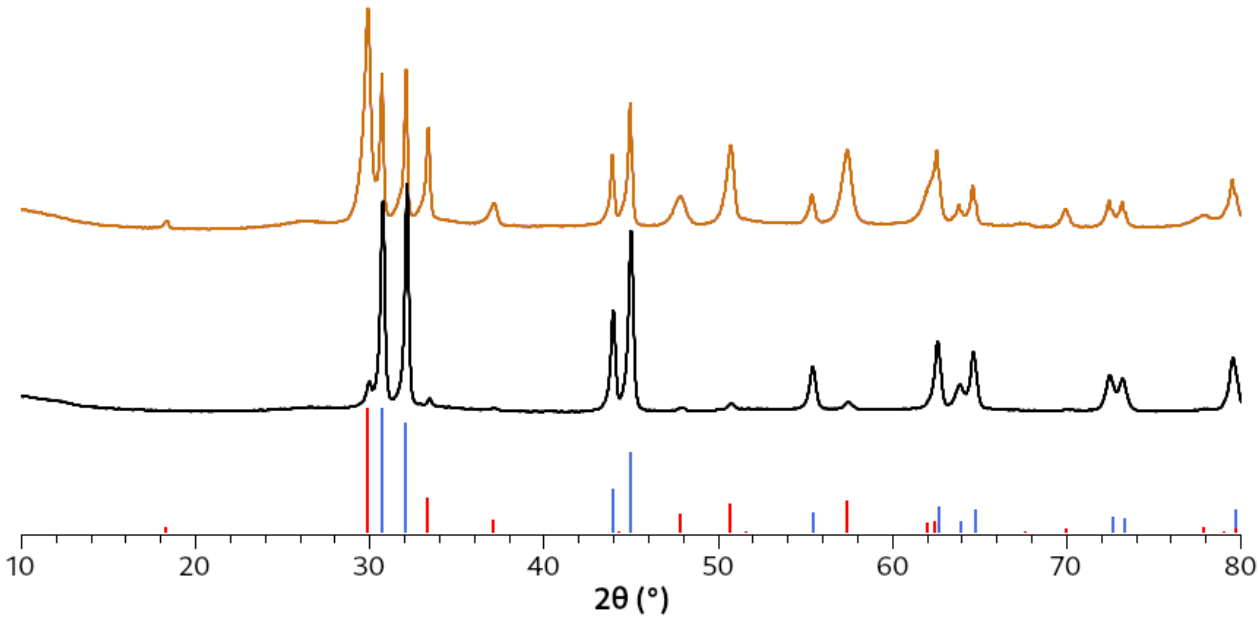

Figure 3.17: Diffraction patterns of a slice of a composite aerogel monolith with 80% Sn loading before (black) and after thermal reduction (orange). In blue, the powder diffraction file of β-Sn and in red that of SnO (both from ICCD).

4. Battery tests

The chemical, structural and morphological characterization of the synthesized materials can provide many clues as to their potential behavior in the Li-ion system. Ultimately though, their performance as actual Li-ion electrodes had to be evaluated in electrochemical cells. The selection of the most suitable structure for the matrix, among the various candidate forms, was made on the same basis.

For that, the materials were integrated into so-called “lithium half-cells”[36]. These are electrochemical cells with a lithium metal electrode acting as both the counter and reference electrode. This means that when a material intended for the anode of Li-ion batteries is tested in a half-cell configuration against lithium, the actual anode is the lithium metal and the cathode is the host material. The first discharge entails the oxidation of metallic lithium and the migration of lithium ions towards the cathode. At the same time, a quantity of electrolyte is decomposed, as the solid-electrolyte interphase forms on the exposed surfaces of the cathode material. When the current draw is reversed, the lithium stored in the tested material returns to the metal electrode. The reason why lithium half-cells are used for testing is that the amount of lithium ions that can be released from metallic lithium and be integrated into an active material is practically limitless, which allows to determine the specific capacity of that material. In full-cells, the capacities of both active materials (in the anode and cathode) have to be known in advance, in order to match their quantities and capacities.

The half-cells are tested using a galvanostatic circuit, which is capable of maintaining a current through an electrochemical cell constant, regardless of the load. The testing apparatus cycles the cells between two preselected voltage values, applying the specified current in one direction to discharge the batteries and in the opposite, to charge them.

The measuring apparatus records the applied current and the corresponding time, which

are combined with the mass of the active material in the following equation to yield the specific (per mass) capacity:

$$C = \frac{I \cdot t}{m} \qquad \text{(Equation 3.1)}$$

where I is the applied current (in amperes), t is the time during which the current was applied (in hours) and m is the mass of the active material (in grams). The expected, theoretical capacity of a material can then be compared to the experimentally determined capacity. The theoretical capacity (in mAh/g) of a material is calculated by the following equation:

$$C_{theo} = \frac{z \cdot F}{3.6 \cdot M} \qquad \text{(Equation 3.2)}$$

where z is the number of electrons exchanged in the electrochemical reaction, F is the Faraday constant (C/mol) and M is the molar mass (g/mol) of the active material. It is easily deduced from the above equation or from the definition of the coulomb in the International Sytem of Units, that 1 Ah = 3600 C, *i.e.* the electric charge transferred by a steady current of one ampere flowing for one hour is equal to 3600 coulombs.

In addition to the determination of the capacity of the active material, galvanostatic measurements also allow to determine the coulombic efficiency of the electrochemical system, a measure of its stability. Coulombic efficiency (CE), also called faradaic efficiency or current efficiency, is defined as follows:

$$CE(\%) = \frac{C_{charge}}{C_{discharge}} \times 100 \qquad \text{(Equation 3.3)}$$

with C_{charge} and $C_{discharge}$ the measured capacity during charge and discharge, respectively. A coulombic efficiency of 100% would mean that it is possible to retrieve all of the energy that was stored in the battery over a full cycle. While a CE nearing 100% is feasible and even more so for Li-ion batteries[37], it is impossible to attain 100%, as at least ohmic losses will always be

present. Suboptimal operating conditions, *e.g.* fast charging or use outside the specified temperature range of a battery, will also lead to a lowered CE. Also, parasitic reactions will consume some of the electrons provided during charging. More importantly, for Li-ion batteries, the SEI formation during the first cycle (or cycles), will obviously cause a decrease in CE for that cycle.

4.1. Battery assembly

The half-cells used for the measurements were assembled into batteries using the CR2032 coin cell format. According to the IEC 60086-3:2021 standard for "watch batteries", the CR2032 casing has a 20 mm diameter and a height of 3.2 mm, both reflected in the naming. The components used in the assembly of the batteries are shown in the exploded view diagram of Figure 3.18. Starting from the bottom end of the battery, a stainless steel spacer is

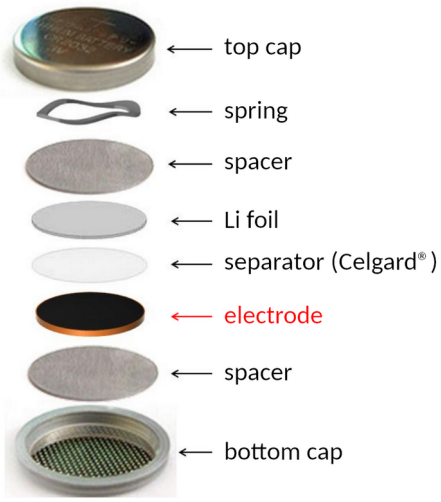

Figure 3.18: Exploded view drawing of a coin cell battery used for electrochemical tests, displaying all the components employed.

placed in contact with the bottom cap and on it, the electrode material is centered. Next is a separator film, which allows the flow of Li ions through its pores, but prevents the electric contact between the anode and the cathode. On top of that is placed the Li electrode, made

by compressing a freshly cleaned and cut disk of lithium foil against another spacer. A stainless steel spring between the last spacer and the top cap is used to maintain the contact of the cell with the battery terminals throughout any volume changes of the active materials. The ionic flow between the electrodes is ensured by the addition of electrolyte solution to both electrode-separator interfaces. Porous materials are also saturated with the electrolyte solution. Once all the components are in place, a crimping press seals the battery by deforming the rim of the top cap around the edges of the bottom cap.

4.2. Evaluation of the matrix form

To decide between the matrix forms that had been prepared – membranes, ordered porous network and disordered porous network – they were used as electrodes in coin cell batteries. The objective was to prepare a scaffold that would not only provide support and conductive pathways to the tin nanoparticles, but also facilitate the diffusion of lithium ions and be active in hosting lithium itself.

As this was going to be a comparative study, the materials were not tested exhaustively and the batteries were left to run only for a few cycles. The batteries were cycled between 0.05 and 3 V, at relatively low currents of 5 – 10 mA/g.

In the following plots, the lithiation of the material corresponds to the discharge curves (starting left at higher potential and moving downward and to the right) and the delithiation to the charge curves (starting left at lower potential and moving upward and to the right). For each of the tests, only the first three cycles are shown.

4.2.1. Membrane

Figure 3.19 shows the charge-discharge curves of a battery with an rGO membrane electrode.

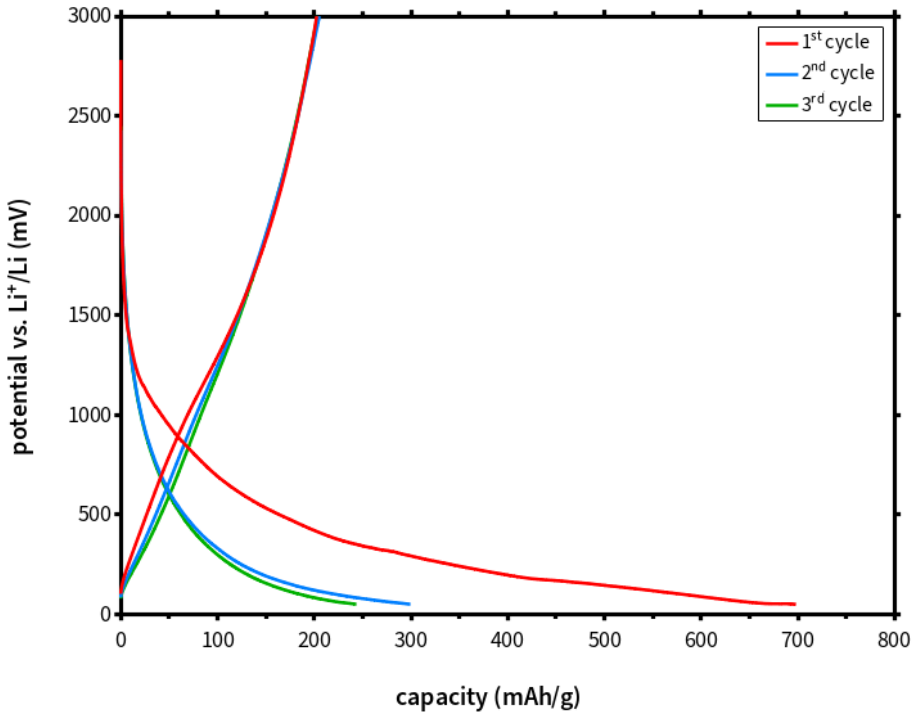

Figure 3.19: First three cycles of a battery with an rGO membrane electrode.

As expected, the formation of the SEI during the first cycle leads to an irreversible capacity loss of ~400 mAh/g. In the next two cycles, the capacity loss continues, but decreasing, 100 mAh/g and then 45 mAh/g, indicating that the formation of the SEI is not completed upon the first discharge. The coulombic efficiency evolves accordingly, 28.6% (1st cycle), 66.7% (2nd cycle) and 81.6 (3rd cycle), reflective of the progressive stabilization of the exposed surfaces. The attained capacity of the material is below that of graphite (372 mAh/g), staying almost constant at 200 mAh/g during these three cycles. A possible interpretation would be that the size and the layering of the rGO sheets limits the amount of Li that can penetrate the structure, with lithiation taking place only on the outer layers of the membrane.

4.2.2. Ordered aerogel made from IL and rGO

Figure 3.20 shows the charge-discharge curves of a battery with an aerogel electrode made from EMI^+TFSI^- and rGO with an ordered internal structure. Similar structures made from GO, without the addition of IL, were too fragile to be used.

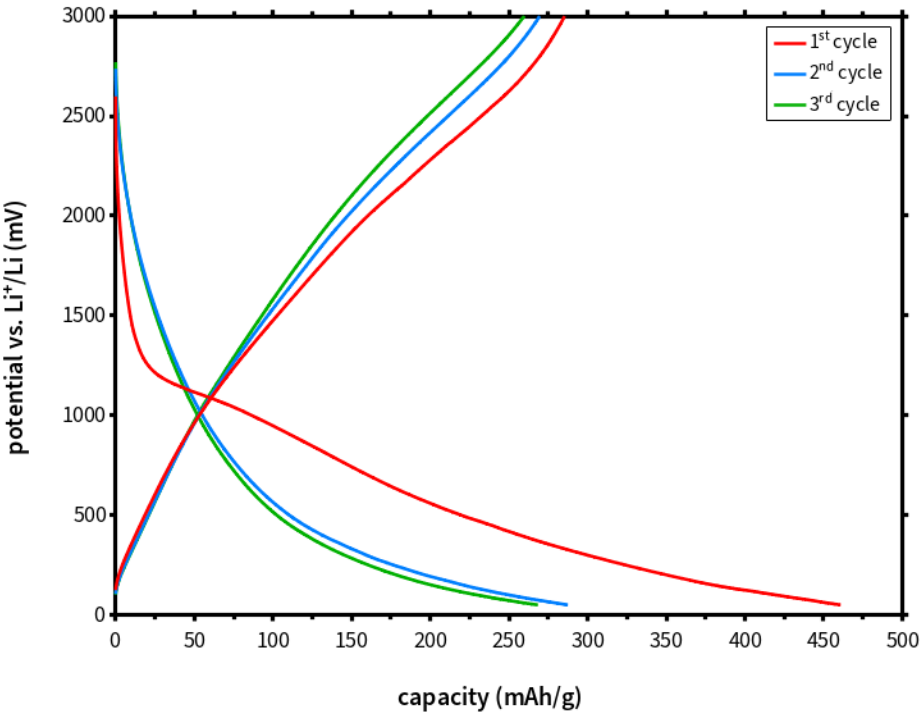

Figure 3.20: First three cycles of a battery with an ordered aerogel made from EMI^+TFSI^- and rGO as electrode.

Again, SEI formation is accompanied by an initial irreversible capacity loss of 175 mAh/g, with progressive stabilization over the next two cycles. The calculated coulombic efficiency is 62.0% (1^{st} cycle), 93.1% (2^{nd} cycle) and 96.2 (3^{rd} cycle). Interestingly, the irreversible capacity loss of this material is lower than that of the membrane, suggesting a decreased amount of exposed rGO surface in the ordered aerogel. However, since the specific capacity is higher than that of the membrane, some amount of the hosted lithium must be intercalated. Still, the specific capacity of the material is lacking, compared to that of graphite, going from 285 mAh/g in the first cycle, to 260 mAh/g in the third.

4.2.3. Disordered aerogel made from IL and rGO

Figure 3.21 shows the charge-discharge curves of a battery with an aerogel electrode made from EMI^+TFSI^- and rGO with a disordered internal structure.

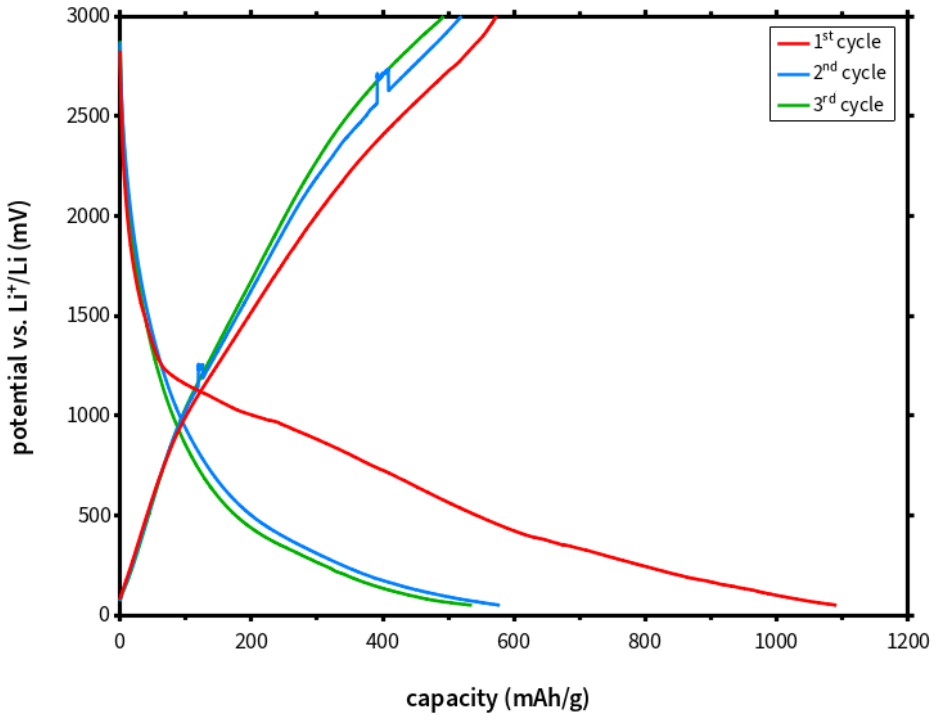

Figure 3.21: First three cycles of a battery with a disordered aerogel made from EMI^+TFSI^- and rGO as electrode.

The disordered aerogel exhibits a much higher initial irreversible capacity loss of 530 mAh/g, indicating a much higher exposed surface area. The coulombic efficiency recovers slightly faster than in the ordered structure: 51.8% (1st cycle), 89.7% (2nd cycle) and 95.2% (3rd cycle). This could mean that all of the reactive sites of the matrix are easily accessible, so passivation is completed sooner. The most striking aspect of the measurements though, is that the attained capacity is considerably higher than that of graphite, 570, 520 and 495 mAh/g in the 1st, 2nd and 3rd cycles, respectively. The only possible explanation for this would be the reversible multilayer deposition on the structure.

4.2.4. Verdict

All three materials exhibit charge-discharge characteristics in line with what has already been reported for graphene-based nanostructures[38]. As expected, the three different forms of reduced graphene oxide are conductive and capable of reversibly hosting lithium, meaning that they could play an ancillary active role while supporting nanostructured tin as the main active material. Their self-supporting forms render the use of binders redundant. Furthermore, they can be cut in the desired dimensions and be used as they are, forgoing the typical preparation methods used in electrode fabrication.

The expanded rGO sheets in the membrane are much larger than the lateral dimensions of graphite particles typically used in batteries. As such, lithiation appears to take place mostly by adsorption on the outer surface and perhaps by some intercalation between the first layers accessible through the gaps where the outermost sheets end. Inevitably, as the sheets are ordered perpendicularly to the diffusion path of lithium ions, the inner parts of the membrane remain inaccessible.

The ordered aerogel can be seen as marginally better. More of its mass is available to lithium ions, as reflected in its increased specific capacity. The lower irreversible capacity loss compared to the membrane, implies a smaller amount of reactive surfaces, so at least some of the hosted lithium ends up intercalated in the structure. However, the gravimetric capacity is lower than that of graphite, indicating that not all of the sheets are available to lithium ions.

Despite the considerable initial irreversible capacity loss, related to an increased surface availability, the disordered aerogel appears as the best choice among the three candidate forms. Not only is all of the theoretical rGO surface exploited during lithiation, but the nature of the structure appears to induce the multilayer deposition of lithium, resulting in a specific capacity exceeding by more than 35% that of graphite. These results, combined with those of the morphological investigations carried out earlier, favored the disordered aerogel

as the most suitable form for the matrix of the composite material.

Experimental details. *All three materials were placed in contact with a disc cut from Cu foil as a current collector and were used in coin cell batteries assembled as shown in Fig. 3.18. A solution of 1 M $LiPF_6$ in ethylene carbonate and dimethyl carbonate 1:1 (v/v) (purity 99.9%) purchased from Solvionic was used as the electrolyte. Li foil (purity > 99.9) was purchased from Sigma-Aldrich. rGO membrane: a disk with a diameter of 10 mm, weighing 1.6 mg was cut from an rGO membrane with a thickness of 0.055 mm. Ordered aerogel: a disk with a diameter of 10 mm, weighing 3.1 mg was cut from a disk with a thickness of 2 mm, which was compressed to 0.4 – 0.5 mm inside the battery. Disordered aerogel: a disk with a diameter of 10 mm weighing 2.4 mg was cut from a disk with a thickness of 2 mm, compressed to 0.4 – 0.5 mm inside the battery. The membrane was wet with 6 drops of electrolyte solution, while the aerogels were saturated with 25 drops of solution. Batteries were sealed using an electronically controlled hydraulic crimping press purchased from MTI Corporation. Between charging and discharging states, a pause of 5 minutes was imposed.*

4.3. First assessment of the ternary composite materials

Having two components capable of hosting lithium in the composite materials, it follows that their combined capacity will be the sum of the products of each material's mass and its individual capacity. Assuming that the entirety of the mass of the matrix can host lithium, its theoretical capacity is 372 mAh for every gram of material. By making the approximation that all of tin exists in its metallic form and assuming that the most lithiated alloy of tin, $Li_{4.4}Sn$ can form, the capacity afforded by tin will be approximately 993 mAh per gram of material. Consequently, the theoretical capacities of the composites (with a given %wt of tin) should be:

- IL-rGOSn40: 620 mAh/g (223 mAh/g from the matrix and 397 mAh/g from tin)
- IL-rGOSn60: 745 mAh/g (149 mAh/g from the matrix and 596 mAh/g from tin)
- IL-rGOSn80: 868 mAh/g (74 mAh/g from the matrix and 794 mAh/g from tin)

The same capacities would be expected for the control samples (rGOSn40, rGOSn60 and rGOSn80), prepared by mixing tin nanoparticles with graphene oxide at the same proportions.

Composite aerogels made from ionic-liquid-functionalized GO and tin nanoparticles were prepared as already described (Chapter 3, section 3). After sectioning the aerogels and discarding the discs with visible defects – mainly voids due to the entrapment of air prior to freeze-casting – a number of batteries were assembled. This time the electrolyte used contained fluoroethylene carbonate (FEC), an additive that has been shown to form stable solid-electrolyte interphases[39,40]. Some of these were malfunctioning right after assembly, as materials can move around while the battery is being crimped in the crimping press, resulting in short-circuits. The control samples made from rGOSn40 and rGOSn80 were lost this way. Complicating matters further, a failure with the instrumentation prevented applying the selected current, 50 mA/g to all but a single of the remaining samples, without any indication that a different current was being applied. As soon as the error was discovered, all the samples were switched to a current regime decreased by a factor of 10, *i.e.* 5 mA/g, prolonging the duration of the measurements. On account of these issues, the results that will be presented in this section have little comparative value and should be considered as a first indication of the potential behavior of the composite materials.

4.3.1. IL-rGOSn40

This composite with a loading of tin nanoparticles of 40 wt% was the only one that was actually cycled at 50 mA/g, shown in Figure 3.22a. Lithium insertion started at a low potential *vs.* Li^+/Li, ~0.25 V, which was unexpected. Lithiation reached a capacity of 50 mAh/g, less than a quarter of the theoretical capacity of the matrix alone. During lithium extraction from the composite all of the stored energy was recovered and the potential appeared to reach a plateau, around 0.36 V. This plateau was maintained (with occasional

spikes), suggesting that a redox equilibrium of some sort had been reached.

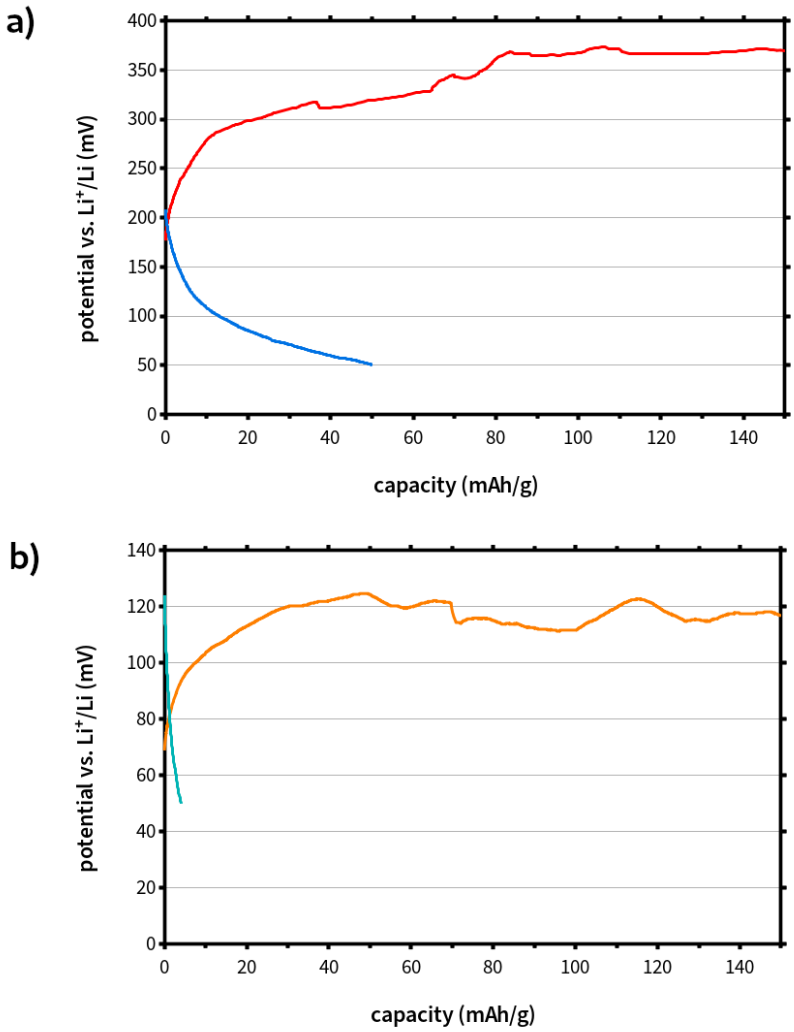

Figure 3.22: a) Lithiation (blue) and delithiation (red) curves of IL-rGOSn40, cycled at 50 mA/g. b) Lithiation (green) and delithiation (orange) curves of IL-rGOSn40, cycled at 5 mA/g.

When the battery was switched to the lower current setting, 5.0 mA/g, Figure 3.22b, the result was rather similar. Lithiation started at the low potential of 0.125 V and stopped after ~5 mAh/g. Current reversal had the same result as before, with a potential plateau being reached at ~0.12 V.

4.3.2. IL-rGOSn60

Similar results were obtained from the composite with a tin loading of 60 wt% shown in

Figure 3.23a. The energy stored during discharge was approximately 70 mAh/g, with lithiation beginning at a low potential *vs.* Li^+/Li, 0.22 V. Lithium extraction momentarily exceeds 0.3 V, with the potential plateauing close to 0.25 V.

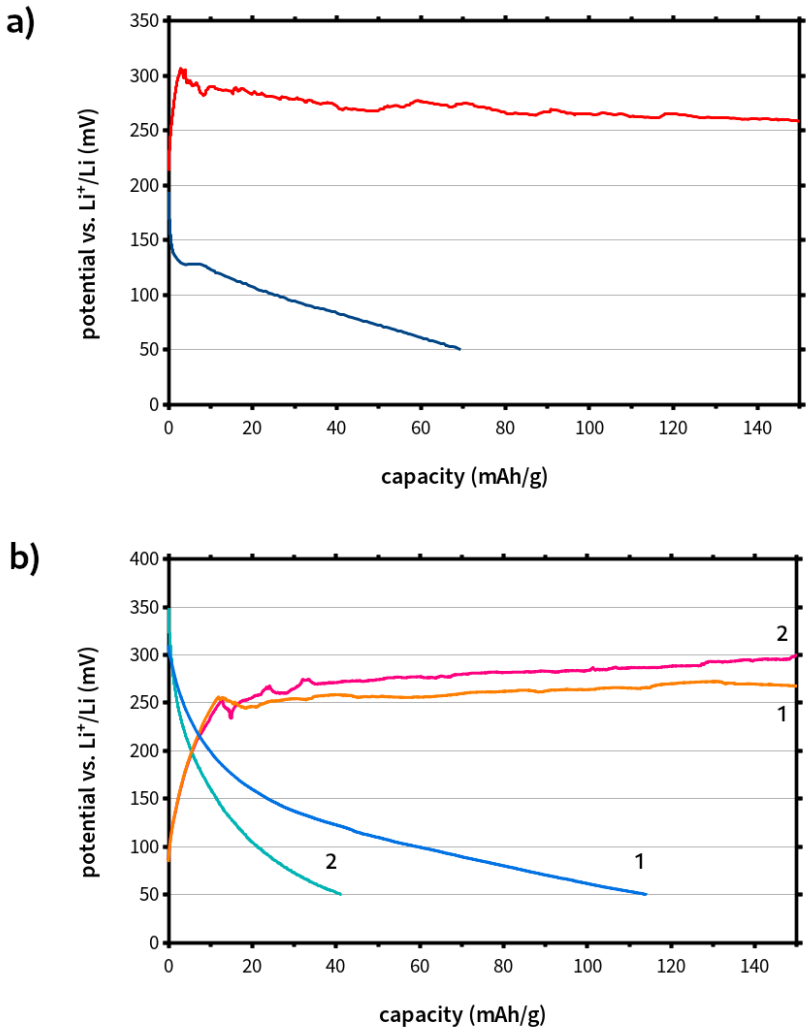

Figure 3.23: a) Lithiation (blue) and delithiation (red) curves of IL-rGOSn60, cycled at 22 mA/g. b) 1st (blue) and 2nd (green) lithiation and 1st (orange) and 2nd (pink) delithiation curves of IL-rGOSn60, cycled at 5 mA/g.

The first discharge at 5 mA/g results in higher lithiation (Figure 3.23b), 115 mAh/g, but the subsequent lithiation stops at 40 mAh/g. In both cycles, lithium extraction barely surpasses 0.25 V, before dropping and plateauing again.

4.3.3. IL-rGOSn80

The first discharge-charge cycle of the composite with a tin loading of 80 wt% at 13.5 mA/g began at a relatively higher potential than the other samples *vs.* Li^+/Li, almost 0.8 V (Figure 3.24a). The energy stored reached 500 mAh/g, which corresponds to 58 % of the theoretical capacity of the composite. However, once more, during lithium extraction the potential rose to 0.49 V before reaching a plateau.

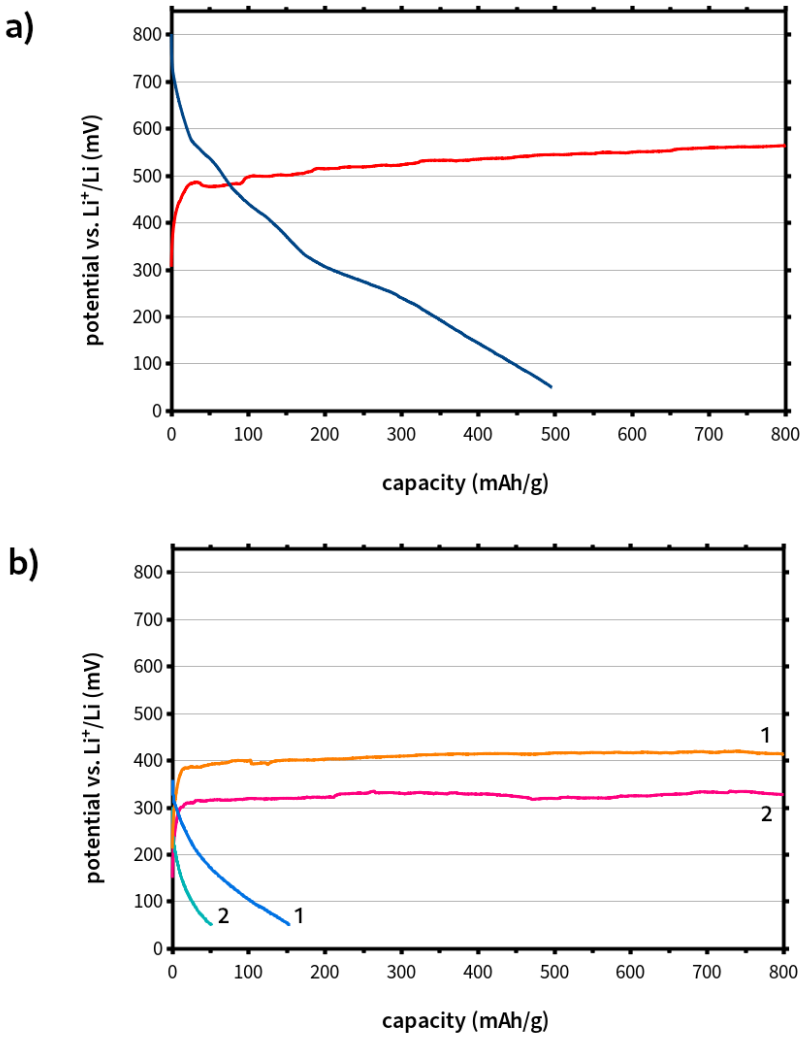

Figure 3.24: a) Lithiation (blue) and delithiation (red) curves of IL-rGOSn80, cycled at 13.5 mA/g. b) 1st (blue) and 2nd (green) lithiation and 1st (orange) and 2nd (pink) delithiation curves of IL-rGOSn80, cycled at 5 mA/g.

Cycling at a current of 5 mA/g (Figure 3.24b) gave fainter capacities during lithiation, approximately 150 mAh/g for the first discharge and 50 mAh/g for the second. In the same cycles, the potential plateaued around 0.41 V and 0.32 V, respectively.

4.3.4. rGOSn60

Charge-discharge curves of the control sample made from GO with a tin loading of 60 wt % at 32.5 mA/g (Figure 3.25a) and 5 mA/g (Figure 3.25b) appear markedly different. The first discharge appears rather “bumpy”, which could be due to reactions taking place during lithium insertion. In this sample, discharge and charge are performed between the selected potential values, 0.05 V and 3.00 V. The first lithium insertion reaches a capacity which corresponds exactly to the capacity of the matrix. Oddly, after the second discharge, both

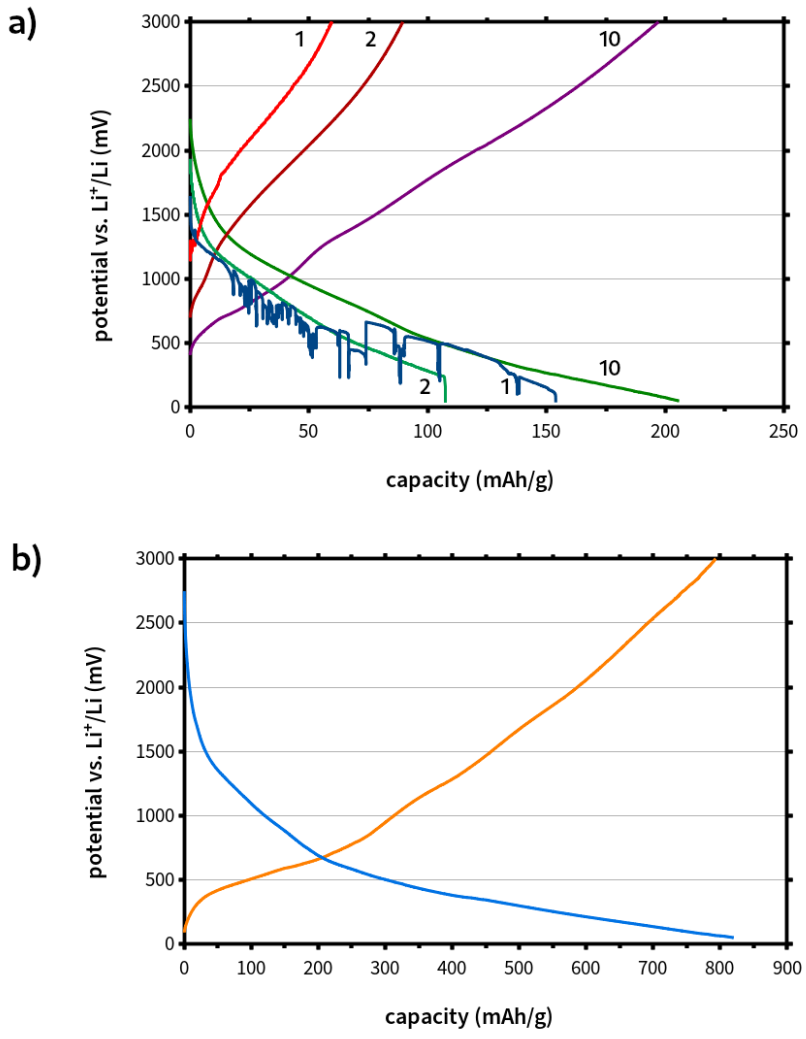

Figure 3.25: a) 1st (blue), 2nd (light green) and 10th (green) lithiation and 1st (red), 2nd (dark red) and 10th (purple) delithiation curves of rGOSn60, cycled at 32.5 mA/g. b) Lithiation (blue) and delithiation (orange) curves of rGOSn60, cycled at 5 mA/g.

charge and discharge capacities increase instead of decreasing. One plausible explanation would be that the electrode material is metastable at the given operating conditions and it is

subjected to transformations as cycling progresses, becoming capable of hosting more lithium in the process. At the tenth cycle, some "steps" start to become apparent in the charge curve, which could indicate some reversible conversion taking place, as would be expected for the reaction of SnO with Li^+.

At 5 mA/g (Figure 3.25b), these "steps" are more clear. More strikingly, the capacity of the material has exceeded the slightly overestimated, theoretical value. This could once more indicate that multilayer lithium deposition takes place in the structure.

While the size of the sample does not allow safe conclusions to be reached, there appears to be a correlation between Sn content in the samples and the potential at which lithiation takes place. The latter seems to be increasing with Sn loading, at least in the measurements conducted at the same current draw per mass for all samples, 5 mA/g. Conversely, this could be seen as an inverse relationship between the amount of functionalized GO and lithiation potential. The fact that the sample with the non-functionalized matrix exhibits a completely different behavior – always with regard to the lithiation potential – would suggest that the functionalized material is responsible for what is observed.

Experimental details. *A solution of 1 M $LiPF_6$ in ethylene carbonate and ethyl methyl carbonate 1:1 (v/v)) with 2 wt% fluoroethylene carbonate (purity 99.9%) purchased from Solvionic was used as the electrolyte. All of the materials were cut into disks with a diameter of 13 mm and a thickness of 2 mm. All the other parameters were the same as in section 4.2.*

5. Conclusions

Experimentation with binary mixtures of the $EMI^{+}TFSI^{-}$ ionic liquid and graphene oxide early on was helpful in understanding the interplay between them and to anticipate practical problems, most of them stemming from the viscosity of the resulting systems. It showed that the ionic liquid had a beneficial effect in the cohesion of the aerogels, most likely through π-π and cation-π interactions. The sturdiness of the binary structures was key in identifying and assessing the eventual disordered porous matrix in a rational design. Despite its macroporosity, that form was capable of achieving a higher gravimetric capacity than graphite, in all likelihood by favoring the reversible multilayer deposition of lithium.

The grafting of the amino-functionalized ionic liquid onto graphene oxide through the epoxide ring-opening reaction did not present any particular challenges, even though the backing literature lacked some precision with regard to synthetic protocols. Performing the grafting with the unpurified mixture of the ionic liquid (as it was recovered after the reduction of the azide precursor) proved to be a viable and above all, economical strategy. While it was not possible to obtain direct evidence of the formation of the N-C bond in the functionalized material, through comparisons with the corresponding physical mixture and GO and base-treated GO, its demonstrably different behavior was shown and indirect evidence was obtained. The functionalized material possessed a markedly different thermal profile and also, the spatial distribution of the species belonging to the ionic liquid was much more uniform on its surface than in the physical mixture. Another conclusion that was reached through these analyses, was that the XPS analysis had overestimated the amount of epoxide groups on graphene oxide. Thermal and ^{13}C analyses did not show any epoxide groups present nor an increase in hydroxyl groups after the reaction. If the grafting reaction was incomplete, either of these should have been true. While this sort of error is not unexpected[41], future work should focus on a more accurate determination of the functional groups present on graphene oxide.

The addition of the Sn-GO nanoparticles to the suspensions of the functionalized graphene oxide, while seemingly simple, had some unforeseen consequences. It was expected that the outer layers of amorphous oxide and reduced graphene oxide could sufficiently shield the metal core of the particles from further oxidation in suspension, as they did in air. Clearly, that was not the case, as evidenced by the diffraction pattern of the composite after lyophilization. In the same vein, the wrapping of the nanoparticles was once more unable to protect them from oxidation during thermal annealing. Perhaps a more serious issue was the incomplete homogenization of the final mixtures, which could prove detrimental in battery cycling. A different handling/engineering solution should be devised to achieve better results. Another interesting finding from the incorporation of the nanoparticles to the suspensions was the stabilizing effect of the grafted ionic liquid to the system. While there was more available supporting surface (in the form of graphene oxide sheets) in a suspension of pristine GO than in a suspension of functionalized GO of the same concentration, the former was not stable over time and the nanoparticles eventually precipitated.

The behavior of the composites as electrode materials in batteries, was utterly unanticipated. While the experiments will be repeated taking into account all the potential points of failure of the testing system, the fact of the matter remains that all of the samples that were measured exhibited the same behavior. Very little lithium was inserted in the structure and upon its release, a continuous redox reaction at near-equilibrium took place. With the data available at the moment, it is impossible to identify the root cause. However, the different behavior of the control sample, with the non-functionalized rGO matrix points to the grafted ionic liquid as the culprit. In addition, the low potential at which lithiation takes place suggests an increased lithiation/delithiation potential against Li^+/Li. In further experiments, the functionalized rGO will be examined in cyclic voltammetry measurements with solutions of the battery electrolyte. Perhaps a combination of XPS and UV photoelectron spectroscopy (UPS) might be able to provide some more insights by comparing the surface energy of the IL-functionalized material to that of pure rGO.

6. References

(1) Mahyari, M.; Shaabani, A.; Bide, Y. Gold Nanoparticles Supported on Supramolecular Ionic Liquid Grafted Graphene: A Bifunctional Catalyst for the Selective Aerobic Oxidation of Alcohols. *RSC Advances* **2013**, *3* (44), 22509. https://doi.org/10.1039/c3ra44696d.

(2) Yang, H.; Shan, C.; Li, F.; Han, D.; Zhang, Q.; Niu, L. Covalent Functionalization of Polydisperse Chemically-Converted Graphene Sheets with Amine-Terminated Ionic Liquid. *Chemical Communications* **2009**, No. 26, 3880. https://doi.org/10.1039/b905085j.

(3) Du, M.; Yang, T.; Ma, S.; Zhao, C.; Jiao, K. Ionic Liquid-Functionalized Graphene as Modifier for Electrochemical and Electrocatalytic Improvement: Comparison of Different Carbon Electrodes. *Analytica Chimica Acta* **2011**, *690* (2), 169–174. https://doi.org/10.1016/j.aca.2011.01.051.

(4) *The IUPAC Compendium of Chemical Terminology: The Gold Book*, 4th ed.; Gold, V., Ed.; International Union of Pure and Applied Chemistry (IUPAC): Research Triangle Park, NC, 2019. https://doi.org/10.1351/goldbook.

(5) Cao, J.; Zhao, X.; Wang, J.; Dou, H.; Liu, C.; Yan, X.; Yan, Y.; Guo, M.; Zhao, W.; Yang, X. Processing Micrometer-Sized Particles in Crumpled Graphene Network for Freestanding Membrane Enabled by Freeze Casting. *Chinese Chemical Letters* **2019**. https://doi.org/10.1016/j.cclet.2019.03.041.

(6) Liu, S.-H.; Chen, C.-C.; Zhang, B.; Wu, J.-H. Fire and Explosion Hazards of 1-Ethyl-3-Methylimidazolium Bis(Trifluoromethylsulfonyl)Imide. *RSC Advances* **2020**, *10* (38), 22468–22479. https://doi.org/10.1039/D0RA01821J.

(7) Griggs, C. S.; Medina, V. F. Graphene and Graphene Oxide Membranes for Water Treatment. In *McGraw Hill Encyclopedia of Science & Technology, 11th Edition*; McGraw Hill.

(8) Huang, X.; Huang, Z.; Liu, Q.; Zhou, A.; Ma, Y.; Wang, J.; Qiu, H.; Bai, H. Organic Solvent-Assisted Lyophilization: A Universal Method of Preparing Two-Dimensional Material Nanoscrolls. *ACS Omega* **2019**, *4* (4), 7420–7427. https://doi.org/10.1021/acsomega.9b00623.

(9) Deville, S. Freeze-Casting of Porous Ceramics: A Review of Current Achievements and Issues. *Adv. Eng. Mater.* **2008**, *10* (3), 155–169. https://doi.org/10.1002/adem.200700270.

(10) Mehio, N.; Dai, S.; Jiang, D. Quantum Mechanical Basis for Kinetic Diameters of Small Gaseous Molecules. *J. Phys. Chem. A* **2014**, *118* (6), 1150–1154. https://doi.org/10.1021/jp412588f.

(11) Broadbent, K. A.; Dollimore, D.; Dollimore, J. The Surface Area of Graphite Calculated from Adsorption Isotherms and Heats of Wetting Experiments. *Carbon* **1966**, *4* (2), 281–287. https://doi.org/10.1016/0008-6223(66)90090-X.

(12) Bautista-Toledo, I.; Ferro-Garcia, M. A. Localizaed N2 Adsorption on Graphites, Graphite Oxides and Exfoliated Graphites. *Materials Chemistry and Physics* **1989**, *21* (4), 335–343. https://doi.org/10.1016/0254-0584(89)90135-1.

(13) Peigney, A.; Laurent, Ch.; Flahaut, E.; Bacsa, R. R.; Rousset, A. Specific Surface Area of Carbon Nanotubes and Bundles of Carbon Nanotubes. *Carbon* **2001**, *39* (4), 507–514. https://doi.org/10.1016/S0008-6223(00)00155-X.

(14) Thommes, M.; Kaneko, K.; Neimark, A. V.; Olivier, J. P.; Rodriguez-Reinoso, F.;

Rouquerol, J.; Sing, K. S. W. Physisorption of Gases, with Special Reference to the Evaluation of Surface Area and Pore Size Distribution (IUPAC Technical Report). *Pure and Applied Chemistry* **2015**, *87* (9–10). https://doi.org/10.1515/pac-2014-1117.

(15) Lowell, S.; Shields, J. E.; Thomas, M. A.; Thommes, M. *Characterization of Porous Solids and Powders: Surface Area, Pore Size and Density*; Scarlett, B., Series Ed.; Particle Technology Series; Springer Netherlands: Dordrecht, 2004; Vol. 16. https://doi.org/10.1007/978-1-4020-2303-3.

(16) Brunauer, S.; Emmett, P. H.; Teller, E. Adsorption of Gases in Multimolecular Layers. *J. Am. Chem. Soc.* **1938**, *60* (2), 309–319. https://doi.org/10.1021/ja01269a023.

(17) Ismail, I. M. K. Cross-Sectional Areas of Adsorbed Nitrogen, Argon, Krypton, and Oxygen on Carbons and Fumed Silicas at Liquid Nitrogen Temperature. *Langmuir* **1992**, *8* (2), 360–365. https://doi.org/10.1021/la00038a006.

(18) Zhang, Y.; Park, S.-J. Imidazolium-Optimized Conductive Interfaces in Multilayer Graphene Nanoplatelet/Epoxy Composites for Thermal Management Applications and Electroactive Devices. *Polymer* **2019**. https://doi.org/10.1016/j.polymer.2019.01.086.

(19) Bonollo, S.; Lanari, D.; Vaccaro, L. Ring-Opening of Epoxides in Water. *Eur. J. Org. Chem.* **2011**, *2011* (14), 2587–2598. https://doi.org/10.1002/ejoc.201001693.

(20) McMurry, J. *Organic Chemistry*, Ninth edition.; Cengage Learning: Boston, MA, USA, 2016.

(21) Zhu, C.; Zhai, J.; Dong, S. Ionic Liquid-Induced Three-Dimensional Macroassembly of Graphene and Its Applications in Electrochemical Energy Storage. *Nanoscale* **2014**, *6* (17), 10077. https://doi.org/10.1039/C4NR02400A.

(22) Vacchi, I. A.; Spinato, C.; Raya, J.; Bianco, A.; Ménard-Moyon, C. Chemical Reactivity of Graphene Oxide towards Amines Elucidated by Solid-State NMR. *Nanoscale* **2016**, *8* (28), 13714–13721. https://doi.org/10.1039/C6NR03846H.

(23) Chai, J.; Li, F.; Hu, Y.; Zhang, Q.; Han, D.; Niu, L. Hollow Flower-like AuPd Alloy Nanoparticles: One Step Synthesis, Self-Assembly on Ionic Liquid-Functionalized Graphene, and Electrooxidation of Formic Acid. *Journal of Materials Chemistry* **2011**, *21* (44), 17922. https://doi.org/10.1039/c1jm13631c.

(24) Teimuri-Mofrad, R.; Abbasi, H.; Hadi, R. Graphene Oxide-Grafted Ferrocene Moiety via Ring Opening Polymerization (ROP) as a Supercapacitor Electrode Material. *Polymer* **2019**. https://doi.org/10.1016/j.polymer.2019.01.084.

(25) Belessi, V.; Petridis, D.; Steriotis, T.; Spyrou, K.; Manolis, G. K.; Psycharis, V.; Georgakilas, V. Simultaneous Reduction and Surface Functionalization of Graphene Oxide for Highly Conductive and Water Dispersible Graphene Derivatives. *SN Applied Sciences* **2019**, *1* (1). https://doi.org/10.1007/s42452-018-0077-9.

(26) Mondal, T.; Basak, S.; Bhowmick, A. K. Ionic Liquid Modification of Graphene Oxide and Its Role towards Controlling the Porosity, and Mechanical Robustness of Polyurethane Foam. *Polymer* **2017**, *127*, 106–118. https://doi.org/10.1016/j.polymer.2017.08.054.

(27) Cai, W.; Piner, R. D.; Stadermann, F. J.; Park, S.; Shaibat, M. A.; Ishii, Y.; Yang, D.; Velamakanni, A.; An, S. J.; Stoller, M.; An, J.; Chen, D.; Ruoff, R. S. Synthesis and Solid-State NMR Structural Characterization of ^{13}C-Labeled Graphite Oxide. *Science* **2008**, *321* (5897), 1815–1817. https://doi.org/10.1126/science.1162369.

(28) Gao, W.; Alemany, L. B.; Ci, L.; Ajayan, P. M. New Insights into the Structure and Reduction of Graphite Oxide. *Nature Chem* **2009**, *1* (5), 403–408. https://doi.org/10.1038/nchem.281.

(29) Thomas, H. R.; Day, S. P.; Woodruff, W. E.; Vallés, C.; Young, R. J.; Kinloch, I. A.;

Morley, G. W.; Hanna, J. V.; Wilson, N. R.; Rourke, J. P. Deoxygenation of Graphene Oxide: Reduction or Cleaning? *Chemistry of Materials* **2013**, *25* (18), 3580–3588. https://doi.org/10.1021/cm401922e.

(30) Vieira, M. A.; Gonçalves, G. R.; Cipriano, D. F.; Schettino, M. A.; Silva Filho, E. A.; Cunha, A. G.; Emmerich, F. G.; Freitas, J. C. C. Synthesis of Graphite Oxide from Milled Graphite Studied by Solid-State ^{13}C Nuclear Magnetic Resonance. *Carbon* **2016**, *98*, 496–503. https://doi.org/10.1016/j.carbon.2015.11.037.

(31) Muschi, M.; Devautour-Vinot, S.; Aureau, D.; Heymans, N.; Sene, S.; Emmerich, R.; Ploumistos, A.; Geneste, A.; Steunou, N.; Patriarche, G.; De Weireld, G.; SERRE, C. Metal-Organic Framework/Graphene Oxide Composites for CO_2 Capture by Microwave Swing Adsorption. *J. Mater. Chem. A* **2021**. https://doi.org/10.1039/D0TA12215G.

(32) Forse, A. C.; Griffin, J. M.; Merlet, C.; Bayley, P. M.; Wang, H.; Simon, P.; Grey, C. P. NMR Study of Ion Dynamics and Charge Storage in Ionic Liquid Supercapacitors. *J. Am. Chem. Soc.* **2015**, *137* (22), 7231–7242. https://doi.org/10.1021/jacs.5b03958.

(33) Dubouis, N.; Lemaire, P.; Mirvaux, B.; Salager, E.; Deschamps, M.; Grimaud, A. The Role of the Hydrogen Evolution Reaction in the Solid–Electrolyte Interphase Formation Mechanism for " *Water-in-Salt* " Electrolytes. *Energy & Environmental Science* **2018**, *11* (12), 3491–3499. https://doi.org/10.1039/C8EE02456A.

(34) Allen, G. L.; Bayles, R. A.; Gile, W. W.; Jesser, W. A. Small Particle Melting of Pure Metals. *Thin Solid Films* **1986**, *144* (2), 297–308. https://doi.org/10.1016/0040-6090(86)90422-0.

(35) Xing, Z.; Lu, J.; Ji, X. A Brief Review of Metallothermic Reduction Reactions for Materials Preparation. *Small Methods* **2018**, *2* (12), 1800062. https://doi.org/10.1002/smtd.201800062.

(36) Rowden, B.; Garcia-Araez, N. Estimating Lithium-Ion Battery Behavior from Half-Cell Data. *Energy Reports* **2021**, *7*, 97–103. https://doi.org/10.1016/j.egyr.2021.02.048.

(37) Winter, M.; Barnett, B.; Xu, K. Before Li Ion Batteries. *Chemical Reviews* **2018**, *118* (23), 11433–11456. https://doi.org/10.1021/acs.chemrev.8b00422.

(38) Omichi, K.; Ramos-Sanchez, G.; Rao, R.; Pierce, N.; Chen, G.; Balbuena, P. B.; Harutyunyan, A. R. Origin of Excess Irreversible Capacity in Lithium-Ion Batteries Based on Carbon Nanostructures. *J. Electrochem. Soc.* **2015**, *162* (10), A2106–A2115. https://doi.org/10.1149/2.0591510jes.

(39) Etacheri, V.; Haik, O.; Goffer, Y.; Roberts, G. A.; Stefan, I. C.; Fasching, R.; Aurbach, D. Effect of Fluoroethylene Carbonate (FEC) on the Performance and Surface Chemistry of Si-Nanowire Li-Ion Battery Anodes. *Langmuir* **2012**, *28* (1), 965–976. https://doi.org/10.1021/la203712s.

(40) Jaumann, T.; Balach, J.; Klose, M.; Oswald, S.; Langklotz, U.; Michaelis, A.; Eckert, J.; Giebeler, L. SEI-Component Formation on Sub 5 nm Sized Silicon Nanoparticles in Li-Ion Batteries: The Role of Electrode Preparation, FEC Addition and Binders. *Phys. Chem. Chem. Phys.* **2015**, *17* (38), 24956–24967. https://doi.org/10.1039/C5CP03672K.

(41) Hesse, R.; Chassé, T.; Streubel, P.; Szargan, R. Error Estimation in Peak-Shape Analysis of XPS Core-Level Spectra Using UNIFIT 2003: How Significant Are the Results of Peak Fits?: Error Estimation in XPS. *Surf. Interface Anal.* **2004**, *36* (10), 1373–1383. https://doi.org/10.1002/sia.1925.

Chapter 4:
Conclusions and perspectives

1. Conclusions

While tin as an anode material could endow Li-ion batteries with considerably increased capacity and faster charge-discharge rates, its practical use is limited by the fact that the alloying process with lithium entails extreme volume changes. The first step in tackling this problem is the nanostructuring of tin and its enmeshment in another material that can adapt to the repeated expansion and contraction, all the while maintaining contact with the tin particles. The starting point of this work was the synthesis of tin nanoparticles in the $EMI^{+}TFSI^{-}$ ionic liquid and the elucidation of the stabilizing influence that the latter holds on the forming nanoparticles. The present research work focused mainly on the harnessing of these favorable interactions between tin and the ionic liquid, in the form of a ternary composite material, comprising the above and a suitable matrix, to be used as an anode in Li-ion batteries.

Another objective parallel to the main focus, was the rational design of this ternary composite material in a way that eschews the conventional battery electrode fabrication practice. The latter involves the use of binders and additives to provide conductive pathways between the particles of the active material and to help it retain its shape, but this in part also increases the dead weight of the batteries. It was deemed feasible to create a structure grafted with the ionic liquid that could contain the tin nanoparticles and simultaneously be self-supporting, conductive and participating in hosting lithium itself.

Graphene oxide had been identified as a substrate amenable to functionalization and also capable of forming self-supporting macroscopic structures. As it is a derivative of graphene, the electrical conductivity of the parent material could be regained to an extent via reduction after grafting, something which would be a boon for its role in the envisaged electrode. For the synthesis of graphene oxide, graphite flakes with a rather large size (< 2 mm) were used. This was done with the intent of having sufficiently long conductive pathways in the composite material and had an effect on various properties, such as the viscosity of the GO

suspensions as a function of concentration. While work on the synthesis of the other two components was ongoing, several post-synthetic modification and shaping techniques for GO were tested and examined with regard to how they could be incorporated in the overall assembly of the composite, and their compatibility with the other components. In regard to that last point, the conditions for the thermal reduction of the material, were chosen. Thermal annealing of graphene oxide at 200°C for 2 hours under vacuum removed a lot of oxygen-bearing species and restored sp^2 domains, without damaging the ionic liquid or causing tin to melt. In terms of post-synthetic modifications, the introduction of mesopores in the GO sheets by treatment with hydrogen peroxide and the chemical and structural alterations induced by the treatment with hydrazine vapors were identified as of particular interest for the intended application and they were investigated accordingly. Microscopy was used to examine the structural changes and XPS the chemical ones. As for shaping the material in tangible architectures, membranes, gels and foams were prepared. This work is detailed in the first part of the second chapter.

Freeze-casting qualified as a versatile technique, that can produce different structures, by tuning the parameters that drive the formation of ice crystals and was ultimately employed in the preparation of the final matrix form. While aerogels (foams) at first glance would seem to be lacking in terms of volumetric capacity as electrode materials, they are compressible and so their porosity can be varied.

Some preliminary battery tests were conducted using membranes, aerogels with a well-ordered internal structure and aerogels with a disordered structure, in order to decide on a form for the composite material. The first two had subpar performance characteristics compared to graphite, but the latter exhibited a higher gravimetric capacity, probably because it allowed the reversible multilayer deposition of lithium. Microscopy observations had already left the impression that the disordered porous network might be the most suitable for the role of an electrode matrix and the electrochemical tests confirmed that suspicion.

At the onset, it was expected that the aforementioned synthesis of tin nanoparticles in EMI^+TFSI^- would be used for the main material of the composite. However, the scale at which the synthesis had been optimized and importantly, the cost, rendered it incompatible with the fabrication methods and the quantities that were eventually envisioned for the composite material. As a result, several alternative methods and their advantages and disadvantages were examined. Not finding any of them particularly appealing, it was decided to try producing tin nanoparticles by size reduction. Since tin has a low melting point and a cooled ball mill was not available, it was co-milled with graphene oxide as a means to prevent the welding of the ground particles, without introducing a foreign element to the composite material. Parameters such as milling time, speed and grinding medium size were examined, as well as the effect of co-milling tin with graphite instead of graphene oxide. The results of these tests were assessed via TEM and SAXS measurements. Even though a thin layer of amorphous tin oxide forms on the nanoparticles during milling, their being wrapped in sheets of graphene oxide protects them from further oxidation in air, which simplifies considerably their handling. The nanoparticles produced via the selected protocol are polydisperse, ranging in size from 4 to 200 nm, with the smaller ones being perfectly spherical and the larger ones having slightly irregular shapes. A lot of the nanoparticles are found in loose aggregates, enveloped by graphene sheets. It is worth mentioning that in this manner, the nanoparticles are produced at gram scale. These endeavors were presented in the second part of the second chapter. This method of producing tin nanoparticles via co-milling had not been encountered in the scientific literature.

Arguably, the principal component of the composite material was the ionic liquid, whose interactions with tin were to be exploited in the fabricated electrode. The interactions of EMI^+TFSI^- with tin nanoparticles were mainly via the aromatic heterocyclic ring and secondarily via the shielding effect of the anion. Considering that and since the ethyl side chain of the imidazolium had a lesser role, it was decided to use it for the introduction of a functional group that would enable the covalent grafting of the cation. Next came the selection of the functional species and after referring to the literature and analyzing the

synthesized graphene oxide, it was decided to add an amino group, which could react with the relatively abundant epoxide groups of graphene oxide. In hindsight, the interpretation of the XPS spectrum overestimated the quantity of the epoxides, yet the amount introduced had an appreciable effect on the cohesion of the final composite and the C-N bond that formed could withstand the thermal treatment protocol, as evidenced by thermal analysis.

The synthesis of the amino-functionalized ionic liquid turned out not to be exactly as described in several publications. Ultimately, a new three-step protocol had to be devised, starting with the nucleophilic substitution of 1,2-dibromoethane by 1-methylimidazole to produce 1-(2-bromoethyl)-3-methylimidazolium bromide. The bromide of the ethyl chain was then substituted with an azide, which upon reduction yielded an amine. A metathesis reaction with LiTFSI salt produced the desired amino-functionalized ionic liquid. This synthetic protocol was accompanied by all the purification challenges that are typically encountered with imidazolium-based ionic liquids with short side chains, which were exacerbated by the addition of polar functional groups. While adhering to the protocol and purifying the intermediates was necessary to characterize them, it was possible to use the unpurified ionic liquid after the reduction of the azide for the functionalization of graphene oxide, thus minimizing losses.

The functionalization of graphene oxide with the modified ionic liquid was perhaps the most straightforward part of this work. However, the characterization of the material and the verification of grafting was much more involved, as is often the case for graphene oxide composites. ^{19}F and ^{13}C NMR spectroscopy showed respectively the presence of the $TFSI^-$ anion in the final material and that the functional groups on the surface of graphene oxide had changed, in accordance with what was expected for the functionalization through the epoxide ring-opening reaction. Ultimately, the strongest – but always indirect – evidence came from comparative thermal analyses of the functionalized material and a physical mixture of the ionic liquid and graphene oxide, as well as elemental mapping of the same via EDX.

The addition of the nanoparticles to aqueous suspensions of functionalized graphene oxide produced thixotropic gels. While the increased viscosity was a desired property for tuning the porosity of the material during freeze-casting, homogenization had to be performed by hand and visually verifying that a black powder was homogeneously dispersed in a black paste was not an easy task. Furthermore, when the viscous suspension was transferred to the freeze-casting container, some air got trapped with it, which led to a quantity of shaped material being discarded, as it presented discontinuities. The contact of the nanoparticles with water and the subsequent thermal annealing caused further oxidation, which has not been quantified up to this point and which would lead to a decrease of specific capacity of the final material. Despite these shortcomings, the ternary composite was prepared and with the targeted morphology, consisting of a cellular network of interconnected cavities, a few tens of nanometers wide, formed by the graphene oxide sheets, with the nanoparticles interspersed throughout the volume of the material.

The results of the tests with the ternary material in half-cells with lithium were surprising. Lithium insertion and extraction seem to take place at an elevated potential versus Li^+/Li, which would account for the low voltages of the cells and the low amount of lithium transferred. According to the galvanostatic measurements, once almost all of the lithium has been extracted from the material, it undergoes a redox reaction at near-equilibrium. The potential value at which the plateau occurs may be either proportional to the amount of Sn nanoparticles or inversely proportional to the amount of functionalized rGO. Without a postmortem analysis of the cycled cells, it is impossible to identify the species that are oxidized/reduced in such a complex system. While the measurements were not conducted at the intended operating parameters, four different samples with three different Sn loadings exhibited the same behavior. It was markedly different from that of the control sample with the non-functionalized rGO matrix. From the latter, a possible conclusion that could be drawn would be that the material exhibits chemical/structural transformations during cycling, which allow it to progressively reach and exceed its theoretical capacity.

2. Perspectives

A lot of open questions remain at the conclusion of this study. The first and most pressing one being if the functionalization of the matrix with the EMI^+TFSI^- ionic liquid does indeed hamper the functioning of the material as an electrode and if yes, by what mechanism. To keep things simple, cyclic voltammetry with functionalized rGO as an electrode might be able to provide some fast answers. If the results of the first tests are indeed reproducible, and the mechanism is identified, the next logical question would be if that effect could be somehow alleviated.

It was mistakenly assumed that the protection afforded against oxidation to the nanoparticles by the coating of rGO would also protect them from oxidation in aqueous suspensions. Quantifying the amount of SnO that forms during that step and during thermal annealing, at least on average, should be fairly easy to accomplish, *e.g.* via TG analyses under inert atmosphere and air.

The evolution of the capacity of the control sample during cycling is indicative of the material undergoing electrochemically induced changes. Considering the commonalities of the IL-rGO-Sn and the rGO-Sn systems, an explanation of the observed behavior is worth pursuing.

If the issue with the functionalized matrix can be resolved, the protocols established for the treatments with hydrazine and hydrogen peroxide at different stages of the preparation of the material could be applied. The treatment with hydrazine vapors was found to enhance the mechanical stability of the matrix, while decreasing the pore size. After thermal reduction, the integration of nitrogen atoms in the lattice could prove advantageous to the functioning of the anode, as it can facilitate electron transfer. Carving mesopores to the structure via the treatment with H_2O_2 might make more material readily available to the incoming lithium ions and also lead to increased C-rates, by multiplying the paths available

to the ions.

The tin nanoparticles wrapped in graphene oxide or graphite could be used in other applications, for instance conductive inks. It would be interesting to optimize further their production, by performing the fine grinding with smaller media, *e.g.* grinding balls with a diameter of 0.5 or 0.2 mm. Preparing oxygen-free nanoparticles, perhaps by degassing graphite under elevated temperature, would also be worthwhile.

The degree of compression of the ternary composite material that would achieve the best compromise between gravimetric capacity and volumetric capacity was meant to be investigated once the material had been prepared, but there was no time. Also, as the material gets compressed, the contact surfaces between graphene sheets increase, which should have an appreciable effect on electrical conductivity.

Touching once more on the subject of porosity, a scheme that could be employed to create hierarchical porosity in the aerogels would be the use of binary solvent mixtures. In short, the addition of a second solvent that interacts with water can influence the organization and growth of ice crystals during freeze-casting. This was briefly investigated, but was not attempted, out of concern for the lyophilizer, which was not suitable for working with solvents other than water.

Appendices

Appendix A: Principle of X-ray photoelectron spectroscopy

The basis of XPS is the photoelectric effect. When electromagnetic radiation of sufficiently high energy hits a material, electrons are emitted. It stands to reason that the binding energy of the electrons in the orbital from which they were ejected will be equal to the energy imparted by the incoming photons minus the kinetic energy of photoelectrons (electrons emitted in this manner):

$$E_{binding} = E_{photon} - E_{kinetic} \qquad \text{(Equation 1)}$$

As the name implies, the electromagnetic radiation employed in XPS is X-Rays and their energy can be high enough to tear off core electrons from the atoms in a sample. Collecting these photoelectrons and measuring their energy and number can produce useful information about the composition of a material, such as the relative atomic abundance and the types of chemical bonds. In practical applications such as XPS and related photoemission spectroscopies, the above equation will contain an extra term, a work function ϕ related to energy losses in the instrument as the photoelectrons are driven to an appropriate detection system. This term is constant for a given instrument configuration and does not vary in a set of consecutive measurements, but it must be accounted for in all calculations, so as to obtain meaningful results from the spectral analyses. Consequently, the previous equation is modified to this:

$$E_{binding} = E_{photon} - E_{kinetic} - \phi \qquad \text{(Equation 2)}$$

2.1. Instrumentation

The basic components of an XP spectrometer are the X-Ray source, the chamber in which the sample is placed and which is kept at high or ultra-high vacuum during the measurement, an electromagnetic lensing system that gathers, focuses and guides the emitted photoelectrons and the analyzer. These are presented in Figure 1. An XPS system at

the Institute of Chemical Engineering Sciences in Patras, Greece is shown in Figure 2.

The X-Ray source consists of a metallic or sometimes bimetallic anode, usually made of Cu, Al, Mg, Ag or less frequently Zr, Y, Ti or other metals. In all recent hardware, the radiation is monochromated.

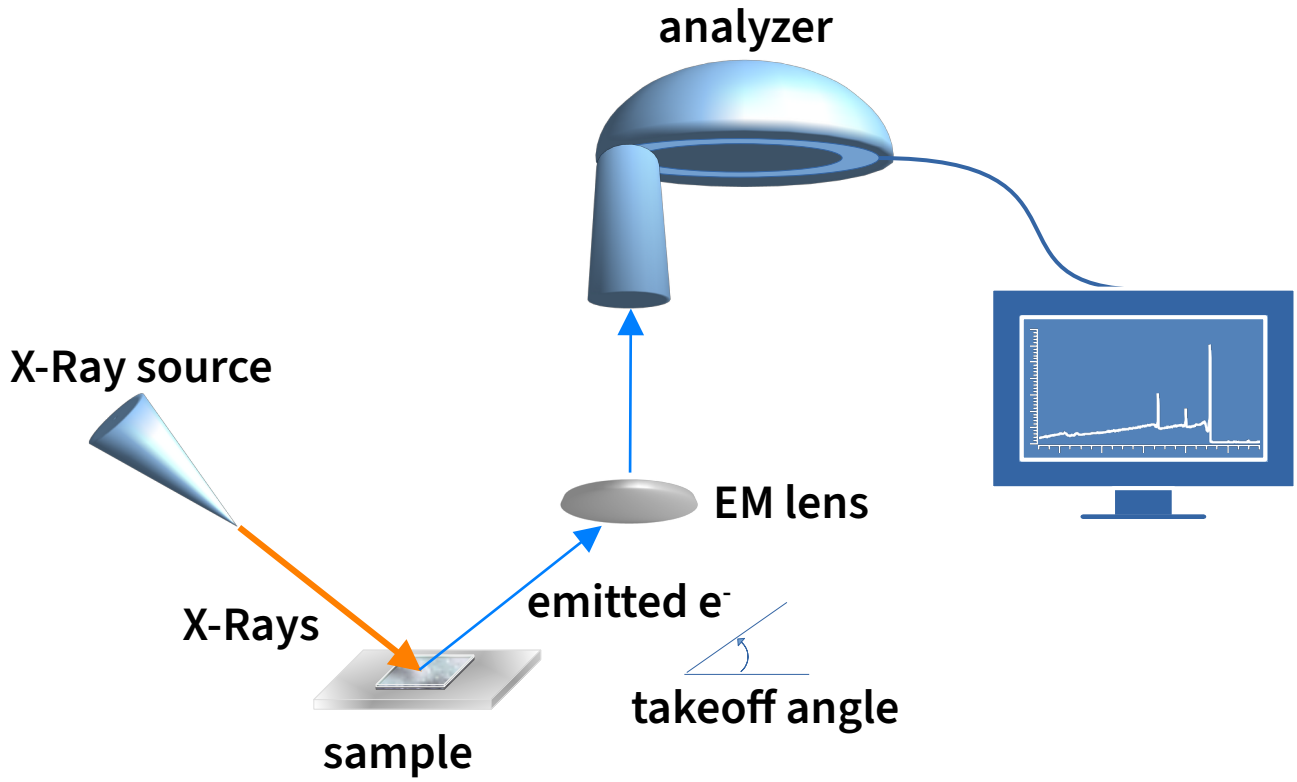

Figure 1: Main components and basic operation of an XPS system.

The most employed analyzer is the hemispherical type, which is made of two concentric, hemispherical metal plates. A voltage is applied between them, creating an electric field which forces incoming photoelectrons to follow a circular trajectory. As a result, photoelectrons with higher kinetic energies will land further than those with lower energies. At the antipodal zone to the entryway, there is a series of detectors, which record the number of photoelectrons.

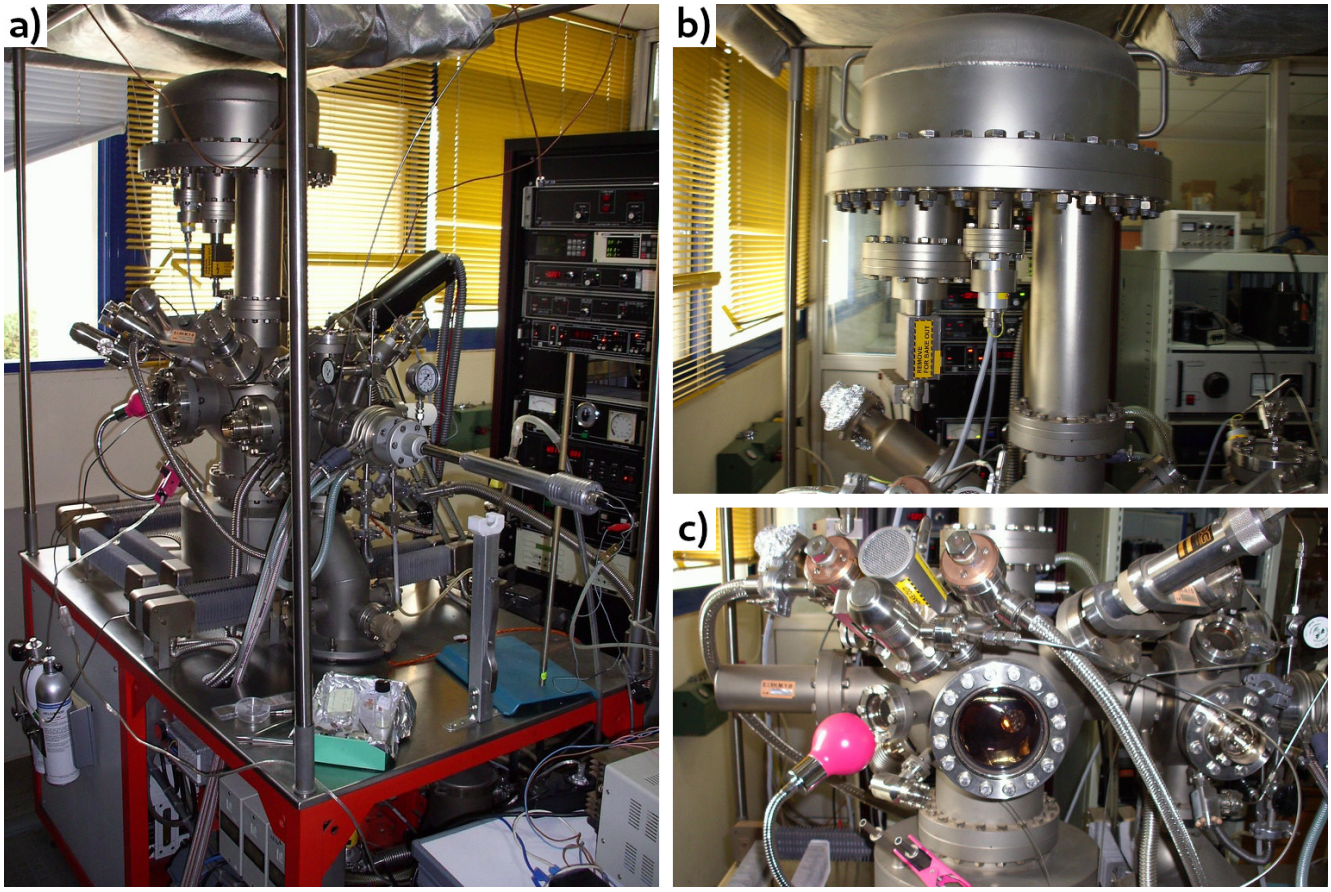

Figure 2: a) XP spectrometer at the Institute of Chemical Engineering Sciences at Patras, Greece. The X-ray source is inside the black tube towards the back. b) view of the detector. c) sample chamber.

2.2. Measurement

The sample to be analyzed, which is usually solid, as the measurement takes place in high vacuum, is inserted in the main chamber of the instrument. The angle of the incoming X-rays can be selected so as to achieve the desired probing depth; beams nearly parallel to the sample surface (at a grazing angle) will expel electrons only from the outermost layer of the sample, whereas beams almost perpendicular to its surface will result in the extraction of electrons from as deep as the radiation wavelength and the composition of the sample (which dictates the mean free path length) permit. In practice, the different combinations of incidence angles and material compositions result in probing depths of a few to a few hundred nanometers. Measuring the same sample at different angles can be useful for

layered structures.

Photo-emitted electrons may take part in inelastic collisions, they might recombine with electron-deficient areas of the material or otherwise get trapped or deflected. The probability of such events increases with the depth, so the signal from analytes in the lower strata will be attenuated with respect to that from layers closer to the surface. This has to be taken into account when performing an analysis, but at the same time it can be used to estimate the depth at which different species are located within a layered sample.

The photoelectrons that escape from the bombarded material are gathered and focused by an electromagnetic lensing system, which guides them towards the analyzer. There, they are separated based on their kinetic energies and their number is counted depending on which of the concentric series of detectors they land on.

The samples are first scanned at a high pass energy (survey scan), in order to locate and identify the different signals emitted from all the analytes that are present. A subsequent scan at low pass energy (high-resolution scan) is conducted to get a more precise image of each signal and to allow quantification.

Within the structure of the materials, the atomic ratios can be calculated by dividing the peak area of each core-level signal by the corresponding relative sensitivity factor (RSF), after making the appropriate corrections related to the nature of the sample, the instrumentation and operating conditions. Complex signals are deconvoluted into separate components, which in turn yield the ratios of atoms of the same element that take part in different bonds, as the position (chemical shift) of each constituent signal depends on the degree of electron bond polarization between nearest-neighbor atoms[1].

Appendix B: Synthesis of Sn nanoparticles in EMI^+TFSI^-

Anhydrous tin(II) chloride (purity ≥ 99.99%) and sodium borohydride (purity 99%) were purchased from Sigma-Aldrich, 1-ethyl-3-methylimidazolium bis(trifluoromethanesulfonyl) imide (purity 99.9%) was purchased from Solvionic. A typical synthesis was carried out as follows:

Everything was prepared in a glovebox with Ar gas atmosphere, with O_2 and H_2O levels kept below or up to 1 part per million. 7.6 mg of $SnCl_2$ (~0.04 mmol) was introduced in a 10 mL vial and dispersed via stirring in 1 mL of EMI^+TFSI^-. In another vial, 15.2 mg of $NaBH_4$ (~0.4 mmol) was dispersed in 1 mL of EMI^+TFSI^-. The two solutions were left stirring on a magnetic stirrer overnight.

The following day, the solution of $SnCl_2$ was siphoned to that of $NaBH_4$, under constant stirring. Within seconds, the resulting solution turned brown and during the first minute, one could observe the formation of black “clouds” in the suspension.

After six hours, the mixture was siphoned into two 1.5 mL eppendorf tubes, which were sealed and removed from the glovebox. The two tubes were centrifuged for 10 minutes at 10000 rpm and then a series of washing steps was performed under N_2 flow, in order to prevent the oxidation of the nanoparticles:

- After discarding the supernatant, the solid in each tube was redispersed in 1 mL of acetonitrile using a vortex mixer (1 min), in order to wash off the remaining ionic liquid. The tubes were centrifuged at 6000 rpm for 5 minutes, after which the supernatant was again discarded. This was repeated a total of seven times. Three more washes were performed in acetone (1 mL in each tube).

- Next, in order to remove the inorganic salts (NaCl and $NaBH_4$) that remained with the nanoparticles, the solid in each tube was redispersed in 0.5 mL of ultra-pure water

with the help of a vortex mixer and then isolated by centrifugation at 10000 rpm for 5 minutes.

- Finally, the solid in each tube was redispersed in 1 mL of acetone with the aid of a vortex mixer and recovered by centrifugation at 6000 rpm for 5 minutes. This was repeated twice, so as to remove any traces of water from the previous washing step. The solid was then dried by flowing N_2 gas through the residue.

The recovered nanoparticles were returned to the glovebox and stored there. At the end of the synthesis, we would usually obtain 2.1-2.5 mg of Sn nanoparticles, so the yield of the synthesis was up to 52%.

Appendix C: On size reduction

The observation that size reduction leads to surface area increase, which is often the intended purpose, can be viewed as the starting point of the basic laws that govern size reduction processes. The thermodynamic work (dW) required to create new surface area (dA) is equal to the decrease of the Gibbs free energy (dG):

$$dW = -dG \text{ or } \Delta W = -\Delta G \qquad \text{(Equation 3)}$$

If σ is the surface energy, or, equivalently, the work required per unit of surface area increase (J/m^2), then:

$$dG = \sigma dA \text{ or } \Delta G = \sigma \Delta A \qquad \text{(Equation 4)}$$

Since σ is a constant and $\Delta A > 0$, then $\Delta G > 0$, which means that the phenomenon of surface area increase is not spontaneous, something also confirmed by experience. As a result, it requires a work expenditure of $\Delta W = -\Delta G$.

Even if the energy losses in the mechanisms of each size-reduction apparatus are not taken into account, the calculations of energy requirements remain incredibly complex. A lot of the energy provided to the material is absorbed by elastic deformations or wasted as heat by the friction between particles or between the particles and the machine. Besides, a volume deformation always precedes fracturing. Leaving friction losses aside, the total useful work required for size reduction should be equal to the sum of the deformation work

$$W_d = k\Delta V \qquad \text{(Equation 5)}$$

and the work required to form new surface area:

$$W_S = \sigma \Delta A \qquad \text{(Equation 6)}$$

which results in the Rebinder equation:

$$W = W_d + W_S = k\Delta V + \sigma\Delta A \quad \text{(Equation 7)}$$

where k is a constant, equal to the deformation work per unit of material volume V.

During the fracturing of large pieces more energy is spent in elastic deformation than size reduction, so $k\Delta V \gg \sigma\Delta A$. In that case, the term $\sigma\Delta A$ can be omitted and the Rebinder equation transforms into equation 5, which is essentially Kick's hypothesis. Kick's Law (1885) – a semi-empirical model – states that the work required to reduce the size of a given quantity of material is constant for the same reduction ratio and is usually presented in the form:

$$\frac{N}{M} = K_K \ln\left(\frac{x_1}{x_2}\right) \quad \text{(Equation 8)}$$

where: N is the axial power of the machine in Watts, M is the feed rate in kg/s, K_K is the Kick constant for a given machine/product system in J/kg and x_1, x_2 are the average particle sizes before and after fracturing.

Conversely, during fine grinding, where the ratio of reduction is great, the term $k\Delta V$ is much smaller than $\sigma\Delta A$, so it can be omitted from the Rebinder equation, which then becomes equation 6. This is the hypothesis behind Rittinger's Law (1867), which states that the work consumed for size reduction is proportional to the new surface created and is usually stated as:

$$\frac{N}{M} = K_R\left(\frac{1}{x_2} - \frac{1}{x_1}\right) \quad \text{(Equation 9)}$$

The Rittinger constant K_R (J·m/kg) for a given system can be calculated from the formula:

$$K_R = \frac{\alpha_{SV}\sigma}{E_c E_m \rho_s} \quad \text{(Equation 10)}$$

with α_{SV} the shape factor (dimensionless), E_c, E_m the efficiency ratio of crushing (size

reduction) and the efficiency ratio of the machine respectively (both dimensionless) and ρ_s the density of the material.

The applicability of Kick's and Rittinger's Laws is scale-dependent. Kick's equation can meaningfully approximate real-world results with particle sizes above ~10 cm, whereas the same holds true for Rittinger's equation when it is applied to systems below ~1 mm. For systems in between these two edge cases, both the deformation and the created surface in the Rebinder equation have to be taken into consideration. Bond (1952) proposed that the work required to form particles of size x_2 from a large feed is proportional to the square root of the surface-to-volume ratio of the product, from which it follows that the work is proportional to the square root of the particle diameter:

$$\frac{N}{M} = K_B\left(\frac{1}{\sqrt{x_2}} - \frac{1}{\sqrt{x_1}}\right) \qquad \text{(Equation 11)}$$

Bond's constant, K_B, is tied to the work index, W_i, through the equation $K_B = 10W_i$. The work index itself is defined as the gross energy required in kilowatt-hours per ton (also called "short ton" = 2000 lb = 907.18474 kg) of feed needed to reduce a very large feed $\left(\frac{1}{\sqrt{x_1}} \approx 0\right)$ to a size such that 80% of the product can pass through a 100 µm screen[2]. As a result of this definition, when Bond's Law (equation 11) is used in calculations, x values should be expressed in µm.

Interestingly, while the "laws" of Kick, Rittinger and Bond were formulated several decades apart and with different assumptions, all three can be derived by integrating the basic differential equation linking work input and size reduction

$$\frac{dW}{dx} = \frac{d\left(\frac{N}{M}\right)}{dx} = -C_x^n \qquad \text{(Equation 12)}$$

for exponent n values of n = -1, n = -2 and n = -3/2 respectively. Accordingly, for each case,

constant C will be equal to K_K, K_R and $5W_i$. Near the limits of applicability of each law, there is some overlap and for a given equipment-material-combination in that range, one may produce more realistic results than the other.

There is an important caveat regarding all of the above equations that contain average particle sizes: how exactly these are defined. The processes employed for size reduction usually produce irregularly-shaped particles and as it has already been mentioned, the smallest particles in a sample may differ from the largest ones by up to four orders of magnitude. There exist a number of definitions of the average size in use: these could be the *volume-surface mean diameter*, the *arithmetic mean diameter*, the *mass mean diameter*, the *volume mean diameter* and others. The particle sizes in different mass or volume fractions of a sample, their number, their shape, *etc.* may be taken into account in these definitions, but presenting them here is beyond the scope of this text; they can be found in most Chemical Engineering and Unit Operations textbooks and manuals. For systems consisting of uniform particles these average diameters would all be identical, but in any other case, they may differ widely. It is therefore crucial to take note which of these is being used each time, *e.g.* when trying to reproduce the results of a documented process.

Finally, the Kick, Rittinger and Bond equations work when a single-component, hard and brittle solid is being comminuted. If the solids are elastic, fibrous or if they are composed of more than one components, they can not be expected to yield meaningful results. This makes it nearly impossible to estimate beforehand the energy requirements and by extension, the processing time required for a desired size-reduction ratio of such samples, that have not been processed before. A study needs to be conducted under a set of operating conditions and consequently, corrective terms should be introduced to the equations.

The actual measurement of the size of the particles before and after size reduction depends on the scale. For macroscopic samples, this is accomplished by sifting the particles through stacks of consecutive screens. These are standardized sieves made of woven wire, with progressively smaller square openings of known dimensions. Dry screening is usually

employed for samples with particle sizes down to a few tens of micrometers. Wet screening, *i.e.* passing the samples through the sieves after they have been dispersed in a liquid, can be of help for smaller particles, typically around 10 μm. However, as the particle size decreases screening is no longer possible, as the electrostatic forces start competing with gravity and in the case of dispersions, the surface tension and capillary forces become important. For these reasons, the analysis of samples consisting of finer particles is performed with the help of other techniques, such as light-scattering or electron microscopy or SAXS.[3,4]

Appendix D: Basics of small-angle X-Ray scattering

Monochromated radiation with a wave vector k_i and intensity I is shone onto a sample and the intensity of scattered radiation is recorded as a function of the scattering angle. Since elastic scattering by definition does not involve any transfer of energy, the magnitudes of the wave vector k_s of the scattered radiation and that of the incident radiation, k_i, will be equal ($|k_s| = |k_i|$). The intensity of scattered radiation I(q) will be a function of the wave vector transfer (also called scattering vector), $q = |k_i - k_s|$ (Fig. 3).

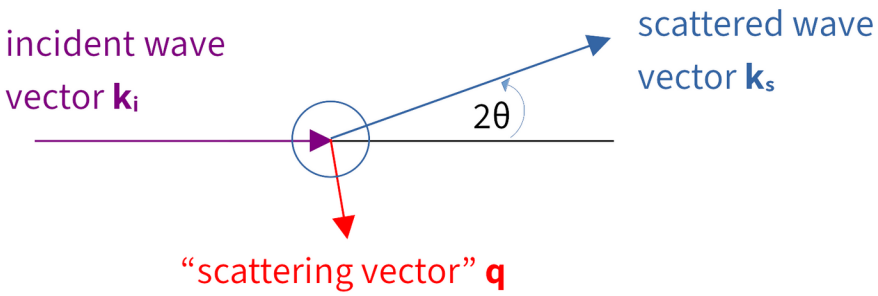

Figure 3: Definition of the scattering vector q used in SAXS.

The magnitude of the scattering vector is defined as:

$$q = \frac{4\pi}{\lambda}\sin\theta \qquad \text{(Equation 13)}$$

where λ is the wavelength of the incident beam and 2θ, the scattering angle.

The intensity of the scattered radiation I(q) for a given system (mixture, suspension, *etc.*) of particles depends on a number of factors, included in the following equation:

$$I(q) = \Delta\rho^2 \Phi_V V_p P(q) S(q) \qquad \text{(Equation 14)}$$

where: $\Delta\rho^2$ is the contrast, Φ_V is the volume fraction of the particles in the system and V_p is the volume of a single particle. P(q) is the shape factor of the particles and is dependent on their geometry (spherical, cubic, needle-like, *etc.*). S(q), the static structure factor (or

structure factor for short) relates the observed diffracted intensity per atom to that produced by a single scattering unit. It can provide useful information about the organization of matter in a sample, such as the arrangement and orientation of scattering particles.[5,6]

Appendix E: Nitrous acid test

To verify the presence of the amine group on the ionic liquid after reduction of the azide, we conducted a nitrous acid test. Primary amines react with nitrous acid to produce unstable diazonium salts, which at room temperature decompose to nitrogen gas.

Two drops of the purified IL were placed in a test tube. To that, 2 mL of HCl 2M was added and the tube was placed in an ice bath. When the mixture had sufficiently chilled, 5 drops of sodium nitrite ($NaNO_2$) aqueous solution 20 wt% were added, in order to generate nitrous acid *in situ*. Soon afterwards, bubbles started to form around the globules of the ionic liquid (Figure 4). The fact that the IL is insoluble in water facilitated the detection of the bubbles, as they formed only on the interface between the two liquids and their evolution lasted a considerable amount of time.

Figure 4: A photograph showing nitrogen bubbles forming on the interface between H_2N-EMI^+TFSI^- and water during a nitrous acid test.

Appendix F: Thermogravimetric analyses of LiBr hydrates

The thermal decomposition profiles of lithium bromide monohydrate dried at high temperature and further hydrated lithium bromide monohydrate are presented in Fig. 5. In both cases, the starting compound was lithium bromide hydrate (purity 99.999%, Sigma-Aldrich). The first sample (Sample 1) was dried in a drying oven at 180°C for 2 h prior to the measurement. The second sample (Sample 2) was prepared by first dissolving a quantity of $LiBr{\cdot}H_2O$ in deionized H_2O and then evaporating the water in a drying oven at 80°C for 3 hours prior to the measurement.

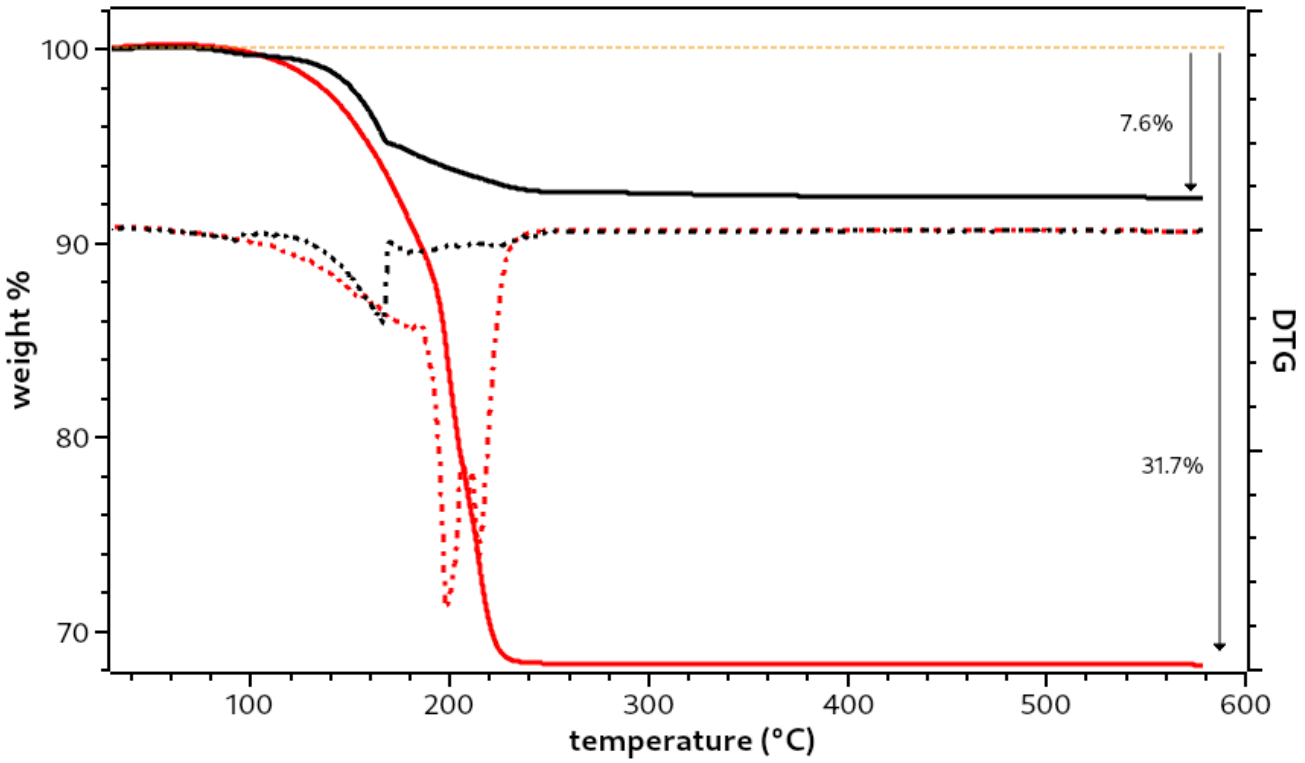

Figure 5: Thermogravimetric analyses (solid lines) and DTG (dotted lines) of LiBr hydrates Sample 1 (black curves) and Sample 2 (red curves) under inert atmosphere (N_2).

Based on the weight loss, Sample 1 could be identified as the hemihydrate (7.58 wt%) and Sample 2 as the dihydrate (31.71 wt%). However according to the literature[7–9], it is very likely that different hydrates coexist in the sample and there does not seem to be an agreement on whether the hemihydrate form actually exists. Based on the phase diagram (Fig. 6) compiled

by Herold and Radermacher[10], the hemihydrated salt corresponds more likely to a mixture of anhydrous LiBr and its monohydrate.

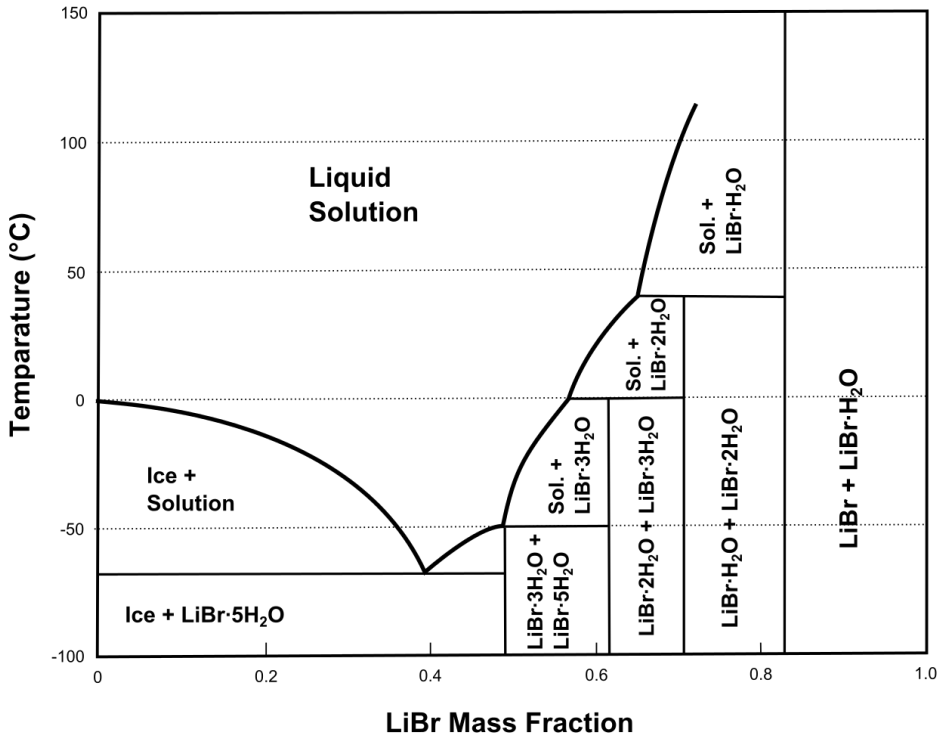

Figure 6: Aqueous lithium bromide phase diagram. Reprinted from [10].

References

(1) Watts, J. F.; Wolstenholme, J. *An Introduction to Surface Analysis by XPS and AES*; 2003.

(2) Bond, F. Crushing & Grinding Calculations Part I. *British Chemical Engineering* **1961**, *6* (6), 378–385.

(3) Σδούκος, Α. Θ. *Φυσικές Διεργασίες της Χημικής Τεχνολογίας*, 1st ed.; Πανεπιστήμιο Ιωαννίνων: Ιωάννινα, 1982; Vol. 1. (Sdoukos, A. T. *Physical Processes of Chemical Technology*, 1st ed.; University of Ioannina: Ioannina, 1982; Vol. 1 – text in Greek)

(4) McCabe, W. L.; Smith, J. C.; Harriott, P. *Unit Operations of Chemical Engineering*, 5th ed.; McGraw-Hill: New York, 1993.

(5) *Small Angle X-Ray Scattering*; Glatter, O., Kratky, O., Eds.; Academic Press: London ; New York, 1982.

(6) Sinha, S. K.; Sirota, E. B.; Garoff, S.; Stanley, H. B. X-Ray and Neutron Scattering from Rough Surfaces. *Phys. Rev. B* **1988**, *38* (4), 2297–2311. https://doi.org/10.1103/PhysRevB.38.2297.

(7) Khandkar, A. C.; Wagner, J. B. On the Thermodynamics of $LiBr{\cdot}xH_2O$(x=0, 1/2, 1) and Electrical Conductivity of $LiBr{\cdot}xH_2O(Al_2O_3)$ Composites. *Solid State Ionics* **1986**, *20* (4), 9. https://doi.org/10.1016/0167-2738(86)90045-7.

(8) Apelblat, A.; Tamir, A. Enthalpy of Solution of Lithium Bromide, Lithium Bromide Monohydrate, and Lithium Bromide Dihydrate, in Water at 298.15 K. *The Journal of Chemical Thermodynamics* **1986**, *18* (3), 201–212. https://doi.org/10.1016/0021-9614(86)90048-0.

(9) Lefebvre, E.; Bennici, S.; Gagnière, E.; Mangin, D.; Auroux, A. Hydration Characteristics of Lithium, Zinc, Potassium and Sodium Salts. *MATEC Web of Conferences* **2013**, *3*, 01003. https://doi.org/10.1051/matecconf/20130301003.

(10) Herold, K. E.; Radermacher, R., Klein, S. A. *Absorption Chillers and Heat Pumps*, 2nd ed.; CRC Press: Boca Raton, 2016.